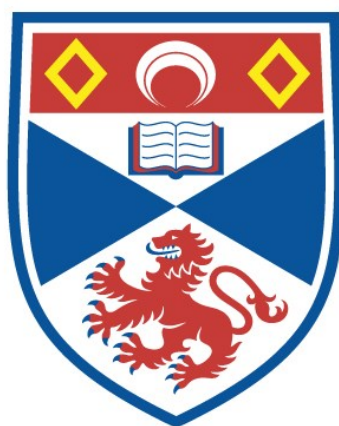


# HOLOSTERIC ND : YAG LASERS

Callum Norrie

A Thesis Submitted for the Degree of PhD  
at the  
University of St Andrews



1991

Full metadata for this item is available in  
St Andrews Research Repository  
at:

<http://research-repository.st-andrews.ac.uk/>

Please use this identifier to cite or link to this item:

<http://hdl.handle.net/10023/13755>

This item is protected by original copyright

# Holosteric Nd:YAG Lasers

A thesis submitted for the degree of Doctor of Philosophy to  
the University of St. Andrews

by

Callum Norrie, B.Sc.

November 1990





ProQuest Number: 10167414

All rights reserved

INFORMATION TO ALL USERS

The quality of this reproduction is dependent upon the quality of the copy submitted.

In the unlikely event that the author did not send a complete manuscript and there are missing pages, these will be noted. Also, if material had to be removed, a note will indicate the deletion.



ProQuest 10167414

Published by ProQuest LLC (2017). Copyright of the Dissertation is held by the Author.

All rights reserved.

This work is protected against unauthorized copying under Title 17, United States Code  
Microform Edition © ProQuest LLC.

ProQuest LLC.  
789 East Eisenhower Parkway  
P.O. Box 1346  
Ann Arbor, MI 48106 – 1346

TH A1405

## ACKNOWLEDGEMENTS

I wish to express my thanks to my supervisor Prof. Wilson Sibbett, to Prof. Malcolm Dunn and to Dr. Bruce Sinclair for their continued encouragement and expertise.

This thesis was undertaken as part of an RARDE contract under the direction of Dr. David Hull and Mr. Robert Lamb.

Thanks must also go to my CASE industrial supervisors Mr. Martin Lawrence & Mr. Alan Levenston at the British Aerospace Research Centre.

I would also like to mention Eileen, Myles, Andy, Fiona, Angus, Martina, Graham, Christina, Bruce and Marina for the hard time they gave me whilst I was in St. Andrews.

Finally, sincere thanks to my mum, dad and sister for their unfailing support throughout my studies.

## DECLARATIONS

I, Callum J. Norrie, hereby certify that this thesis has been composed by myself, that it is a record of my own work, and that it has not been accepted in partial or complete fulfilment of any other degree or professional qualification. I was admitted to the Faculty of Science of the University of St. Andrews as a candidate for the degree of Ph.D on October 1986.

In submitting this thesis to the University of St. Andrews I understand that I am giving permission for it to be made available for use in accordance with the regulations of the University Library for the time being in force, subject to any copyright vested in the work not being affected thereby. I also understand that the title and abstract will be published, and that a copy of the work may be made and supplied to any bona fide library or research worker.

C. Norrie

November 1990

I hereby certify that the candidate has fulfilled the conditions of the Resolution and Regulations appropriate to the Degree of Ph.D.

W. Sibbett

Research Supervisor

November 1990

## ABSTRACT

A miniature Nd:YAG laser that was transversely pumped by a quasi-cw laser-diode array has been designed and constructed. This laser was injection seeded by a continuous wave single-frequency Nd:YAG laser that was also pumped by a laser-diode array. This was the first reported holosteric, or *all-solid-state*, laser that was capable of generating single frequency pulses in a high quality single transverse mode beam which it achieved at peak powers up to 7 kW.

Two different types of laser-diode array were used in this work, and both have been characterised with respect to their use as pump sources for solid-state lasers. A fibre-coupled type SDL-2430-H2 laser-diode array, which emitted 100 mW from the end of a 100  $\mu\text{m}$  core diameter fibre at the Nd:YAG absorption wavelength of 809 nm, was used to longitudinally pump a continuous wave Nd:YAG laser. Spatial hole-burning encouraged this laser to operate on several longitudinal modes, with an output power of up to 31 mW. With the addition of an etalon and a Brewster angled plate to the cavity of this laser, single longitudinal mode operation was achieved at an output power level of 10 mW. The frequency from this laser was stabilised against thermal drift by phase sensitive locking to the resonance of an external reference cavity.

The pump source for the transversely pumped Nd:YAG laser was an SDL-922-J quasi-cw laser-diode bar, which emitted from its 1 cm wide aperture pulses of 200  $\mu\text{s}$  duration with energies up to 5 mJ at repetition rates between 10 - 100 pps. The characteristics of this laser-bar that were measured include a frequency chirp of 5 nm through the pulse, which was found to have a significant effect on the pumping of the Nd:YAG medium. An analysis of the pump-rate distribution throughout the Nd:YAG laser-rod was undertaken with reference to the transverse mode structure of this laser. This was used as the basis of a full rate-equation-based model of the transversely pumped laser. Fundamental transverse mode pulses with energies of 1.1 mJ were

generated when the aperture provided by the Nd:YAG rod itself was used to suppress higher order modes.

Upon Q-switching the transversely pumped laser using an acousto-optic modulator, single transverse mode pulses with peak power of up to 13 kW were produced. This laser was induced to operate on a single longitudinal mode by injection seeding with the single frequency diode-pumped laser. Operating at a peak power of 7 kW, this holosteric laser was particularly "well-behaved" with a pulse-to-pulse intensity stability of 6% over 100 pulses. A LiNbO<sub>3</sub> electro-optic Q-switch configuration was implemented as optical damage to the acousto-optic component had limited the intracavity flux intensity. Development of these lasers towards higher peak power microlaser systems for applications including range-finding and surgery is continuing.

## Contents

### Chapter 1 : Introduction

1.1	A short history of holosteric lasers .....	1
1.2	Thesis outline .....	4

### Chapter 2 : Laser-diode pumps for solid-state lasers

2.1	Introduction to laser-diodes .....	7
2.1.1	Single-stripe laser-diodes .....	8
2.1.2	Quantum-well laser-diodes .....	9
2.1.3	Catastrophic facet damage .....	9
2.1.4	Coherent linear arrays .....	11
2.1.5	Laser-diode bars .....	13
2.1.6	Surface-emitting laser-diodes.....	15
2.2	Cw laser-array characterisation .....	16
2.2.1	Optical power calibration.....	17
2.2.2	Electrical-optical efficiency .....	17
2.2.3	Transverse mode structure.....	18
2.2.4	Longitudinal mode structure.....	19
2.3	Laser-bar characterisation.....	20
2.3.1	Laser-bar protection .....	21
2.3.2	Optical power characterisation.....	22
2.3.3	Transverse mode structure.....	23
2.3.4	Temperature control of laser-bars.....	23
2.4	Conclusions .....	29

Chapter 2 references

Chapter 2 figures

### Chapter 3 : Cw Nd:YAG laser longitudinally pumped by a cw laser-diode array

3.1	Introduction .....	31
3.2	Nd:YAG gain medium .....	32
3.2.1	Spectroscopy of Nd:YAG .....	33
3.2.2	Diode-array pump absorption in Nd:YAG.....	34
3.3	Miniature end-pumped laser-cavity.....	35
3.3.1	Mode-waist-geometry .....	36
3.3.2	Dye laser excitation .....	38
3.4	Pumping with fibre-coupled laser-diodes.....	38
3.4.1	Experimental arrangement .....	38
3.4.2	Modelling of fibre-coupling .....	39
3.4.3	Overcoming aberrations.....	41
3.5	Performance of diode-pumped cw Nd:YAG laser.....	42
3.5.1	Optical power characteristics .....	42
3.5.2	Transverse mode structure and beam divergence .....	42
3.5.3	Loss measurements.....	43
3.6	Output power model for cw microlaser .....	44
3.6.1	Pump beam profile.....	45
3.6.2	Pumping rate .....	45
3.6.3	Rate equation analysis.....	47
3.6.4	Single-pass gain.....	49
3.6.5	Results .....	50
3.7	Longitudinal mode characteristics .....	51
3.7.1	Spatial hole burning .....	51
3.7.2	Single-frequency operation .....	52
3.7.3	Frequency stability.....	55



3.8	Dynamic laser behaviour.....	59
3.8.1	Relaxation oscillations.....	59
3.8.2	Small amplitude modulation of pump .....	61
3.8.3	Large amplitude modulation .....	62
3.9	Conclusions .....	63

Chapter 3 references

Chapter 3 figures

#### **Chapter 4 : Long-pulse operation of a Nd:YAG laser transversely pumped by a quasi-cw laser-diode bar**

4.1	Introduction .....	64
4.2	Nd:YAG laser configuration .....	65
4.3	Characterisation of long-pulse operation.....	67
4.3.1	Transverse mode structure.....	67
4.3.2	Output power.....	69
4.3.3	Longitudinal mode characterisation.....	70
4.4	Pump-rate distribution .....	74
4.4.1	Absorption of laser-bar pump emission by Nd:YAG crystal .....	74
4.4.2	Small-signal-gain distribution .....	76
4.5	Modelling of quasi-cw side-pumped Nd:YAG laser .....	78
4.5.1	Introduction.....	78
4.5.2	Pump-rate distribution.....	79
4.5.3	Mode-overlap Formalism.....	82
4.5.4	Thresholds for both TEM <sub>00</sub> and TEM <sub>01</sub> modes.....	84
4.5.5	Single transverse mode output power .....	87
4.6	Conclusions .....	89

Chapter 4 references

Chapter 4 figures

## **Chapter 5 : Q-switching of Nd:YAG holosteric lasers**

5.1	Introduction .....	91
5.1.1	Pumping interval.....	92
5.2	Acousto-optic Q-switching .....	93
5.3	Repetitive acousto-optic Q-switching of cw-pumped laser .....	95
5.4	Synchronised AO Q-switching of pulse-pumped laser.....	96
5.4.1	Initial cavity configuration .....	96
5.4.2	Second cavity configuration .....	97
5.5	Electro-optic Q-switching of pump-pulsed laser.....	107
5.5.1	Cavity configuration.....	108
5.5.2	Cavity dump Q-switching.....	109
5.6	Conclusions .....	110
5.7	Chapter 5 Appendix - Q-switch devices .....	112
5.7.1	Newport AO Q-switch & driver.....	112
5.7.2	Isle Optics AO Q-switch & driver.....	112
5.7.3	Lasermetric EO Q-switch & driver.....	113

Chapter 5 references

Chapter 5 figures

## **Chapter 6 : General conclusions and future work**

115

## **Publications**

## Chapter 1

### Introduction

---

#### 1.1 A short history of holosteric lasers

The first use of semiconductor sources to pump a solid-state laser was by Newman in 1963, who showed that gallium arsenide (GaAs) incoherent light emitting diodes (LEDs) with emission wavelengths of 880 nm excited fluorescence at 1.064  $\mu\text{m}$  in Nd:CaWO<sub>4</sub> [1.1]. Newman was aware of the technological significance of his work, though it was to be over 20 years before its potential would be realised in a truly practical system. Laser action was observed in a gallium arsenide diode by Hall et al in 1962, and it is the great advancement in semiconductor laser technology since then that has fostered the interest in holosteric lasers [1.2]. The first pumping of a solid-state laser by a laser-diode, which was reported by Keyes and Quist in 1964, consisted of five GaAs laser-diodes ( $\lambda = 840 \text{ nm}$ ) which pulse pumped an U<sup>3+</sup>:CaF<sub>2</sub> crystal rod ( $\lambda = 2.613 \mu\text{m}$ ), with the entire laser enclosed within a liquid helium filled dewar [1.3].

Nd:YAG crystal became a popular gain medium in the 1960's because of its excellent optical and spectroscopic characteristics and was established as an obvious candidate for excitation by laser-diodes. This was duly achieved by Ross in 1968 with a transversely pumped laser employing a single GaAs laser-diode cooled to 170 K to pump the weak 867 nm absorption band [1.4]. Pumping of the stronger 810 nm absorption band by a gallium-arsenic-phosphide (GaAsP) LED was reported in 1973 by Draegert [1.5], who also noted that this pump wavelength was achievable at room temperature by gallium-aluminium-arsenide (GaAlAs) laser-diodes; a combination that was later to prove most effective.

Longitudinal pumping was demonstrated as an alternative to transverse pumping of holosteric lasers by Chesler & Draegert in 1973, when they used a GaAsP LED to

pump a Nd:YAG rod at 860 nm [1.6]. As the brightness of this source was low, the sides of the thin rod were coated to reflect unabsorbed pump light to maintain a high pumping intensity along the length of the rod. This waveguide approach to increasing pump power densities was extended though the use of fibres as the active medium by Stone & Burrus in 1974 with the pumping of a Nd:glass fibre laser by a GaAs laser-diode [1.7]. Diode-pumped fibre lasers have since increased in importance to become a distinct and technologically important topic which now includes erbium doped fibre amplifiers operating at 1.5  $\mu\text{m}$  [1.8].

The first instance in which the enhanced brightness of laser-diodes over LED sources was used to advantage was by Rosenkrantz in 1973 when he used a GaAs laser-diode to longitudinally pump a bulk Nd:YAG laser [1.9]. However, as the concentration of the  $\text{Nd}^{3+}$  in YAG is limited to a maximum of 1.4% by crystal stress, attention turned to stoichiometric materials in which the active ion is not a dopant, but is a component of the crystal lattice itself. Laser-diode pumping of the stoichiometric  $\text{NdP}_5\text{O}_{14}$  (NPP) was reported by Chinn et al in 1975 [1.10], though  $\text{LiNdP}_4\text{O}_{12}$  (LNP) became the preferred stoichiometric material because of its yet higher neodymium concentration and its resultant lower threshold was demonstrated by Saruwatari in 1976 [1.11]. LNP is now receiving renewed interest because of its use in “micro-chip” or “cube-lasers”, because the short cavity lengths and resultant single-longitudinal mode operation that the high absorption permits [1.12,1.27].

The recent upsurge of interest in holosteric lasers had to await the development of high power coherent laser-diode arrays by Scifres et al in 1982, which opened the way to sources of significant brightness and intensity [1.13]. It was not though until 1985 that the first pumping of a Nd:YAG laser with a laser-diode array was reported by Sipes [1.14]. In 1987 the practicality of such a laser was demonstrated by Berger et al who achieved cw output power of 370 mW in a single-transverse mode from a Nd:YAG laser pumped by a single array [1.15]. Berger and coworkers then increased the pump power to a longitudinally diode-pumped laser to 1.9 W by using optical fibres to couple

together the output from seven laser diodes [1.16]. Ongoing research into increasing the brightness from laser-diodes includes further developments such as surface emitting laser-diodes, with the prospect of increasing further the power which may be effectively coupled into longitudinally pumped lasers [1.17].

The quality of the output achievable from a holosteric laser was first realised by Zhou et al in 1985, with the demonstration of a monolithic Nd:YAG laser which had frequency jitter of less than 10 kHz [1.18]. Motivated by the need of a source for gravitational wave detection using laser interferometry, linewidths have been reduced with the aid of active stabilisation to around 1 mHz [1.19]. Narrow linewidth holosteric lasers have also been injection locked and it is conceivable that relatively high powered lasers may be constructed from phase-locked laser modules [1.20].

With the development of the high power quasi-cw laser-bar by Harnagel et al in 1986, research interest was reawoken in the transverse pumping configuration that had previously employed LED's [1.21]. The greatly enhanced power and intensity from these laser-bars made the transverse pumping configuration eminently more practical and effective as highlighted by Hanson & Haddock in 1988 [1.22]. Stacking of laser-bars has since resulted in an efficient pump module capable of delivering 60 mJ, which, along with the obvious scalability of the transverse pumping configuration, has encouraged the belief that laser-bars will progressively replace the comparatively inefficient flashlamp. The potential of the combination of high output power with excellent beam quality that was demonstrated by the injection-seeded transversely pumped Q-switched laser of Norrie et al [1.23], has recently been dramatically manifested by Burnham et al in a laser/amplifier combination that was capable of generating green frequency doubled 450 mJ pulses in a single longitudinal mode [1.24].

In the recent flurry of research into holosteric lasers, the monolithic non-planar Nd:YAG ring laser demonstrated by Kane & Byer in 1985 has been particularly

significant [1.25]. Designated not too attractively as the MISER, this laser produces a cw single longitudinal mode beam with a frequency stability of 1 kHz in 1 ms [1.26]. Another example that shows holosteric lasers to be a distinct laser genre rather than a hybrid of laser-diodes and flashlamp pumped lasers is represented by the tightly folded resonator laser. This miniature Nd:YAG slab laser uses the distinct multiple dual-lobed beam pattern from a monolithic bar of ten coherent diode-arrays, to combine the scaling capability of transverse pumping with the efficiency of longitudinal pumping. Demonstrated by Baer and colleagues in 1989, this laser generated a remarkable 3.8 Watt cw in the fundamental transverse mode when pumped by a single 10 W cw laser-bar [1.28].

---

## 1.2 Thesis outline

Fundamental to the progress made in the field of holosteric lasers has been the remarkable advances made in the performance of laser-diodes. In Chapter 2 this progress is traced from the basic homojunction laser-diode through to the phase-locked laser-diode array and the laser-bar, with the emphasis on the high-brightness operation required for longitudinal pumping of holosteric lasers and the high power required for transverse pumping. Two types of laser-diodes with emission wavelengths around 809 nm were used in this research; a fibre-coupled continuous-wave SDL-2430-H2 which emitted 100 mW and a quasi-cw SDL-922 laser-bar which emitted 5 mJ pulses at repetition rates up to 100 pps. A full characterisation of these laser-diodes including their output power, their transverse and longitudinal modes, and the influence of temperature on their performance, all of which are critical to an understanding of the pumping process, are discussed in later chapters.

In Chapter 3 the design, construction and optimisation are described for a cw Nd:YAG laser which was longitudinally pumped by a fibre-coupled laser-diode array. The pumping process is examined in terms of the optimum pump and cavity mode waists to



ensure oscillation in the fundamental transverse mode. A full rate-equation-based model is derived which relates the output power to pump power, with theoretically predicted results compared with those taken experimentally. This cw laser was designed and constructed as a source for injection seeding the transversely pumped Q-switched laser described in chapter 5. To achieve the necessary single longitudinal mode for injection seeding, both etalon based and twisted-mode cavity schemes were investigated. The influence of relaxation oscillations on the frequency stability of this laser is discussed together with results taken when active stabilisation was employed.

Progress towards higher power and higher energy operation of holosteric lasers has involved pumping of the gain medium transversely to the axis of the resonator as a larger number of laser-diodes may be employed in the pumping process. Chapter 4 describes the operation of a Nd:YAG laser that was transversely pumped by a single quasi-cw laser-diode bar and is an initial step towards considerably higher power. Because of the transverse nature of the pumping, careful cavity design was necessary to attain TEM<sub>00</sub> operation from this laser. This prompted a detailed theoretical and experimental investigation of the pump rate distribution within the Nd:YAG, which developed into a rate equation model generalised to obtain the output power of the TEM<sub>00</sub> and the TEM<sub>01</sub> modes.

The exploitation of the long upper-state lifetime in solid-state materials such as Nd:YAG crystals, and the ability of these microlasers to be Q-switched, is a contributory reason for the interest in diode-pumped lasers as opposed to laser-diodes alone. Central to chapter 5 is the Q-switching of a transversely pulse-pumped Nd:YAG laser, which allowed very high peak pulse powers from the Nd:YAG laser to be generated using only modest average pump powers. Using both acousto-optic and electro-optic Q-switches, a full analysis was undertaken of the power characteristics of this laser which possessed excellent beam quality. Longitudinal mode characteristics of

this laser are then presented along with results from injection seeding using the stabilised single-frequency cw holosteric laser described in chapter 3.



## Chapter 2

### Laser-diode pumps for solid-state lasers

---

#### 2.1 Introduction to laser-diodes

In a laser-diode, the forward bias injection of charge across a p-n junction creates electron-hole pairs that subsequently recombine, with the simultaneous emission of optical radiation [2.3]. If the injected current is sufficiently great a population inversion in the active region is created which causes gain proportional to the density of the electron-hole pairs. With resonant optical feedback provided by the cleaved facets of the crystal, laser emission will occur when the available gain exceeds the loss.

The diode in which laser action was first demonstrated was a homojunction diode of gallium arsenide (GaAs) in which the active layer was formed at the junction between n- type and p- type layers of the same semiconductor. Improved laser performance was subsequently exhibited by the double heterostructure laser-diode, in which the active layer was sandwiched between layers of greater bandgap energy. These outer layers of gallium aluminium arsenide (GaAlAs) improved the confinement of both the optical field and the charge carriers in the plane parallel to the diode junction.

The introduction of a particular fraction of aluminium into the active layers allowed the bandgap of the lasing transition to be specified. In this way, laser-diode composition could be tailored, between ~680-860 nm, to the peak absorption of the solid-state material to be pumped. Fine control of the bandgap energy and hence the wavelength can be achieved by controlling the operating temperature of the laser-diode. Progress towards high power has been greatest in laser-diodes composed of GaAlAs because of the relative simplicity of these structures. However, high-power is in prospect from laser-diodes composed of indium gallium arsenide phosphide (InGaAsP) in which the accessible wavelength range has been extended to cover between 1.0-1.7  $\mu\text{m}$ .

### 2.1.1 Single-stripe laser-diodes

Having confined charge-carriers and flux in the plane parallel to the junction by the double heterostructure, consideration was given to their confinement in the plane perpendicular to the junction. The width of laser action in this plane may be controlled by gain-guiding, in which a metallic contact stripe on the upper layer defines the width of carrier diffusion, and consequently defines the gain width. A laser-diode of this type, with around 20  $\mu\text{m}$  stripe width, the Telefunken TXSK 2103, was used by ourselves for initial optical pumping experiments. This laser-diode emitted up to 20 mW output power in a single transverse mode and in several longitudinal modes [2.4].

In applications such as telecommunications and compact-disc players, it is a common requirement that the laser-diode should emit in the fundamental transverse mode, such that the beam may be focussed to a small diffraction-limited spot. This is often achieved through the use of index guided lasers in which a waveguide constrains the optical mode in the lateral plane.

One type of index-guided laser-diode is the buried heterostructure stripe laser, in which the lasing filament is entirely embedded in material of wider bandgap that strongly guides the optical mode. An example of this type is the Hitachi HLP 1400, which was used by A. Finch as a pump for a miniature Nd:YAG laser [2.5,2.6]. Emitting up to 15 mW output power, the high beam quality from this single transverse mode, single longitudinal mode laser ensured a low pump threshold.

Using the latest structures, index-guided GaAlAs laser-diodes have been shown to operate in single longitudinal mode and single-transverse mode at power levels up to 150 mW [2.7]. However, the maximum output power from index-guided laser-diodes remains less than from gain-guided devices, as the tight optical mode causes catastrophic facet damage at a lower power level, as described in section 2.1.3.

### 2.1.2 Quantum-well laser-diodes

A breakthrough towards high power laser diodes suitable for diode-pumping was the advent of the quantum-well semiconductor laser. Quantum-well laser-diodes show reduced susceptibility to thermally induced degradation that limits high power continuous operation in conventional laser-diodes. Quantum-well devices are characterised by an active layer composed of one or more sublayers each of a few nanometers thickness. The extreme thinness of these sublayers necessitates that quantum-well lasers are grown by one of the epitaxial techniques of liquid-phase-epitaxy (LPE), molecular-beam-epitaxy (MBE), or chemical-vapour-deposition (CVD). As the thickness of the active layer becomes comparable with the quantum mechanical wavelength of the electrons, the properties of the material change. The resultant quantization of energy levels enhances carrier recombination, with the consequence that threshold currents of quantum well lasers are substantially lower than for conventional “bulk” semiconductor lasers. This reduces the heating-load on the semiconductor, so that higher continuous output powers can be achieved without sacrificing the lifetime of the device.

The width and the number of layers determines, through the overlap between the optical mode and the gain, the properties of the quantum-well laser-diode. Single-quantum-well (SQW) laser-diodes have only one layer within the active area. SQW laser-diodes exhibit the least optical loss and have the lowest threshold and highest differential quantum efficiency. They are also able to dissipate heat most readily, and are often the preferred option for operation at high continuous powers.

### 2.1.3 Catastrophic facet damage

An upper bound on the optical power available from laser-diodes is imposed by catastrophic facet damage, (CFD). In this process, a surface-state effect prevents an inversion of charge-carriers from being created in the region near the facet. As loss at

the facet is greater than gain, the material is absorbing and the facet region becomes locally heated. At power densities of around  $1 \text{ MWcm}^{-2}$  [2.8], heat generation in GaAlAs occurs faster than heat transfer, and the temperature of the facet rises. This causes a localised reduction in the bandgap energy, and even greater absorption in the region close to the facet. Thermal runaway progresses until the active region near the facet melts in catastrophic fashion. For laser-diodes with an aperture  $10 \mu\text{m} \times 1 \mu\text{m}$ , the CFD limit corresponds to an output power of 100 mW.

Progress towards higher output power was achieved by spreading the optical power over a larger area at the facet. This was done in the perpendicular plane by increasing the gain-guiding stripe width, though this is limited to around  $200 \mu\text{m}$ , beyond which filamentary lasing occurs in the lateral direction.

Several structures have also been developed in order to widen the optical mode in the plane parallel to the junction, as in a conventional double-heterostructures the active region in this plane is less than  $1 \mu\text{m}$  wide. One of the most successful has been the separate confinement heterostructure (SCH), see figure 2.1. In this device, there are two outer cladding layers with less aluminium in the GaAlAs, and hence lower refractive index. The outer heterojunctions confine the optical mode to a larger volume than the inner heterojunctions which confine the charge carriers. An example of a broad stripe separate confinement heterostructure laser is the Sony SLD 304, which emits at a power level up to 1 Watt from an  $100 \mu\text{m}$  wide active region, [2.9]. The laser-diode beam has a single-lobed far-field pattern, but its beam divergence is considerably greater than the diffraction limit [2.10].

A further increase in the catastrophic damage limit has been achieved by fabricating a "window" at the facet region, in which there is reduced absorptivity [2.11]. Through various possible techniques, including the diffusion of impurities, the bandgap of the material at the facet is increased so that the window is more transparent to the lasing wavelength.

#### 2.1.4 Coherent linear arrays

Enthusiasm for diode-pumping of solid-state lasers came with the development of the laser-diode array at Spectra Diode Laboratories [2.12-13]. An array consists of a number of laser-diode elements side by side on the same semiconductor substrate, as shown in figure 2.2. As with broad-stripe laser-diodes, amplified spontaneous emission limits the lateral emitting length to around 200  $\mu\text{m}$ . Consequently the number of 10  $\mu\text{m}$  wide individual emitters in an array is limited to around twenty. Arrays were the first type of laser-diode from which the output power was significantly above the required threshold for optical pumping of solid-state materials [2.14].

A coherent phased array is one in which the optical mode in each laser stripe influences the phase of the two adjacent stripes in a process called evanescent coupling. This occurs when the stripes are in close proximity, and the confinement of the optical modes by gain guiding is not absolute. Evanescent coupling ensures that there is a precise phase relationship between the modes in adjacent stripes, which defines the transverse "supermode" emitted by the array. If the phase difference between adjacent stripes in a diode-array is zero, then all the radiation from the phased array is emitted in the fundamental transverse mode. Zero phase difference between stripes has unfortunately been difficult to achieve in practical devices [2.15]. Most coherent phased-arrays tend to oscillate with the adjacent stripes locked in anti-phase, causing a dual-lobed transverse mode in the far-field, [2.16], of greater divergence than that from a diffraction limited single-transverse mode. In most low pump-power configurations the presence of this dual-lobed far-field pattern degrades the coupling efficiency as the brightness of the laser-diode is reduced. However the dual lobed pattern is used to advantage in the tightly folded resonator pump geometry which combines the efficiency of a longitudinally pumped laser with the scaling capability of a transversely pumped laser [2.17].

An example of a coherent phased array is the SDL-2420-H1 which emits up to 200 mW of optical power into a dual-lobed far field pattern [2.18]. This coherent array consists of 10 gain-guided SQW-SCH elements across a width of 100  $\mu\text{m}$ . This was the pump laser used in the holosteric laser system described in chapter 3, though in this case a fibre-coupled package was used.

The arrays that are currently commercially available are specified at 0.5 and 1.0 W, with 100  $\mu\text{m}$  and 200  $\mu\text{m}$  apertures respectively, and have estimated lifetimes of 40,000 hours [2.19]. Since the specified output power level is commonly set at around a quarter of the catastrophic facet damage limit, these lasers may be driven harder, though this is at the expense of longevity. These arrays, and also the broad-stripe Sony laser-diode which emits 1 Watt of optical power, achieve this high power at the expense of brightness, as their beams exhibit only partial spatial coherence.

One interesting approach to achieve single transverse mode operation from high power laser-diodes is injection-locking. This involves coupling an optical beam from a high-quality master laser-diode into the semi-coherent laser-diode, in order that the slave laser should take on the characteristics of the master. This has shown to improve the characteristics of weakly gain-guided arrays and broad-stripe lasers, and is an approach that lends itself to integration within the laser-chip [2.20].

Recently, the maximum output power from arrays with 100  $\mu\text{m}$  and 200  $\mu\text{m}$  wide active areas, has been increased to 6 Watts and 8 Watts respectively [2.21]. These high powers were achieved by the application of non-absorbing coatings called windows to the facets of the arrays, which overcame the problem of catastrophic facet damage. The power from these arrays is presently limited by an overheating which occurs throughout the entire active region.



### 2.1.5 Laser-diode bars

For end-pumped solid-state materials, the brightness of the source is of prime importance, whereas for side-pumped configurations raw optical power is often more important. The laser-diode bar has successfully achieved this higher power. Laser-bars consist of a number of independent semiconductor lasers on a single substrate. These individual sources, which can be broad-stripe devices or coherent-arrays, are optically isolated from one another. As up to 50 individual emitters can be packed onto a single 1 cm wide substrate, the intensity from a laser bar is considerably greater than that which can be achieved from a battery of individual laser diodes. Although expensive at present, diode-bars are a scalable and inherently cost effective way of achieving the high pump powers necessary for transverse pumping of solid-state materials.

#### 2.1.5.a Cw laser-bars

Recent milestones in the output power from cw laser-bars have been extremely impressive, with a maximum of 76 Watts cw output power reported for a 1 cm wide SQW-SCH laser-bar [2.22]. In this bar, the packing density (ie, the ratio of total active aperture width to substrate width) was particularly high at 30%. Devices with lower packing densities benefit from lower temperatures at the active region, and commensurately longer lifetimes. With a packing density of 20%, devices similar to the commercially available SDL-3490, which is rated at 10 W, have an extrapolated lifetime of over 17,000 hours [2.18, 2.24]. These bars are of the "20 \* 10" type, in that they consist of 20 coherent arrays each comprising 10 SQW-SCH elements. Such laser-bars should prove to be good pump sources for cw transversely pumped solid-state lasers.

### 2.1.5.b Quasi-cw laser-bars

A device that successfully circumvents the limitations of thermal dissipation, and one that has particular applicability in the pumping of Nd:YAG, is the quasi-cw laser-bar [2.25]. Developed primarily by Spectra Diode Laboratories, this quasi-cw laser-bar emits high-power pulses of typically 200  $\mu$ s duration at repetition rates up to 100 Hz. Using a low-order multiple quantum well structure with 3 layers, these laser-bars have 1,000 stripes on 10  $\mu$ m centres across a 1 cm substrate, with each stripe defined by proton bombardment. Every 250  $\mu$ m along the bar there are 10  $\mu$ m wide grooves etched in the active layer to prevent lateral amplified spontaneous emission. Consequently, quasi-cw laser bars typically comprise 40 coherent-arrays each of 25 stripes. The SDL-3220-J laser-bar, which emits pulses with 25 Watts peak power, was the pump source for the transversely-pumped lasers described in chapters 4 and 5.

Commercial single-bars which are currently available have peak powers of up to 60 Watts [2.18]. The maximum reported peak power prior to catastrophic facet damage from such a laser-bar is 134 W, at an average power of around 1 Watt [2.26]. In future both the average power and the peak power from quasi-cw bars should increase, as SQW-SCH structures and facet windows are adopted to improve the thermal dissipation and increase the CFD limit.

### 2.1.5.c Stacked bars

To further increase the output power for optical pumping, linear laser-bars have been stacked with interleaved heat-sink spacers [2.27]. Laser-bars can in principle be stacked to any height to create a 2-dimensional pump module. However, as waste heat from the diode must be transferred by the spacers to the common heatsink at the back, the thermal resistance of the assembly is increased. Stacked bars commercially available include the CVD-450 with an emitting area of 1 cm<sup>2</sup> with output power greater than 1.7 kW for pulses of 400  $\mu$ s duration [2.28]. As the spatial coherence from these



stacks is poor, stacks can be regarded as efficient solid-state narrow spectral band flashlamps.

In a single linear laser-bar, the impedance is low as the individual laser-diode stripes are electrically biased in parallel. When stacked, laser-bars are connected in series, giving the benefit of increased impedance which reduces the line losses from the supply [2.29]. It is perhaps prudent however, for configurations involving a number of stacked bars, to connect the stacked bars in parallel with a constant current supply. In addition, the present high cost of these devices should encourage consideration as to the advisability of an independent power supply for each stack.

#### **2.1.6 Surface-emitting laser-diodes**

The pump source of the future is considered by many to be the surface emitting laser-diode. These devices differ radically from other laser diodes, in that they emit perpendicular to the substrate. As such, surface emitters allow the fabrication of monolithic 2-D planar arrays. Surface emission has been achieved in two ways.

Type I surface-emitters lase parallel to the surface and deflect the light perpendicular to the surface by etched reflectors or gratings. Most interest has focussed on grating surface emitters (GSEs), as their waveguide structure allows coherent coupling of the arrays, though maintaining coherence across a large area is problematic [2.30]. In pulsed operation, multimode output power of 16 W at a slope-efficiency of 65 % has recently been reported from a GSE [2.31]. The coating of a protective passivation layer on the grating of a GSE remains a difficult practical problem.

Type II surface emitters are those with a vertical cavity with the feedback mirrors parallel to the top and bottom surfaces of the semiconductor wafer. Though type II devices have demonstrated low threshold currents of about 1 mA and packaging densities of more than 1 million lasers/cm<sup>2</sup> [2.32], the present short gain length of ~10  $\mu\text{m}$  will limit their use to low power though high brightness applications.

A challenge common to all surface emitters is the removal of waste heat, as the active region is separated from the heat sink by the thickness of the crystal substrate. Whilst progress towards surface-emitting laser-diodes is still in the research phase, they offer the prospect of monolithic 2-D arrays with very high powers and narrow beam divergences.

---

## 2.2 Cw laser-array characterisation

The GaAlAs laser-diode selected to pump our cw Nd:YAG laser was a Spectra-Diode Labs SDL-2430-H2 [2.18]. This laser-diode consists of an array of ten elements of the multiple-quantum-well separate-confinement-heterostructure type, and is supplied mounted in a hermetically sealed TO-3 can, with a fibre pigtail as illustrated in figure 2.3 a. Coupling loss into the 100  $\mu\text{m}$  core diameter fibre of around 50% reduces the nominal 200 mW of optical power emitted from the facet to a maximum specified output power of 100 mW from the fibre.

The good spatial quality of the beam from the fibre, which is discussed in section 2.2.3, was an important consideration in the selection of a fibre-coupled laser-diode. Using this good quality beam, simple coupling optics are all that is required to achieve efficient pumping of the Nd:YAG crystal. In addition, optical feedback, which can cause instability in the output of laser-diodes that are directly accessible, is circumvented by fibre-coupling.

The SDL-2430-H2 laser-diode was driven by an SDL-800 driver, in which provision was made for transient suppression protection circuitry for the laser-diode. This driver provided dc current up to 1000 mA, and had analogue modulation capability at frequencies up to 100 kHz. Connections to the laser-diode head from the driver enabled the laser-diode optical power to be monitored, and allowed stabilised thermo-electric control of the laser-diode temperature. It was considered that the selection of

this laser-diode/driver package offered the most direct approach to pumping solid-state materials.

### 2.2.1 Optical power calibration

Initial characterisation of the laser-diode involved the measurement of optical power against drive current, at three different operating temperatures, as shown in figure 2.4. The optical power was measured with a Scientech power meter, and the current reading displayed by the driver was confirmed using a coil meter. At an operating temperature of 20 °C, the threshold current,  $I_{th}$ , was 235 mA and the differential slope-efficiency,  $\eta_s$ , was 0.65 mW/mA. The photodiode within the laser-diode package was calibrated using figure 2.4, to ensure the accuracy of the laser-diode optical-power readings as displayed by the driver.

Increasing the operating temperature from 273 to 293 K increased the threshold current from 205 to 235 mA, as a result of a change in the Boltzmann distribution of carriers. The temperature dependence of threshold current is given by

$$\frac{\text{threshold current at } T_2}{\text{threshold current at } T_1} = \exp [(T_2 - T_1)/T_0], \quad (2.1)$$

where  $T_0$  for our multiple-quantum-well laser-diode is typically 130 K, [2.35]. The ratio of threshold currents for the 20 K temperature shift shown in figure 2.4 is 1.14, which is in acceptable agreement with the value of 1.16 obtained from the above equation. A consequence of this effect is that temperature tuning the laser wavelength to match the absorption peak of a solid state material also affects the output power from the laser diode.

### 2.2.2 Electrical-optical efficiency

Laser-diode electrical-optical efficiency is given by the ratio of laser output power to electrical input power. The optical power is obtained from the product of the

differential slope-efficiency and the current above threshold. The electrical power is obtained from the product of the drive current and the applied voltage.

Necessary to the formulation of the electrical-optical efficiency is the voltage/current relationship, which is illustrated in figure 2.5. This is characterised by a breakover voltage,  $V_b$ , which is nominally the bandgap energy of 1.53 V, and a series resistance,  $R_s$ , of around 1.25  $\Omega$  [2.36].

The electrical-optical efficiency as a function of drive current is shown for our laser-diode in figure 2.6. This was obtained from the measured optical/current characteristics shown in figure 2.4, and the typical voltage/current curve displayed in figure 2.5. At an output power of 100 mW, the electrical-optical efficiency is relatively low, at around 13%, and may be attributed to the ~50% efficiency for coupling into the optical fibre [2.35] and is not to be confused with the “wall-plug efficiency”, which also includes the electrical requirements of the thermo-electric cooler and of the driver itself.

As the resistive losses in the diode are proportional to the square of the current, the rate of increase in efficiency tails off with increasing current. Within the drive current limit set by catastrophic facet damage, the efficiency will actually start to decrease, such that the current at which maximum efficiency occurs does correspond to the current for maximum optical power.

### 2.2.3 Transverse mode structure

The window-packaged version of the laser-diode that we employed was the SDL-2430-H1 [2.18]. As discussed in section 2.1.4, the beam from this coherent array has a dual-lobed transverse mode structure in the far-field. Effective focussing of this pump beam is therefore rather difficult.

In the SDL-2430-H2 an optical fibre pigtail of 1 m length is butted close to the facet by the manufacturers. This 0.3 NA step-index multi-mode fibre is made of fused silica,

and has a 100  $\mu\text{m}$  diameter core, 140  $\mu\text{m}$  diameter cladding and an outer plastic jacket with 0.5 mm diameter [2.35]. The fibre pigtail acts as a spatial mode converter, with the dual-lobed far-field beam pattern from the diode spatially scrambled by the multimode fibre. The beam emerges from 1 metre of fibre with a symmetrical profile that is somewhere between a top-hat function and a Gaussian function, with nearly all the energy contained within a cone of  $14^\circ$  half-angle [2.35]. As the beam from 1 m of fibre is spatially incoherent, there is no transverse mode in the Gaussian sense, and geometrical optics is applicable. Output from a shorter fibre results in a more featured spatial profile which may degrade pumping efficiency.

#### 2.2.4 Longitudinal mode structure

As expected for a gain-guided device, the laser-diode was found to lase on several longitudinal modes as illustrated by the frequency spectra in figure 2.7. Measured at five different output power levels with a 1 m long monochromator (Monospek 1000), the number of longitudinal modes above threshold increased as the drive current increased. With seven modes oscillating at an output power of 80 mW, the spectral width was around 2.5 nm. The intermode spacing of 0.34 nm corresponds to a laser-diode cavity length of 270  $\mu\text{m}$ .

A feature evident from figure 2.7 is the fine structure that appears on the individual modes at higher output powers. This is attributed to the presence of laser-diode-array “supermodes” which are similar to transverse modes in other lasers. For our laser-diode, the transverse mode structure is scrambled by the multimode optical fibre, so the presence of these supermodes is of only slight importance in the pumping of solid-state materials.

Spectra similar to those shown in figure 2.7 were taken for a fixed output power of 50 mW, with the temperature of the diode varied using the internal Peltier cooler. The information from these spectra was amalgamated and is displayed as a “dot-diagram” in

figure 2.8. This demonstrates the variation in frequency of individual modes as a function of heat-sink temperature, with the dot-size giving an approximate indication of the relative intensity of a particular mode.

Demonstrated by figure 2.8, the rate of shift in wavelength of individual modes as a function of temperature is  $0.06 \text{ nm/}^{\circ}\text{C}$ . This is attributed to the variation of the refractive index, and hence the cavity length, of the laser-diode with temperature. More significantly, due to a change in the band-gap energy, the central wavelength tunes with temperature at the rate of  $0.23 \text{ nm/}^{\circ}\text{C}$ .

---

### 2.3 Laser-bar characterisation

The type of laser-diode bar selected to transversely pump our long pulsed and Q-switched Nd:YAG lasers was the SDL-3220-J, shown in figure 2.9 [2.18]. 1000 individual MQW-SCH elements form 40 coherent arrays spaced uniformly along the  $1 \text{ cm} \times 1 \text{ }\mu\text{m}$  emitting area, as described fully in section 2.1.5.a. Pulsed at repetition rates up to 100 pps, it is termed “quasi-cw” because of its long pulse durations of up to  $200 \text{ }\mu\text{s}$ . The rated peak power of 25 Watts corresponds to a maximum pulse-energy of 5 mJ, and a maximum average power of 500 mW, which places the laser-bar at the upper end of the class IIIb safety category.

An SDL-922 high power quasi-cw laser-diode driver was used to provide current for the quasi-cw laser-diode bar. Optimized for low impedance laser-diode bars, the driver is designed to produce pulses free from overshoot or ringing which would damage the laser bar. Specified to give a maximum current of 100 A, this driver provides relatively long pulses of 20 -  $200 \text{ }\mu\text{s}$  duration at low duty factor with repetition rates of 10 - 100 pps. The output from the driver’s current monitor was confirmed by an external current probe, which showed a risetime and a falltime of  $\sim 15 \text{ }\mu\text{s}$  and  $\sim 10 \text{ }\mu\text{s}$  respectively.



### 2.3.1 Laser-bar protection

As with other semiconductor devices, the laser-bar is susceptible to damage from static discharge so protection in transit was provided by an anti-static container and a shorting contact across the connections. Similarly, a grounded wrist strap was worn when the laser-bar was placed in a mount, which was itself in electrical contact with an earthed optical table.

Supplied mounted on a J-type heatsink, the facets of the laser-bars are open to the environment and are susceptible to "mechanical" damage. To protect the laser-diode bar from dust particles the entire laser mount was enclosed within a large perspex box. As the laser-diode was operated at temperatures close to 0 °C, dry-nitrogen was flowed across the facet to prevent moisture condensing on the facet. Placing a small sachet of dessicant in the rear of the laser-bar housing proved difficult, though this option is worth consideration for future systems.

During the work described in this thesis, three laser-diode bars have undergone complete or partial failure. The first sign of failure for each was a drop in output power which, on inspection, was found to be caused by the extinction of emission from one or more groups of individual emitters. It appears that the electrical characteristics of the failed elements were unaffected, such that failure mechanism could be catastrophic facet damage or a dislocation within the stripe. The one laser-bar that has been operated beyond this partial failure stage suffered complete failure shortly afterwards at which point the device became an open circuit, indicating an alternative failure mechanism.

After the failure of the second laser-bar it was decided to operate subsequent laser-bars at 10 pps rather than 100 pps. This reduced both the thermal loading on the diodes and also the number of shots in a given period and has had a beneficial effect on their lifetime.

Responsibility for the demise of the first laser-bar was accepted by the manufacturers, who were at this time having difficulties with product reliability. Nevertheless, subsequent confidence in their product has led SDL to market quasi-cw laser-diode bars with peak powers more than doubled to 60 Watts. Claims by SDL for improved product reliability in subsequent batches of production, cannot be substantiated by our, admittedly qualitative, findings. The adoption of a shot-counter within a future current driver would allow more substantive statements on device lifetimes to be made.

### 2.3.2 Optical power characterisation

Initial characterisation of the pulsed laser-diode involved a comparison of the optical power against the drive current throughout the 200  $\mu$ s duration of a pulse. Demonstrated in figure 2.10, the optical power does not follow the smoothed top-hat shape of the current pulse, but diminishes throughout the length of the pulse. This can be attributed to a continuing temperature shift and resultant increase in threshold current throughout the pulse.

Initially absolute measurements of the energy and power from laser-bars proved difficult to make with the available detectors, as the beam from laser-bars is large. For the first laser-bar, measurements of peak power and hence energy were taken from the characterisation data supplied by the manufacturer. It was later found possible to remove the thermal enclosure from a Scientech detector head, to allow the laser-diode to be brought into close proximity of the absorbing sheet. However, without the thermal enclosure the detector head was susceptible to fluctuations in temperature from the atmosphere caused in part by the laser-bar Peltier coolers, and the effect of which was most pronounced when the laser was operated at 10 Hz. A detector which has overcome these problems is the Molectron J25 HR, which is a pulsed energy meter and which uses the pyroelectric effect to give absolute measurements of pulse energy. Results taken with the detector for the pulse energy against current are shown in figure 2.11 for pulse repetition rates of 10 Hz and 100 Hz respectively.



As with the cw laser-diode the voltage/current relationship is characterised by a breakover voltage of 1.53 V, and a series resistance. However, as the laser-bar consists of 1000 elements in parallel, the resistance is shown by data-sheet no.4 to be correspondingly much lower at around  $0.0075\ \Omega$  [2.38]. Under room-temperature operation at 40 A, 30 pps repetition-rate and 200  $\mu\text{s}$  pulse-duration, the 25 Watts peak optical power is achieved with 35% electrical-optical efficiency.

### **2.3.3 Transverse mode structure**

The far-field transverse mode pattern from a laser-bar was dual lobed in the plane perpendicular to the junctions, and is consistent with the overlap of the dual-lobed patterns from the individual coherent phased arrays that make up a laser bar. This was confirmed upon focusing the beam, in which the image of each of the 40 individual arrays was discernible. In the near field, the full width half maximum divergence in the plane of the junction was measured for a laser-bar to be  $21.8^\circ$ .

### **2.3.4 Temperature control of laser-bars**

For efficient pumping of solid-state lasers that have narrow spectral absorption bands, such as Nd:YAG, the wavelength of the laser-diode source must be at a specific value. As the wavelength of a laser-diode is temperature dependent ( $\sim 0.3\ \text{nm}/^\circ\text{C}$ ), temperature control of the laser-diode allows wavelength tuning to the peak of the absorption band. As the lifetime of a laser-diode is extended by operation at lower temperatures, the central wavelength of each laser-bar was specified to be  $809 \pm 5\text{--}0\ \text{nm}$  at  $25\ ^\circ\text{C}$ . This usually necessitated that each laser-bar was cooled to a temperature of around  $5\text{--}10\ ^\circ\text{C}$ . Running laser-diodes at lower temperatures has been shown to extend their lifetime, as there is reduced generation of thermal defects within the semiconductors [2.3]. An additional consideration relevant to the temperature control of laser-bars is that their facets are open to the environment. Even with dry nitrogen flowing across the facet, the danger of water-vapour condensing discouraged their operation below the humidity dependent dew point temperature of  $\sim 4\ ^\circ\text{C}$ .

Unlike the cw laser-diode used for end pumping, (SDL-2430-H2), quasi-cw laser bars are supplied without integral temperature control, which made it necessary for the system described in this section to be constructed. The cooling system which was adopted utilized Peltier cooling elements and radiative heat-dissipation and is shown schematically in figure 2.12.

#### **2.3.4.a Temperature control system**

To ensure low thermal resistance between the brass heatsink of the laser-bar and the Peltier cooler, a copper housing was constructed with zinc oxide paste between it and the laser-bar. Care was taken that the thermal grease was not close to the facet of the laser-bar, as grease "creeps" and can damage unprotected facets. Indium foil, thermally conductive epoxy and low-temperature solders are alternatives to thermal grease.

The thermo-electric heat pumps were both single stage Peltier coolers, (Marlow MI1063), and were chosen for their large heat removal capacity. The square heat-pumps had 29.64 mm long sides and at the maximum drive current of 6 A the applied voltage was  $\sim 7.5$  V. When current passes from the n- to the p- type semiconductor material, the temperature  $T_C$  of the interconnecting tab decreases and heat is absorbed from the surroundings. This heat is conducted through the semiconductor materials by electron transport to the other end of the junction,  $T_H$ , and released. As Peltier elements are not 100% efficient, the heat to be dissipated by the hot-side heatsink is the sum of that to be removed from the cold-side and the heat generated internally by the Peltier elements.

Heat generated at the hot side of the Peltier coolers was dissipated by convection using finned heat-sinks. Initially the cooling system utilized a single MI 1063 Peltier cooler, with an aluminium block clad with extruded fins as the heatsink. This system proved inadequate when the laser-bar was operated at 100 Hz, and so was replaced by a pair of Peltier heatpumps with the more extensive heatsink illustrated in figure 2.12. More

detail about the performance of the heatsink is given in the section below on the thermal-account of the system.

To keep the temperature of the laser-bar constant, a controller was used which compared the resistance of a thermistor in thermal contact with the laser-bar, to that of a variable bridge resistor. The initial temperature controller which was built in-house was capable of delivering a constant current up to 4 A, at around 4 V [2.6]. Coarse switching of the drive current to the Peltier elements involved a mechanical relay, which was activated if the thermistor resistance was well above the set-point. Fine temperature control was provided by a solid-state relay, which gave proportional control through current pulses of variable length within 75 ms time slots. This controller could maintain the temperature of the laser-bar to within 0.1 °C, however, as the mechanical relay was found on occasion to cause the laser-bar supply to switch off, a temperature controller which used all-solid-state-relay was adopted. The controller chosen was a Photon Control model 290 (special) bipolar peltier driver, that was capable of driving 3.5 A at  $\pm 12$  V.

To monitor the cold heatsink temperature independently from the thermistor a k-type thermocouple was inserted into one of the holes within the laser-bar brass heatsink adjacent to the thermistor and connected to a digital temperature indicator (RS 616-419). This thermocouple did not measure the temperature of the active region within the laser-bar. It is shown in the later section on temperature tuning, that when the bar is running at full specification, the active-region was a time-averaged 27 °C hotter than the thermocouple.

#### **2.3.4.b Thermal account**

When laser-bar no. 4 was operating within a room whose temperature was 25 °C\*, the cold-side heat-sink was maintained at a temperature  $T_c$  of 5 °C, which resulted in a

---

\* At 10 pps with pulses of 200  $\mu$ s duration and current of 40 A.

temperature for the hot heat-sink  $T_h$  of 31 °C. It can be shown that the temperature of the cold side would be 3 °C were the same amount of work done by the Peltier element at a hot side temperature of 27 °C [2.37]. The voltage applied to each Peltier stage was measured to be 3.5 V, which corresponds to a current through each stage of 1.8 A. At this drive current level the effective cold side temperature in the absence of a thermal load is -1 °C.

From the 4 °C difference between the effective cold-temperature that was achieved, 3 °C, and the effective cold-temperature that is anticipated from the known level of current, -1 °C, it can be shown that the active heat-load that was dissipated by each heat-pump was ~2.5 Watts. The active heat-load that was generated internally by the laser-bar was around 100 mW at 10 Hz, rising to 1 Watt at 100 Hz. This is calculated from the ~35% electrical-optical conversion efficiency determined in section 2.3.2. The heat load dissipated by the heat-pump,  $Q_a$ , was, however, dominated by the ~5 W of heat that is absorbed at the cold-side of the Peltier coolers by the laser-bar and its surrounding copper block.

The ratio of active heat removed by each Peltier,  $Q_a/2 = 2.5$  W, to the power supplied to each Peltier,  $Q_p = 6.3$  W, is respectably high at 0.40. Though this system proved satisfactory in the short-term, upward drift in the laser-bar temperature would occur when the room-temperature was high, or the laser-bar was operated at greater than 10 Hz. This temperature rise has been attributed to the heat-sinks, which with a thermal-resistivity of ~0.7 W/°C are operating at the limit of their heat dissipation capability. Although a fan was effective in increasing the heat dissipation from the heat-sinks, this had the disadvantage for our particular laser design that it disturbed the air within the cavity, causing fluctuations in the optical length of the cavity.

To reduce the heat-load absorbed by the system, a reduction in the mass of the copper block, (presently 110 g), is being implemented. This will have the additional advantage of improving the response time of the cooling to new settings in temperature. More

significantly, liquid-cooling of the heat-sinks is being implemented for this system as this allows greater heat-dissipation, and removes the dependence of the cooling system on the temperature of a laboratory environment. Liquid cooling is certainly the favoured option for stacked-bars, where the heat-dissipation requirements and dimensional constraints are more severe.

#### **2.3.4.c Temperature tuning**

Each of the laser-bars was purchased with its central wavelength,  $\lambda_p$ , selected to be 809 (+5, -0) nm at 25 °C. Wavelength specifications given by SDL were obtained under the condition of pulses of 200  $\mu$ s duration, at a repetition rate of 30 pps. Operation of these laser-bars at the peak absorption wavelength of Nd:YAG (808.5 nm), required tuning of the wavelength by changing the temperature of the laser-bar's own heatsink to between 5 and 10 °C.

Further, it became evident, as shown in figure 2.13 that the wavelength of operation was a function of drive-current and repetition rate. This can be attributed to the heating of the active area caused by increased current and higher repetition rate. From an extrapolation of data illustrated in figure 2.13, the shift in wavelength from 0 A to 50 A is 9 nm when the repetition rate was 100 Hz. This is equivalent to a local temperature increase of ~27 °C which is generated by the ~2 Watts of heat dissipated in the active region. Hence, the thermal resistivity of the laser-bar is ~13.5 °C/Watt.

Operation at a fixed wavelength is of particular concern in the pumping of solid-state materials, such that the base temperature must be altered appropriately to maintain a fixed wavelength during measurements of optical-power from the laser-bar against drive-current. In addition, active temperature control of the base heatsink is required to compensate for changes in internal heating with changing pulse repetition rate.

#### 2.3.4.d Longitudinal mode structure

To obtain the maximum information about the frequency structure of the pulsed laser diode, the spectrum was measured as a function of time. With the laser array operated at maximum average-power (25 W, 200  $\mu$ s, 100 Hz), portions of the output beam were imaged onto the input slit of a 1 m scanning monochromator (Monospek 1000). Throughout the 200  $\mu$ s pulse-interval, a fast photodiode monitored the radiation transmitted by the monochromator at a fixed wavelength. This procedure was repeated as the monochromator was stepped at 0.05 nm intervals over the range from 804 to 816 nm. From this large amount of data, the spectral content of the laser emission was analysed at eight instants during the laser pulse, and the time-resolved spectrum plotted in three-dimensions, as shown in figure 2.14. The time resolved spectrum shows that the individual laser modes are spread over an instantaneous bandwidth of some 2 nm, which is comparable with that from the c.w. laser arrays described in the previous section. The mode separation of 0.27 nm corresponds to a diode cavity length of 340  $\mu$ m.

Significantly, the centre of this spectral band shifts by 4.8 nm over the the 200  $\mu$ s duration of the pulse, as shown in figure 2.15. This is due most probably to the thermally-induced change in the bandgap of the GaAlAs. The linearity of the wavelength shift indicates that there is only slight diffusion of heat away from the active region throughout the pulse [2.14]. It is interesting to note that the wavelength shift of 4.8 nm during the 200  $\mu$ s pulse corresponds to a rise in temperature of 16 °C. Therefore the active-region of the laser-diode is increasing in temperature at the rate of some 80,000 °Cs<sup>-1</sup>.

With the 1 cm laser bar consisting of 1000 elements, it was felt necessary to investigate the variation in frequency of the emission across the array. The radiation from 18 portions of the facet was analysed with the monochromator. Across the laser bar, it was found that there was a variation in the central wavelength of 1.5 nm, see figure



2.16. Although these measurements were taken for only the first pulse diode-array, our data complement those taken by the manufacturer for a range of diode-arrays [2.14]. It has been suggested that there are two likely sources of wavelength spread along the facet; nonuniformity in the growth of the epi-layers and non-uniform bonding which will cause temperature variations across the array. Spread caused by the former should appear even at low power levels, whereas that caused by the latter should appear only at high power levels, where the heat dissipation becomes significant. For most of the cw laser-bars tested by the manufacturers, the spread is much smaller at lower power levels and widens with power level, indicating that the latter factor has larger significance than the former at 10 W.

The shift in wavelength throughout the pulse is significant with respect to the width of the absorption feature in Nd:YAG at 809.5 nm. When the wavelength shift is combined with the spatial variation in frequency across the facet, the effective linewidth is around 6 nm. The implications of this increased linewidth are discussed in chapter 4.

---

## 2.4 Conclusions

It is clear that developments in diode-pumping technology are for the most part led by the advances in the laser-diode technologies. It has been noted that diode-powers have doubled every 2-years for the last decade, though the power from a single diode may now be close to its fundamental maximum. Partly motivated by optical satellite communications, research is ongoing towards development of high-powered single-transverse-mode cw laser-diodes. The improved coherence of such devices will offer some advantage to bulk end-pumped solid-state lasers, though the major beneficiaries are likely to be waveguide-lasers and fibre-lasers.

Though stacks and surface emitting diodes consist of a number of individual lasers, they should be considered not such much as "laser" pump sources but more as flashlamps having a narrow spectral bandwidth. Consequently, side-pumped



geometries are more appropriate to these sources of raw optical power than are end-pumped geometries. It is anticipated that advances in high power laser-bars will cause the replacement of flashlamps by laser-bars at increasingly high powers. Presently, only low duty cycle quasi-cw bars are stacked together because of the constraint arising from heat dissipation. The stacking of cw bars is obviously more demanding, such that fibre coupling of cw bars is a likely approach towards a cw high power solid-state laser [2.33].

## Chapter 2    References

- 2.1     D.L. Sipes "Highly efficient neodymium: yttrium aluminium garnet laser end pumped by a semiconductor laser array" *Appl. Phys. Lett.* **47** (1985) 74
- 2.2     M. Sakamoto, M.R. Cardinal, J.G. Endriz, D.F. Welch & D.R. Scifres "Performance characteristics of high power cw, 1 cm wide monolithic AlGaAs laser diode arrays with a 2 mm total aperture width" *Electron. Lett.* **26** (1990) 423
- 2.3     G.H.B Thomson "Physics of semiconductor laser devices" Wiley, Chichester, 1985.
- 2.4     Telefunken electronic "Selection guide optoelectronic devices"
- 2.5     Hitachi "Optoelectronic devices databook"
- 2.6     A. Finch "Diode pumping of a miniature Nd:YAG laser" MSc project report, Univ. St.Andrews, September 1985
- 2.7     D.F. Welch, W. Streifer & D.R. Scifres "High-power index-guided lasers emitting in a single transverse mode" *Tech. Digest, Conf. on Lasers and Electro-Optics*, 1988, paper WB4
- 2.8     C.H. Henry, P.M. Petroff, R.A. Logan & F.R. Merritt "Catastrophic damage of AlGaAs double heterostructure laser material" *J. Appl. Phys.* **50** (1979) 3721
- 2.9     Sony "Discrete semiconductor databook"
- 2.10    M. Sakamoto & Y. Kato "High-power (710 mW cw) single-lobe operation of a broad area AlGaAs double heterostructure laser grown by metalorganic chemical vapour deposition" *Appl. Phys. Lett.* **50** (1987) 869
- 2.11    D.F. Welch, W. Streifer, R.L. Thornton & T. Paoli "2.4 W cw, 770 nm laser arrays with non-absorbing mirrors" *Electron. Lett.* **23** (1987) 523
- 2.12    D.R. Scifres, R.D. Burnham & W. Streifer "High power coupled multiple stripe quantum well injection lasers" *Appl. Phys. Lett.* **41** (1982) 118
- 2.13    W. Streifer et al, "Phased array diode lasers" *Laser Focus*, June 1984, 100
- 2.14    W. Streifer, D.R. Scifres, G.L. Harnagel, D.F. Welch, J. Berger & M. Sakamoto "Advances in diode laser pumps" *IEEE J. Quan. Electron.* **24** (1988) 883
- 2.15    L.J. Mawst, D. Botez, T.J. Roth & G. Peterson "High-power, in-phase-mode operation from resonant phase-locked arrays of antiguided diode lasers" *Appl. Phys. Lett.* **55** (1989) 10
- 2.16    D. Botez, L.J. Mawst, P. Hayashida, G. Peterson & T.J. Roth "High-power, diffraction-limited-beam operation from phase-locked diode-laser arrays of closely spaced "leaky" waveguides (antiguides)" *Appl. Phys. Lett.* **53** (1988) 464

## Chapter 2    References

- 2.17    T.M. Baer, D.F. Head & M. Sakamoto "High efficiency diode-bar pumped solid state laser using a tightly folded resonator" Tech. Digest, Conf. on Lasers and Electro-Optics, Baltimore, 1989, paper FJ5
- 2.18    Spectra Diode Labs product guide May 1990
- 2.19    D.F. Welch, B. Chan, W. Streifer & D.R. Scifres "Performance characteristics of high-brightness cw laser diode arrays" Electron. Lett. **23** (1987) 892
- 2.20    M.K. Chun, L. Goldberg & J.F. Weller "Injection-beam parameter optimization of an injection-locked diode-laser array" Opt. Lett. **14** (1989) 272
- 2.21    D.F. Welch et al "High-power, 8W cw, single quantum well laser diode array" Electron. Lett. **24** (1988) 113
- 2.22    M. Sakamoto, D.F. Welch, J.G. Endriz, D.R. Scifres & W. Streifer "76 W cw monolithic laser diode arrays" Appl. Phys. Lett. **54** (1989) 2299
- 2.25    G.L. Harnagel et al "High-power quasi-cw monolithic laser diode linear arrays" Appl. Phys. Lett. **49** (1986) 1418
- 2.26    G.L. Harnagel, P.S. Cross, C.R. Lenn, M. Deito, & D.R. Scifres "Ultrahigh power quasi cw monolithic laser diode arrays with high power conversion efficiency." Electron. Lett. **23** (1987) 743
- 2.27    R. Scheps & J. Myers "Performance and aging of a broad area structure" Appl. Opt. **29** (1990) 341
- 2.28    Laser Diode Inc. CVD-400 series data sheet
- 2.29    D. Krebs "Diode laser arrays for optical pumping of Nd:YAG lasers" Tech. Digest, Soc. Phot. Inst. Eng. **783** (1987)
- 2.30    N.W. Carlson et al. "Phase-locked operation of a grating-surface-emitting diode laser array" Appl. Phys. Lett. **50** (1987) 1301
- 2.31    D.F. Welch, R. Parke, A. Hardy, R. Waarts, W. Streifer & D.R. Scifres "High power, 16 W, grating surface emitting laser with a superlattice substrate reflector" Electron. Lett. **26** (1990) 757
- 2.32    J.L. Jewell et al. Proc. Seventh Int. Conf. on Integ. Optics and Opt. Fiber Comm., Kobe, Japan, July 1989 paper 18 2-6 (PD)
- 2.33    C. Chang-Hasnain, D.P. Worland and D.R. Scifres "High intensity fiber-coupled diode laser array" Electron. Lett. **22** (1986) 65
- 2.34    H. Yamanaka et al "Progress in super high power laser diodes with a broad area structure" Tech. Digest, Conf. on Lasers and Electro-Optics, Anaheim CA, 1990, paper CFA2

## Chapter 2    References

- 2.35      Spectra Diode Labs "Laser diode operator's manual and technical notes" March 1988
- 2.36      Spectra Diode Labs 2430-H2 data sheet
- 2.37      Marlow Industries - Peltier cooler guide
- 2.38      Spectra Diode Labs - 3220-J data-sheet (no.4)

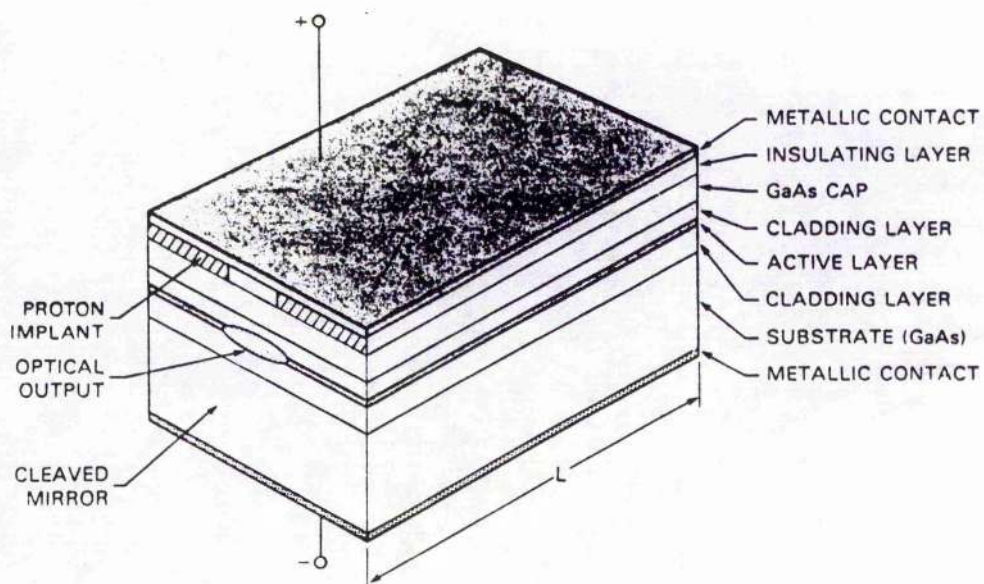


Figure 2.1 Structure of a single-stripe separate confinement heterostructure GaAlAs laser-diode.

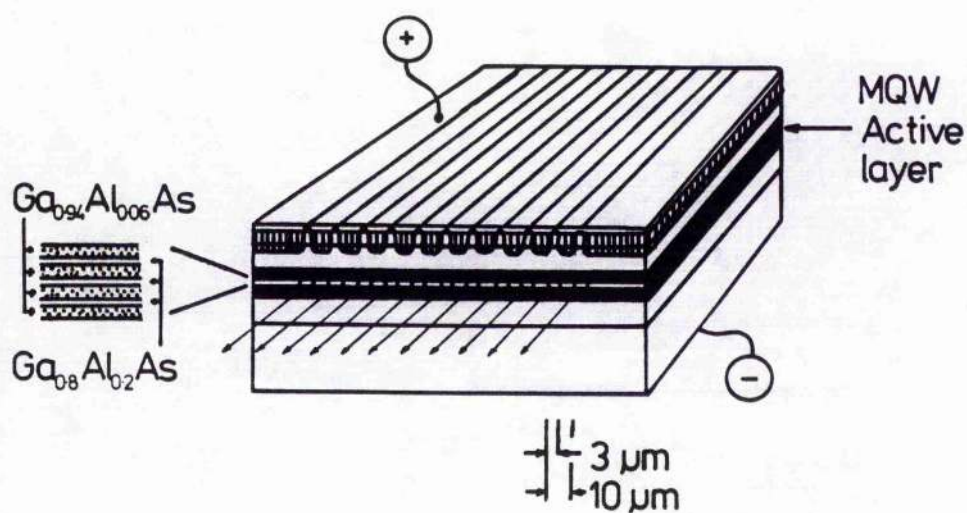
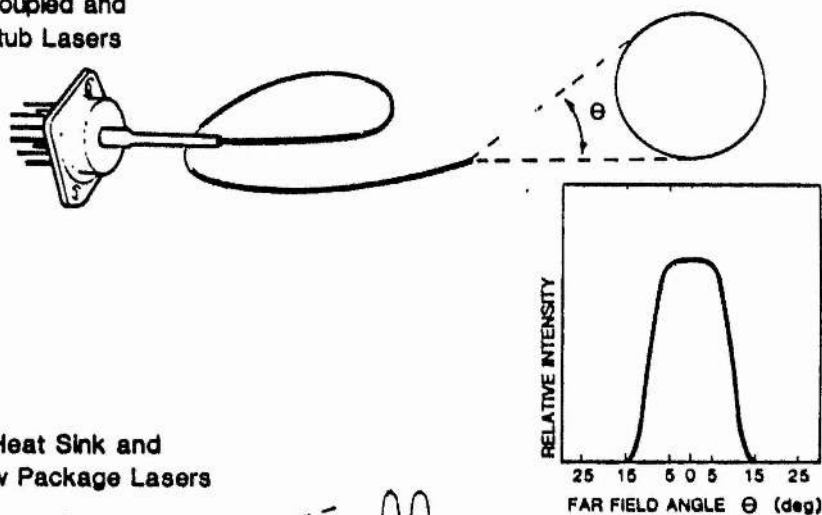


Figure 2.2 Structure of a multiple-quantum-well phase-locked GaAlAs laser-diode array.

Fiber Coupled and  
Fiber Stub Lasers



Open Heat Sink and  
Window Package Lasers

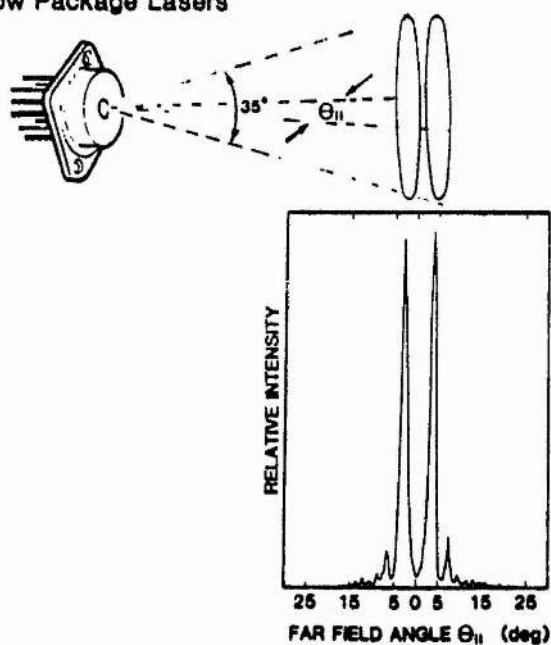


Figure 2.3

- a) SDL laser-diode type 2430-H2 in a TO-3 fibre-pigtail package with  $100\ \mu\text{m}$  core diameter fibre and beam of  $14^\circ$  half-angle divergence.
- b) SDL laser-diode type 2430-H1 in a window package with dual-lobed far-field mode pattern.

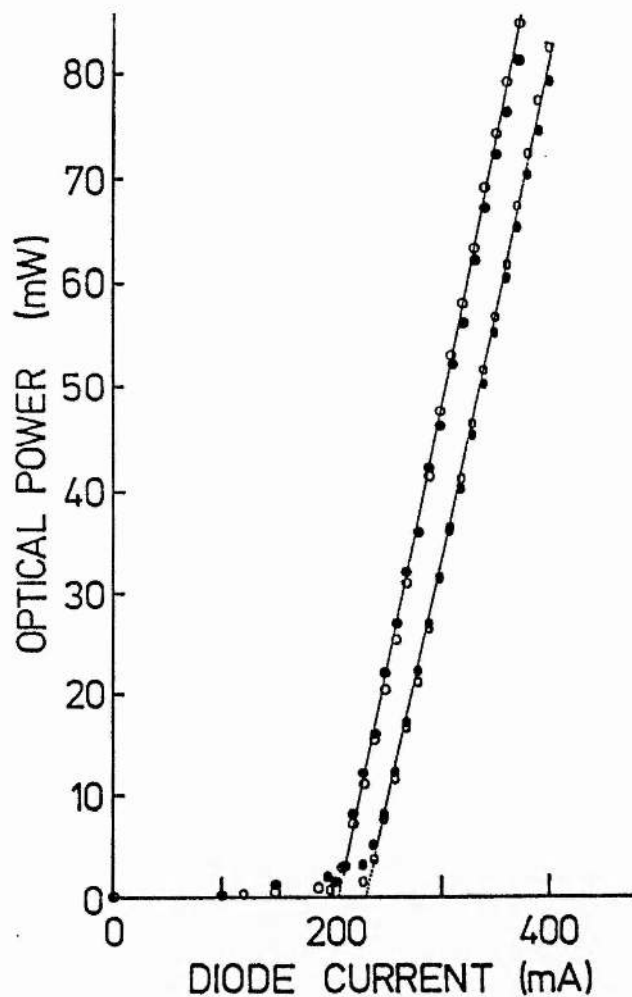


Figure 2.4

Power measured at the end of the laser-diode's fibre as a function of diode current. The open markers represent the power measured by a Scientech power meter, and the filled markers represent the power measured by the monitor photodiode in the laser can. The circles and ovals indicate the power measurements made with the diode heatsink cooled to 0° and 20° C respectively.



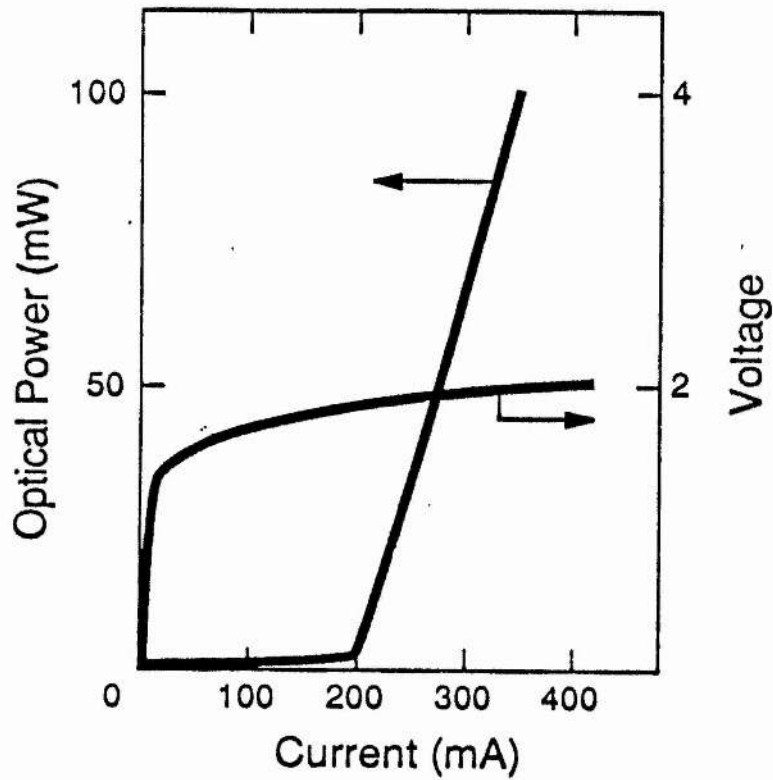


Figure 2.5 Optical power and applied potential for a typical SDL type 2430-H2 laser-diode as a function of drive current.

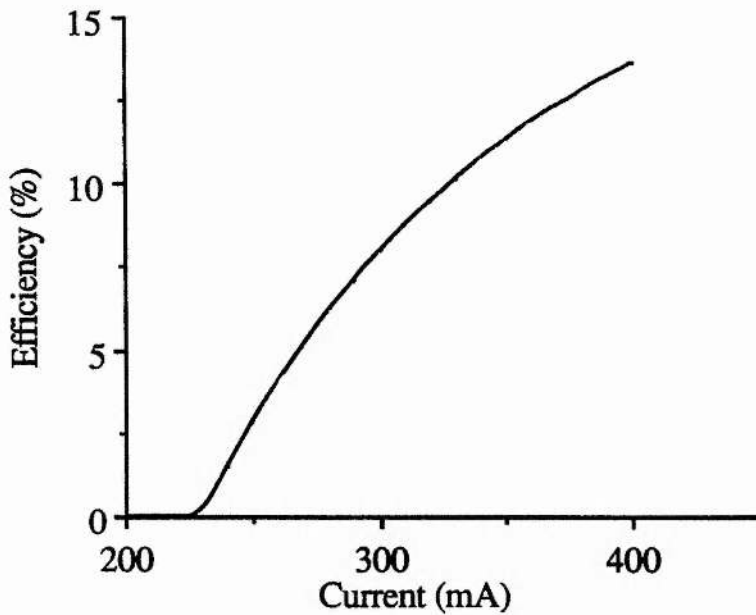


Figure 2.6 Electrical-to-optical conversion efficiency for a typical SDL type 2430-H2 laser-diode against current. Coupling the light into the optical fibre reduces the efficiency for this fibre-coupled laser-diode to around half of that for the window packed laser-diode type 2430-H1.

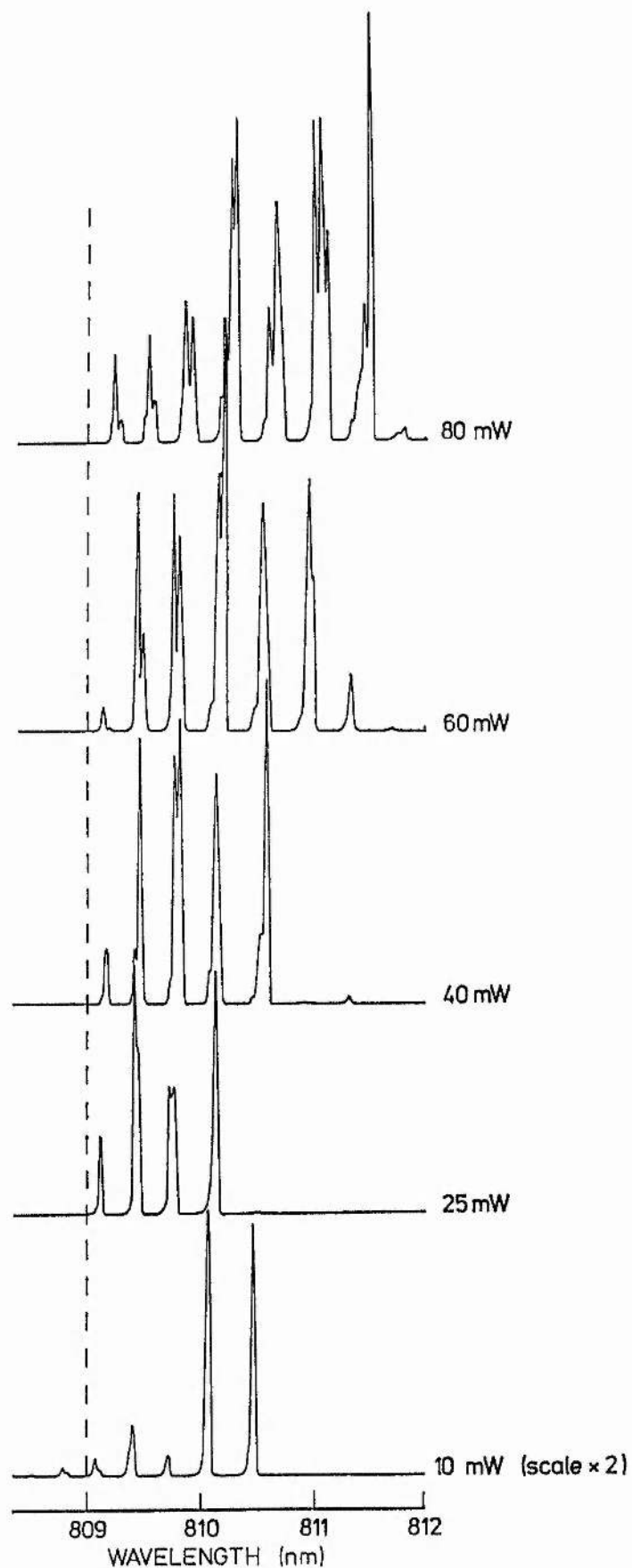
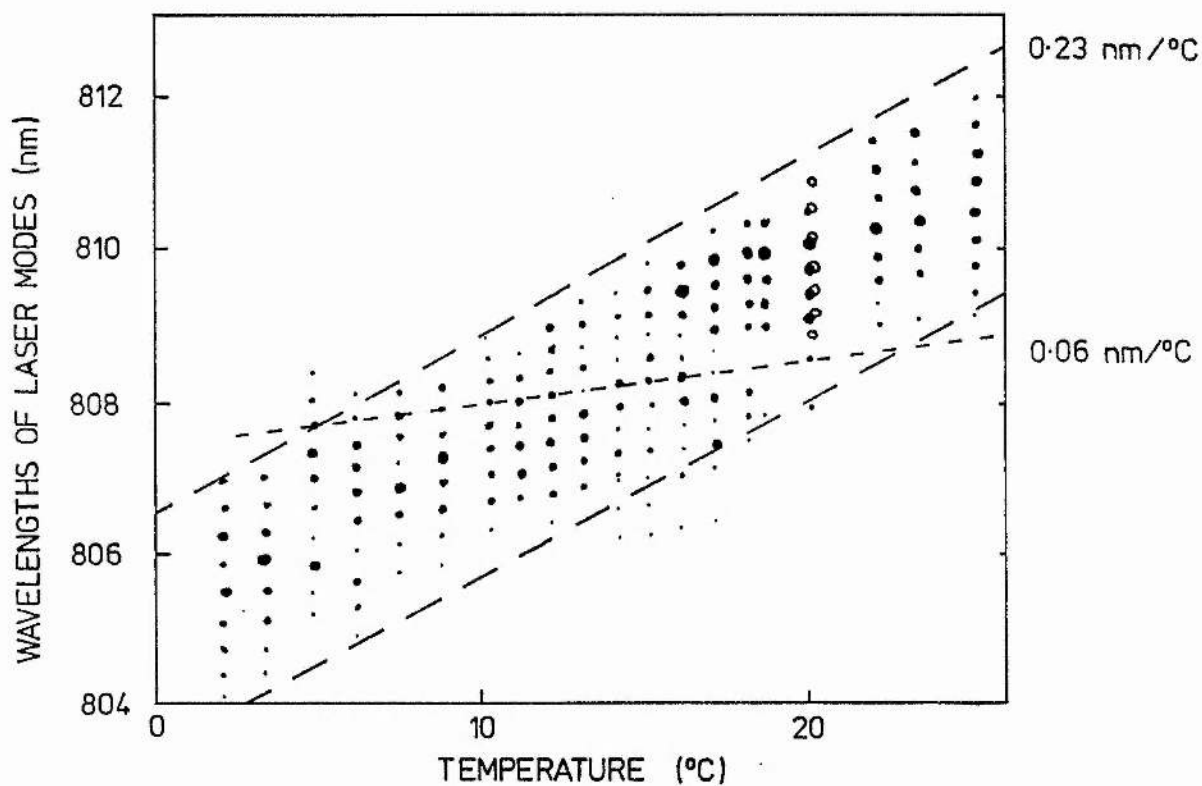


Figure 2.7 Laser-diode array frequency spectra for 5 different power levels showing wavelength bandwidth increasing with optical power.



**Figure 2.8** The measured wavelengths of the laser-diode longitudinal modes are indicated in this figure as a function of temperature, with the size of the marker corresponding to the relative strength of that mode. The total power out of the fibre was 50 mW.

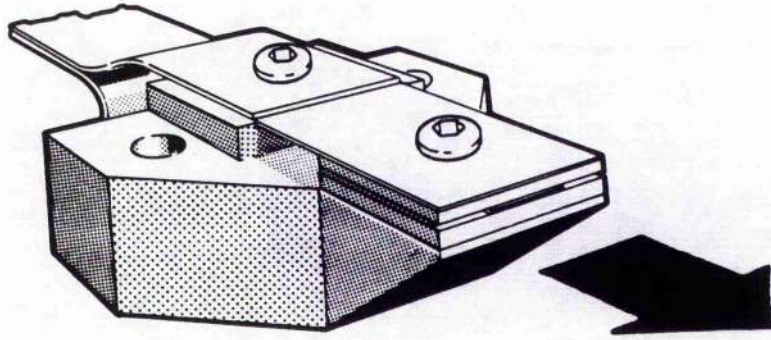


Figure 2.9 Quasi-cw laser-diode bar type SDL-3220-J with emission over a length of 1 cm.

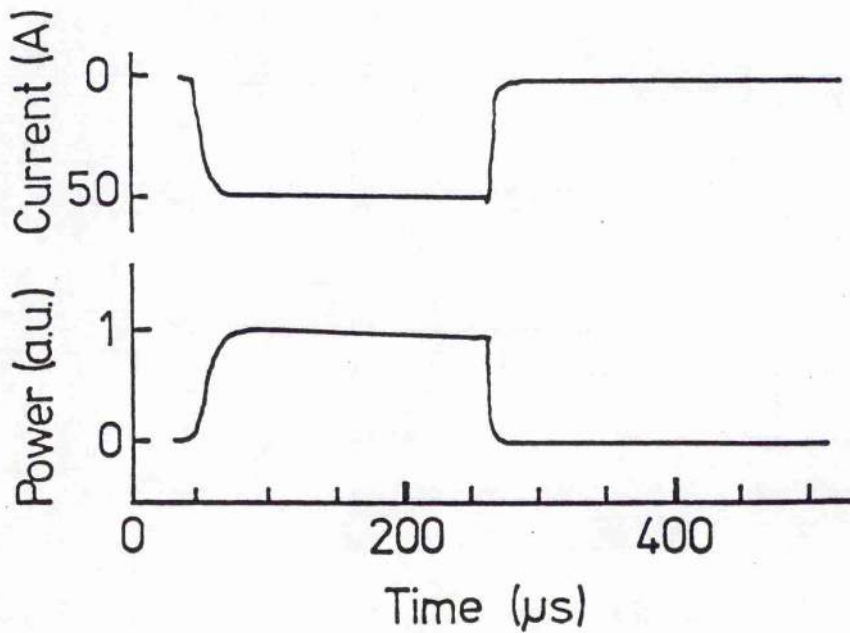


Figure 2.10 Quasi-cw laser-bar current (top) and optical power (bottom) as a function of time through the 200  $\mu\text{s}$  pulse duration.

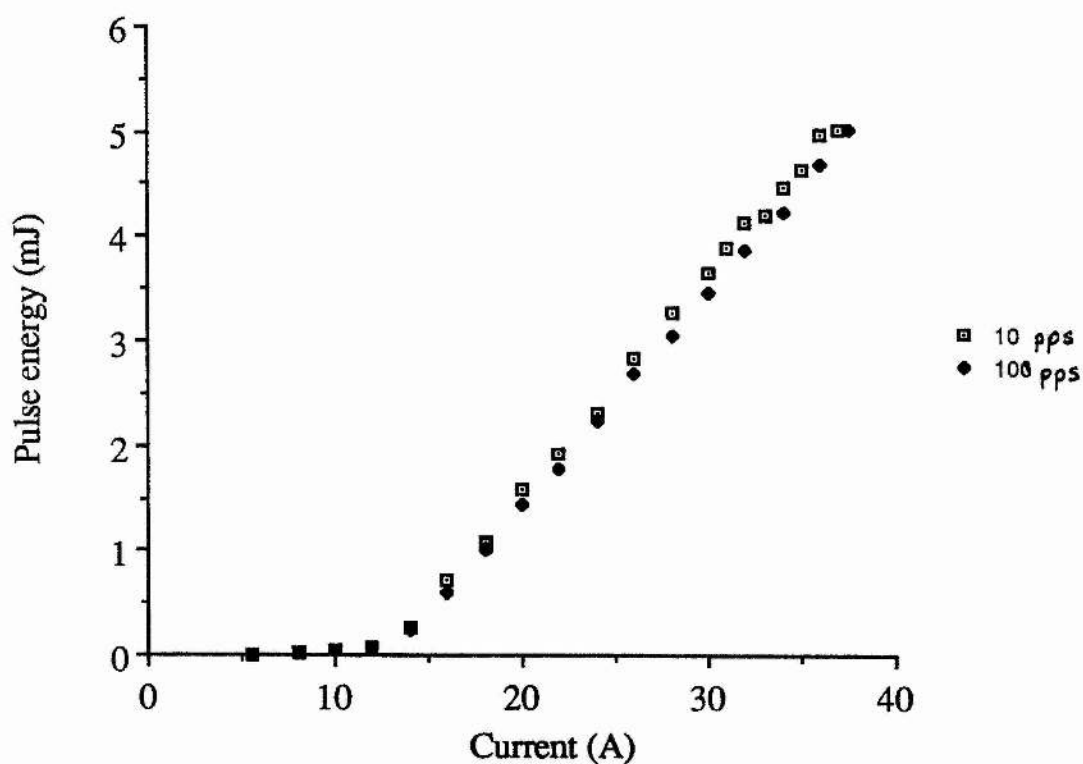


Figure 2.11 Energy per pulse for a laser-bar which shows that the pulse energy at full current at 100 pps is slightly less than at 10 pps. This is attributed to greater heating in the active region at 100 pps which causes the lasing threshold to increase.

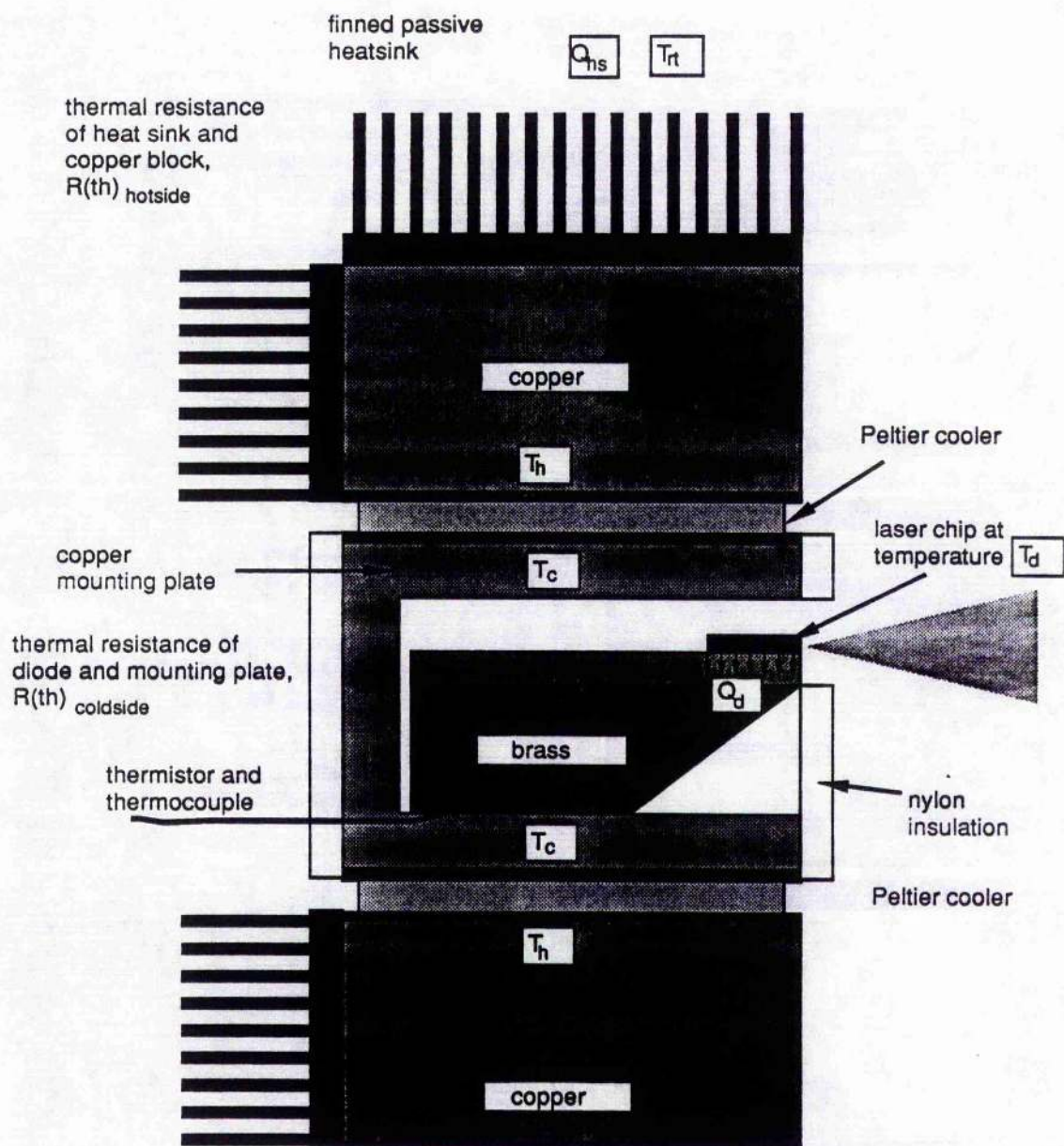


Figure 2.12 Cooling arrangement for quasi-cw laser-diode bar.

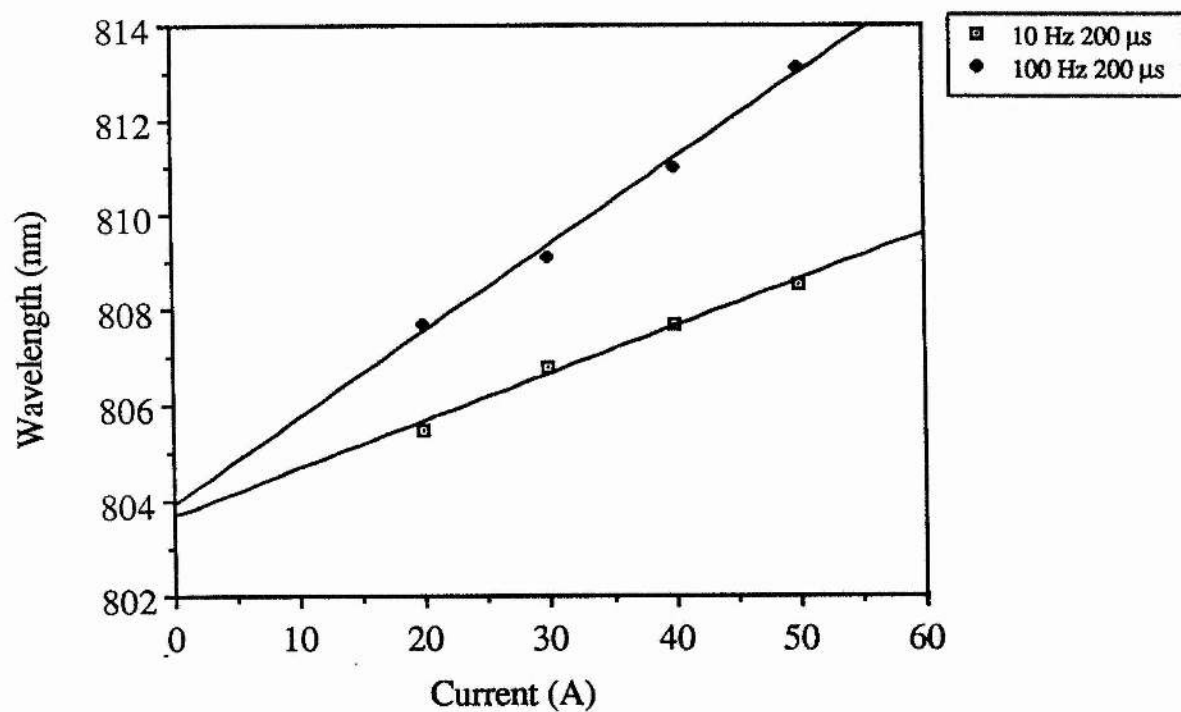


Figure 2.13 Graph of central wavelength from the quasi-cw laser-diode bar as a function of drive current at 10 pps and 100 pps.



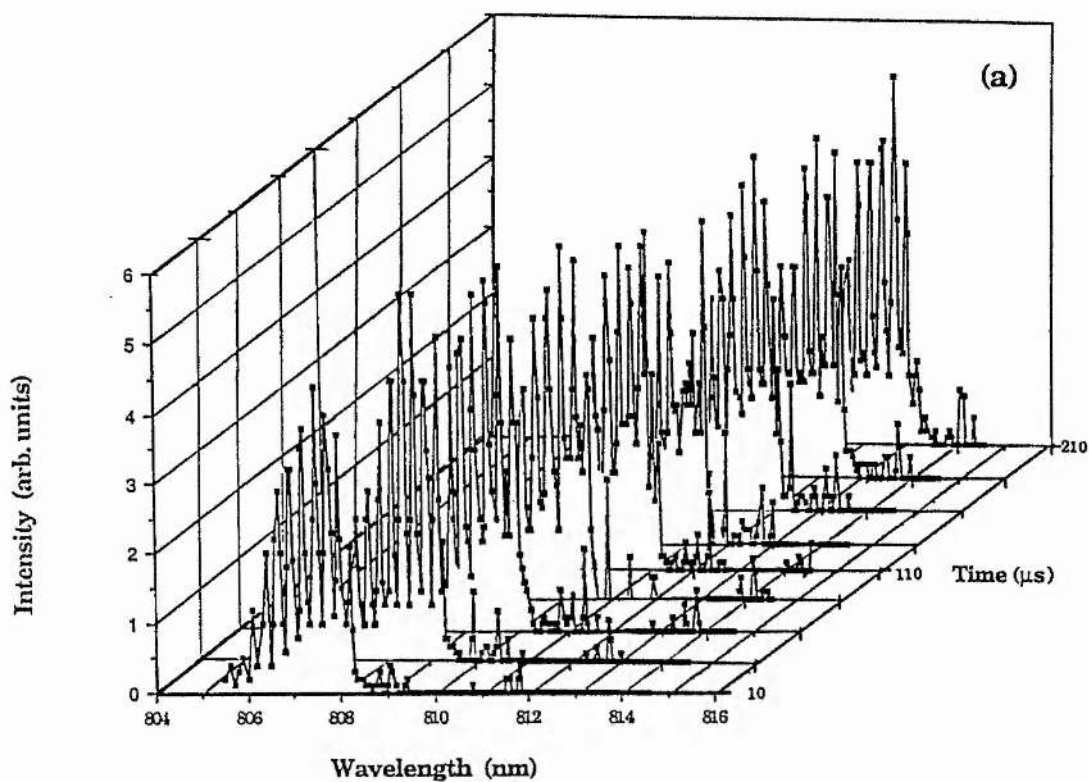


Figure 2.14 Pseudo-3D representation of the frequency spectra from the quasi-cw laser-diode as a function of time into the current pulse.

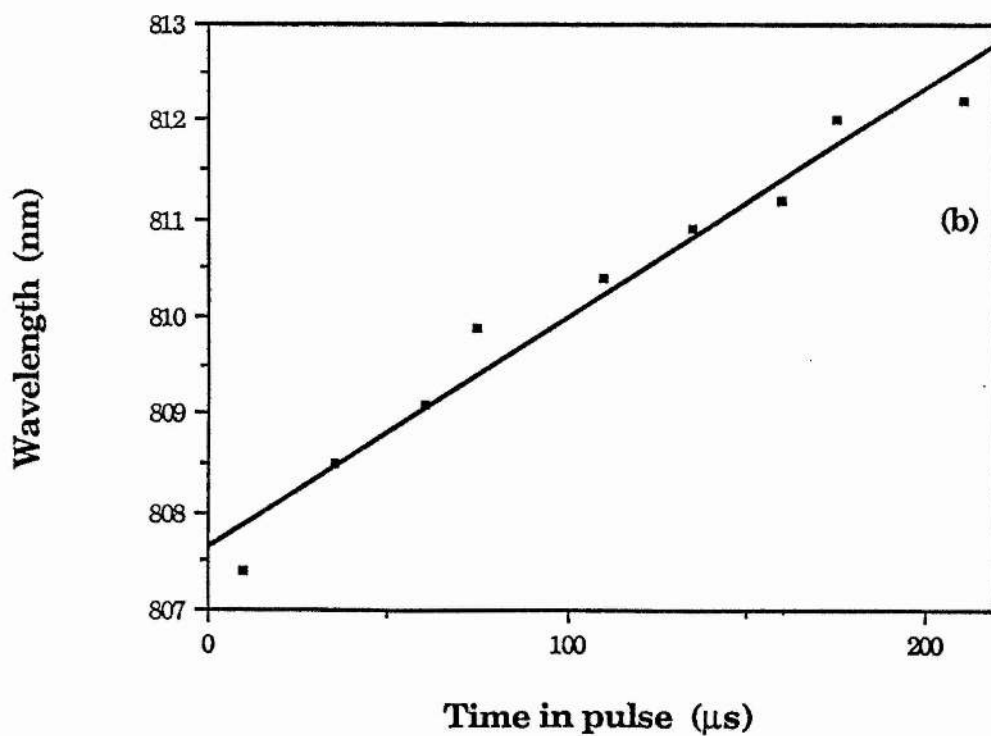


Figure 2.15 Central wavelength from the quasi-cw laser-diode bar showing a dynamic frequency chirp of 4.5 nm over the period of the pulse.

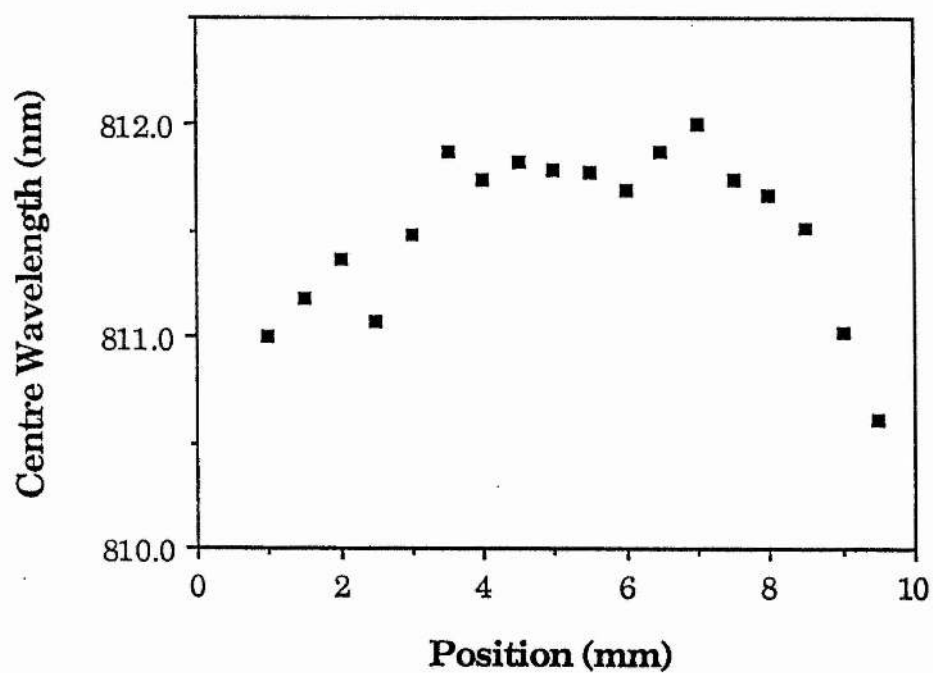


Figure 2.16 Variation in the central wavelength of the laser-diode bar as a function of position across the 1 cm long emitting facet.

## Chapter 3

### Cw Nd:YAG laser longitudinally pumped by a cw laser-diode array

---

#### 3.1 Introduction

This chapter is concerned with a study of the Nd:YAG laser, longitudinally pumped by an 100 mW SDL-2430-H2 fibre-coupled laser-diode array. An introduction to Nd:YAG discusses the properties of the material and details the spectroscopic parameters relevant to laser-diode pumping and lasing at  $1.064\text{ }\mu\text{m}$ . A ray-tracing model of the pump-coupling process determines the spot size and the beam divergence of the pump beam within the Nd:YAG laser rod. The design criteria for the Nd:YAG laser cavity are presented along with the theory behind a full rate-equation based model for the steady-state performance of this laser.

Characteristics of the transverse and longitudinal mode structure are presented with emphasis on single longitudinal mode operation and frequency stability. Several techniques that enable single longitudinal mode operation to be achieved from a diode-pumped cw Nd:YAG were analysed, with a etalon based laser along with a twisted mode cavity laser implemented experimentally. A discriminant for the active stabilisation of the etalon based laser was provided by a dither oscillation of the piezo-ceramic in combination with a temperature stabilised reference cavity.

The analogue modulation capability of the laser-diode provided an effective means to study experimentally the dynamic laser behaviour of the Nd:YAG laser. The relative modulation of the Nd:YAG laser beam is examined as a function of the pump beam modulation with respect to the frequency of relaxation oscillations. A heterodyne measurement of the beat frequency of two steady-state laser-diode pumped Nd:YAG lasers shows that relaxation oscillations are a source of frequency noise.

### 3.2 Nd:YAG gain medium

Well-known as a laser material for many years, neodymium doped yttrium aluminium garnet, Nd:YAG is still overwhelmingly the most commonly used flashlamp pumped solid-state laser material [3.2]. The YAG host lattice is robust enough to allow conventional rod fabrication techniques, has high thermal conductivity and can be of good optical quality. Ions such as neodymium within the YAG lattice typically exhibit fluorescence of narrow spectral linewidth, such that the corresponding laser transitions can benefit from a high stimulated emission cross-section. In consequence, Nd:YAG oscillators can have low pump power thresholds that are suitable for excitation by laser-diodes.

$\text{Nd}^{3+}$  dopant ions substitute with  $\text{Y}^{3+}$  ions during the crystal growing process to become incorporated randomly into the lattice, such that dopant level of neodymium is restricted to  $<1.5\%$  (atomic) as crystals of higher neodymium concentration suffer from strain, concentration quenching and reduced thermal conductivity. For the cw end-pumped lasers a doping level of nominally  $1.0\%$  was selected, though uniformity of doping throughout the boule is  $\pm 0.1\%$ , to give good optical quality and low laser phase-front distortion in the crystal. Nd:YAG with a higher percentage of neodymium, nominally  $1.3\%$  atomic, was selected for the transversely pumped laser described in chapter 4, as pumping efficiency is more critically dependent upon absorptivity for this laser than for the end-pumped counterpart.

An important consideration in the selection of quality laser material was the degree of birefringence observed when the Nd:YAG boule cross-section was placed between crossed polarisers and illuminated by a tungsten lamp. Axially symmetric strain induced birefringence was visible in the boule, along with distortions at the core induced by the Czochralski growth process. For lasers which have intracavity polarisation selective elements, such as the twisted mode cavity laser and the linearly

polarised laser described in section 3.7.2, good laser performance is dependent upon selection of material with a minimum of birefringence.

### 3.2.1 Spectroscopy of Nd:YAG

The active ion in Nd:YAG is the trivalent neodymium ion, for which a diagram of the energy levels is given in figure 3.1 [3.1]. Pumping with laser-diodes emitting around 809 nm excites  $\text{Nd}^{3+}$  ions from the ground state manifold to the pump bands of the  $^4\text{F}_{5/2}$  and  $^2\text{H}_{9/2}$  manifolds. These excited ions emit non-radiatively, decaying rapidly to the metastable  $^4\text{F}_{3/2}$  level which has a fluorescence lifetime of  $\sim 230 \mu\text{s}$  [3.32]. Split into two levels,  $\text{R}_1$  and  $\text{R}_2$ , of slightly differing energy, this manifold contains the upper levels for all the common lasing transitions in Nd:YAG. A full listing of the possible transitions, the lasing wavelengths and the branching ratios is given by Koechner [3.2].

The laser transition with the highest transition probability is the  $1.064 \mu\text{m}$  line, from the upper  $\text{R}_2$  level of the  $^4\text{F}_{3/2}$  manifold to the  $^4\text{I}_{11/2}$  state. Rapid thermal replenishment from the  $\text{R}_1$  level,  $<10 \text{ ns}$ , ensures that the Boltzmann distribution determines that 39% of all the ions in  $^4\text{F}_{3/2}$  state exist in the  $\text{R}_2$  level at room temperature [3.3]. The short lifetime of  $<10 \text{ ns}$  of the lower level is due to rapid decay of the neodymium ions to the ground state, though as the lower  $^4\text{I}_{11/2}$  level is essentially unpopulated, the  $1.064 \mu\text{m}$  transition can be considered for most purposes as a four-level laser transition [3.3]. The parameters relevant to laser action in Nd:YAG at  $1.064 \mu\text{m}$ , are summarised below in table 3.1.

Nd atom density (1% atomic), $N_{\text{tot}}$	$1.4 * 10^{20} \text{ cm}^{-3}$	[3.2]
Stimulated emission cross-section at $1.064 \mu\text{m}$ , $\sigma_e$	$7.4 * 10^{-19} \text{ cm}^2$	[3.31]
Fluorescence lifetime of $^4\text{F}_{3/2}$ state, $\tau_2$	$230 \mu\text{s}$	[3.32]
Fraction of ions in $^4\text{F}_{3/2}$ state in level 2 at room temperature, $f_2$	39%	[3.12]
Refractive index of Nd:YAG at $1.064 \mu\text{m}$ , $n_L$	1.82	[3.2]

Table 3.1 - Spectroscopic laser parameters of Nd:YAG

Although the 946 nm transition is not considered in this work, it is perhaps worth noting that the laser model for this wavelength is significantly different from the  $1.064 \mu\text{m}$  transition in two aspects. Firstly, the upper laser level is the  $R_1$  level in the  $^4\text{F}_{3/2}$  manifold, rather than the  $R_2$  level in the case of the  $1.064 \mu\text{m}$  transition. More significantly, the lower laser level for the 946 nm transition is in the ground state manifold,  $^4\text{I}_{9/2}$ . As there is significant thermal population of the lower level, the 946 nm Nd:YAG laser acts as a quasi-3-level system.

### 3.2.2 Diode-array pump absorption in Nd:YAG

The absorptivity of 1% doped Nd:YAG across the spectrum that is accessible to GaAlAs laser-diode pumps is shown in figure 3.2 [3.1]. The dominant feature is a peak centred at 808.5 nm of approximately 1 nm width, at which the maximum absorptivity is  $\sim 0.8 \text{ mm}^{-1}$ .

The laser-diode array selected to pump our cw laser was a Spectra-Diode Labs SDL-2430-H2, which emitted on several longitudinal modes with an overall spectral bandwidth of  $\sim 2 \text{ nm}$ , as shown in figure 2.12. To obtain the optimum pump efficiency of the Nd:YAG laser, the laser-diode wavelength was temperature tuned to obtain maximum pump absorption by maximising the overlap, or convolution, of the laser-diode spectrum and the Nd:YAG absorption peak at 808.5 nm. The percentage of

pump light transmitted by a sample of Nd:YAG measured as a function of laser-diode temperature is shown in figure 3.3. For the laser-diode operating at 100 mW, the maximum absorptivity of  $0.70 \text{ mm}^{-1}$  was found to occur at  $15^\circ\text{C}$ . It should be noted that this absorptivity is an approximate figure and that each of the laser-diode's longitudinal modes experiences a different absorptivity such that a single exponential decay term cannot strictly be used to express the overall transmitted intensity.

Changes in laser-diode temperature necessitated corrections in the laser-diode drive-current to maintain a constant output power, as the threshold current for the laser-diode was a function of temperature.

It is worth noting that in laser designs that require maximum absorption, there may be a role for index-guided laser-diodes. The emission from an index-guided laser-diode is normally single longitudinal mode, and as such emits with a spectral width that is narrow compared to the absorption peak at 808.5 nm. Though index guided laser-diodes are generally of lower power than gain guided devices, the higher absorption efficiency is of benefit in pumping lasers, such as microchips, which have a short length of crystal in which to absorb the pump light.

---

### 3.3 Miniature end-pumped laser-cavity

The Nd:YAG laser rods employed for the end-pumped laser were cylindrical and of length 5 mm [3.4], such that around 97% of the pump light entering the rod was absorbed within a single pass. For the four level  $1.064 \mu\text{m}$  transition, the rod length is not a critical dimension as the scattering loss and reabsorption in Nd:YAG are slight. For convenient handling of the rods, they were specified to be 3 mm in diameter, which is around 10 times greater than the width of either the pump mode or the lasing mode. The plano-plano polished surfaces were slightly wedged at  $0.5\text{-}1.0^\circ$  with respect to each other, to inhibit etalon effects between the rod surfaces.



In order to focus tightly the pump light into the Nd:YAG it was necessary that a short focal-length lens be placed close to the rod. This called for one of the Nd:YAG cavity reflectors to be coated directly onto the surface of the rod, rather than the use of a discrete mirror. The dichroic coating on the rod was specified to be highly reflecting at the laser wavelength, (>99.5% at 1.064  $\mu\text{m}$ ), and of high transmittance at the pump wavelength, (84% at ~810 nm)\*.

The application of an anti-reflection coating at 1.064  $\mu\text{m}$  to the opposite side of the rod, gave flexibility in cavity design as it allowed the cavity length, along with the reflectivity and radius of curvature of the output coupling mirror, to be altered. Although this was at the expense of increased parasitic loss from the introduction of two additional surfaces, access to the cavity was necessary to facilitate the inclusion of mode-selecting elements.

A photograph of the experimental breadboarded laser is shown in figure 3.4, with a schematic of the cavity design given in figure 3.5. Alignment of this cavity was found to be straight-forward, and could be achieved by adjustment of the position of the focused pump beam, or by tilting the output coupler, such that there was maximum overlap between the pump volume and the lasing mode.

### 3.3.1 Mode-waist-geometry

An important consideration in the design of low power diode-pumped lasers is the minimization of the pump threshold. For end-pumped lasers, with the pump beam concentric with the cavity mode, the threshold pump power,  $P_{\text{th}}$ , may be derived from the mode overlap integral between the pump and laser beams [3.6],

$$P_{\text{th}} = \frac{h\nu_p}{\sigma_e \tau_2} \frac{\pi \beta_t}{4} \left( \frac{\bar{w}_l^2}{\bar{w}_p^2} + \frac{\bar{w}_p^2}{\bar{w}_l^2} \right) \quad (3.1)$$

---

\* Initial coatings performed by Technical Optics, Onchan, Isle of Mann. Latterly, the Nd:YAG rods were coated by Laser Optik, Germany.

where  $\nu_p$  is the pump frequency,  $\beta_t$  is the total round trip loss and  $\bar{w}_l^2$  and  $\bar{w}_p^2$  are the squares of the mean mode radii of the laser and pump beams.

In this case, where the waist of the Gaussian 1.064  $\mu\text{m}$  laser-beam is located at one end of the laser rod, the square of the mean mode radii of the laser beam,  $\bar{w}_l^2$ , is related to the mode waist,  $w_{ol}$ , by,

$$\bar{w}_l^2 = w_{ol}^2 \left( 1 + \frac{1}{3} \left( \frac{\lambda_l L}{\pi n_L w_{ol}^2} \right)^2 \right), \quad (3.2)$$

where  $n_L$  is the refractive index of the medium,  $\lambda_l$  is the laser wavelength and  $L$  is the interaction length between laser and pump [3.7]. For our laser,  $L$  may be approximated to the absorption depth of the pump beam which was 1.4 mm. The laser mode waist for which the threshold pump power is a minimum,  $w_{ol(\text{optimum})}$ , is found by differentiating equation (3.2) with respect to the mode waist.

$$w_{ol(\text{optimum})} = \left( \frac{\lambda_l L}{\sqrt{3} \pi n_L} \right)^{1/2} \quad (3.3)$$

Substituting values for  $n_L = 1.82$ ,  $\lambda_l = 1.064 \mu\text{m}$  and  $L = 1.3 \text{ mm}$  gives an optimum laser mode waist of 12  $\mu\text{m}$ . However, in section 3.4.2 on diode-pump configurations, it is shown that for a fibre-coupled pump source, the pump beam waist  $w_{op}$  is  $\sim 75 \mu\text{m}$ . Consequently, there was little benefit in choosing a cavity design having the optimum beam waist, as the pump waist size would dominate in equation (3.1) for the pump threshold. The criterion that was more important than threshold was that to ensure single transverse mode operation, it was necessary for the pump volume to lie within the volume of the  $\text{TEM}_{00}$  cavity mode. Consequently, mirror radii of curvature and cavity lengths for the Nd:YAG lasers described in this chapter were selected to give a mode waist of  $\sim 75 \mu\text{m}$ .

### 3.3.2 Dye laser excitation

Laser emission from the microlaser cavity was initially achieved by pumping with a Spectra-Physics 380 D ring dye laser, the emission from which was of better quality and narrower linewidth than that from a laser-diode. It was visibly apparent when the dye laser wavelength was tuned to the peak of the 588.6 nm absorption in Nd:YAG. With output couplers of nominally 100% and 99% reflectivity, the threshold pump power was 2 and 5.5 mW respectively, whilst the slope-efficiency was 0.6 and 13% respectively. Dye-laser pumping proved an effective way to align the cavity prior to laser-diode pumping.

Recently there has been considerable development of the titanium-doped sapphire laser, which is tunable in the near-infrared between 670 and 1100 nm. Offering excellent beam quality, at an output power of hundreds of milli-Watts, this solid-state laser has been used to simulate the action of diode-lasers pumps [3.8].

---

## 3.4 Pumping with fibre-coupled laser-diodes

The selection of a fibre-coupled laser-diode, rather than a laser-diode with an open facet, was based largely on the relative simplicity of the pump coupling optics. Experimental details of the pump arrangement are given in this section along with a ray-tracing based analysis of the focussed pump beam. The effect of the pump optics in inducing aberrations in the focussed pump spot is detailed, with the results obtained used later in this chapter in the full rate-equation based model of laser performance.

### 3.4.1 Experimental arrangement

A schematic of the fibre-coupled/single spherical lens pump arrangement is shown in figure 3.5. The multimode fibre had a core diameter of 100  $\mu\text{m}$  and beam divergence from the fibre of  $14^\circ$  half-angle, as described in section 2.2.3. In order to achieve a

tight focus of this highly divergent beam in the Nd:YAG rod, a spherical lens with a high numerical aperture was used\*. The separation between the fibre-end and the spherical lens was adjusted by hand to be  $\sim 1$  mm, with both fibre and lens clamped in place within a machined aluminium block. A more elegant engineering solution would involve a commercial fibre-holding chuck. This assembly was mounted on a 3-axis translation stage which allowed the lens to be positioned about 1 mm from the centre of the dichroically coated surface of the Nd:YAG rod.

As evident from the basic analysis in section 3.3.1, there is an optimum pump focus spot-size at which the threshold-pump power is a minimum. This occurs when the mean square of the waist of the pump is a minimum over the interaction length with the laser mode. The effect of pump spot size upon threshold pump power and total output power was experimentally examined, and the results are shown in figure 3.7. The spot-size was altered by adjusting the distance between the fibre-end and the lens. As the size of the focussed spot was small it proved difficult to measure the spot-size directly. Consequently, spot-sizes were obtained by measuring the angle of divergence of the focussed pump beam, and citing the conservation of brightness for the emission from the fibre, (50  $\mu\text{m}$  radius, half-angle divergence of  $14^\circ$ ). These calculated spot sizes are a lower bound to the actual spot sizes, as no account was taken for aberration through the lens. Nevertheless, it is shown in figure 3.7 that an exact separation between fibre-end and spherical lens was not critical for efficient focussing of the pump beam.

### 3.4.2 Modelling of fibre-coupling

To assess the effect of aberrations upon the focussed spot size, a computer program was developed to trace the paths of a large number of rays from the fibre, through the spherical lens, and into the Nd:YAG rod. The arrangement that was modelled is shown

---

\* Melles Griot 06 LMS 205, 5 mm diameter, 0.34 N.A. anti-reflection coated with  $\text{MgF}_2$

in figure 3.8. The fibre face was modelled as a 2-dimensional array of one thousand emitting points, with a radial Gaussian intensity distribution. From each of these points, a cone of rays with a  $14^\circ$  half angle was propagated through the lens and into the rod. The rod was divided into a number of elements, with the number of rays entering an element taken as a measure of the power density. A profile of the calculated intensity distribution in the rod, which takes into account the absorption of the pump, is shown in figure 3.9.

Using this model, the pump beam in the Nd:YAG rod was ascertained to have a divergence angle of  $5^\circ$  and a  $70\text{ }\mu\text{m}$  waist. The model also confirmed that the focussed spot size was not critically dependent upon the fibre-sphere distance, but was determined for the most part by spherical aberration and coma. A summary of the pump characteristics is given below in table 3.2.

Optical power after lens	100 mW
Transmissivity of dichroic to pump	84%
Beam waist radius	$70\text{ }\mu\text{m}$
Divergence in crystal	$5^\circ$
Position of waist in crystal	0.7 mm into crystal
Peak absorption cross-section at 810 nm, $\sigma_a$	$5.1 \times 10^{-20}\text{ cm}^2^*$

Table 3.2 Fibre-coupled pump beam characteristics

To check the validity of this model, free-space spot sizes were compared with those obtained from the model in which the refractive index of the Nd:YAG rod was set to unity; it was obviously impossible to measure the pump beam intensity inside the rod directly. Values for the beam waist near the focus were calculated by the ray-tracing

---

\* This is calculated from  $N_{\text{tot}}$  in table 3.1, and an absorptivity of  $0.70\text{ mm}^{-1}$  as found in section 3.2.2.

model and also measured with a scanning photodiode with pinhole, and are in good agreement as shown by figure 3.10.

### 3.4.3 Overcoming aberrations

Because of the high numerical aperture of the spherical lens, the aberrations in the pump beam introduced by this simple lens were particularly severe. Consequently, it was felt that the pumping efficiency could be improved by the use of two spherical lenses to reduce the refraction at each surface. Somewhat surprisingly, when the two spherical focusing lenses were incorporated the output power from the Nd:YAG laser was markedly lower. It was noted, however, that the output power from the Nd:YAG laser increased when the second sphere-to-rod distance was decreased, and that the output power was still increasing when the second sphere was at the surface of the rod. This indicates that the distance between the back surface of the second sphere and the back focal plane is very small, and that optimum coupling required the pump light to be focussed some way into the rod as shown in figure 3.6.

A possible alternative to the spherical lens is the gradient index lens, in which the refractive index varies radially, so that images are formed by continuous refraction [3.9]. The amount of aberration that a gradient index lens would introduce in this instance needs to be quantified. Sophisticated multi-element lenses are also available to compensate for spherical aberration, coma, astigmatism and sphero-chromatism. Such lenses were found to be necessary for the 946 nm diode-pumped laser which required a particularly tightly focussed pump beam [3.30]. However, modelling described later in section 3.6 shows that this is not the case for lasing from the four-level 1.064  $\mu\text{m}$  transition.

### **3.5 Performance of diode-pumped cw Nd:YAG laser**

#### **3.5.1 Optical power characteristics**

Measurement of the optical input power from the diode is described in chapter 2.2.1, and the output power at 1.064  $\mu\text{m}$  was measured by a Scientech power meter. A coloured glass filter absorbed the residual 810 nm pump radiation. The initial laser configuration shown in figure 3.5 had an output coupler with 5 cm ROC and 98% reflectivity, and a mirror-rod spacing of 4.5 mm. Due to the poor quality of the coating on the rod the pump threshold was 18 mW, and the slope efficiency was only 18%. Improved performance was obtained with a new laser-rod, for which the output coupler was changed to a 7.5 cm ROC with 98-99% reflectivity. This laser had a measured threshold of 21 mW, a slope efficiency of 39%, and a maximum output power of 31 mW when pumped with 100 mW as shown in figure 3.11. This performance is equal to that achieved in a similar commercial laser\*.

#### **3.5.2 Transverse mode structure and beam divergence**

The spatial profile of the output beam from the Nd:YAG laser was scanned with a pinhole apertured photodiode at a distance of 1 m from the Nd:YAG rod. The comparison between the experimental points and a Gaussian function in figure 3.12 show that the transverse mode structure was a clean symmetrical Gaussian mode. Further studies showed that single transverse mode could be reliably obtained, without resorting to a pinhole within the cavity, by ensuring that the pump mode volume was no larger than the volume of the fundamental cavity mode.

---

\* Spectra-Physics - 7200Y1 pump module, 7900Y-106 laser head - specified at 35 mW randomly polarised at 1.064  $\mu\text{m}$ .



Beam scans were repeated at other distances from the laser, with measurements of the half-width at the  $e^{-2}$  intensity points showing a full angle divergence of  $0.83^\circ$ . Based on a beam waist of  $58 \mu\text{m}$ , which was calculated from the geometry of the resonator, the anticipated divergence after taking into account the output coupler which acts as a diverging lens, was  $0.96^\circ$ .

### 3.5.3 Loss measurements

To determine the amount of parasitic loss in the cavity, a glass plate was used as a variable reflectivity output coupler in a laser with a 10 cm ROC high reflectivity mirror. This plate which was mounted close to the Brewster angle constrained the plane of polarisation, such that the percentage of light reflected out of the cavity could be determined as a function of plate angle using the appropriate Fresnel equation [3.35]. The accuracy of this technique was confirmed by showing that the calculated transmittance of the nominally high reflectivity mirror was constant at 0.04% over almost the entire range of plate angles, and was in acceptable agreement with the experimentally measured value of 0.06%.

The total measured output power is plotted as a function of the calculated total output coupling in figure 3.13. This shows that the net single pass gain,  $g_0$ , was 8% and the optimum transmissivity was 1.6%. Also determined from this graph was the total parasitic loss in the cavity,  $\beta_p$ , which is related to the optimum output coupling,  $\beta_{opt}$ , and maximum output coupling while still lasing,  $\beta_m$ , by [3.15],

$$\beta_p = \frac{\beta_{opt}^2}{\beta_m - 2\beta_{opt}} \quad (3.4)$$

This gives a value for the parasitic loss of 0.53%, which however includes scattering loss introduced by the output-coupling plate which reduced the maximum output power from this laser from 31 mW to 17 mW. As the introduction of the Fresnel plate doubled the number of intra-cavity surfaces, the parasitic loss in the absence of the plate has been estimated at 0.3% in subsequent modelling of the laser.

### 3.6 Output power model for cw microlaser

In order to obtain a greater understanding of the pumping process, a rate-equation based model was formulated to determine the laser output power as a function of the relevant pump and cavity parameters. This allowed us to theoretically optimise the laser and to assess potential improvements quantitatively. The pump model is fairly general, and is applicable to 3- and 4-level longitudinally pumped lasers for which the pump light is symmetric, and concentric with the cavity axis. In addition to analyses of Nd:YAG lasers, the model has been applied to a comparison between diode-pumping and Ti-sapphire pumping of Nd:MgO:LiNbO<sub>3</sub> [3.8]. The code for the programs was written in FORTRAN by Andrew Wray [3.33].

The pump parameters are those given in table 3.2 namely: pump power, waist size, divergence and position of the pump waist, the transmissivity of the dichroic mirror and the absorption cross-section. The cavity parameters and their respective values are given below in table 3.3.

Beam waist	75 $\mu\text{m}$
Crystal length	5 mm
Parasitic loss, $\beta_p$	0.3%
Output coupling transmissivity, $\beta_{\text{out}}$	2%

Table 3.3 Cavity parameters used in model

As the pump beam and cavity mode were circularly symmetric and concentric, each of the 600 axial slices within the rod was further divided into circular annuli as shown schematically in figure 3.15. The width of each annulus was increased exponentially with radius so that each annulus has the same flux although a different flux density.

### 3.6.1 Pump beam profile

The model described differs from those proposed for a three-level laser by Fan and Byer [3.12] and Risk [3.13]. These models were based upon non-diverging Gaussian pump and Nd:YAG beams. It is felt that the approach taken here, which also takes into account the divergence of the pump beam, is likely to be more accurate.

As discussed in section 3.4.2 on pump coupling, the beam waist is dependent upon aberrations induced by the high numerical aperture spherical lens. The result of the model was to show that the pump beam within the Nd:YAG rod may be taken as a Gaussian converging beam of 5° half-angle and waist of 70  $\mu\text{m}$ . Rather than a Gaussian beam profile, a top hat distribution with width equal to the Gaussian waist and a triangular distribution with width equal to 1.3 times the Gaussian waist were chosen for the model. Either profile appears satisfactory, with values obtained from each being in close agreement with experimental results.

### 3.6.2 Pumping rate

In a determination of the output power from the model, the pumping rate,  $R$ , and its relationship to the pump power is necessary. The rate of pumping is the rate at which ions are excited from the ground state to the upper laser  $^4F_{3/2}$  manifold per unit volume. All ions excited into the pump bands subsequently reach this manifold, so the pump rate may be expressed in terms of the change in pump intensity,  $dI_p$ ,

$$R = \frac{dI_p}{h\nu_p dv} \quad (3.5)$$

where  $h\nu_p$  is the energy of a pump photon, and  $dv$  is unit volume. The change in pump intensity,  $dI_p$ , can be related to the pump absorption cross section,  $\sigma_A$ , and the density of ions in the ground state,  $N_0$ , through,

$$dI_p = I_p \sigma_A N_0 dx \quad , \quad (3.6)$$

where  $I_p$  is the pump intensity and  $dx$  is an incremental length along the cavity. The density of ions in the ground state may, in turn, be written in terms of the saturation pump intensity term,  $I_{sa}$ , and the total density of active ions,  $N_{tot}$ ,

$$N_o = \frac{N_{tot}}{1 + I_p/I_{sa}} \quad (3.7)$$

The saturation intensity,  $I_{sa}$ , is defined as the pump intensity required to reduce the ground state population to one half of the total number of active ions, and may be expressed as [3.33],

$$I_{sa} = \frac{h\nu_p}{\tau\sigma_A} + 2f_2 \frac{I_L\sigma_s\nu_p}{\sigma_A\nu_L} \quad (3.8)$$

The first term gives the saturation intensity in the absence of stimulated emission. This term is equivalent to the flux intensity that is achieved by one pump photon being incident upon an area equal to the absorption cross-section of the medium in a period given by the fluorescence lifetime of its upper-state. For Nd:YAG pumped at 808.5 nm, this saturation intensity term is 12.8 kWcm<sup>-2</sup>. The second term in equation (3.8) for the saturation intensity is the pump flux required to compensate for repopulation of the ground state by stimulated emission. For an estimated intracavity flux of 3 Watts at 1.064  $\mu$ m, this term is equal to 42 Wcm<sup>-2</sup> and is small in comparison to the first term. Though included in the model, the saturation of the pump is not an important consideration in the laser we consider, as the peak pump intensity in our laser was only ~ 650 Wcm<sup>-2</sup>, which is small compared to the saturation intensity.

The change in pump intensity,  $dI_p$ , can then be obtained from equations (3.6) and (3.7),

$$dI_p = \frac{I_p\sigma_A N_T dx}{1 + I_p/I_{sa}} \quad (3.10)$$

from which, along with equation (3.5), the following expression for the saturated pump rate is obtained

$$R = \frac{\sigma_A N_T}{h\nu_p} \frac{I_p}{1 + I_p/I_{sa}} \quad (3.11)$$

In the computer model a routine obtains an array of values for the saturated pump intensity throughout the rod. The values for the pump intensity,  $I_p$ , at each annulus in the first section are found from a consideration of the pump power and the pump profile. The intensity profile incident upon the next section was found by subtracting the absorbed pump power, obtained using equation (3.9), and redistributing the transmitted power into the specified profile shape. This revised pump profile, whether rectangular or triangular, takes account of pump divergence.

### 3.6.3 Rate equation analysis

The basis for the rate equations used in this model is the Nd:YAG energy level diagram shown in figure 3.1. As discussed in the section on the spectroscopy of Nd:YAG, lasing occurs from level  $R_2$ , and it is an expression for population in this level,  $N_{R2}$ , that is determined in this section. This is the upper of the two levels of similar energy that make up the  $^4F_{3/2}$  manifold. The relative populations of levels  $R_1$  and  $R_2$  are assumed to be constant, since there is rapid thermalisation between them [3.3]. That is, the population of the  $R_2$  level is a constant fraction of the total upper level population,

$$N_{R2} = f_2 (N_{R1} + N_{R2}) , \quad (3.11)$$

where  $f_2$  is obtained from the Boltzmann distribution and is constant for a given temperature. As the lifetime of the  $^4I_{11/2}$  lower level was short at  $<10$  ns [3.3], all of the ions in the upper laser level contributed to a population inversion. The differential equations for the populations of the ground-state level, and the two upper levels,  $R_1$  and  $R_2$ , are [3.15],

$$\frac{dN_0}{dt} = -R + \frac{N_{R2}}{\tau_2} + \frac{N_{R1}}{\tau_2} + 2 \frac{I_L \sigma_s N_{R2}}{h\nu} \quad (3.12)$$

$$\frac{dN_{R2}}{dt} = R - \frac{N_{R2}}{\tau_2} - 2 \frac{I_L \sigma_s N_{R2}}{h\nu} - K_{21} N_{R2} + K_{12} N_{R1} \quad (3.13)$$

$$\frac{dN_{R1}}{dt} = -\frac{N_{R1}}{\tau_2} + K_{21}N_{R2} - K_{12}N_{R1} \quad (3.14)$$

where  $R$  is the rate of pump excitation per unit volume from the ground state to the  $^4F_{3/2}$  manifold,  $I_L$  is the intracavity flux intensity at 1064 nm, and  $K_{12}$  and  $K_{21}$  are thermalisation coefficients for the transition from  $N_{R1}$  to  $N_{R2}$ . Equations 3.12 - 3.14, which may all be equated to zero for steady-state cw operation, may be simplified to one equation involving level  $R_2$ , the upper state for the 1.064  $\mu\text{m}$  lasing transition. This allows one to write the rate equation for the population of the upper laser level,  $N_{R2}$ , as,

$$\frac{dN_{R2}}{dt} = f_2R - \frac{N_{R2}}{\tau_2} - 2f_2 \frac{I_L \sigma_s N_{R2}}{h\nu_L} \quad (3.15)$$

where  $f_2$  is the fraction of ions in level  $R_2$  of the  $^4F_{3/2}$  manifold, (39%). The first term,  $f_2R$ , is the pumping rate of the upper state and the other two terms express the depopulation of the upper level by spontaneous and stimulated emission respectively. Included in the stimulated emission term is a factor of two which accounts for flux propagating in the cavity in both directions.

In steady state cw operation, the time derivative of the upper state population is zero, so that the upper level laser population is given by,

$$N_{R2} = \frac{f_2 R \tau_2}{1 + 2f_2 \frac{I_L \sigma_s N_{R2}}{h\nu_L}} \quad (3.16)$$

Well above threshold, stimulated emission is dominant in the denominator of the above equation, so that the upper level laser population may be rewritten as,

$$N_{R2} = \sqrt{\frac{h\nu_L R \tau_2}{I_L \sigma_s}} \quad (3.17)$$

with the upper state population proportional to the square root of the pumping rate.

### 3.6.4 Single-pass gain

The model involves the determination of the saturated gain over a single pass of the cavity,  $\alpha_{sp}$ , which is found by determining the saturated gain over successive sections of the laser rod. The gain within a cylindrical section,  $\alpha_{section}$ , is found from the product of the stimulated emission cross section,  $\sigma_s$ , and the upperstate population integrated over the length of the section.

$$\alpha_{section} = \int_{section} N_{R2} \sigma_s dx \quad (3.18)$$

The increased flux intensity from all the annuli gives the total power increase for a particular section. In the model the laser mode propagates down the cavity, and the increase in intensity is calculated at each section. This increased optical power is then used to set the magnitude of the Gaussian intensity profile entering the next section. The justification for this flux redistribution is that diffraction within the stable cavity geometry acts to maintain a Gaussian radial intensity distribution.

The laser mode within the cavity was taken to be cylindrical, with a radial Gaussian intensity distribution. This is justifiable, as the mode size does not differ much from one end of the rod to the other. For cavities that utilise a tightly focused resonator, for instance the diode pumped 946 nm laser, this assumption is invalid [3.30].

The single pass saturated gain is found from the difference between the optical power before the flux passes down the rod,  $P_{lo(start)}$ , and after the flux has undergone a single pass of the rod,  $P_{lo(end)}$ ,

$$\alpha_{sp} = \frac{P_{lo(end)} - P_{lo(start)}}{P_{lo(start)}}, \quad (3.19)$$

where the laser power in the section at the end of the rod is compared with the laser power in the section at the start of the rod.



In the program the initial circulating power  $P_{lo(start)}$  is taken as 0.025 W. Given this initial value, the saturated pumping rate is computed, and from this the single pass saturated gain is obtained. For steady state operation of the laser, the saturated round-trip gain is equal to the round trip loss. If the saturated gain is greater than the single pass loss,  $1/2 \beta_{rt}$ , where,

$$1/2 \beta_{rt} = 1/2 (\gamma + \ln\left(\frac{1}{R_1 R_2}\right)) \quad (3.20)$$

then the value of the initial circulating power is increased for the next iteration of the program. Upon obtaining parity of gain with loss, the output power is calculated from the final value of the intracavity optical power, using,

$$P_{out} = 1/2 (1 - R_2) P_{lo(start)} \quad (3.21)$$

where  $R_2$  is the reflectivity of the output coupler.

The output power as a function of the pump power is obtained by running the entire program at different pump powers.

### 3.6.5 Results

Using the pump and cavity parameters in tables 3.2 and 3.3, the model was run to obtain the output power against pump power and the results for both the triangular and the rectangular pump beam profiles were plotted in figure 3.16. The calculated pump threshold of 18 mW and slope-efficiency of 35% are in fair agreement with the experimental values of 25 mW and 39% as obtained from figure 3.11.

The model was also run with the output power computed as a function of the transmissivity of the output coupling mirror. The results, plotted in figure 3.14, show a value for the net small-signal round-trip gain of 10% that is close to the 8% that was experimentally determined using the Fresnel plate in section 3.5.3. In addition, the model confirms that our selection of an 1.5% transmissivity output coupler was close to the optimum to obtain the maximum output power of ~30 mW from this laser.

Further results from the computer model included the dependence of the output power upon the length of the Nd:YAG rod, as shown in figure 3.17. For the given pump and cavity parameters and with a single-pass of the pump light, it is predicted from figure 3.17 that for the microchip lasers described in section 3.7.2.d the output power from a 1 mm long rod would be around  $2/3$  of that from a rod in which there was full absorption of the pump.

---

### 3.7 Longitudinal mode characteristics

A necessary property of a cw laser-source that is used for the injection-seeding is that the cw source operates in a single longitudinal mode. Unfortunately, Nd:YAG lasers commonly lase on a number of longitudinal modes, due to an effect called spatial hole-burning, which is discussed below. Also described, are means of achieving single longitudinal mode operation in diode-pumped lasers. Furthermore, the frequency stability, both short term (jitter) and long-term (drift), are discussed with particular reference to injection-seeding.

#### 3.7.1 Spatial hole burning

Spatial hole burning is an effect in which the first longitudinal mode to lase causes periodic saturation of the gain along the axis of a standing wave laser cavity. This results in a "spatial-grating" of undepleted population inversion, which encourages modes at additional frequencies which are out of phase with the main longitudinal mode [3.14].

The frequency separation between modes as measured with a scanning confocal Fabry-Perot interferometer was  $17 \pm 2$  GHz. The comparatively large uncertainty was caused by non-linearity of translation in the piezo-ceramic scanner. The mode spacing between adjacent modes of the laser was calculated from the length of the cavity to be  $3.543 \pm 0.004$  GHz, which means that every fourth or fifth cavity mode was oscillating.

### 3.7.2 Single-frequency operation

#### 3.7.2.a Intracavity etalon mode selection

The use of intracavity etalons to establish single longitudinal mode operation is a well established technique in which multiple-reflections within the etalon suppress those frequencies which do not fall within the pass-band of the filter. As the resonator length for the diode-pumped laser was typically a few centimetres, the inter-mode frequency spacing was large which necessitated the use of thin etalons with suitably large free-spectral range to achieve single longitudinal mode operation.

The free-spectral range, FSR, of the etalon is given as a function of the optical thickness of the etalon,  $FSR = c/2nd$ . For a 1 mm thick etalon of refractive index 1.5, the maximum free-spectral-range is 100 GHz, and is  $\sim 70$  GHz when the etalon is at an angle of  $45^\circ$  to the laser propagation direction.

A range of solid uncoated glass etalons between 0.115 mm and 1.0 mm thick were inserted in the cavity shown in figure 3.18. These etalons, which exhibit low scattering loss, were mounted on a galvanometer (General Scanning G208) which was used to adjust the angle of the etalon and hence the optical thickness. The etalons cannot be oriented at too great an angle, otherwise transverse walk off reduces the finesse and more importantly increases loss at any frequency in the laser [3.15]. The 1.0 mm thick etalon was found to be the most effective when used in the laser and up to 14 mW of single frequency output power was obtained for 100 mW pump power.

It was subsequently observed that this ostensibly SLM laser actually emitted two closely spaced frequencies of orthogonal polarization. This existence of two polarizations was attributed to the coupling of energy between polarizations by the birefringence of the Nd:YAG crystal. Upon insertion of a plate at the Brewster angle true single frequency operation was achieved at the further reduced output power of 10 mW.

### 3.7.2.b Twisted cavity mode laser

An alternative method for ensuring single longitudinal mode operation is the twisted cavity mode technique. In such a laser a polarising element, eg a plate mounted at the Brewster angle, defines a plane of polarization. Light polarized linearly by this element becomes circularly polarized after passing through a quarter wave plate, and into the gain medium. A second quarter wave plate after the laser rod acts to make the light linearly polarised again, so that upon reflection at a cavity mirror the reflected flux is circularly polarised with opposite sense upon its second pass through the gain medium. In consequence the amplitude of the electric field vector, and hence the intensity of the flux, is uniform along the laser rod. This prevents spatial hole-burning in which nodes of undepleted gain encourage alternative longitudinal modes to oscillate.

Work done by Nigel Gallaher within the group at St.Andrews on a diode-pumped twisted cavity mode Nd:YAG laser has resulted in approximately 8 mW of cw TEM<sub>00</sub> single frequency output at  $\lambda = 1.064 \mu\text{m}$  from 100 mW of 809 nm pump light. In this laser, the rod is placed between two low order ( $5\lambda/4$ ) quarter wave plates, with one of the quarter wave plates acting as a dichroic mirror for the pump and laser radiation.

An advantage for this laser over the etalon mode selection technique is that the structure is more stable as there are no moving parts such as galvanometer mounted etalons. Further, there is potentially higher efficiency as all of the inverted gain medium along the optic axis can contribute to the lasing mode intensity. Care must be taken in the selection of low birefringence Nd:YAG material, as birefringence disrupts the polarization state between the quarter wave plates. The twisted cavity mode technique is obviously unsuitable for highly birefringent materials such as Nd:YLF.

### 3.7.2.c Unidirectional ring laser configuration

The ring laser is a highly successful way of obtaining single longitudinal mode operation in many laser types, and this configuration is used in a number of commercial

lasers systems. Ring lasers consist in essence of three or more mirrors, with an optical diode that ensures that the flux travels around the ring in only one direction. As the flux is a travelling wave, the intensity is uniform along the axis of the laser cavity and so spatial hole burning is avoided.

A recent attractive development, and one stimulated by advances in laser-diode excitation, is the ring laser within a single piece of laser material [3.16]. The monolithic nature of this laser and the low intensity noise from the laser-diode pump combine to create an intrinsically stable source. This laser which has been named the MISER\* is presently the only laser used commercially to injection-seed flash-lamp pumped Q-switched lasers, and as such it offers a bench mark for the design of a stable cw single mode laser\*.

#### 3.7.2.d Microchip lasers

A concept that is a partial solution to the problem of spatial hole burning is the microchip laser in which the cavity length is particularly short, and in consequence the intermode spacing is large [3.18]. If the intermode-spacing is greater than the bandwidth of the gain medium, then no more than one longitudinal mode can have sufficient gain to oscillate. The location of that mode can be centralised within the gain bandwidth by thermal or piezo-tuning of the cavity length [3.19]. Microchip lasers have also been referred to as Fabry-Perot lasers, since the cavity mirrors themselves act as a mode selection etalon. The highest single-mode-cw output power reported to date from a diode-pumped Nd:YAG microchip is 22 mW [3.18].

Increased interest in the microchip laser concept resulted from a demonstration of a laser operation with a chip with plane mirrors. This has obvious benefits for fabrication costs as it allows a large number of lasers to be diced from a single wafer of

---

\* MISER - Monolithic Isolated Single-mode End-pumped Ring laser

\* Lightwave Electronics - Series 100 Injection Seeding System.

gain material. As plano-plano cavities are normally unstable, it is thought that thermal lensing by the pump or cavity flux introduces stability. Divergence of the TEM<sub>00</sub> output beam was shown to vary with pump power, though at high pump powers unpredictable results were observed [3.18].

Microchip lasers are particularly suitable for diode laser pumping, with direct close-coupled pumping without intermediate optics. Increased pump efficiency results from the use of stoichiometric materials which have high pump absorption. These materials, of which LNP is an example, have the active ion as an intrinsic part of the crystalline structure rather than as a dopant [3.21]. With the reduction in length of cavity in microchip lasers there is a decrease in the cavity lifetime. One beneficial effect of this is the ability for microchip lasers to produce pulses of tens of nanoseconds duration by gain switching the pump medium. Of recent interest is microchip hosts that exhibit nonlinear optical properties. These hold out the prospect of single frequency electro-optically tunable lasers, and also the self-frequency-doubling of microchip lasers.

### 3.7.3 Frequency stability

Stable narrow linewidth lasers have a number of applications, including injection seeding of Q-switched lasers, high resolution spectroscopy, gravity wave detection, and coherent communication. Contributions are being made by laser-diode pumped lasers in all these areas, due to their good inherent short-term frequency stability. This frequency stability is demonstrated by a free running linewidth of around 10 kHz, which compares with ~100 kHz for the distributed feedback laser-diode, and ~10 MHz for the flashlamp pumped Nd:YAG laser [3.1]. This section deals with the construction and performance of a stabilised cw laser for injection seeding, and with the general aspects of narrow linewidth cw diode-pumped lasers.



### 3.7.3.a Cw laser for injection seeding

The single frequency cw laser used for injection-seeding was the experimental laser arrangement illustrated in figure 3.18, except that the mounting of the output coupler was adapted to include a high-voltage piezo-ceramic tube to permit active stabilisation. To enable heterodyne measurements of the frequency stability of this laser, a second similar laser was constructed. Although having the same elements, the second laser benefited from a more solid construction, being built within a substantial invar cylinder. The output coupler for this second laser was mounted on a miniature low-voltage piezo-electric mount (Photon Control ASM 20), that enabled alignment of the laser cavity as well as control of the cavity length.

The short-term linewidth and the drift in the laser was determined by a measurement of the heterodyne beat signal between the two lasers. This was achieved by mixing the beams from the two lasers on a high-speed photodiode (BPW 28), taking care to ensure good matching of the phase-fronts from both lasers. The beat signal was monitored on a HP 70000 series spectrum analyser which had a bandwidth of 10 Hz - 2.9 GHz. The short-term heterodyne signal between the lasers showed a 500 kHz linewidth in a sweep of 10 ms, and a long term drift between the lasers of 25 MHz in 1 minute. Upon enclosing the lasers within a lead clad chip-board box, and moving them to a quieter laboratory, the free-running linewidth was reduced to 10 kHz. This measurement was limited by the resolution bandwidth of the spectrum analyser.

For the purpose of injection seeding, active stabilisation of the laser was necessary to reduce the frequency drift of the open cavity laser. This involved the use of a reference cavity as a frequency discriminant, with the stabilisation implemented through an electronic-based servo system. The three principal stabilisation techniques which use the frequency discriminant provided by a reference cavity are side-of-fringe locking, r.f. modulation locking, and dither or phase-sensitive-detection (PSD) locking. An



experimental implementation of the PSD locking scheme is described below, along with a discussion of some of the features of the other two locking schemes.

The PSD locking scheme that was implemented involved the scanning of the laser frequency by the application of a dither signal to the piezo-ceramic mounted mirror, which was made to oscillate in position at a frequency of 700 Hz. The modulated laser beam was passed through the reference cavity described below and the transmitted intensity detected by a photodiode. Upon passing the signal through a phase-sensitive detector an error signal is obtained which is equal to the derivative of the reference cavity transmission. The zero crossing providing the null point to which the laser was locked. The servo electronics were constructed within the department from a design obtained from the National Physical Laboratory [3.36].

The reference cavity was a 10 cm long Fabry-Perot confocal interferometer having a free spectral range of 750 MHz. The cavity formed by 99% reflectivity mirrors had a measured finesse of 60. These mirrors were replaced with nominally high reflectivity mirrors which had a finesse of 135 which corresponds to a transmission peak of 5.5 MHz FWHM. The cavity was constructed from a cylinder of invar, which has a low coefficient of thermal expansion of  $0.9 \times 10^{-6} \text{ }^{\circ}\text{C}^{-1}$ . Enclosed within a polystyrene housing, the cavity was thermally stabilised using a platinum resistance thermometer, a nichrome wire heater, and a CAL temperature controller.

To enable optimum frequency discrimination, the dither signal was set such that the frequency excursion of the laser was 3 MHz, which was 0.35 times that of the reference cavity linewidth [3.22]. This frequency excursion was measured over a sweep period of 50 ms, which was necessarily greater than the dither period of  $\sim 1.4$  ms. In spite of being thermally stabilised, the reference cavity will itself suffer thermal and pressure drift, and as such will only provide an absolute frequency reference if it is locked to an rf frequency reference or hyperfine transition such as that in molecular iodine.

### 3.7.3.b Considerations for the future

In general, the method that is chosen for active stabilisation is dependent upon the frequency noise spectrum of the free-running laser, after whatever passive stabilisation is used, and the frequency spectrum over which a low noise source is required. A particularly severe stabilisation specification is that for a future laser for gravitational wave detection, which is required to emit around 100 W of output power with noise of less than  $10^{-5}$  Hz/ $\sqrt{\text{Hz}}$  at frequencies between 10 Hz and 10 kHz [3.23]. Notwithstanding the somewhat extreme requirements for the laser for gravitational-wave detection, the low free-running phase-noise common to diode-pumped lasers means that it is not always necessary to employ elaborate active stabilisation.

By monitoring the reflection from stable ultra-high finesse reference interferometers, measurements of the linear spectral noise density can be made. Frequency fluctuations in the laser signal are converted to intensity fluctuations, which are detected by a photodiode and sampled by a spectrum analyser which performs a fast Fourier transform. This provides information about the frequency of the noise, and enables the source of noise to be ascertained more readily. This technique was used to find that the high voltage transducer to the piezo-controlled mirror mount was generating noise at  $\sim 14$  kHz, and that the power supply to the scanning galvanometer mounted etalon was causing noise at  $\sim 1$  kHz.

As diode-pumped lasers are intrinsically low-noise sources, there can be considerable advantage in using passive stabilisation to shield these lasers from parasitic outside influences. As was described above, the short-term frequency noise was reduced from  $\sim 500$  kHz to  $< 10$  kHz by enhanced acoustic damping. Passive stabilisation can also be used to reduce the long-term frequency drift through thermal expansion. This can be achieved by using materials with a low coefficient of expansion such as invar, or by using a composite cavity in which the thermal expansion of the materials cancel out [3.34].

The locking technique that is perhaps the most straightforward is side-of-fringe locking, in which the laser frequency is locked half-way down the transmission peak of a reference cavity. Variations in the transmitted or reflected intensity provide an error signal for the servo loop that controls the frequency of the laser. In this technique it is necessary that the signal from the interferometer is compared with that from the laser directly, to prevent fluctuations in the intensity of the laser being interpreted as frequency fluctuations. Though side-of fringe locking is an appropriate technique for reducing jitter in diode-pumped lasers, it may introduce long-term drift due to inexact matching of the photodiodes that monitor the laser intensity and the reference cavity.

Perhaps the ultimate technique is radio-frequency (RF) sideband locking, which was developed by Drever and Hall [3.24]. This technique involves applying an rf phase modulation to the laser signal through an electro-optic device external to the laser-cavity. An error signal is provided by mixing the laser signal with that reflected from the reference cavity, which is operated in reflection mode for reduced response time. This provides noise rejection over a bandwidth right up to the RF modulation rate. When applied to a diode-pumped Nd:YAG laser, this technique has been shown to reduce the white spontaneous noise to around 1 mHz, which is well below the Schawlow-Townes limit for this laser of 130 mHz [3.25]. This scheme, which has been applied to a number of lasers, is overly sophisticated for injection seeding.

---

### **3.8 Dynamic laser behaviour**

#### **3.8.1 Relaxation oscillations**

Relaxation oscillations are periodic fluctuations in the intensity of a laser-beam which result from a perturbation to the gain or loss of the laser. In diode-pumped solid-state lasers, relaxation oscillations are evident when there is a sharp rising edge to the pump pulse. Rather than following the intensity of the pump pulse, the output from the laser

consists initially of spiking, followed by quasi-sinusoidal oscillations which are damped exponentially. Relaxation oscillations occur in lasers in which the lifetime of the excited state is substantially greater than the laser cavity decay time. This is the situation with the diode-pumped Nd:YAG laser, in which the upper-state lifetime of 230  $\mu$ s is much greater than the typical cavity decay time of  $\sim 10$  ns.

The experimental examination of relaxation oscillations involved the application of a square wave from a signal generator to the analogue input of the diode driver. This raised the pump power to the Nd:YAG crystal from zero to a level well above threshold, causing an instantaneous population inversion with little flux and the consequent relaxation oscillations, as shown in figure 3.19

The ringing in the laser oscillator is analysed by Siegman using rate equations for the population inversion and the intra-cavity flux for a single-longitudinal mode laser; the results of which are presented here [3.15]. It is difficult to obtain an analytic solution to the coupled rate equations for the spiking at the start of the laser emission, as the upper state population and the intracavity flux are changing rapidly. In the regime after the spiking, a small signal analysis of the coupled rate equations does yield the following explicit expression for the intensity of the damped quasi-sinusoidal oscillations.

$$P(t) = P_{ss} + P_1 \exp\left(\frac{-r\gamma_2 t}{2}\right) \cos\left(\sqrt{(r-1)\gamma_2\gamma_c} t\right), \quad (3.22)$$

where  $P(t)$  is the instantaneous laser power,  $P_{ss}$  is the steady state laser power,  $P_1$  is a constant related to the amplitude of the oscillations and  $r$  is the amount of times above threshold the laser is being pumped.  $\gamma_2$  is the decay rate of the upper level, and  $\gamma_c$  is the cavity decay rate.

It was not possible to determine upper state lifetime from the exponential decay of the oscillations, as beating between longitudinal modes partially masked the effect. Measurements of the period of the small signal oscillations as a function of pump rate

above threshold can however establish a value for the cavity decay rate, and hence the loss within the cavity. For the initial system which was operating at a low output power due to a defective coating, this method confirmed that the degradation in performance was due to high value of parasitic loss of 2%.

### 3.8.2 Small amplitude modulation of pump

The relaxation oscillation frequency is also evident in the response of solid-state lasers to small modulations of the pump rate. At modulation frequencies that are small compared to the intermode frequency separation, the solid-state laser acts as a weakly damped oscillator with a resonance at the relaxation oscillation frequency. On solving the differential equations for the population inversion and the intracavity flux in the presence of a small perturbation, one obtains a transfer function between the modulation depth of the laser intensity,  $\tilde{n}_1$ , which is related to the pump modulation depth,  $R_{pl}$ , by a linear transfer function [3.26].

$$\frac{\tilde{n}_1}{R_{pl}} = \frac{\omega_{sp}^2 / \gamma_c}{\omega_{sp}^2 - \omega_m^2 + 2j\gamma_{sp}\omega_m} \quad (3.23)$$

where  $\omega_{sp} = \sqrt{(r-1)\gamma_2\gamma_c}$ ,  $\gamma_{sp} = r\gamma_2/2$ , and  $\omega_m$  is the modulation frequency.

This transfer function was demonstrated experimentally by modulating the laser-diode pump to the Nd:YAG laser, and monitoring the intensity of the laser-diode and the Nd:YAG laser simultaneously on an oscilloscope [3.26]. With the laser-diode biased such that the Nd:YAG laser was 1.5 times above threshold, the modulation depth of the laser-diode was 6.5% of the dc laser-diode power over that required to reach threshold for the Nd:YAG laser.

The resultant transfer function shown in figure 3.20 demonstrates that at low modulation frequencies the Nd:YAG laser intensity follows that of the laser-diode, but that at a frequency of 130 kHz the modulation depth of the Nd:YAG laser increased from 6.5% to 81%. When the modulation frequency passed through the relaxation

oscillation frequency of 130 MHz there was a phase change of  $90^\circ$  between the diode modulation and the Nd:YAG modulation. This frequency provided an upper limit to the rate at which the intensity of this Nd:YAG laser could be modulated and beyond which the modulation depth diminished.

The resonant enhancement of small signal perturbations at frequencies near the relaxation oscillation frequency has a deleterious effect upon the noise characteristics of the laser. This was illustrated by the sidebands at the relaxation oscillation frequency in the heterodyne frequency measurements for an unmodulated laser.

### 3.8.3 Large amplitude modulation

In the analysis of small amplitude modulation in the previous section, the linear transfer function was dependent upon the modulation depth being small in comparison to the dc pump level. If the modulation depth is increased, then the transfer function from diode-pump to Nd:YAG laser output is nonlinear, and controlled repetitive spiking of the Nd:YAG output can occur [3.27].

With the Nd:YAG laser biased at 1.5 times the threshold level, (a laser-diode pump power of 30 mW), repetitive spiking was demonstrated upon application of a sinusoidal modulation with amplitude of 20 mW to the pump beam at a frequency of 67 kHz. The resultant spikes of 2  $\mu$ s duration are shown in figure 3.21, with the peak output power in the spikes being ten times that at the cw bias level. At this modulation depth, a decrease in the modulation frequency caused a train of relaxation oscillations to appear on each cycle, whereas an increase in the modulation frequency caused the peak intensity of the spikes to decrease. Modulation at other frequencies and modulation depths can result in more complex spiking patterns involving harmonics and subharmonics of the relaxation oscillation frequency.

As the upper-state has a long fluorescence lifetime and acts as a buffer to modulation of the pump rate, to achieve intracavity modulation of the laser intensity requires



modulation of the loss within the cavity. By careful selection of the loss function to maintain as near uniform single-pass gain, it is theoretically possible to achieve binary intensity modulation with an index of 45 at a rate of 50 Mbits<sup>-1</sup> from a miniature solid-state laser [3.28].

---

### 3.9 Conclusions

The choice of the fibre-optic package for the cw laser diode provided a straightforward and effective approach to coupling the pump radiation into the longitudinally pumped Nd:YAG crystal laser. The ray-tracing model of the pump beam profile determined the effect of aberrations in the pump-coupling optics and provided the pump profile within the Nd:YAG laser rod. The pump profile was input into the rate equation based-model of the output power of the Nd:YAG laser; the results from which were in good agreement with those obtained experimentally.

To achieve single longitudinal mode from a cw Nd:YAG laser an etalon based technique and a twisted mode cavity technique were implemented experimentally. With the etalon scheme, a Brewster angled plate was included to ensure the oscillation of a single linear polarisation, and it was also necessary to have a galvanometer controlled etalon mount which was an additional source of frequency noise. The twisted mode cavity laser proved the more satisfactory with regard to jitter as it was intrinsically more rigid. Long-term drift in the frequency of the etalon based laser was reduced by locking the frequency of this laser to a temperature stabilised reference etalon, and as such this laser was able to provide a suitable source for injection seeding as described in chapter 5.



## Chapter 3    References

- 3.1    B. Zhou, T.J. Kane, G.J. Dixon & R.L. Byer "Efficient, frequency-stable laser-diode-pumped Nd:YAG laser" *Opt. Lett.* **10** (1985) 62
- 3.2    W. Koechner "Solid state laser engineering" Springer Verlag, Berlin, 2nd edition, 1989
- 3.3    G.M. Zverev, Yu.D. Golyaev, E.A. Shalaev & A.A. Shokin "Neodymium activated yttrium - aluminium - garnet (YAG:Nd) lasers" *J. Soviet Laser Research* **8** (1987) 189
- 3.4    Nd:YAG rods supplied, cut and polished by AWK Associates, GEC Hirst Research Centre and JK Lasers (presently incorporated into Lumonics).
- 3.6    W.J. Kozlovsky, T.Y. Fan & R.L. Byer "Diode-pumped continuous-wave Nd:glass laser" *Opt. Lett.* **11** (1986) 788
- 3.7    M.J.F. Digonnet & C.J. Gaeta "Theoretical analysis of optical fiber laser amplifiers and oscillators" *Appl. Opt.* **24** (1985) 333
- 3.8    C.J. Norrie & B.D. Sinclair "Report on Nd:MgO:LiNbO<sub>3</sub> microchip lasers" Interim report to RSRE/SERC 6th July 1990
- 3.9    Melles Griot Optics Guide 4
- 3.11    A. Owyong, G.R. Hadley, P. Esherick, R.L. Schmitt & L.A. Rahn "Gain switching of a monolithic single-frequency laser-diode-excited Nd:YAG laser" *Opt. Lett.* **10** (1985) 485
- 3.12    T.Y. Fan & R.L. Byer "Modelling and cw operation of a quasi-three-level quantum Nd:YAG laser" *J. Quan. Elect.* **23** (1987) 605
- 3.13    W.P. Risk "Modelling of longitudinally pumped solid-state lasers exhibiting re-absorption losses" *J. Opt. Soc. Am.* **5** (1988) 1412
- 3.14    H.G. Danielmeyer "Lasers" volume 4, ed. A.K. Levine & A.J. DeMaria. Marcel Dekker, New York 1976
- 3.15    A.E. Siegman "Lasers" University Science Books, Mill Valley, Ca 1986
- 3.16    T.J. Kane & R.L. Byer "Monolithic, unidirectional single-mode Nd:YAG ring laser" *Opt. Lett.* **10** (1985) 65
- 3.18    J.J. Zayhowski & A. Mooradian "Single frequency microchip Nd lasers" *Opt. Lett.* **14** (1989) 24
- 3.19    A. Owyong & P. Esherick "Stress-induced tuning of a diode-laser-excited monolithic Nd:YAG laser" *Opt. Lett.* **12** (1987) 999
- 3.21    G.J. Dixon & R.H. Jarman "Properties of miniature lithium neodymium tetraphosphate microlasers with high intensity IR pumping" Conf. on Lasers and Electro-optics, Baltimore April 1989, paper TuJ62

## Chapter 3    References

- 3.22    M.J. Nakazawa "Phase-sensitive detection on Lorentzian line shape and its application to frequency stabilization of lasers" *J. Appl. Phys.* **59** (1986) 2297
- 3.23    G.A. Kerr "Experimental developments towards a long-baseline laser interferometric gravitational radiation detector" Doctoral thesis presented to the University of Glasgow, April 1986
- 3.24    R.W.P. Drever, J.L. Hall, F.V. Kowaski, J. Hough et al "Laser phase and frequency stabilization using an optical resonator" *Appl. Phys. B* **31** (1983) 97
- 3.25    D. Shoemaker, A. Brillet, C.N. Man, O. Cregut & G. Kerr "Frequency-stabilized laser-diode-pumped Nd:YAG laser" *Opt. Lett.* **14** (1989) 609
- 3.26    H.G. Danielmeyer & F.W. Ostermayer, Jr "Diode-pump-modulated Nd:YAG laser" *J. Appl. Phys.* **43** (1972) 291
- 3.27    S.R. Chinn, H.Y.P. Hong & J.W. Pierce "Spiking oscillations in diode-pumped NdP<sub>5</sub>O<sub>14</sub> and NdAl<sub>3</sub>(BO<sub>3</sub>)<sub>4</sub> lasers" *IEEE J. Qu. El.* **12** (1976) 189
- 3.28    J.C. Vanderleeden "Miniature intra-cavity modulated solid-state lasers and their use in optical communication systems" *Opto-electronics* **6** (1974) 393
- 3.29    A. Owyong, G.R. Hadley, P. Esherick, R.L. Schmitt & L.A. Rahn "Gain switching of a monolithic single-frequency laser-diode-excited Nd:YAG laser" *Opt. Lett.* **10** (1985) 485
- 3.30    J. Hong, B.D. Sinclair, W. Sibbett & M. Dunn "Diode laser array pumped Q-switched Nd:YAG laser operating at 946 nm" *Tech. Digest, Conf. on Lasers and Electro-optics*, Anaheim CA, 1990 paper CWC7
- 3.31    M.D. Shinn, F.P. Milanovich & J.N. Roe "Stimulated emission cross section for the laser transition in YAG:Nd." *Tech. Digest, Conf. on Lasers and Electro-optics*, Baltimore, 1990 paper WM5
- 3.32    A.A. Kaminskii "Laser crystals" *Opt. Sci.* vol 14, Springer, Berlin 1981
- 3.33    A. Wray "Modelling of laser diode-pumped Nd:YAG microlasers: Summer project, University of St. Andrews, September 1988
- 3.34    S. Halaj "Nd:YAG diode pumped laser" Diploma research project, University of St. Andrews, June 1990.
- 3.35    E. Hecht & A. Zajac "Optics" Addison-Wesley, Reading MA.
- 3.36    K.C. Shotton & W.R.C. Rowley "An electronic servocontrol system for stabilized lasers and similar applications" National Physical Laboratory report number OU28 (1975)

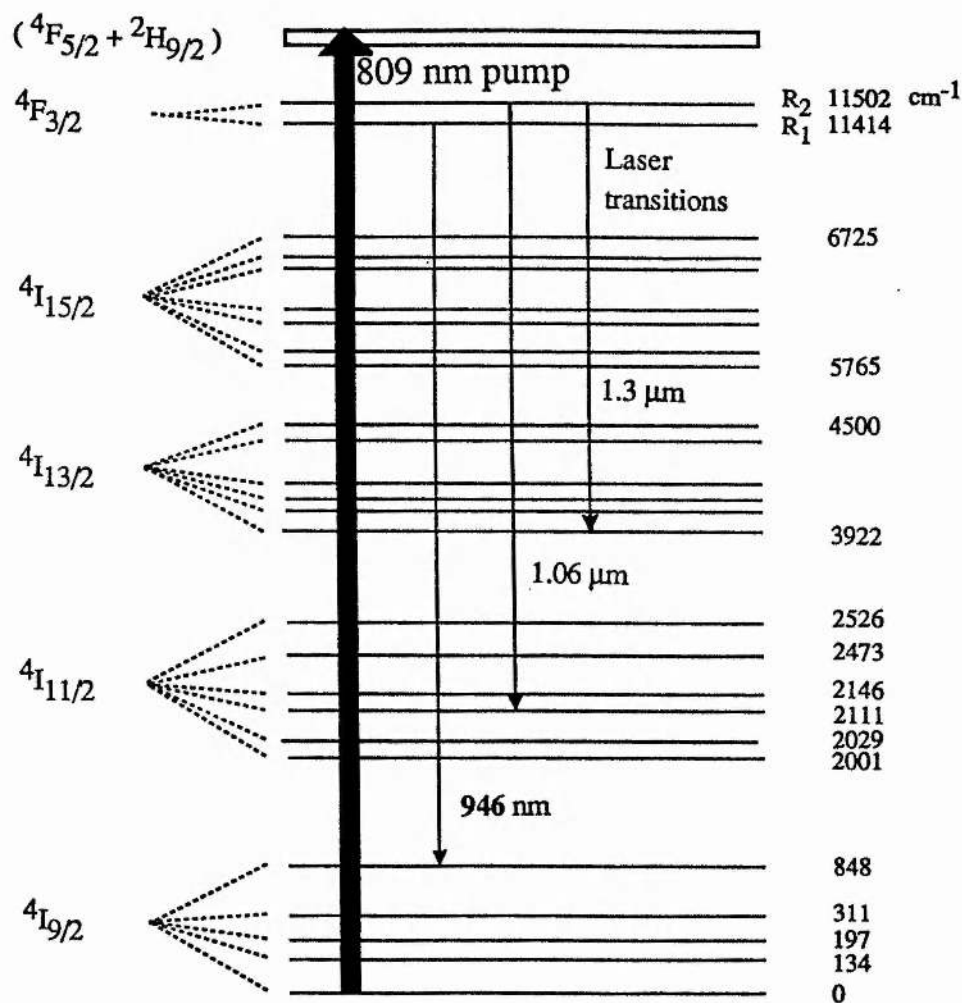


Figure 3.1 Energy-level diagram of Nd:YAG crystal.

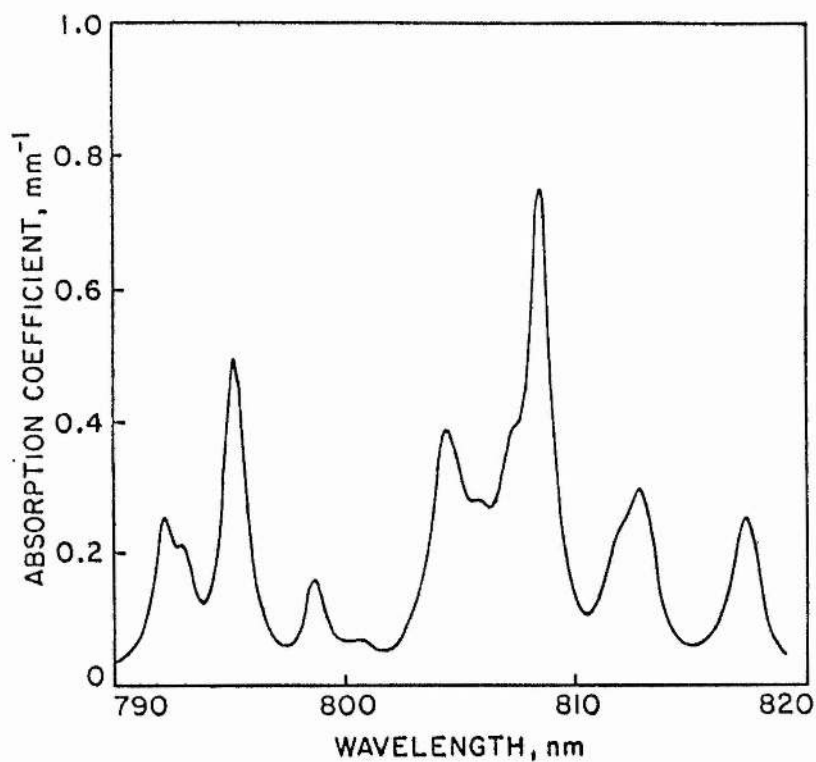


Figure 3.2 Absorptivity of Nd:YAG crystal over the spectral region around 809 nm

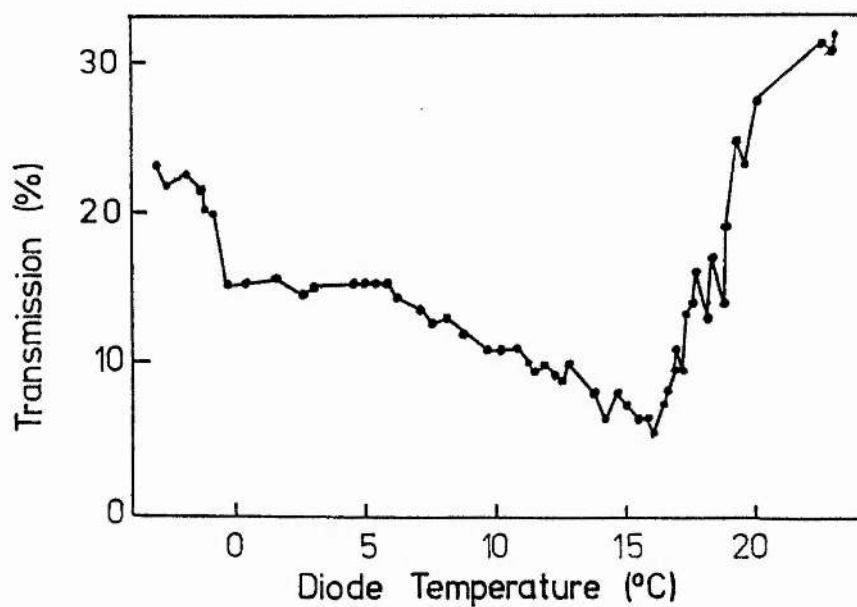


Figure 3.3 Percentage transmission of laser-diode pump emission by 5 mm Nd:YAG rod as a function of the laser-diode temperature and hence mean wavelength.

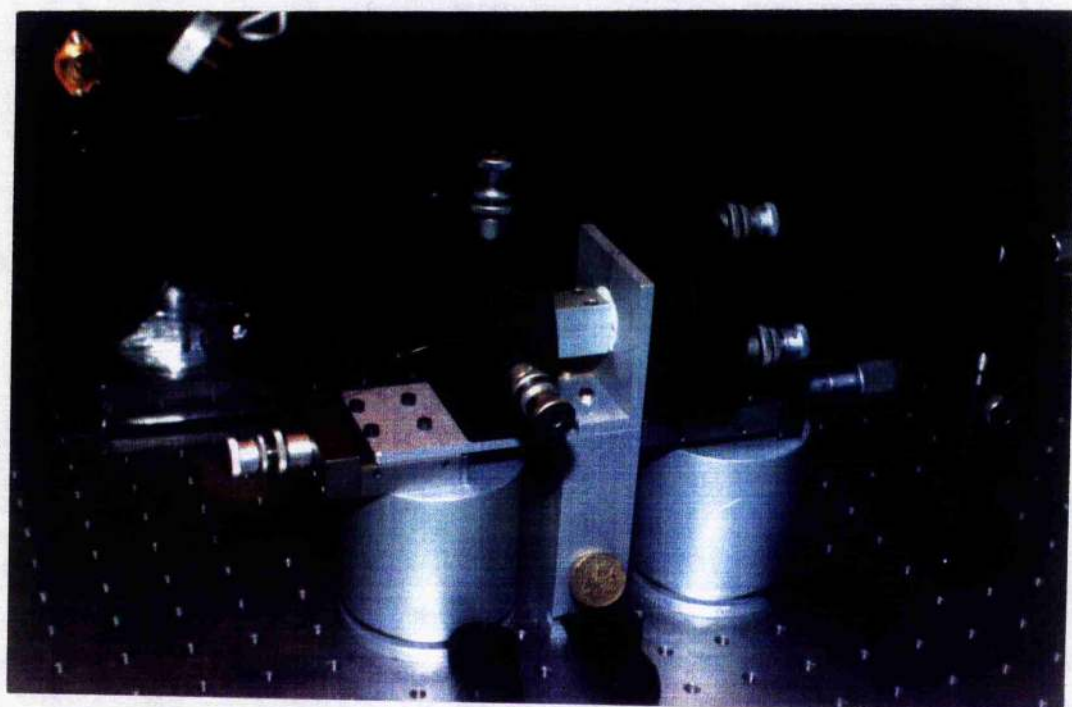


Figure 3.4. Photograph of "bread-board" cw Nd:YAG laser, end-pumped by a fibre-coupled 100 mW laser-diode array.



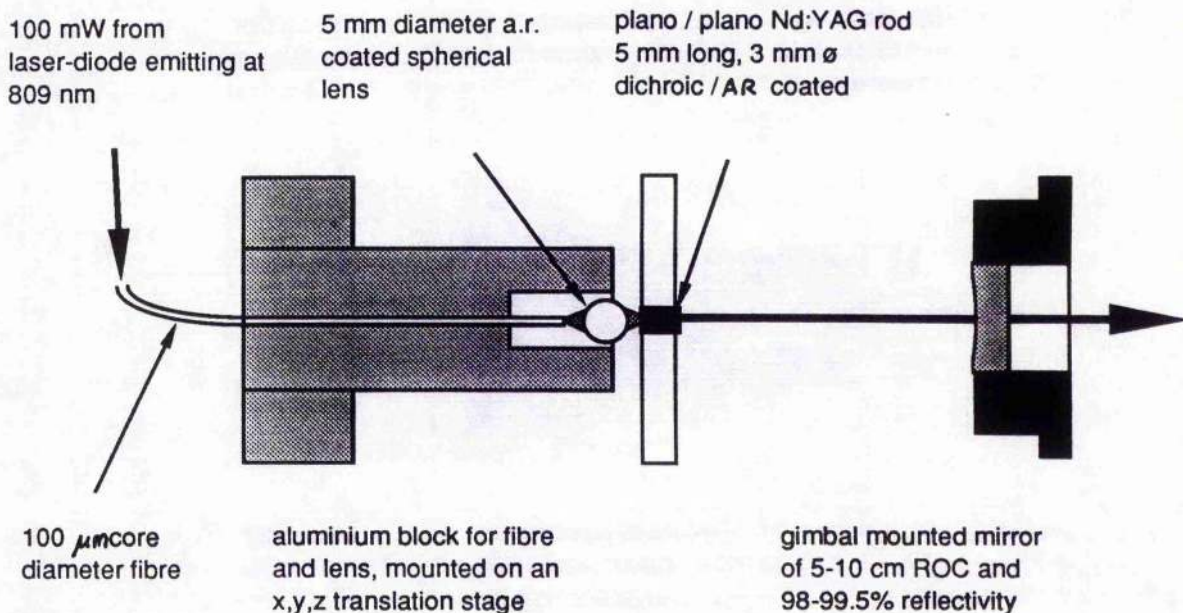


Figure 3.5 Schematic diagram of "bread-board" cw Nd:YAG laser, end-pumped by a fibre-coupled 100 mW laser-diode array.

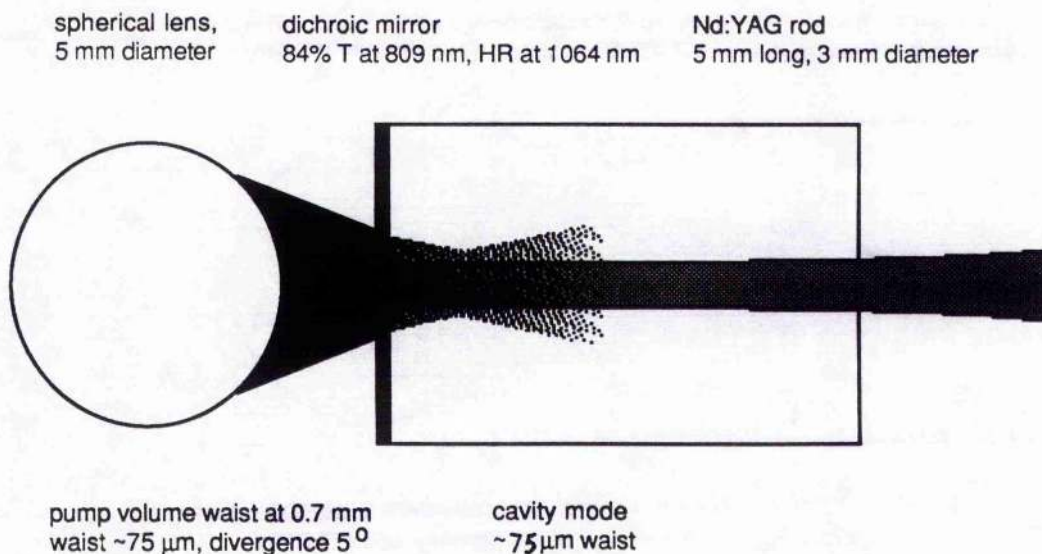


Figure 3.6 Schematic diagram of overlap between the pump volume and the cavity mode. The pump beam is characterised by an absorption depth of around 1.3 mm, and a waist of  $\sim 75 \mu\text{m}$ , 0.7 mm into the Nd:YAG rod. The cavity mode radius at  $\sim 75 \mu\text{m}$  is constant over the absorption depth of the pump.

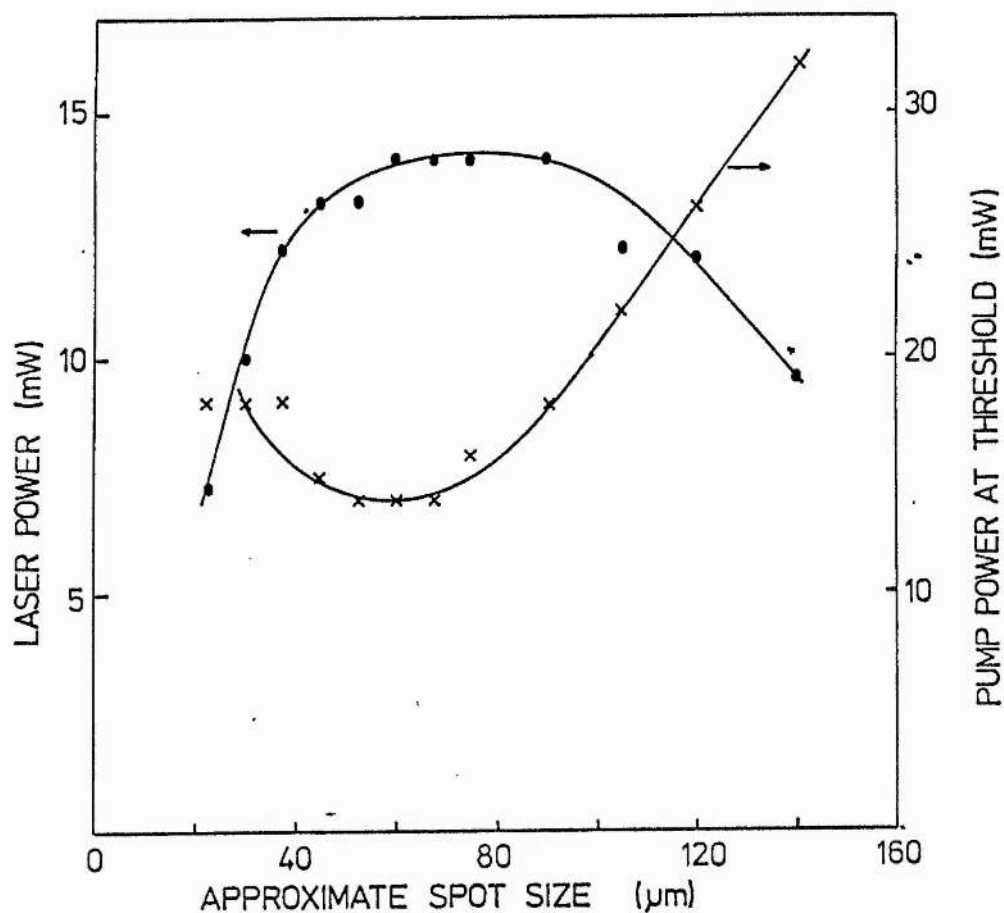


Figure 3.7 Optimisation of the Nd:YAG laser threshold and output power as a function of pump spot-size. Pump power was 100 mW, and the output coupler was 5 cm ROC, 99% R.

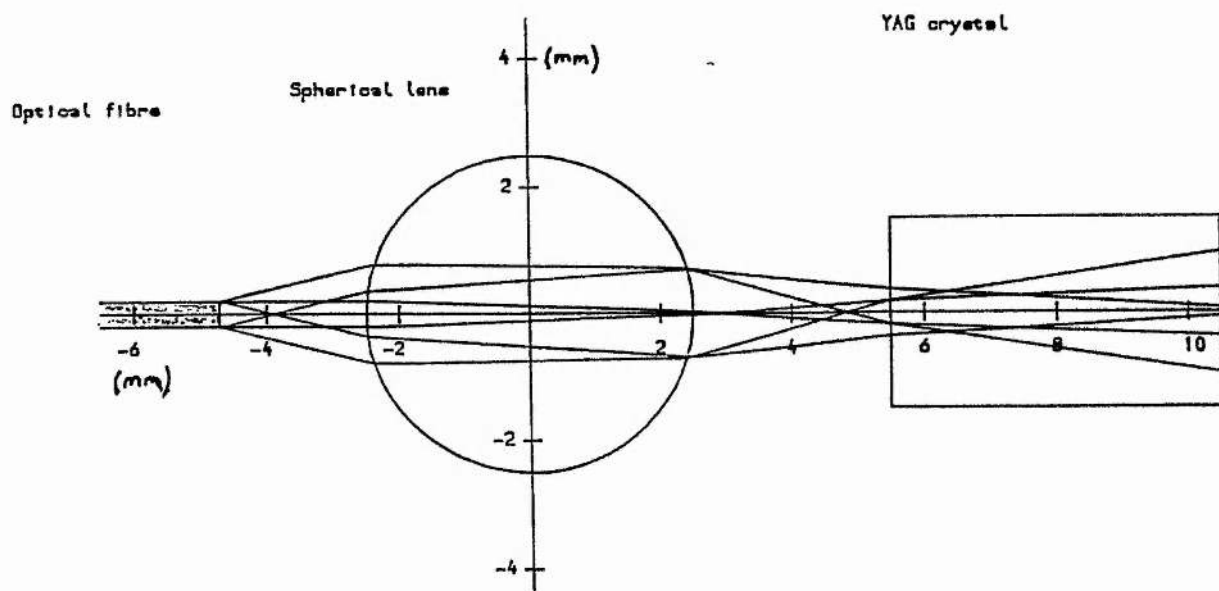


Figure 3.8 Single-sphere pump-coupling configuration modelled to determine pump spot size within Nd:YAG rod.



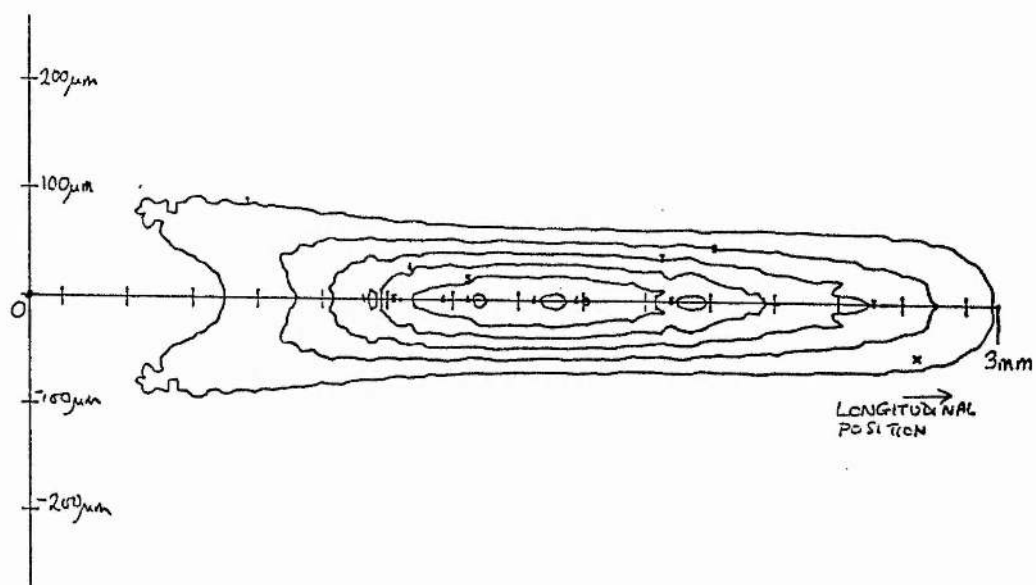


Figure 3.9 Modelled pump power distribution in Nd:YAG rod showing  $\sim 75 \mu\text{m}$  beam waist.

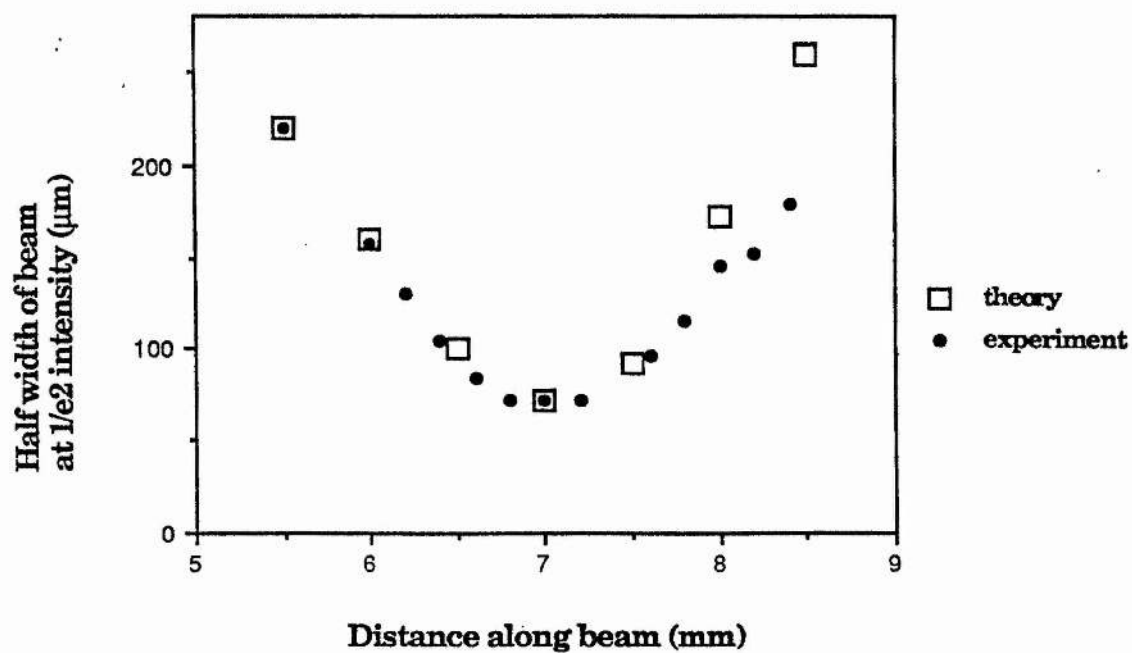


Figure 3.10 Comparison of theoretical and experimental results for the pump beam divergence in air.

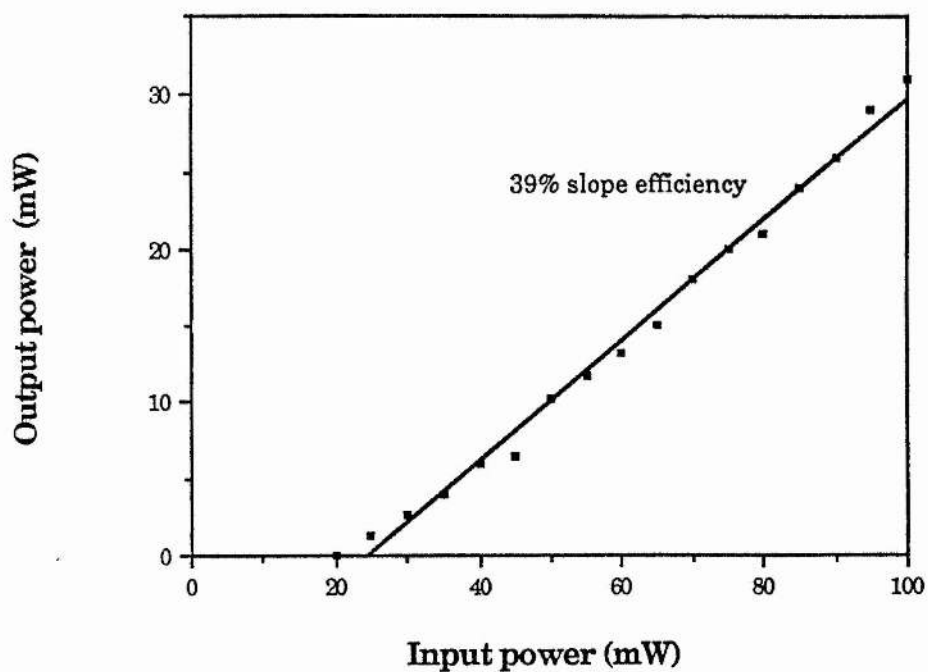


Figure 3.11 Output power from the cw Nd:YAG laser as a function of pump power. The output coupler was 7.5 cm ROC, 98-99% R

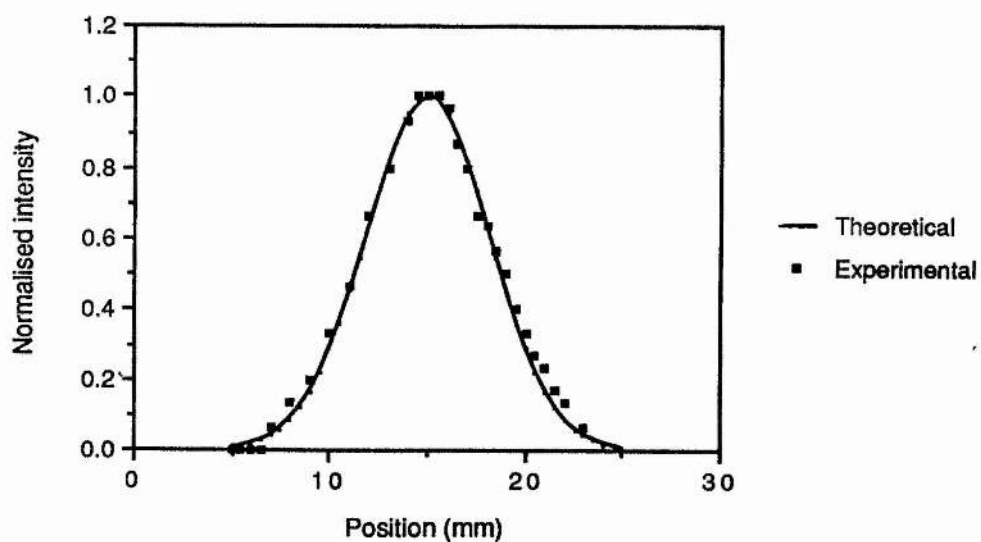


Figure 3.12 Gaussian beam profile of cw laser in the horizontal plane.

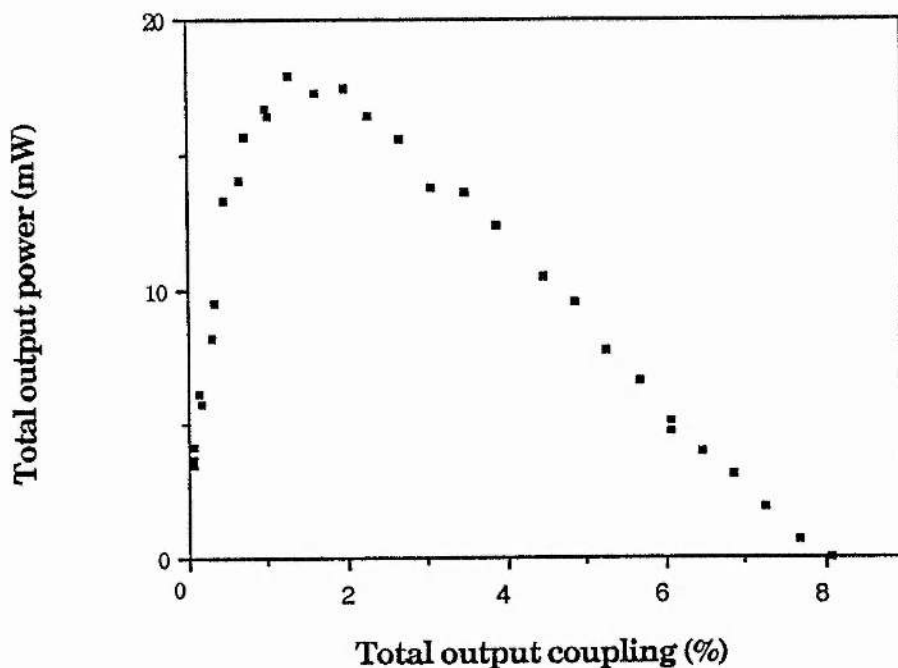


Figure 3.13 Experimental output power from the Nd:YAG laser as a function of output coupling. The laser was pumped by 95 mW, and the output coupler was 10 cm ROC, HR. Variable output coupling provided by a 2 mm CVI uncoated glass etalon.

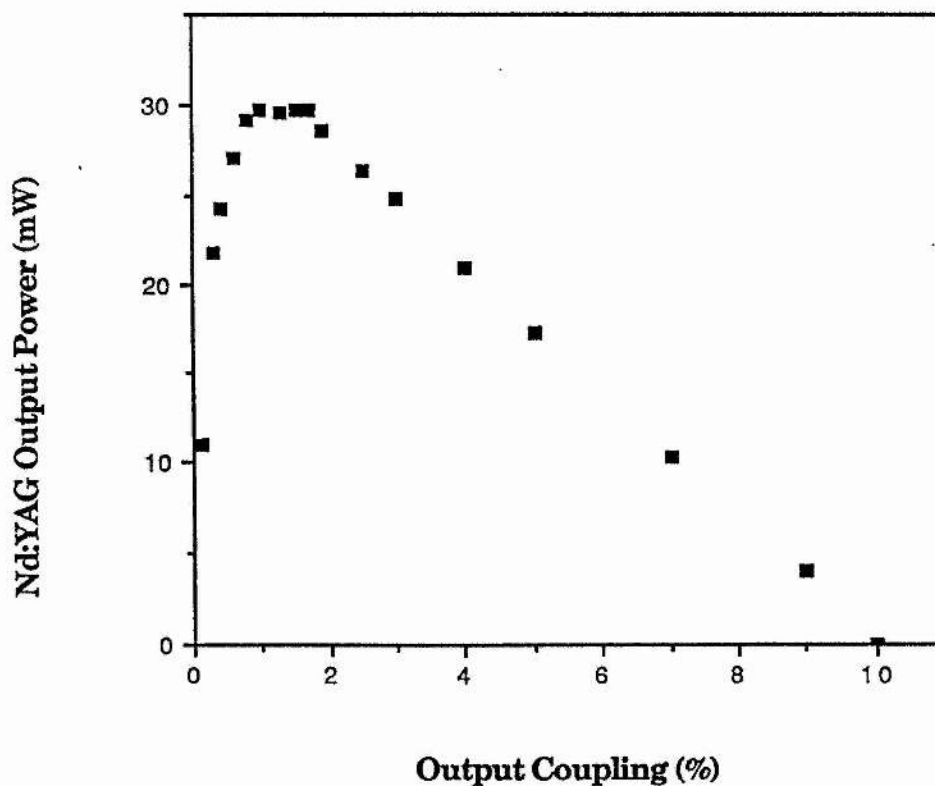


Figure 3.14 Theoretically calculated dependence of the Nd:YAG output power on output coupling. Laser parameters as for figure 3.13.

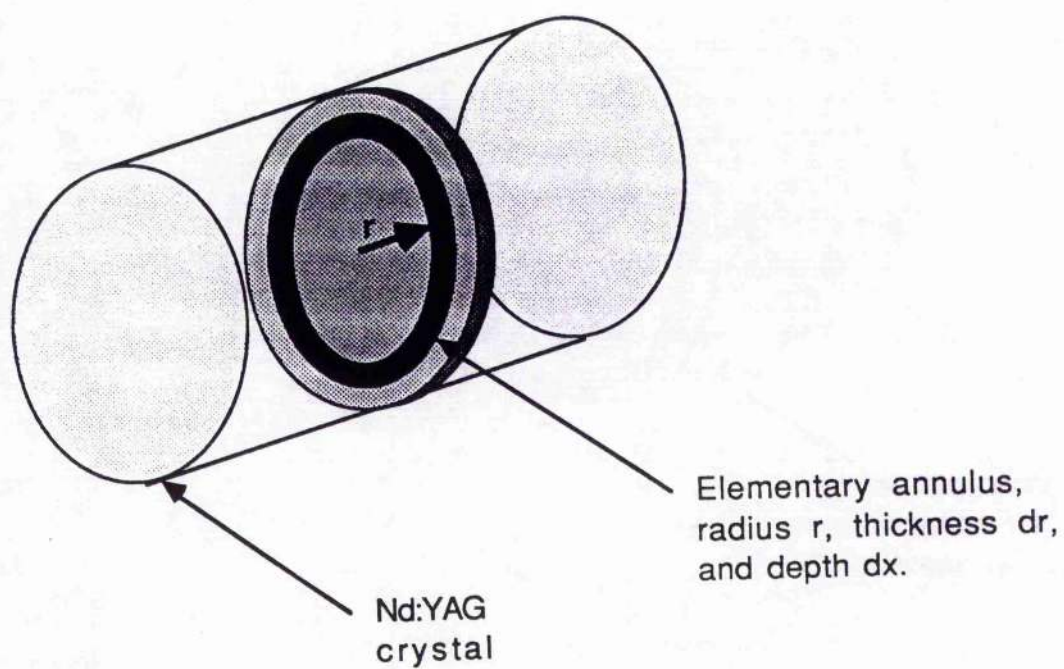


Figure 3.15 Schematic of annuli and sections used in rate-equation model of output power of the Nd:YAG laser.

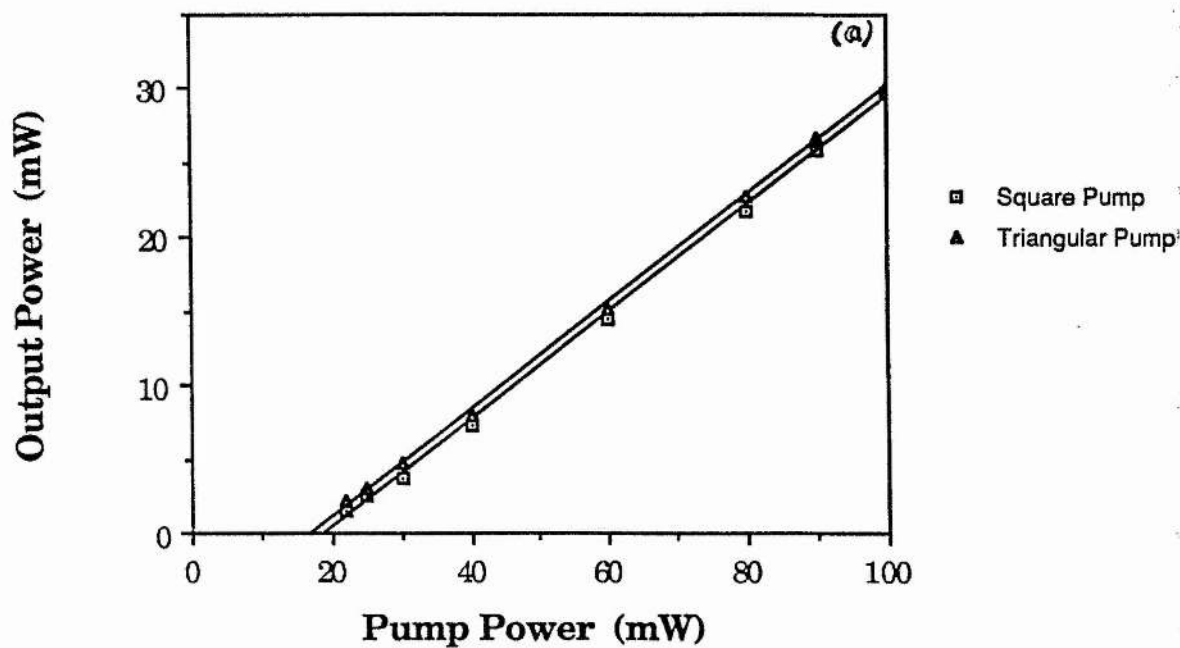


Figure 3.16 Theoretical output power as a function of pump power for the Nd:YAG laser under conditions of a square and a triangular pump profile.

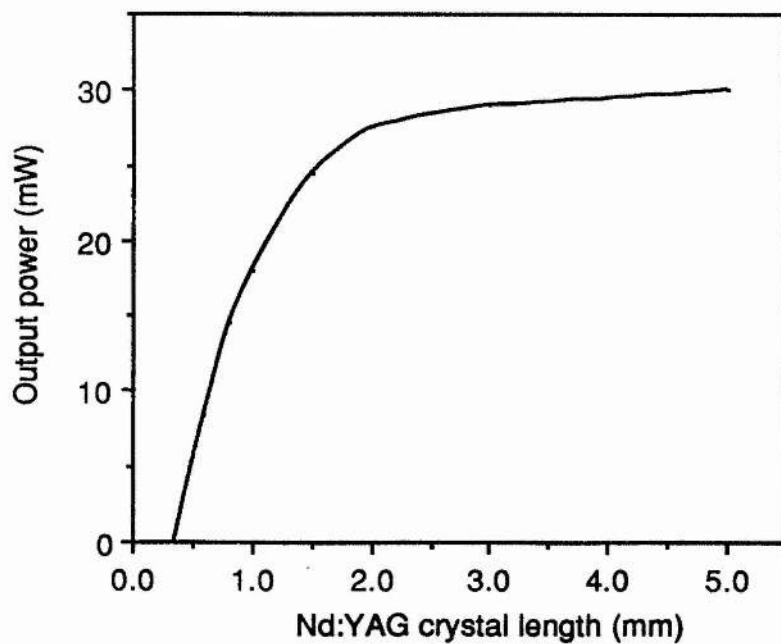


Figure 3.17 Theoretical output power against pump power as a function of crystal length.

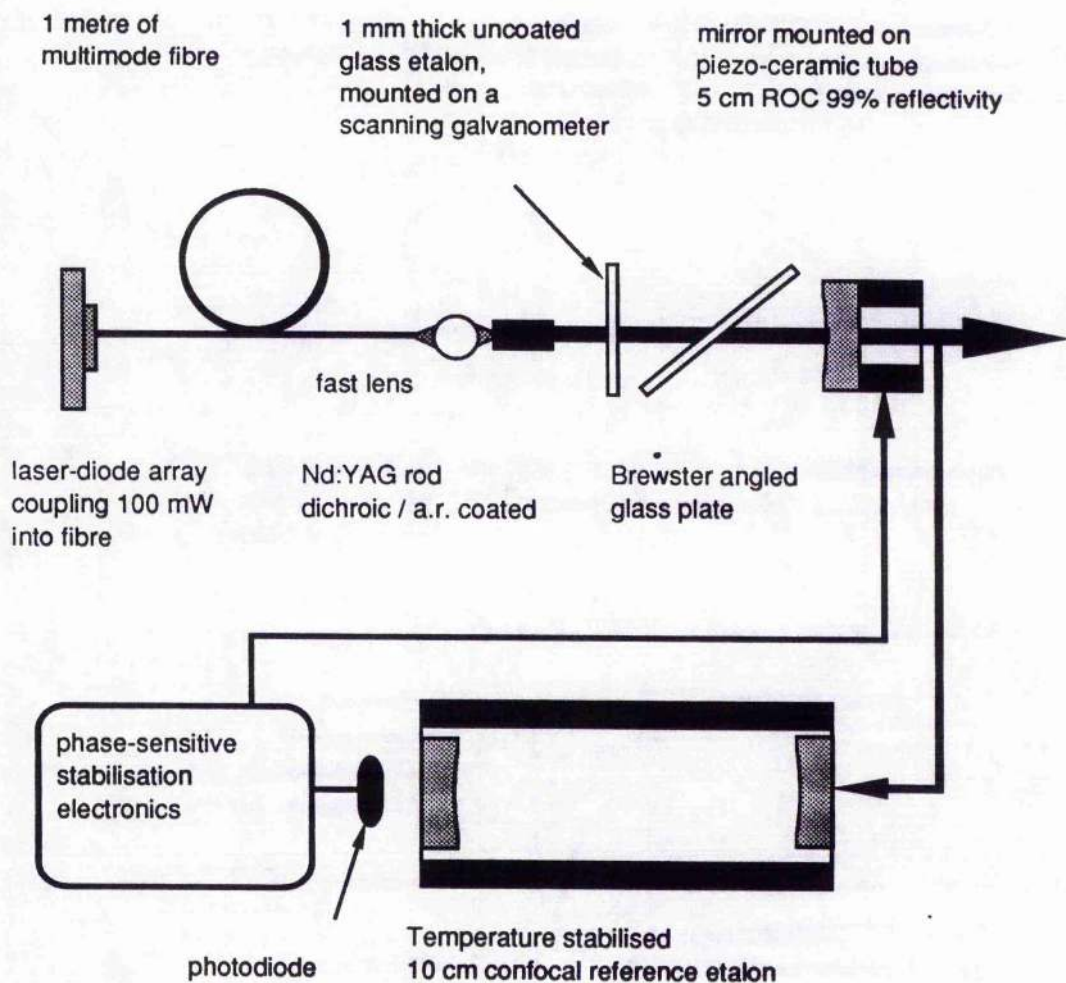


Figure 3.18 Schematic of cw laser with Brewster plate and etalon and output coupler with piezo control.

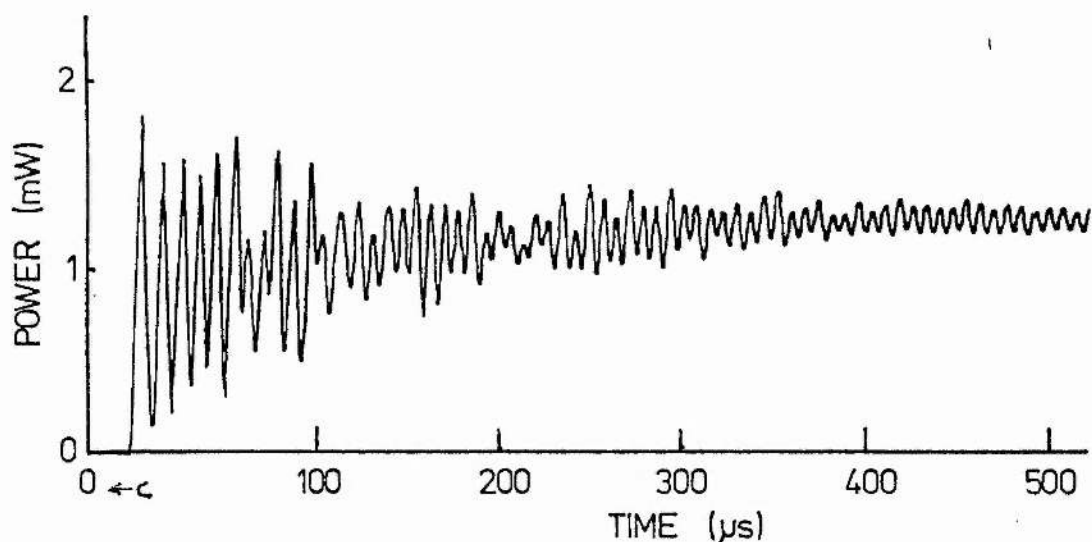


Figure 3.19 Relaxation oscillations of the Nd:YAG laser when the pump power was abruptly switched from zero to 30 mW. Output coupler was 98-99% R, 7.5 ROC.

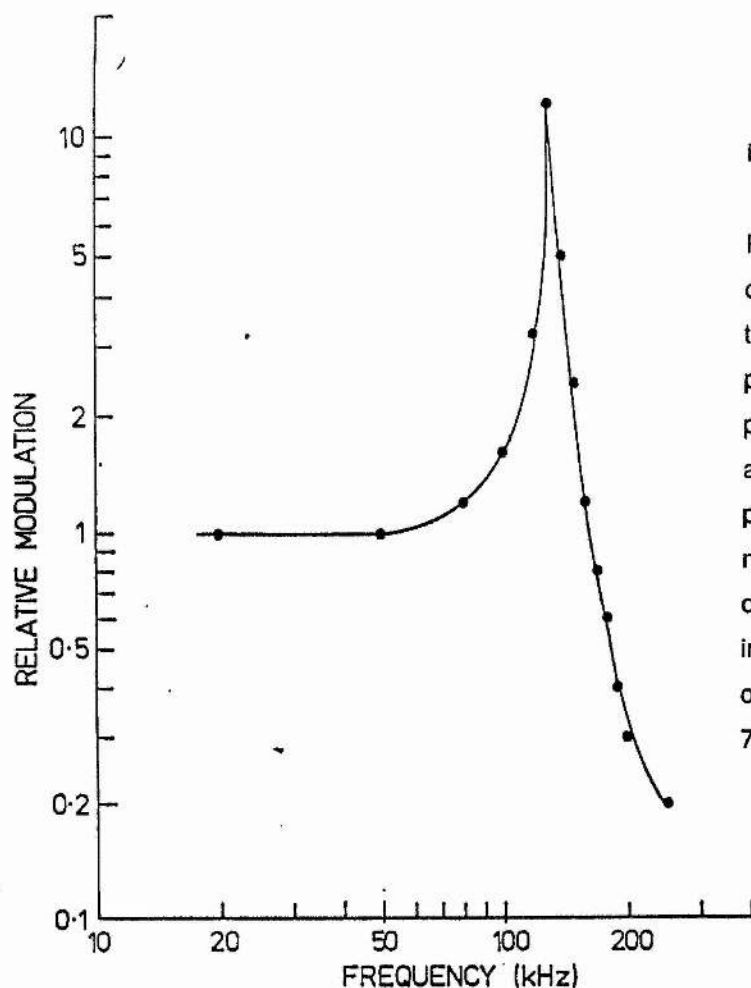


Figure 3.20

Response of the Nd:YAG laser oscillator to small modulations of the input power. The pump power was modulated 1.5 mW peak to peak, corresponding to a 6.5 % modulation in the pump power above threshold. The modulation of the YAG laser is quoted relative to this 6.5% input modulation level. The output coupler was 98-99% R, 7.5 cm ROC.



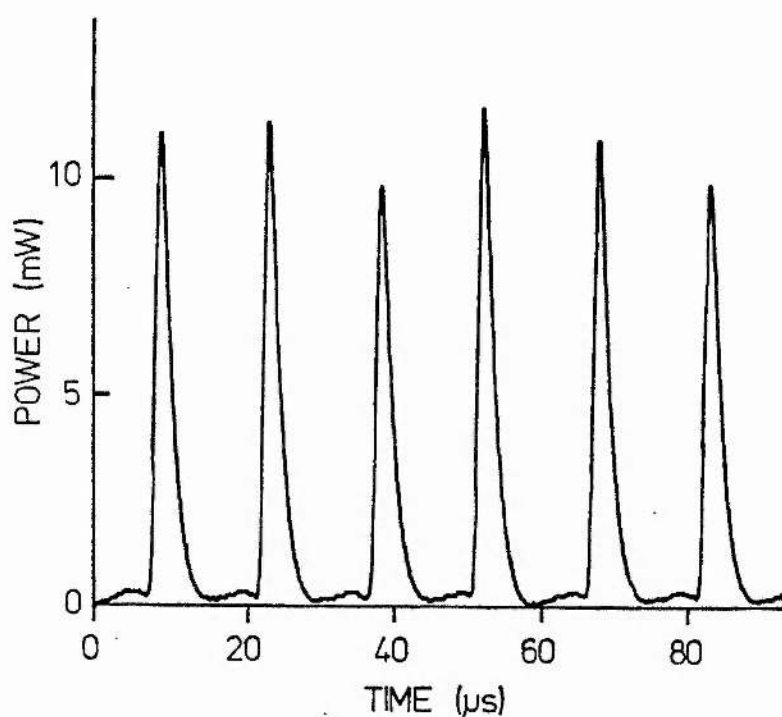


Figure 3.21 Pump modulation induced spiking of the Nd:YAG laser. The pump power was modulated by 67% at 67 kHz, to obtain 2  $\mu$ s long Nd:YAG pulses (FWHM) with 11 mW peak power. The mean pump power was 30 mW, the average output power was 1.1 mW, and the output coupler was 98-99% R, 7.5 cm ROC.

## Chapter 4

### Long-pulse operation of a Nd:YAG laser transversely pumped by a quasi-cw laser-diode bar

---

#### 4.1 Introduction

In this chapter the operation of a miniature Nd:YAG laser that was transversely pumped by a quasi-cw laser-diode bar is described. Both lens-coupled and close-coupled pumping configurations were examined, with the goal of obtaining the maximum output power in the fundamental transverse mode of the Nd:YAG laser at  $1.064\ \mu\text{m}$ . Because of the transverse nature of the pumping, the Nd:YAG laser was found to favour multi-transverse mode operation, and the attainment of  $\text{TEM}_{00}$  operation with good efficiency presented a greater challenge than for the end-pumped laser described in chapter 3. A variety of cavity geometries were studied with regard to the overlap between the pumped volume and the cavity mode. As a result it proved possible to obtain  $\text{TEM}_{00}$  without resorting to an additional aperture within the cavity.

An experimental study of the pump rate distribution involved measurements of the absorption in the Nd:YAG crystal and the effect of the frequency chirp on the small-signal gain throughout the pumping interval. To obtain a picture of the pump power distribution in the rod, spatially resolved measurements of the small signal gain were taken along with images of the fluorescence from the ends of the rod.

An extensive model of the pumping process was based upon a ray-tracing program which determines the rate of pumping throughout the Nd:YAG rod. This computer generated distribution of pump power is compared with that from the spatially resolved study of the single-pass small-signal gain. With this model it is then possible to determine the output power from the Nd:YAG laser, with particular consideration being given to the transverse mode structure. Using a rate equation analysis of the overlap

between the pump power distribution and intracavity flux, a calculation is made as to whether the  $TEM_{00}$  or the  $TEM_{01}$  mode has the lower pump threshold, and its value is ascertained. The pump power threshold for the second mode is then determined after taking into account the intracavity flux from the first mode which saturates the gain. With the third and final part of the model values for the output power of the Nd:YAG laser as a function of input power are generated. This shows a non-linear slope efficiency, discussed in section 4.5.5, which is attributed to the asymmetric pump power distribution.

---

## 4.2 Nd:YAG laser configuration

The transversely pumped Nd:YAG laser was initially constructed in a “breadboard fashion” on an optical table, as shown in figure 4.1, but was transferred to an aluminium subrail as the cavity design became more mature. The pump source was a single laser-diode bar (SDL-3220-J) as described in chapter 2. To match the emission wavelength of the laser-bar to the 810 nm absorption peak in Nd:YAG, the temperature of the laser-bar was actively controlled using Peltier elements that were in thermal contact with a heavily finned copper heatsink.

In all the transversely pumped lasers that were studied here the active material was a Nd:YAG crystal which had a nominal atomic neodymium dopant concentration of 1.3%. This dopant level was higher than that for the end-pumped laser, as higher absorptivity was necessary for improved transverse pumping efficiency. The Nd:YAG crystal was cut and polished into rods which were 12 mm long, and 1, 1.5 and 2 mm in diameter. The end surfaces of the rods were either at Brewster’s angle or perpendicular to the axis of the rod; in the latter case they were anti-reflection coated for 1.064  $\mu\text{m}$ . Each rod was given a low grade polish around its barrel to increase the transmission of the pump light. This could be improved upon further by the adoption of an anti-reflection coating at the pump wavelength. Rods were mounted in a close

fitting polished brass housing which acted as a back reflector for pump light that was not absorbed in a single pass. Improved reflectivity would be achieved by the application of a reflective coating to the brass housing or the back of the rod [4.1].

At the 25 W pump power level that was available from the single bar, it was necessary to have a small pump volume within the Nd:YAG to maximise the population inversion and hence the gain. The extent to which this could be realized was dependent upon the spatial distribution of the pump light from the laser-bar which was emitted from a  $1\text{ cm} \times 1\text{ }\mu\text{m}$  area, with a FWHM divergence of  $22^\circ$  in the plane parallel to the laser-bar junctions. The pump beam was shown in chapter 2 to be partially coherent, and consequently not conducive to tight focusing.

In the first transversely pumped laser started in this project the pump configuration involved a pair of lenses\* which collimated and focused the pump light into the Nd:YAG rod. The primary reason for the use of coupling optics was that the lenses could be integrated into the laser-bar mount to protect the facets of the laser bar from contaminants such as dust and condensation. The degree of protection offered by this primitive window, which is shown in figure 4.2, was not proven, though it is most likely that a hermetically sealed package would contribute to device longevity. For the Nd:YAG laser configuration that is shown in figure 4.3, the peak long-pulse multi-transverse mode output power was 1.9 W. The low level of pumping efficiency that this represents is attributed to a combination of aperture loss and coma; problems which might be overcome by specialised aspheric lenses.

On removing the coupling lenses, and coupling the pump light from the laser-bar directly into the Nd:YAG rod, the output power from the above cavity configuration increased to 6.5 W. For optimum pumping efficiency the laser-bar was positioned 0.2 mm from the side of the rod. The rod was aligned with respect to the cavity axis using

---

\* Lenses were both anti-reflection coated at 800 nm, and were of 25 mm focal length and 0.4 N.A.

a helium-neon laser, and the correct positioning of the laser-bar with respect to the rod was ensured using a CCD camera which monitored the fluorescence at  $1.064\ \mu\text{m}$  from both ends of the rod. An example of the resultant images is given in section 4.4.2. Care was taken that the upper contact to the laser-diode did not touch the brass housing of the Nd:YAG rod, as this would have caused the drive current to short circuit the laser-bar.

---

### 4.3 Characterisation of long-pulse operation

The temporal profile of a typical Nd:YAG output pulse in long-pulse operation is shown along with the laser-bar drive current pulse in figure 4.4. The distinct Nd:YAG laser relaxation oscillations are a consequence of the sharp rising edge of the pump pulse. After a short period of spiking at the start of the pulse, the relaxation oscillations in the output damp down to a continuous level of output power. The delay between the start of the pump pulse and the onset of lasing is the time required for a population inversion to build up in the Nd:YAG rod. To maintain the same output pulse characteristics from the Nd:YAG laser at repetition rates between 10 and 100 Hz, the laser-bar temperature had to be altered to maintain the same output power and wavelength.

#### 4.3.1 Transverse mode structure

The transverse mode characteristics of a laser depend upon the spatial overlap between the pump-distribution and the fundamental mode volume of the cavity [4.6]. In the longitudinally pumped lasers described in the previous chapter, the symmetry between the co-axial pump and cavity modes encouraged TEM<sub>00</sub> mode. However, as the pulsed laser was side-pumped by a single laser-bar, the pump-rate distribution was highly asymmetric and at one side of the rod. As a result, the constraint of this laser to operate efficiently in the fundamental-transverse-mode presented a greater challenge than it did for the end-pumped laser.

The cavity configuration that was first adopted consisted of a rod, with faces cut at Brewster's angle, positioned at the waist of a cavity formed by two 10 cm ROC mirrors that were 14 cm apart. This is shown schematically in figure 4.3. The Brewster-angled faces induced the mode area of fundamental mode of the cavity to be elliptical within the rod, though the polarisation was linear, as shown schematically in figure 4.5. For the cavity illustrated in figure 4.3, the waist ( $HWe^{-2M}$ ) was  $225\text{ }\mu\text{m}$  in the horizontal plane and  $125\text{ }\mu\text{m}$  in the vertical plane. The transverse-mode pattern from this laser was typically  $TEM_{9,0}$ , with the mode structure in the horizontal plane as shown in figure 4.6. This multimode pattern indicates that the mode-waist within the rod was significantly less than the pumped waist in the horizontal plane. When the laser-bar was close-coupled to the rod, the peak output power increased from 1.9 to 6.5 W, whilst a similar multi-transverse mode structure was observed.

The conventional technique for reducing a multimode laser to single transverse mode is the introduction of an aperture at a focus within the cavity which presents additional loss for higher order transverse modes. However, it was felt that aperturing of higher order modes could be achieved by the edge of the Nd:YAG rod itself. Single transverse mode operation was achieved when the Brewster-angled rod of 2 mm diameter was replaced by a similar rod with a diameter of 1.0 mm. Unfortunately, the maximum pump power to excite the smaller rod was limited to 15 W, as catastrophic facet damage had reduced the number of active elements in the laser-bar. Consequently, the influence of aperturing by the rod in achieving single mode operation cannot in this instance be differentiated from the level of pump power.

The rod with faces at Brewster's angle was replaced by a 1.5 mm diameter Nd:YAG rod with AR coated faces that were perpendicular to the cavity axis, that was to allow for the twisted cavity mode technique to be introduced and which is described in section 3.7.2.b. The reconfigured cavity, which is shown schematically in figure 4.7, had a beam waist in the rod of  $425\text{ }\mu\text{m}$  ( $HWe^{-2M}$ ) which resulted in single transverse mode operation as shown in figure 4.8. It is felt that increased pumping efficiency would



probably have resulted from a return to the Brewster angled 2 mm rod, with the cavity configured to give a beam radius in the horizontal and vertical planes of  $\sim 600\text{ }\mu\text{m}$  and  $\sim 330\text{ }\mu\text{m}$  respectively.

#### 4.3.2 Output power

For the laser shown schematically in figure 4.7, measurements were made for the  $\text{TEM}_{00}$  output energy as a function of the laser-bar pump energy. The energies of the pump pulses and the  $1.064\text{ }\mu\text{m}$  laser pulses were converted into peak powers by dividing by the respective pulse durations. The resultant graph of output power given in figure 4.9 shows a threshold pump power of 9.2 W and a slope efficiency of 21.8% for  $\text{TEM}_{00}$  operation.

It should be noted that obtaining the pump power for the slope-efficiency graph is somewhat complicated, since the pump power from the laser-bar cannot be measured directly whilst the laser-bar is pumping the rod. The pump power must be calculated from the laser-bar drive current. The complication arises in that the wavelength of operation, which must be kept fixed to maintain the same pump absorption, is a function of current. Consequently, as the current is altered the temperature of the laser-bar must be altered to maintain the laser-bar at the same wavelength. Unfortunately, the threshold drive current to the laser-bar is a function of temperature, so as a result the laser-bar output power is not linearly proportional to the drive current.

It was of particular interest for this laser to calculate the amount of parasitic loss, as the amount of clipping of the laser beam by the laser rod is a key parameter in the characterisation of this laser. This was achieved using the Fresnel plate output coupling method described in chapter 3, with the resultant graph of output power against output coupling plotted in figure 4.10. This shows a maximum output coupling of 28% and an optimum output coupling of 6-7%, from which the parasitic loss was determined using equation 3.4 to be 2.25-3.5%. When the laser was running with the Fresnel



plate in the cavity there were 10 surfaces per round trip with each surface contributing to the total parasitic loss. Hence, it is only possible to estimate the clipping loss of the optical flux by the edge of the Nd:YAG rod to be  $\sim 1.25 - 2.5\%$ .

#### **4.3.3 Longitudinal mode characterisation**

The study of the longitudinal mode characteristics of the long-pulse laser involved alternative techniques to the scanning confocal interferometer that analysed the spectrum of the cw laser. For a scanning interferometer to make a single shot measurement of the spectrum of the long-pulse laser would have required that the piezo-driven mirror be oscillated at a rate of  $\sim 50$  kHz, which was beyond the capability of the available driver. In practice the main technique employed was a static plane-parallel interferometer with computer aided monitoring that permitted observation of the entire fringe from individual pulses. Measurements of the pulse-to-pulse stability of the long pulse laser obtained using a slow scanning interferometer are also given, as well as a description of a novel system for intra-pulse frequency measurement that is presently under construction.

To monitor the single-shot frequency spectrum of the long-pulse laser, a static plane-parallel interferometer was used along with a particular computer aided interferometry (CAIN) package. This technique, which was also employed to monitor the frequency spectrum of the Q-switched laser in chapter 5, is shown schematically in figure 4.11. The pulsed beam from the Nd:YAG laser was expanded, then focussed to diverge through a static plane-parallel Fabry-Perot etalon made of plates of 97% reflectivity and separated by 1.03 cm. The resultant concentric circular fringes were imaged at the back focal plane of the imaging lens such that approximately 2 free-spectral-ranges were within the detector area of the CCD camera, (8.5 mm \* 6.4 mm).

The fringes were detected and analysed by a computer aided system that was built within the department by James Wade and Michael Lusty to study the frequency

characteristics of a distributed feedback dye laser [4.3]. This used a charge coupled device (CCD) camera\*, which provided a high resolution video output that exhibited a linear response to flux intensity. The video output of the CCD camera was digitized by the video-frame store which was triggered by a TTL signal from the driver of the pulsed-laser diode. Upon the user pressing the "sample" key on the dedicated Archimedes computer, a frame was captured by the frame-store and displayed on the monitor. The frame-store could then be interrogated by the computer, and the image displayed in pseudo-colour with 7-bit resolution.

The pictures obtained were linearly distorted because the image from the CCD camera had an aspect ratio of 4:3 which was mapped onto computer memory with an aspect ratio of 1:1. Thus, the circular interference fringes that were observed using this system appear elliptical in figure 4.12. The presence of 5 longitudinal modes was due to spatial hole burning which has already been discussed in detail for the end-pumped laser in chapter 3.

With a routine for the computer a horizontal scan of 5 adjacent lines was taken across the entire width of a given interference pattern, and the radial intensity distribution plotted. As this was wasteful of the available information, a more sophisticated routine was used by which the intensity could be averaged radially around the fringes. To obtain a frequency spectrum in which the radius of the fringes was linearly related to frequency, further software was developed in the department by Stuart Fancey [4.4]. For a plane-parallel interferometer the fringe radius,  $r$ , is related to the laser wavelength,  $\lambda$ , using the following equation [4.5],

$$m\lambda = 2d \left( 1 - \frac{4r^2}{8f^2} \right) \quad (4.1)$$

---

\* EEV P46110 photon camera

where  $m$  is the order of the fringe,  $d$  is the mirror spacing and  $f$  is the focal length of the lens used to image the fringes. Expressing this equation in terms of the frequency increment,  $\Delta\nu$ , gives,

$$\Delta\nu = 2k (r^2_{m\nu} - r^2_{m\nu+\Delta\nu}) \quad (4.2)$$

where  $m\nu$  and  $m\nu+\Delta\nu$  are the orders at those particular frequencies.  $k$  is a scaling factor given by

$$k = \frac{mc}{16df^2} \quad (4.3)$$

which is a constant over a single free-spectral-range (FSR) of the etalon. To make the radial coordinate linear with frequency over a single order, the user was required to define a free-spectral-range on the stored data. This was done by marking equivalent points in adjacent orders of the non-linear radial intensity distribution with the cursor. The computer program was then implemented to produce a linear frequency spectrum such as that shown in figure 4.13. A scaling was provided for the frequency difference across the spectrum by the free-spectral-range of the etalon, which was measured from the plate separation. When this calibration was applied, the intermode spacing for the long-pulsed laser was found to be 2.37 GHz, which corresponds to laser oscillations on every third cavity mode.

To measure the pulse-to-pulse frequency stability, a plane-parallel interferometer was used in a slow scanning mode. A collimated laser beam from the pulsed-laser was injected into an interferometer, a mirror of which was scanned over a couple of free-spectral-ranges in a period of 10 s\*. During this time interval, the central fringe of the fringe pattern was detected by a fast photodiode (BPW 28), and the signal fed into the digitizer unit of a spectrum analyzer\*. The sample base of this digital storage facility consisted of 15,000 points, from which the peak search facility selected those data

---

\* Photon-Control ASM-20 piezo-mount.

\* Hewlett Packard 70700 digitizing unit

points which corresponded to the detection of a laser pulse. The 1000 points obtained in this way, each one from a separate laser pulse, are displayed in figure 4.14 as a composite frequency spectrum. This confirmed the results from the single shot computer aided interferometry; showing that the long-pulsed Nd:YAG laser was operating on five longitudinal modes, each separated by  $\sim 2.3$  GHz. The fact that a clear mode structure is discernible in this spectrum shows that over the sample period of 10 s the pulse-to-pulse frequency jitter is less than the intermode spacing.

A further technique is under development to allow the measurement of frequency shifts within the duration of the laser pulse. As with the computer aided interferometry system outlined above, light from the pulsed laser will be focussed through a static interferometer. But rather than monitor the entire 2-dimensional fringe pattern once per laser pulse, a linear slice across the centre of the fringe pattern will be detected about 20 times throughout the pulse. This will require the information detected by the CCD to be read out faster than  $10\ \mu\text{s}$  which is beyond the capability of available linear CCD arrays which must shift the charge serially along the array

To overcome the limitation imposed on the scanning rate by the serial extraction of the signal, a novel array is under construction in the department by Matthew Emberson. This will utilize a 2-dimensional CCD, in which all the pixels are masked from light with the exception of a single horizontal row. After the  $10\ \mu\text{s}$  detection time slot the charge generated in the unmasked row will be shifted in parallel in  $<1\ \mu\text{s}$  to the masked row of pixels below. In this way the masked pixels of the array will act as an almost instantly accessible temporary store for the charge generated in the unmasked row. This process of shifting the charge down within the 2-dimensional array will be repeatable up to  $\sim 50$  times, building up a historical record of the flux incident on the linear array every  $10\ \mu\text{s}$ . At the end of this detection phase, the charge will be available to be accessed at a more leisurely rate by a personal computer. It is expected that this device will find additional applications to that for which it has been designed.

---

#### **4.4 Pump-rate distribution**

The pump rate distribution (PRD) is the rate of excitation of active ions at all points within the Nd:YAG rod. The PRD is the link between the characteristics of the pumping laser and the output from the Nd:YAG laser, and is the prime feature in the computer model of the pump process which is described later in this chapter.

The pump-distribution model required several experimentally determined input parameters including the diode beam divergence, the distance between the diode facet and the rod, and the absorptivity of the Nd:YAG rod to the pump light. A discussion follows on the important effect that absorptivity has on the pump rate distribution, and consequently the performance of the transversely pumped laser.

To check the validity of the computer modelled PRD that is given in section 4.5.2, spatially resolved measurements were taken of the small signal gain throughout the rod. This involved using a probe beam from the cw diode-pumped Nd:YAG laser, which was focused axially through the Nd:YAG rod, and scanned in raster fashion to build up a 2-dimensional array of gain measurements. These gain measurements, and the pumping rate values obtained from them, are presented for comparison with the computer generated pump distribution.

##### **4.4.1 Absorption of laser-bar pump emission by Nd:YAG crystal**

A key consideration in the modelling of the pump process was the absorption characteristics of the Nd:YAG rod to the laser-bar pump radiation. The absorptivity can be calculated from a convolution of the absorption spectrum of the laser crystal with the spectral profile of the pump laser. The time-resolved frequency spectrum of the pulsed laser-bar (shown in figure 2.17) indicates that about 5 modes were oscillating with an instantaneous bandwidth of 2 nm. A calculation of the absorption is made more difficult by the shift in central wavelength of ~5 nm throughout the pump pulse

duration, as shown in figure 2.18. The magnitude of the shift in wavelength is quite significant with respect to the width of the 810 nm absorption feature in the Nd:YAG crystal, as shown in figure 4.15 [4.2].

To examine the effect of the frequency sweep on the absorption, the single-pass small-signal gain of the close-coupled pulsed Nd:YAG laser was studied. The experimental arrangement is shown in figure 4.16. The single frequency 1.064  $\mu\text{m}$  output from the cw diode-pumped Nd:YAG laser was focused through the Nd:YAG rod, and the temporal response of the small signal gain monitored by a BPX 65 photodiode. The intensity of the probe beam was low enough at  $\sim 1$  mW to ensure that the population inversion was not significantly depleted by the probe beam. Consequently, the change in intensity detected by the photodiode as the laser-bar was pulsed gave a measure of the small-signal gain.

The frequency sweep throughout the laser-bar pulse manifested itself in a change in pump absorptivity. This introduced a temporal variation into the pumping rate which translated into a variation in the small-signal gain. This effect was observed by temperature tuning the laser-bar to 4, 8 and 20°C, such that the wavelength at the start of the pulse changes with respect to the absorption feature in the Nd:YAG crystal. The relative gradients of the three profiles at different times throughout the pump pulse give an indication of the time dependent absorptivity, as shown in figure 4.17.

By varying the laser-bar temperature it was possible to temperature tune the initial laser-bar wavelength to maximise the total gain available, as was the case for long-pulse laser operation. Alternatively, the temperature could be lowered, such that the gain available at the end of the pump pulse was maximised as was appropriate for Q-switched operation. In this way there was maximum pump absorption at the end of the pump pulse such that fluorescent decay was minimised.

The influence of the time varying spectrum of the laser-bar on the PRD in the crystal could not be excluded from having an effect upon the transverse mode of the laser.



When the cavity mode volume within the rod was slightly less than that required to achieve  $TEM_{00}$  mode, the transverse mode structure was found to change from  $TEM_{00}$  to  $TEM_{01}$  during the pulse. This may also be due to the increase in unsaturated gain in the wings of the fundamental mode throughout the pump pulse.

To prevent over complexity in this first attempt at modelling the transversely pumped laser the pumping rate was taken as constant, even though the frequency chirp of the laser bar causes a time dependent absorption. This was achieved by a time-averaged convolution of the frequency spectrum of the laser-bar with the absorption profile of Nd:YAG. The absorption spectrum of the 1.3% doped Nd:YAG in the wavelength range of the diode-pump, which is shown in figure 4.18, was measured using a Ti:sapphire probe beam. The diode-spectrum shown in figure 2.17 was convolved with the Nd:YAG absorptivity at 7 instants throughout the pulse for the case when the diode spectrum was most closely matched to the Nd:YAG absorption. From these the time averaged absorptivity was computed to be  $0.52 \text{ mm}^{-1}$

It is recommended that when rods are fabricated for transverse pumping, a thin blank of the same material should also be cut and polished. Direct measurement of the transmissivity of the test sample to the emission from the laser-bar, whether pulsed or cw, would give more accurate information on the absorptivity of the material, which is necessary for a better model of the pumping process.

#### 4.4.2 Small-signal-gain distribution

The pumping-rate per unit volume for the transversely pumped laser has been modelled in a computer program called SIDEPUIMP, which is detailed in section 4.5.2. This section contains a description of the experimental small-signal gain measurements that were used to check the validity of this pump distribution model.

The experimental arrangement which is shown in figure 4.16 consisted of a  $1.064 \mu\text{m}$  cw probe beam, focussed axially into the rod. After passing through the rod, the



intensity of the probe beam was monitored by a photodiode. By monitoring the relative change in the intensity detected by the photodiode as the laser-bar was pulsed the small-signal gain could be deduced. The probe beam was focussed by an 8 cm lens to give a free-space spot size of 60  $\mu\text{m}$ . This was scanned in the x and y planes by two 45° mirrors on translation stages. An array of values for the small signal gain was obtained with 100  $\mu\text{m}$  resolution.

At the low intensity level of the probe beam used for the small signal measurements, the upper state population was not significantly depleted by the probe beam. Hence, the probe beam intensity after passing through the crystal is given by,

$$I(z_c) = I(0) \exp [ N(t) \sigma z_c ], \quad (4.4)$$

where  $\sigma$  is the stimulated emission cross-section, and  $z_c$  is the length of the crystal.

The instantaneous population inversion,  $N(t)$ , can then be obtained in terms of the single pass small signal gain,  $\alpha$ , defined by

$$\alpha = I(z_c) / I(0), \quad (4.5)$$

using

$$N(t) = (1 / \sigma z_c) \ln [ \alpha ]. \quad (4.6)$$

For our condition of pumping for a finite interval,  $\tau_p$ , the population at the end of the pumping interval,  $N(\tau_p)$ , is related to the pumping rate,  $R_p$ , by

$$N(\tau_p) = R_p \tau_2 [ 1 - \exp (-\tau_p / \tau_2) ]. \quad (4.7)$$

where  $\tau_2$  is the fluorescence lifetime of the upper laser level. Hence, the pumping rate can be found from a measurement of the single-pass small-signal gain at the end of the pump pulse,

$$R_p = \frac{\ln \alpha}{\sigma z_c \tau_2 [ 1 - \exp (-\tau_p / \tau_2) ]}. \quad (4.8)$$

For the parameters for the transversely pumped laser, this becomes

$$R_p = 9.26 * 10^{27} \ln [\alpha] \text{ m}^{-3}\text{s}^{-1} \quad (4.9)$$

The spatially resolved measurements of the small signal gain were converted into a grid of natural logarithms by the program EXP. These were stored in a grid file called EXPCON, and plotted out with contours proportional to the pumping rate density in figure 4.19. The contours are spaced at intervals of  $\ln[\alpha]$  of 0.1.

The general features of the pump rate distribution shown in figure 4.19 are confirmed by the false-colour image in 4.20 which depicts the fluorescence at the end of the laser rod when it was pumped by the laser-bar. The curved front surface of the rod acted as a lens to collimate the pump light, such that the pump light predominantly fills a strip across the laser rod, with a "hot-spot" at the side of the rod from which the pump light emanated. This picture was taken with a filter placed between the rod and the CCD camera to absorb the 810 nm pump light whilst transmitting the fluorescence at 1.064  $\mu\text{m}$ . The magnified image of the end of the rod was transferred to the computer aided frame store system described in section 4.3. Images obtained by this system were useful in the alignment of the laser-bar with respect to the laser rod. Although qualitatively informative, the contours cannot be equated with particular levels of population inversion because the camera is not detecting light from a single plane.

---

## 4.5 Modelling of quasi-cw side-pumped Nd:YAG laser

### 4.5.1 Introduction

The purpose of the model was to determine the output power of the quasi-cw Nd:YAG laser as a function of input power. The first part of the model is a calculation of the steady state pump-rate distribution within the Nd:YAG rod. This is then used to determine whether the TEM<sub>00</sub> mode or the TEM<sub>01</sub> mode has the lower pump threshold, and the value of the threshold pump power. Particular consideration was given to the transverse mode structure of the laser output, as it was important to achieve operation in

the fundamental transverse mode. At a subsequent stage in the model the threshold is determined for the other mode in the presence of gain saturation by the first mode. The final part of the model is then to obtain a table of output power against input power for the laser over the pump range in which there is only one transverse mode lasing.

The rate equation analysis follows that of Kubodera and Otbuka [4.6], and involves a calculation of an integral of the product of the pump rate distribution and the flux density over the volume of the laser crystal. The formalism behind this approach is presented along with the theory behind the pump threshold and output power calculations. The computer code based on this model was developed in the department by a summer-student called Andrew Wray [4.8].

#### 4.5.2 Pump-rate distribution

The first stage in the general modelling of the transversely pumped laser was to obtain the rate of excitation of active ions at all points within the Nd:YAG rod. To obtain this pump rate distribution, a program was written which traced 3300 individual rays from the laser-bar as they passed through the Nd:YAG rod. Although Gaussian beam optics can in principle be used to describe the propagation of a beam from a laser-diode, the description of the wavefront when it was only partially inside the rod was found to be complicated. The program that determines the pump-rate distribution, SIDE PUMP, produces a data-file which can be passed to other programs for threshold and output power calculations.

The pump light from the laser bar is taken to have a Gaussian intensity profile in the plane of the laser-bar junctions with a divergence that was measured to be  $21.4^\circ$  FWHM. The lesser divergence in the axial direction of the rod resulted in a pump distribution that was fairly uniform along the length of the rod, and permitted the calculation of the pump distribution to be restricted to two dimensions. Each of the total of 3300 rays had an initial weighting of one unit, and was labelled by its angle to

the pump axis. The Gaussian intensity profile with its measured divergence determines the angular spread of the rays. The on-axis peak of the intensity profile resulted in the largest number of rays having an initial angle of divergence close to zero, with the maximum ray angle corresponding to 1.7% of the peak intensity.

Propagation of each ray is accomplished by determining the point on the crystal surface at which each ray is incident, and the angle of incidence for that particular ray, as shown in figure 4.21. The fraction of that ray's weighting that is lost due to Fresnel reflection is calculated, and subtracted from the ray's weighting as it enters the rod. The angle of incidence is also used to determine the refracted angle of each ray as it enters the rod. The crystal is divided into a 2-D array of 100 x 201 pixels, in which each pixel corresponds to a thin filament that runs the length of the rod. The degree of pumping of a pixel by a particular ray is given by the loss in that ray's weighting due to absorption in that pixel. This is dependent upon the angle of the ray, and the position at which the ray enters and leaves the pixel.

Upon crossing the crystal, the rays are then reflected by the back surface of the rod and by the reflective brass rod housing. The procedure for modelling the back reflection is similar to that for the front surface. The pump distribution is calculated for only the half of the rod above the x-axis because of the symmetry of the pump profile.

Conversion of the theoretical data of absorbed rays per pixel  $N(x,y)$  into a distribution giving pump rate per unit volume  $R(x,y)$  involves multiplication by a factor,  $K$ ,

$$R(x,y) = K \cdot N(x,y) \quad (4.10)$$

where  $K$  is given by

$$K = \frac{P_p}{h\nu \Sigma I_r} \quad (4.11)$$

$P_p/h\nu$  is the pump output power divided by the energy of a pump photon, and is the rate of photon emission by the pump-diode.  $\Sigma I_r = 3300$  is the sum of the initial ray

weightings, and  $v$  is the pixel volume which is given by the cross-sectional area of a pixel multiplied by the crystal length.  $K$  is printed with each contour plot and can be applied to the numerical value shown at any point in the plot.

The program SIDEPUMP determines the pump-rate distribution after the relevant pump parameters, which are given in table 4.1 along with their values, have been entered. To make this contour plot comparable with that obtained from the small signal gain measurements in section 4.4.2, a program called COARSE averages the  $100 \times 201$  array into a  $14 \times 28$  array of  $105 \mu\text{m}$  squares. The resultant low resolution contour plot obtained using the parameters in table 4.1 is shown in figure 4.22, and is stored in the grid file RUFCON.

Radius of crystal	0.75 mm
Separation of diode and crystal	0.2 mm
FWHM divergence of pump	$21.4^\circ$
Absorptivity of Nd:YAG to pump	$0.52 \text{ mm}^{-1}$
Back reflection by brass mount	30%

Table 4.1 - Pump rate distribution parameters

A comparison between the computer generated pump distribution and that obtained from the measurements of the small signal gain (figure 4.19) shows that the computer generated distribution fills a narrow strip across the rod, and is in consequence of a higher intensity. It is not known at this stage whether the model or the experiment is responsible for this deficiency.

Upon calculation of the pump rate distribution, routines within the program SIDEPUMP allow the user to create graphical cross-sections, contour plots and data

files containing all the information about the distribution and its associated parameters\*. The fraction of the pump power that is absorbed within the rod,  $\eta_a$ , is also calculated using the program. This is a parameter that is necessary for the calculation of the pump thresholds described in section 4.54. These data files may then be accessed by programs by which the thresholds and slope efficiencies for the Nd:YAG laser can be determined. The program SIDE PUMP has the potential to be developed to give the absolute population inversion distribution at the end of a diode pump-pulse. This would allow a detailed pump model for the Q-switched transversely pumped laser described in chapter 5.

### 4.5.3 Mode-overlap Formalism

On obtaining the pump rate distribution, the calculation of the output power from the Nd:YAG laser was based upon rate equations for the population inversion density and the intracavity flux density. The three-dimensional rate equations for the population inversion density  $n(x,y,z)$  for the situation of more than one transverse mode is given by [4.6],

$$\frac{dn(x,y,z)}{dt} = r(x,y,z) - \frac{n(x,y,z)}{\tau_2} - f_2 \frac{c\sigma n(x,y,z)}{n_1} \sum_i s_i(x,y,z) . \quad (4.12)$$

where  $r(x,y,z)$  is the pump rate density distribution, and  $s_i(x,y,z)$  is the flux density distribution of the  $i$ -th transverse cavity mode. The second and third term on the RHS of equation 4.12 take account of the depopulation of the upper lasing level by spontaneous emission, and stimulated emission by all transverse modes, respectively. The other parameters and their values are given in table 4.2.

The three dimensional rate equation for  $S_i$ , the number of intracavity photons in the  $i$ -th transverse mode is given by

---

\* All the data files and programs are in SAVA directory (PHRAW), and their associated contour plots are in the gridfile CONTOUR.

$$\frac{dS_i}{dt} = \frac{f_2 c \sigma}{n_1} \iiint_{\text{cavity}} n(x,y,z) s_i(x,y,z) dv - \frac{\delta_i}{\tau_{RT}} S_i \quad (4.13)$$

The first term on the RHS of this equation denotes the increase in intracavity flux due to stimulated emission, whilst the second term denotes both parasitic and output coupling loss from the cavity.  $\delta_i$  is the fractional round trip loss for the  $i$ -th transverse mode, which includes output coupling, scattering and absorption loss, and mode-clipping loss.  $\tau_{RT}$  is the cavity round trip time, such that  $\tau_{RT}/\delta_i$  is the cavity decay time for the  $i$ -th mode.

Stimulated emission cross-section at 1.06 $\mu\text{m}$ , $\sigma$	$7.4 * 10^{-19} \text{ cm}^2$	[3.31]
Fluorescent lifetime of $^4F_{3/2}$ state, $\tau_2$	230 $\mu\text{s}$	[3.32]
Fraction of ions in $^4F_{3/2}$ state in level 2, $f_2$	39%	[3.12]
Refractive index, $n_1$	1.82	[3.2]

Table 4.2 - Spectroscopic laser parameters of a Nd:YAG crystal

It proves useful to introduce normalised distributions for the pump rate density and the flux density, which are defined such that,

$$r'(x,y,z) = \frac{1}{R} r(x,y,z) \quad \iiint_{\text{cavity}} r'(x,y,z) dv = 1 \quad (4.14)$$

where  $R$  is the total number of atoms excited per second in the laser crystal, and

$$s'_i(x,y,z) = \frac{1}{S_i} s_i(x,y,z) \quad \iiint_{\text{cavity}} s'_i(x,y,z) dv = 1 \quad (4.15)$$

where  $S_i$  is the total number of intracavity photons in the  $i$ -th mode.

In the steady state, the rate equations for the population inversion density and the intracavity flux may be equated to zero, such that,

$$Rr'(x,y,z) = \frac{n(x,y,z)}{\tau_2} + f_2 \frac{c \sigma n(x,y,z)}{n_1} \sum_i S_i s'_i(x,y,z) \quad (4.16)$$



$$1 = \frac{f_2 c \sigma \tau_2}{\delta_i n_1} \iiint_{\text{cavity}} n(x,y,z) s_i'(x,y,z) dv \quad \text{for all } i, \quad (4.17)$$

Expressing equation 4.16 explicitly in terms of the inversion density one obtains,

$$n(x,y,z) = R r'(x,y,z) \left( \frac{1}{\tau_2} + \frac{f_2 c \sigma}{n_1} \sum_i S_i s_i'(x,y,z) \right)^{-1} \quad (4.18)$$

Equations 4.17 and 4.18 are then combined to eliminate the population inversion, and in so doing the flux density is directly related to the pumping rate distribution by,

$$\frac{1}{R} = \left( \frac{f_2 c \sigma \tau_{RT} \tau_2}{\delta_i n_1} \right) \iiint_{\text{cavity}} \frac{r'(x,y,z) s_i'(x,y,z)}{1 + f_2 \frac{c \sigma \tau_2}{n_1} \sum_i S_i s_i'(x,y,z)} dv \quad (4.19)$$

In this overlap integral the pumping rate is related to the loss and the intracavity flux of the  $i$ -th transverse mode. The replacement of the population inversion by the pumping rate makes the saturation of the gain by the intracavity flux explicit in the denominator of this equation.

#### 4.5.4 Thresholds for both TEM<sub>00</sub> and TEM<sub>01</sub> modes

To determine which transverse mode, the TEM<sub>00</sub> or the TEM<sub>01</sub>, has the lowest threshold a program called OVERLAPD has been written. Though the model accommodates the possibility of either mode being the first to lase, all the scenarios so far modelled have involved the TEM<sub>00</sub> mode lasing first, it is this situation that is considered here for simplicity. On obtaining the threshold for the first transverse mode, OVERLAPD calculates the threshold of the TEM<sub>01</sub> mode, whilst taking into account the intracavity flux from the first mode. The saturation of the gain by the first mode increases the threshold for the second mode by depleting the available gain. At increased rates of pumping, higher order transverse modes such as TEM<sub>02</sub> will also reach threshold but they are not included in this treatment.

At the first threshold, the intracavity flux for both modes is zero, that is,

$$S_i = 0 \quad \text{for all } i. \quad (4.20)$$

Substituting this into equation 4.19, the threshold for the fundamental transverse mode is given by,

$$R_{th00} = \frac{\delta_{00} n_1}{f_2 c \sigma \tau_{RT} \tau_2} \left[ \iiint_{\text{cavity}} r'(x,y,z) s'_{00}(x,y,z) dv \right]^{-1} \quad (4.21)$$

To find the threshold for the TEM<sub>01</sub> mode, gain saturation by the TEM<sub>00</sub> mode is included in equation 4.19, such that,

$$R_{th01} = \frac{\delta_{01} n_1}{f_2 c \sigma \tau_{RT} \tau_2} \left[ \iiint_{\text{cavity}} \frac{r'(x,y,z) s'_{01}(x,y,z)}{1 + f_2 \frac{c \sigma \tau_2}{n_1} S_{00} s'_{00}(x,y,z)} dv \right]^{-1} \quad (4.22)$$

But  $S_{00}$ , the intracavity fundamental flux at the TEM<sub>01</sub> threshold is unknown at this stage. However, the threshold pump power for the TEM<sub>01</sub> mode may also be expressed in terms of the flux distribution of the TEM<sub>00</sub> mode.

$$R_{th01} = \frac{\delta_{00} n_1}{f_2 c \sigma \tau_{RT} \tau_2} \left[ \iiint_{\text{cavity}} \frac{r'(x,y,z) s'_{00}(x,y,z)}{1 + f_2 \frac{c \sigma \tau_2}{n_1} S_{00} s'_{00}(x,y,z)} dv \right]^{-1} \quad (4.23)$$

Equating 4.22 and 4.23,

$$\frac{1}{\delta_{00}} \iiint_{\text{cavity}} \frac{r'(x,y,z) s'_{00}(x,y,z)}{1 + f_2 \frac{c \sigma \tau_2}{n_1} S_{00} s'_{00}(x,y,z)} dv = \frac{1}{\delta_{01}} \iiint_{\text{cavity}} \frac{r'(x,y,z) s'_{01}(x,y,z)}{1 + f_2 \frac{c \sigma \tau_2}{n_1} S_{00} s'_{00}(x,y,z)} dv \quad (4.24)$$

The solution is found by varying  $S_{00}$ , the intracavity photon number of the fundamental mode, until equality is achieved. Once a value for  $S_{00}$  has been found for the pump threshold of the TEM<sub>01</sub> mode, then the value of the pump rate  $R_{th01}$  can be obtained from equation 4.22.

The values for the pump thresholds for both transverse modes are calculated using the relation,

$$P_{thi} = \frac{h\nu_p}{\eta_a} R_{thi} \quad (4.25)$$

where  $\eta_a$  is the fraction of the pump power absorbed in the Nd:YAG rod and is calculated in the SIDEPUIMP program.

For the situation in which the TEM<sub>01</sub> mode lases first, and the threshold for the TEM<sub>00</sub> mode is sought, the analysis is very similar. The result in this case would differ only in that the saturation term in the denominator of the above equations would include the flux distribution for the TEM<sub>01</sub> mode,  $S_{01}s'_{01}(x,y,z)$ , rather than the flux distribution for the TEM<sub>00</sub> mode.

The threshold for the TEM<sub>00</sub> and TEM<sub>01</sub> transverse modes were calculated using OVERLAPD for the pump-rate distribution with parameters given in table 4.1 and for the cavity parameters given in table 4.3. The results, which are plotted in figure 4.23, show that the threshold for the TEM<sub>00</sub> mode is lower than that for the TEM<sub>01</sub> at all positions across the rod. However, when the mode position is close to the axis of the rod, then the threshold for the TEM<sub>01</sub> mode is less than the available pump power, such that both modes will lase.

This was confirmed experimentally with a laser configured according to the parameters in table 4.3. Both the model and experiment concur in the finding that when the cavity mode was positioned close to the laser bar then only TEM<sub>00</sub> mode would lase. This is attributed to the edge of the rod acting as an aperture which caused greater clipping loss for the TEM<sub>01</sub> mode than for the TEM<sub>00</sub> mode.

Cavity length	240 mm
Mode waist in rod	420 $\mu\text{m}$
Parasitic losses	1%
Output coupling	10%
Lateral position of mode within rod	0.4 - 1.1 mm

Table 4.3 - Laser parameters used in OVERLAPD

#### 4.5.5 Single transverse mode output power

The steady-state Nd:YAG laser output power is calculated by the program called OVERLAPB as a function of laser-bar pump-power. This program produces a table of output against input power for either the  $\text{TEM}_{00}$  or  $\text{TEM}_{01}$  mode in the presence of saturation of the mode-overlap integral by the intracavity field. As the program is unable to deal with the situation in which more than one transverse mode is lasing simultaneously, the program OVERLAPD must be used first to ascertain that pump regime is one in which only one mode is lasing.

OVERLAPB solves equation 4.19 numerically for a particular mode  $j$ . The program may be thought to work in reverse in that it determines the input power from the output power. The intracavity flux is obtained from the output power using the relation,

$$S_i = \frac{\tau_c P_{\text{out}i}}{T h \nu_l} \quad (4.26)$$

From this value of intracavity flux, the saturated gain as represented in equation 4.19 can be found for the particular transverse mode that is lasing. The pumping rate  $R$  is then determined by integrating the cavity mode distribution/pump distribution product in the presence of the saturation term for a given output power. The input pump power is then related to the pumping rate by

$$P_{in_i} = \frac{h\nu_p}{\eta_a} R_i \quad (4.27)$$

OVERLAPB generates a table of input powers  $P_{in}$  against output powers  $P_{out}$ , which can then be displayed graphically.

Program OVERLAPB was run for a laser with the pump and cavity parameters given in tables 4.1 and 4.3\*, and with a mode-position of 0.525 mm into the rod from the laser-bar. At this mode position it was computed using OVERLAPD that the Nd:YAG laser would oscillate solely in the  $TEM_{00}$  mode at 25 W pump power. The graph of output power against pump power is shown in figure 4.24 for the  $TEM_{00}$  mode. This shows a cw pump threshold of 6 W and a slope efficiency which increases with pumping rate of approximately 20%.

An interesting result from the OVERLAPB program is that the slope-efficiency continues to increase at pump levels well above threshold. This may be explained by considering the slope-efficiency as the product of four contributory efficiency terms.

$$\eta_{sl} = \eta_{qu} \cdot \eta_a \cdot \eta_{oc} \cdot \eta_{ov} \quad (4.28)$$

where $\eta_{qu}$ is the quantum efficiency	$= 0.76 (\lambda_p/\lambda_l)$ ,
$\eta_a$ is pump efficiency,	$= 0.55$ (SIDE PUMP)*
$\eta_{oc}$ is the output coupling efficiency	$= 0.68 (T/(T+\delta_0+L))^*$
$\eta_{ov}$ is the overlap efficiency.	$\approx 0.70$ (OVERLAPB)*

The overlap efficiency is a measure of the efficiency of extraction of flux from the inversion in the Nd:YAG rod. As the flux intensity increases with pumping rate above

---

\* The output coupler was optimised at 6.5%

\* This is the fraction of pump power absorbed within the Nd:YAG rod, calculated by the model SIDE PUMP for the parameters given in table 4.1.

\* The output coupling efficiency is the ratio of output coupling loss to total flux loss in the cavity.  $T$  is the transmissivity of the output coupler (6.5%), and  $\delta_0$  is the round trip cavity loss for the  $TEM_{00}$  mode calculated in the program OVERLAPD (2%), and  $L$  is the other parasitic losses (1%)

\* The overlap efficiency is not calculated explicitly by OVERLAPB, but is obtained from the computed slope-efficiency.

threshold, stimulated emission increasingly dominates over spontaneous emission. As such, the overlap efficiency is the only term in 4.28 which is a function of pump power. For most lasers the slope efficiency increases with pump power when the laser is just above threshold, but soon becomes constant. This is the case for the end-pumped laser described in chapter 3, in which the pump distribution is coaxial with the cavity mode, giving good saturation of the gain by the intracavity flux.

The reason for the nonlinear slope-efficiency shown for the transversely pumped laser in figure 4.24 is the asymmetry of the pump-rate distribution. In the region of the rod near the laser-bar the pump-rate density is at its highest, but the optical flux intensity is low as this corresponds to the wings of the mode. In consequence, there is poor extraction of the inversion close to the rods at low pump powers. As the pump power increases stimulated emission dominates increasingly, and a slight nonlinearity in the slope-efficiency arises.

The graph of Nd:YAG laser output power against pump power that was obtained experimentally, for the quasi-cw operation with transverse pumping is shown in figure 4.9. This gives a cw pump threshold of 9.2 W and a slope efficiency which also increases with pumping rate of approximately 21.8 %. There was no obvious evidence for the nonlinear slope-efficiency due to the latitude of error on the experimental data.

---

#### 4.6 Conclusions

The approach used in the design of the long-pulsed laser described in this chapter was to maximize the gain by achieving the maximum pump power density. In addition, the intrinsic asymmetry of the pump distribution in the Nd:YAG rod was exploited such that the aperture provided by the rod inhibits higher order transverse modes. This proved successful with quasi-cw operation at  $1.064\text{ }\mu\text{m}$  achieved in TEM<sub>00</sub> mode with a threshold of 9.2 W and a slope-efficiency of 21.8%.

Work is continuing to determine the source of the inconsistency between the modelled pump rate distribution, and the pump rate distribution as determined from the experimental small-signal gain measurements. It is expected that this will remove the discrepancy between the threshold value as computed by the OVERLAPB program and the threshold value obtained experimentally. Once the computer model is validated, it will be a valuable basis for the design of multiple-pump laser-rod configurations currently under consideration.



## Chapter 4    References

- 4.1    L.C. Conant & C.W. Reno "GaAs laser diode pumped Nd:YAG laser" Appl. Opt. 13 (1974) 2457
- 4.2    C.J. Norrie, B.D. Sinclair, N. Gallaher, W. Sibbett & M.H. Dunn "Measurement of frequency sweep in a quasi-c.w. diode-laser array, and its implication for pumping solid-state lasers" J. Mod. Opt. 36 (1989) 1
- 4.3    M. Lusty "Temporal and frequency characteristics of distributed feedback dye lasers" Ph.D. Thesis, University of St.Andrews, Department of Physics and Astronomy, June 1989
- 4.4    S.J. Fancey "Computer aided interferometry" Senior Honours Project, University of St.Andrews, Department of Physics and Astronomy, April 1989
- 4.5    W. Demtroder "Laser spectroscopy" Springer Verlag, Berlin, 3rd edition 1988
- 4.6    K. Kubodera and K. Otsuka "Single transverse-mode LiNdP<sub>4</sub>O<sub>12</sub> slab waveguide laser" J. Appl. Phys. 50 (1979) 653
- 4.8    C.J. Norrie "Diode laser pumped solid state lasers" RARDE Contract Report no. 7, University of St.Andrews, Department of Physics and Astronomy, Jan. 1990

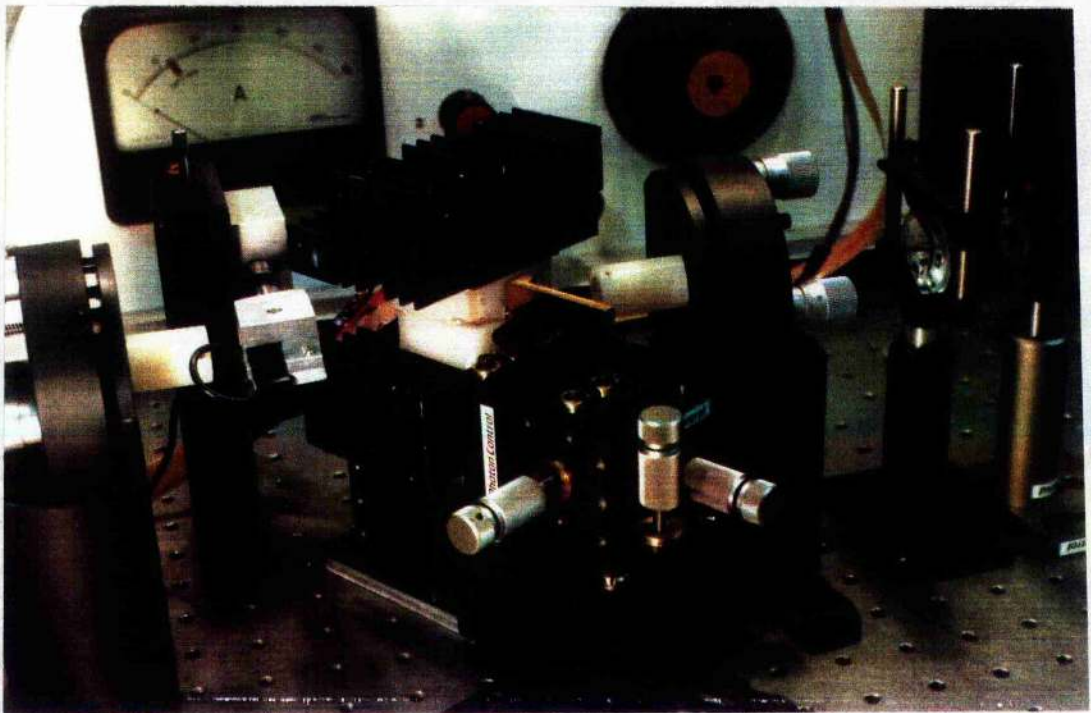


Figure 4.1 Photograph of directly coupled transverse system, with acousto-optic Q-switch and extracavity frequency doubling crystal.

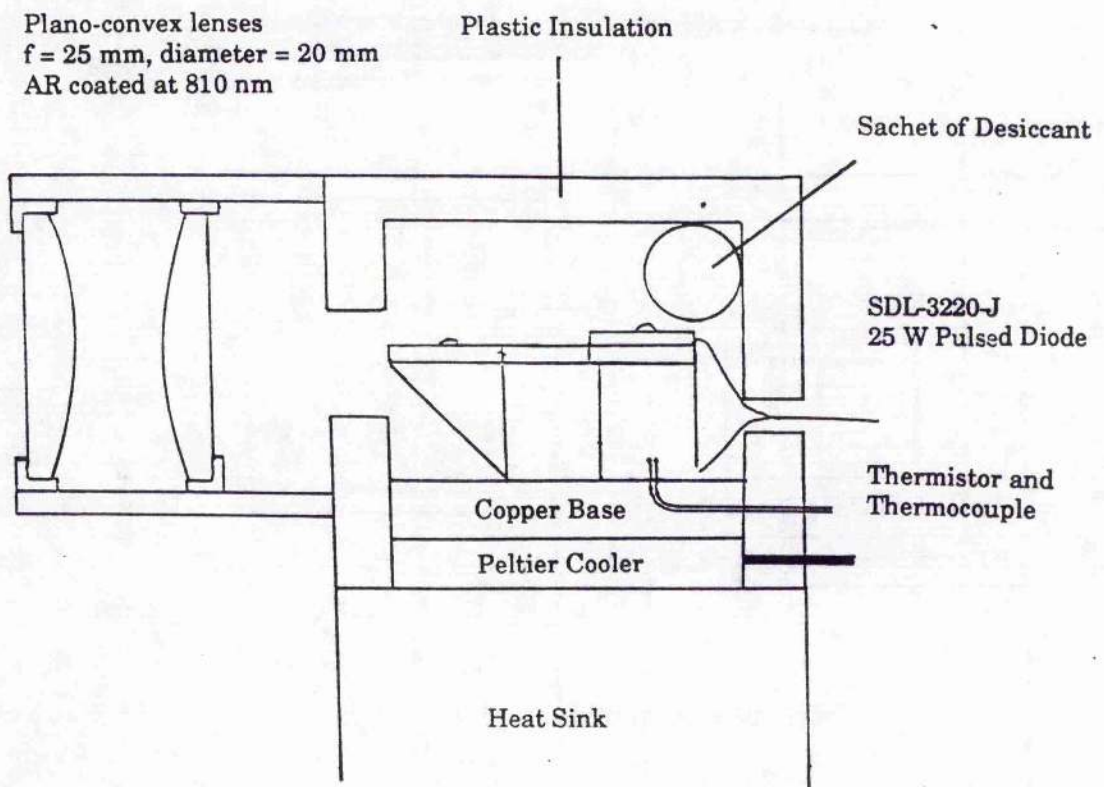


Figure 4.2 Schematic of twin lens diode focussing scheme.

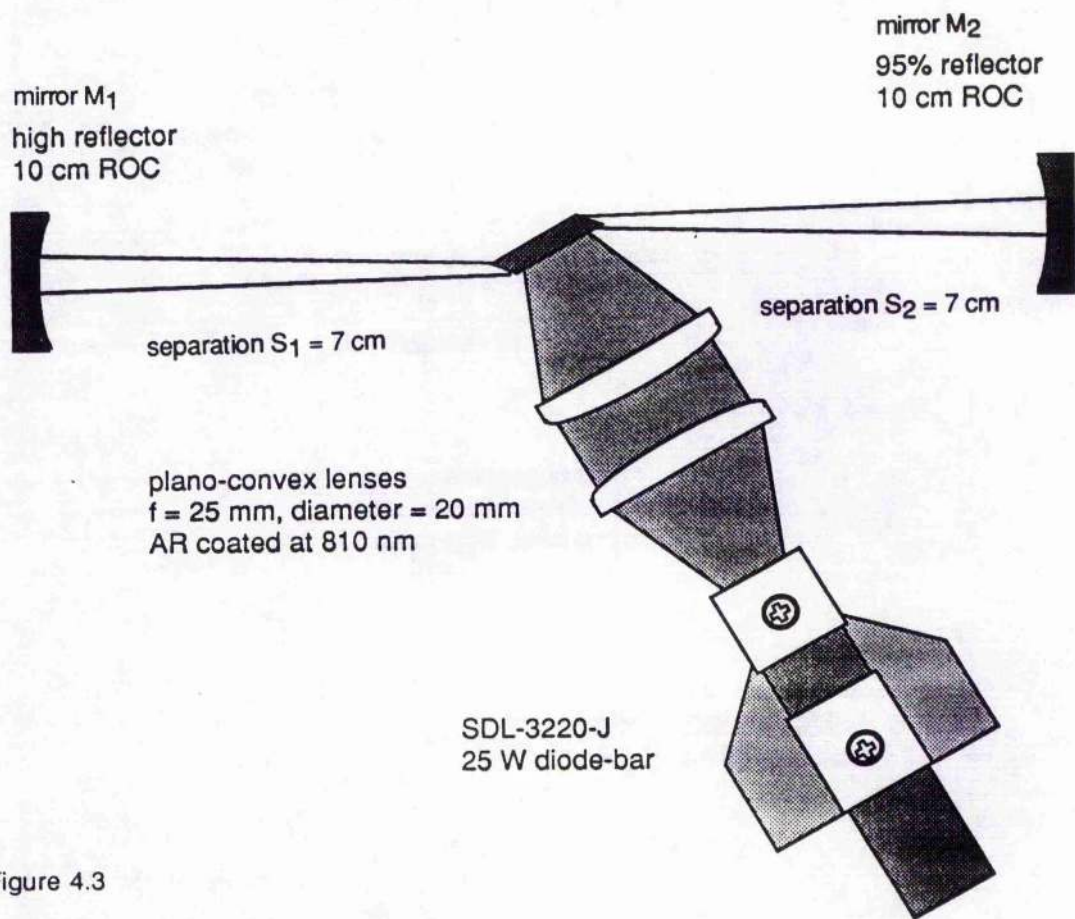


Figure 4.3

Schematic showing the pumping scheme and cavity configuration for the first transversely pumped laser constructed by ourselves. When the lenses were removed it was discovered that the close-coupled pump geometry was considerably more efficient.

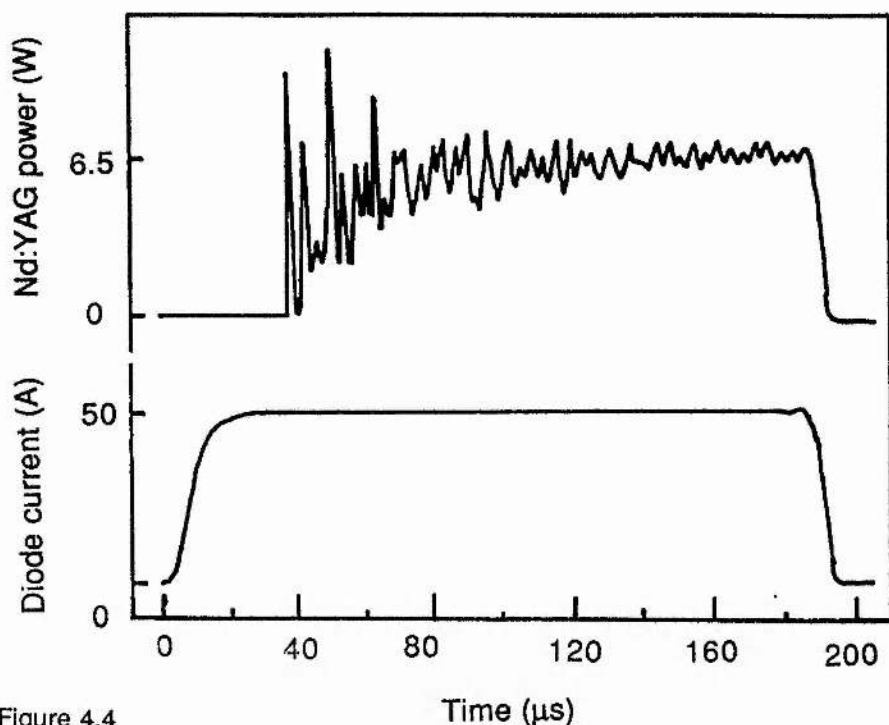


Figure 4.4

The lower trace shows the current pulse to the SDL-3220-J laser bar. The upper trace shows the temporal response of the Nd:YAG laser in long-pulse mode, when pumped by a close-coupled laser bar. The laser configuration was that shown in figure 4.3, in which the output was 6.5 W in a multimode transverse beam pattern.



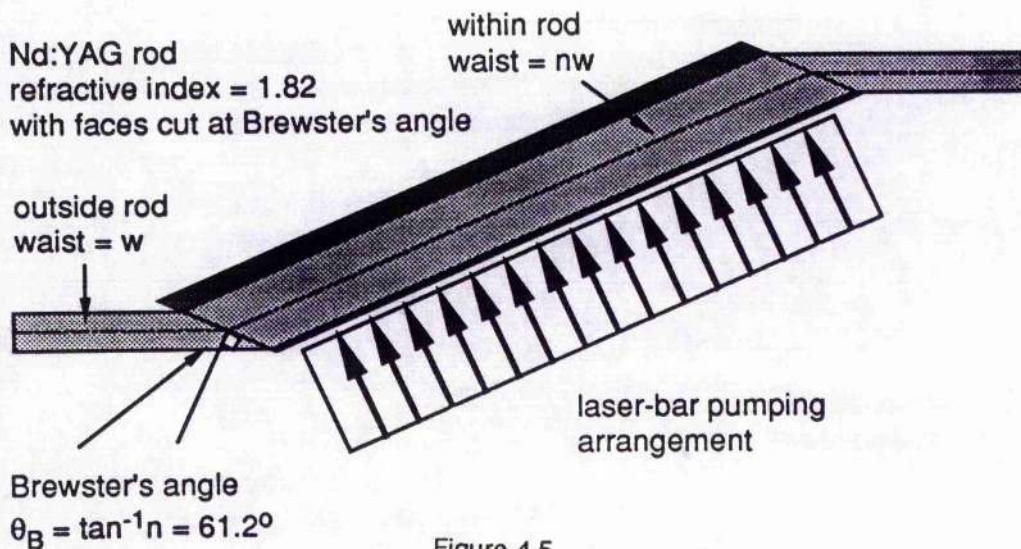


Figure 4.5

Schematic to show how the Brewster angle in the Nd:YAG rod stretches the cavity mode waist in the plane parallel to the laser bar. With an aspect ratio of  $n:1$ , this elliptical mode overlaps with the pumped volume better than a circular mode.

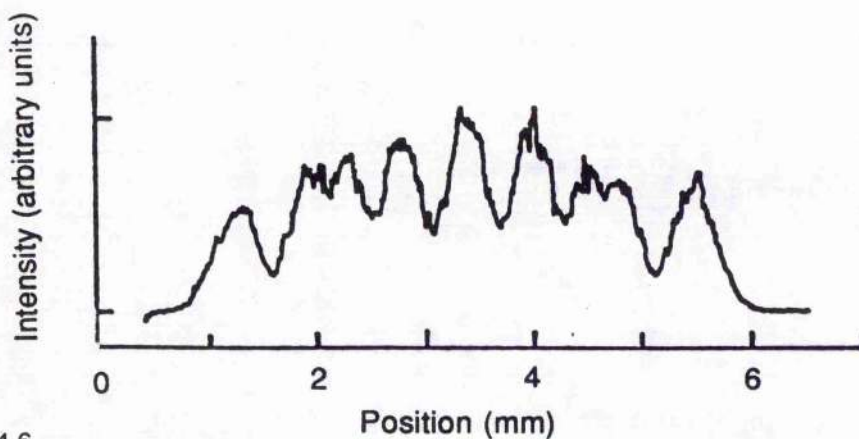


Figure 4.6

Transverse mode structure of the Nd:YAG laser in the horizontal plane, measured using a linear CCD array. The laser was set up as described in figure 4.3. There was only one mode in the vertical plane.

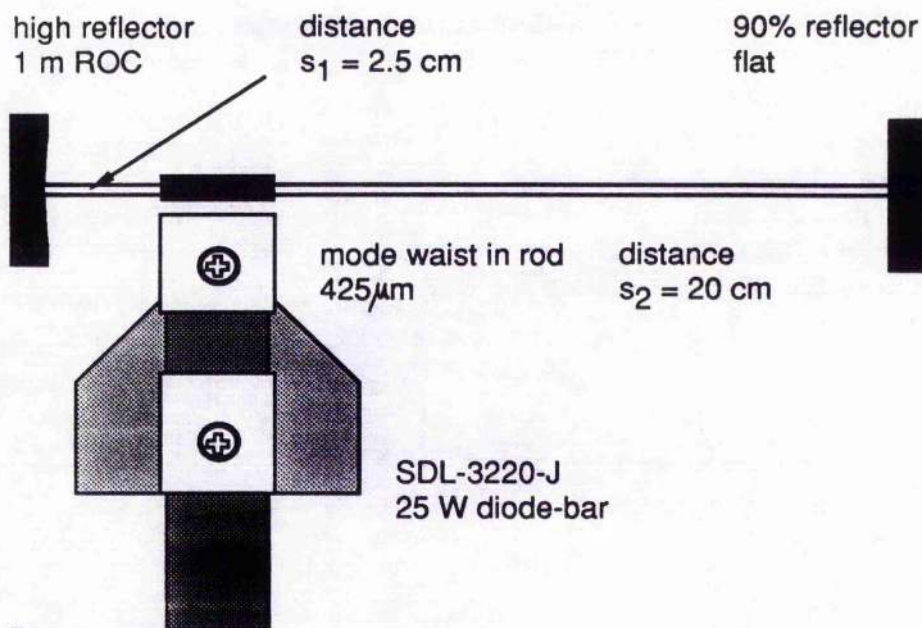


Figure 4.7

Cavity geometry for  $\text{TEM}_{00}$  transverse mode structure with an  $\text{AR}$  coated rod. The cavity waist size within the rod was  $425 \mu\text{m}$ .

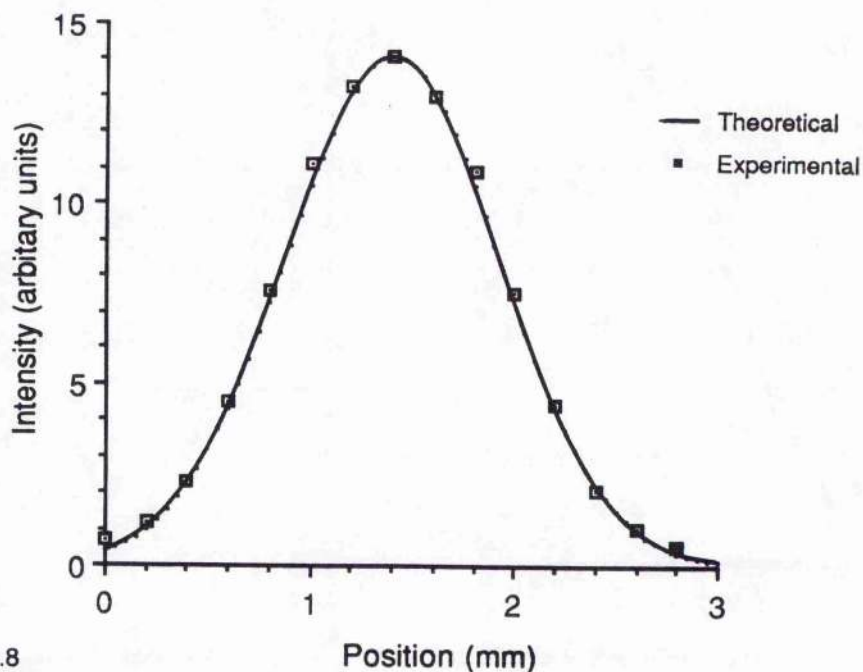


Figure 4.8

Transverse mode structure in the horizontal plane for the laser shown in figure 4.7 showing a single transverse Gaussian mode.

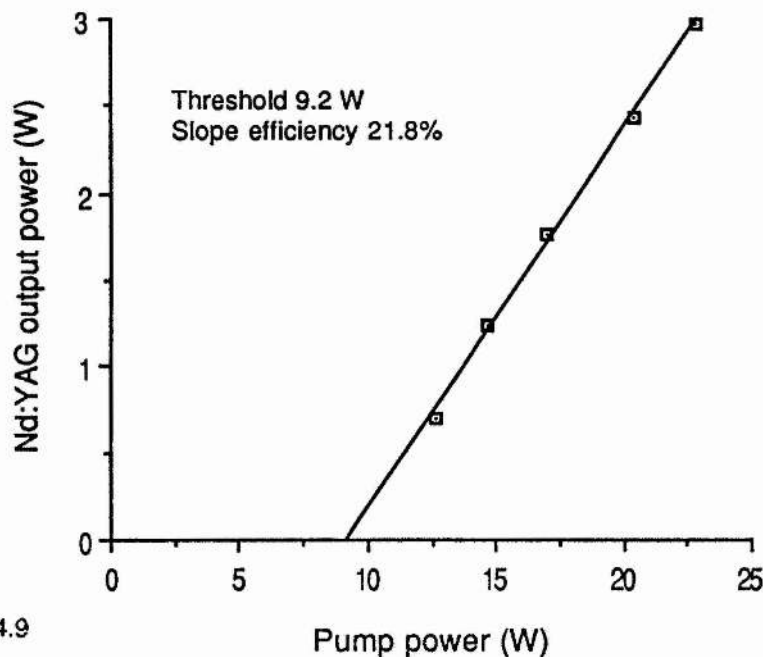


Figure 4.9

Output power against pump power for Nd:YAG laser in long-pulse TEM<sub>00</sub> operation. The laser-bar was pumping 25 Watts in pulses of 200  $\mu$ s duration at a repetition rate of 10 Hz, and the laser cavity configuration was that as shown in figure 4.7. The duration of the output pulses was measured in order to calculate the peak output power from the Nd:YAG laser.

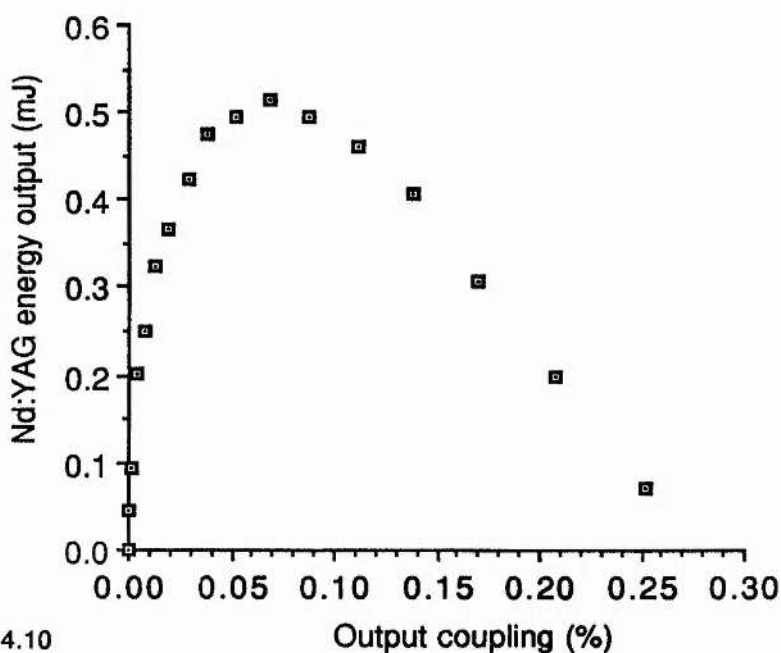


Figure 4.10

Output power against output coupling for the Nd:YAG laser shown in figure 4.7, with a the output coupling mirror replaced by a HR mirror. An intracavity plate was rotated in order to act as a variable reflectivity output coupler as described in chapter 3.XXXX.



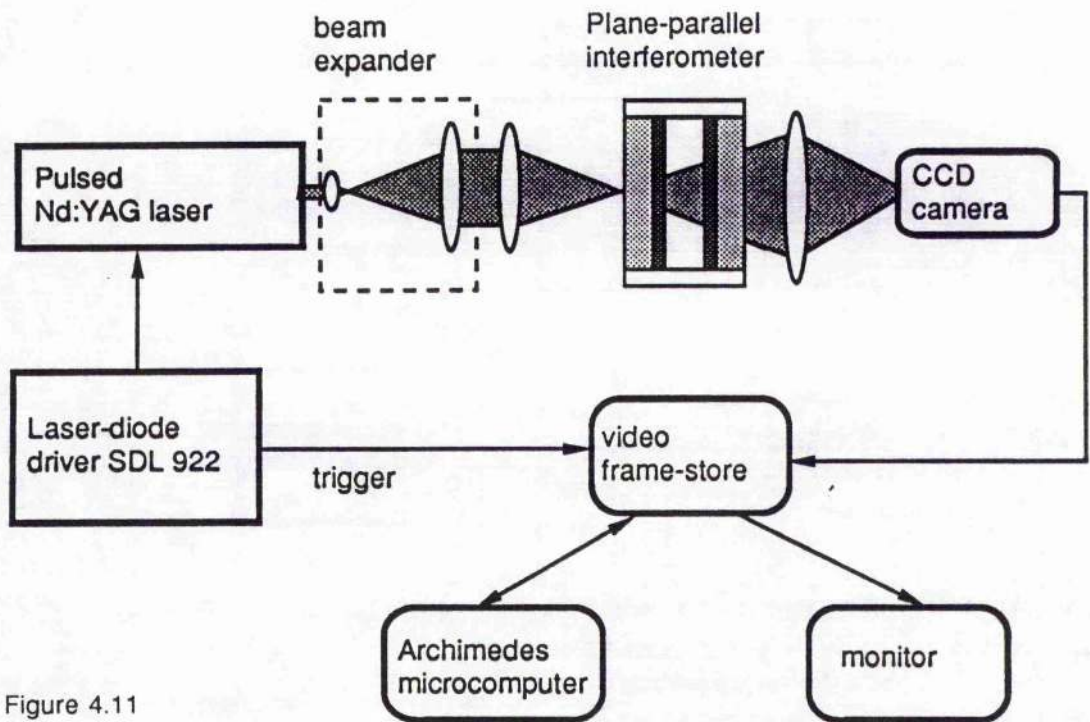


Figure 4.11

Schematic of computer aided plane-parallel interferometer that was used to monitor the single shot frequency characteristics of the Nd:YAG in both long-pulsed and Q-switched operation. The plate spacing was  $\sim 1$  cm, giving a free spectral range of  $\sim 15$  GHz.

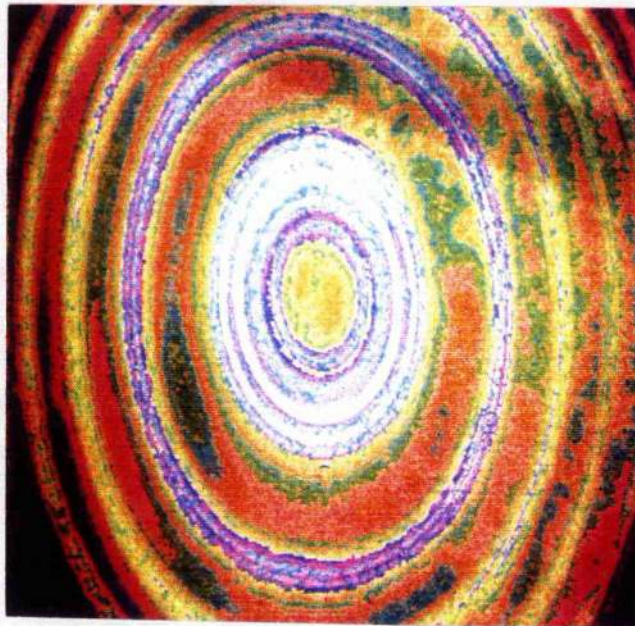


Figure 4.12

Photograph of interference fringes for laser in long-pulse mode taken using a computer aided interferometry system showing the laser operating on 4 longitudinal modes.

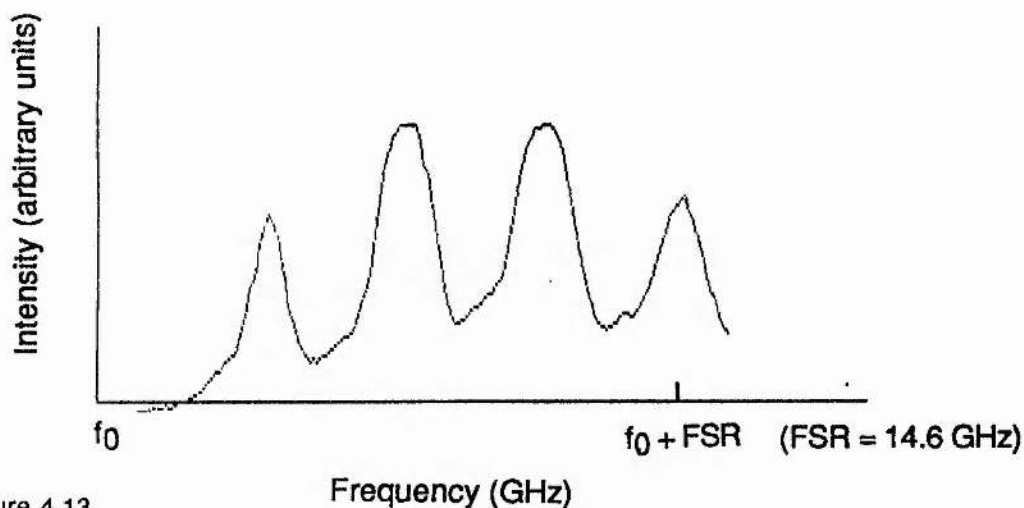


Figure 4.13

Frequency scan obtained from an average radial intensity distribution of the interference pattern shown in figure 4.11. This shows that the intermode frequency spacing is  $\sim 2.3$  GHz, corresponding to three times the cavity mode spacing of 0.75 GHz.

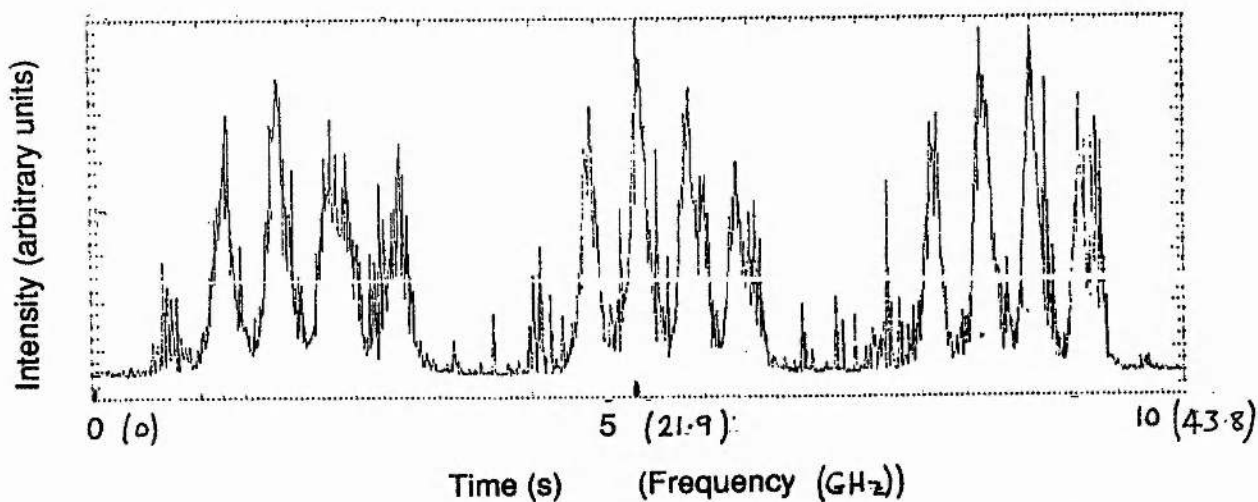


Figure 4.14

Composite frequency spectrum obtained over a slow scan sweep of 10 s duration by the slow scanning Fabry-Perot interferometer, which had a free spectral range of 14.6 GHz. Recorded from 1000 pulses, this confirms the frequency spectrum obtained by the single-shot static Fabry-Perot, and shows that there is good pulse to pulse frequency stability.



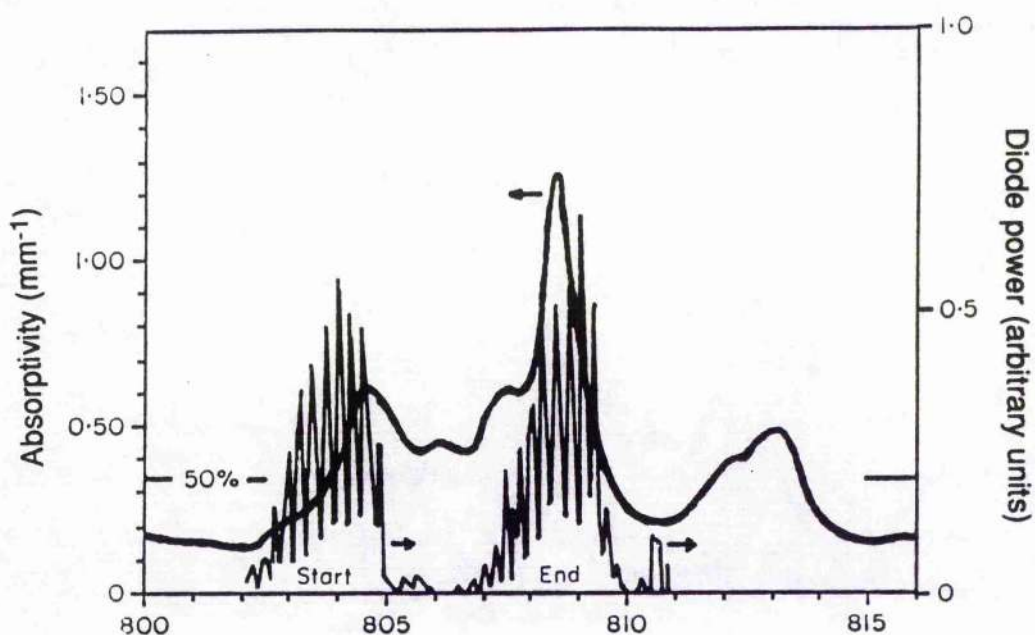


Figure 4.15

Absorption spectrum of Nd:YAG with the spectral output of the diode array near the start and end of the pulse superimposed upon it. The 50% lined indicates the absorptivity at which half the pump light is absorbed in a 2 mm path length.

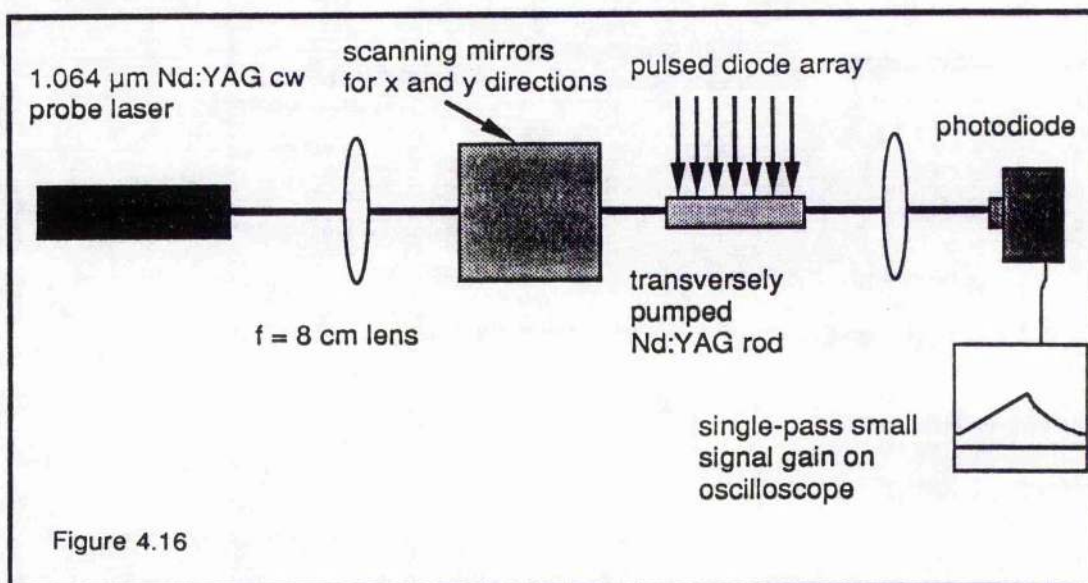


Figure 4.16

Schematic diagram of the experimental configuration for the single pass small-signal gain measurements of the Nd:YAG rod when transversely pumped. In the experiment described in section 4.4.1 on the temporal profile of the gain, the scanning mirrors were not used. In the experiment described in section 4.4.2 on the spatial distribution of gain within the rod, the peak small-signal was monitored.

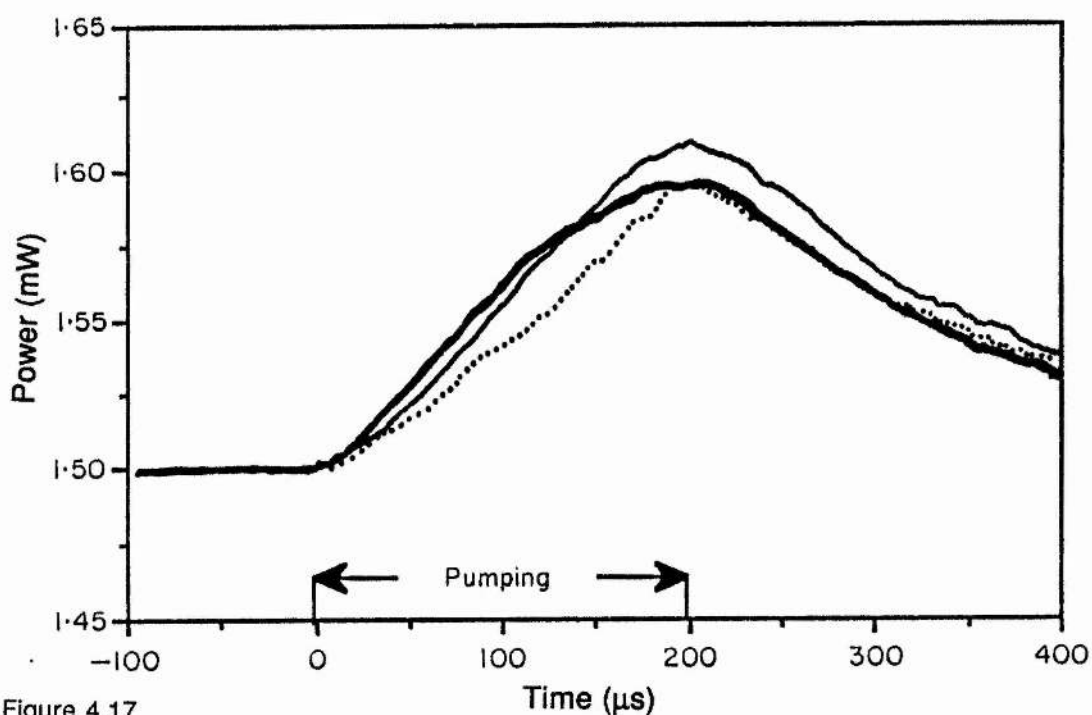


Figure 4.17

Small-signal gain in the side-pumped Nd:YAG rod measured during the 200  $\mu\text{s}$  long, 25 W pump pulse, with different temperatures of the diode-laser heat-sink and therefore different wavelength of the diode array-output: 4°C (dotted curve), 8°C (thin curve) and 20°C (thick curve).

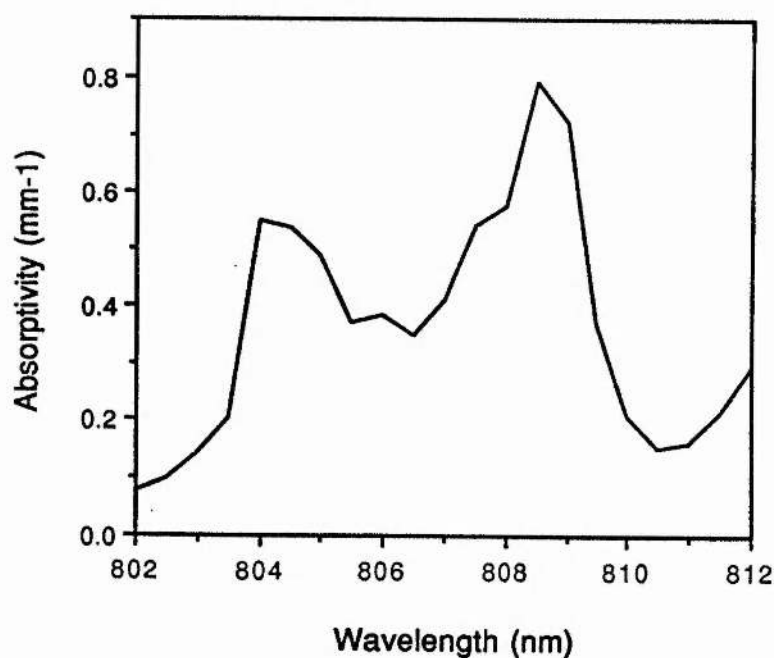


Figure 4.18

Absorptivity of 1.3% doped Nd:YAG measured using a Ti:sapphire laser probe beam scanned over the 809 nm absorption feature.

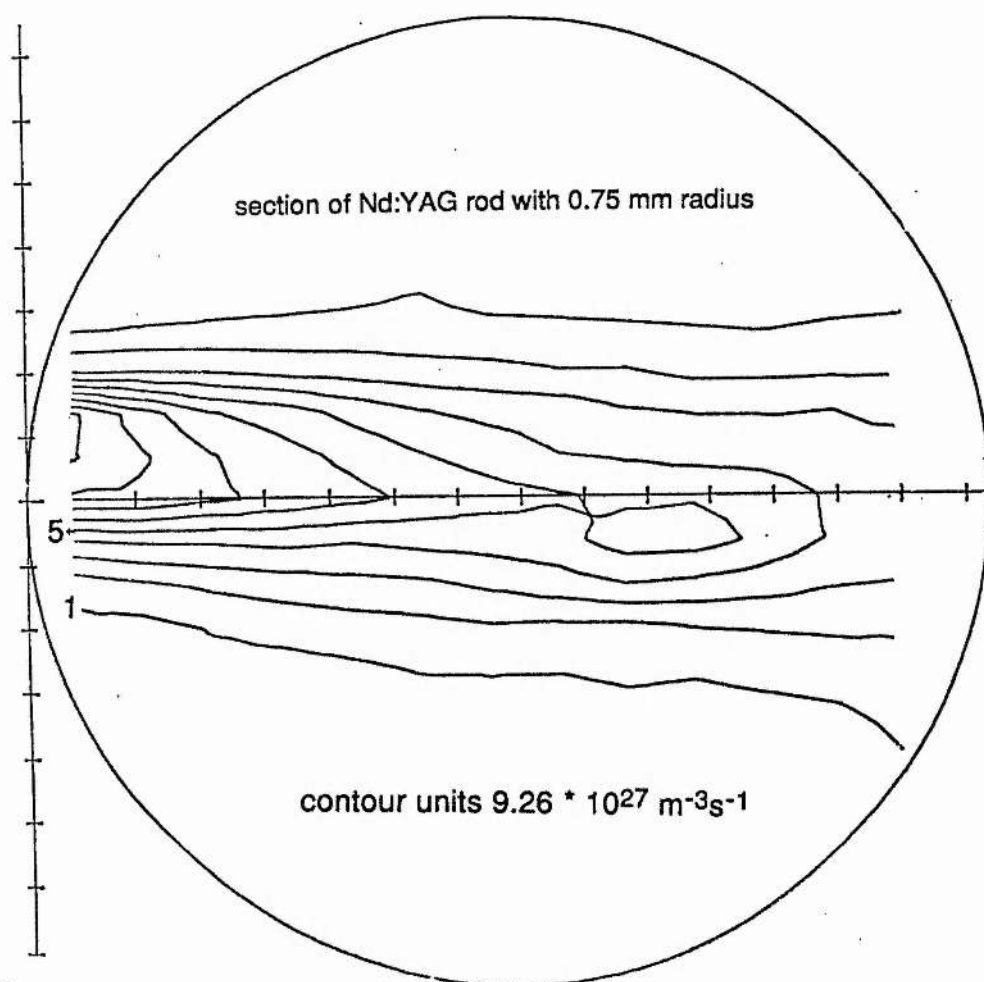


Figure 4.19

Contour plot of the pumping rate per unit volume which was obtained from the single-pass small-signal-gain measurements. The program EXPCON gives a plot with contours proportional to  $\ln[\alpha]$ , in increments of 0.1, so that a conversion factor of  $9.26 \times 10^{27} \text{ m}^{-3}\text{s}^{-1}$  is required to convert the contour values given in this plot into a pumping rate density distribution.

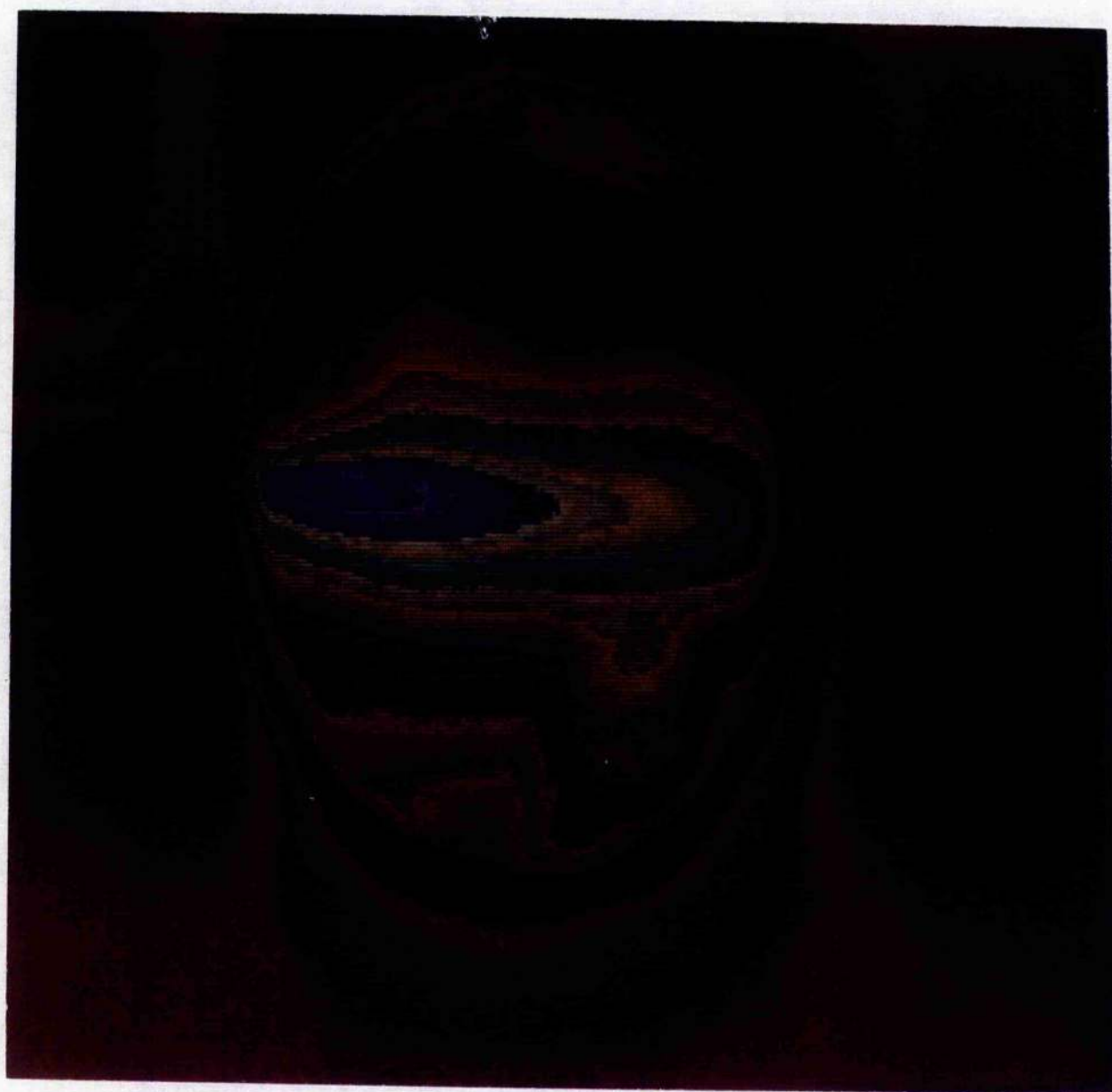


Figure 4.20 Pseudo-colour image of the fluorescence from the end of the transversely pumped Nd:YAG rod.

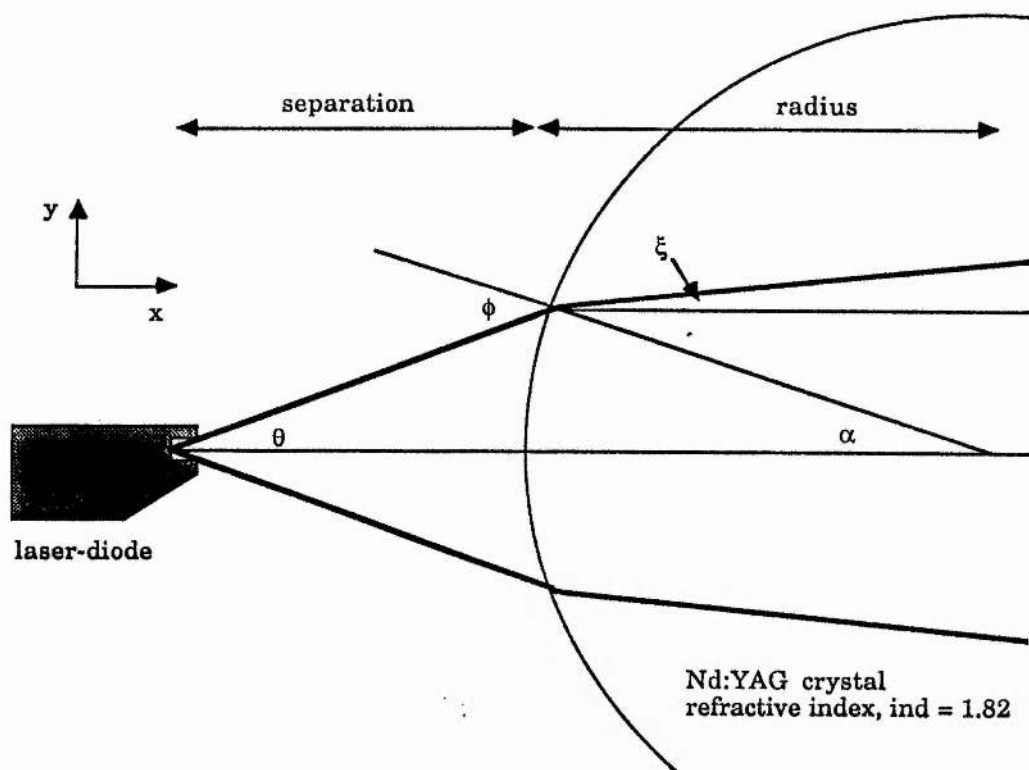


Figure 4.21

Schematic diagram of the ray-tracing geometry used in the SIDE PUMP program. The Gaussian intensity distribution of the pump light is transformed into the angular distribution of 3300 individual rays, each of unity weighting. These rays are then refracted at the rod surface, with the Fresnel reflection loss removed from the weighting of each ray. Reflection by the back of the rod and the reflective housing is also taken into consideration.



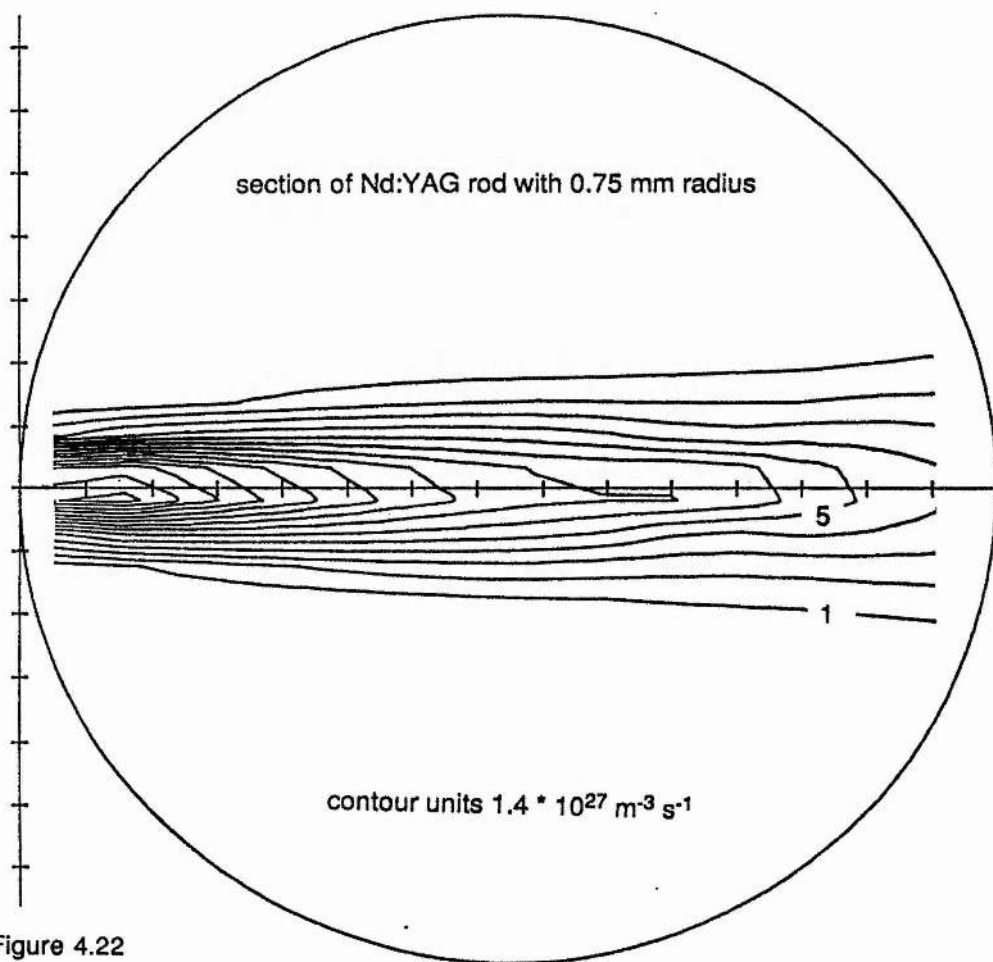


Figure 4.22

Contour plot from the program SIDEPUMP which determines the pumping rate of ions per unit volume in the Nd:YAG rod side-pumped by a laser-bar. This contour plot was obtained with the parameters shown in table 4.X. This contour plot was made to have the same 100  $\mu\text{m}$  resolution as the experimentally determined plot of the pumping rate distribution by using the program COARSE.

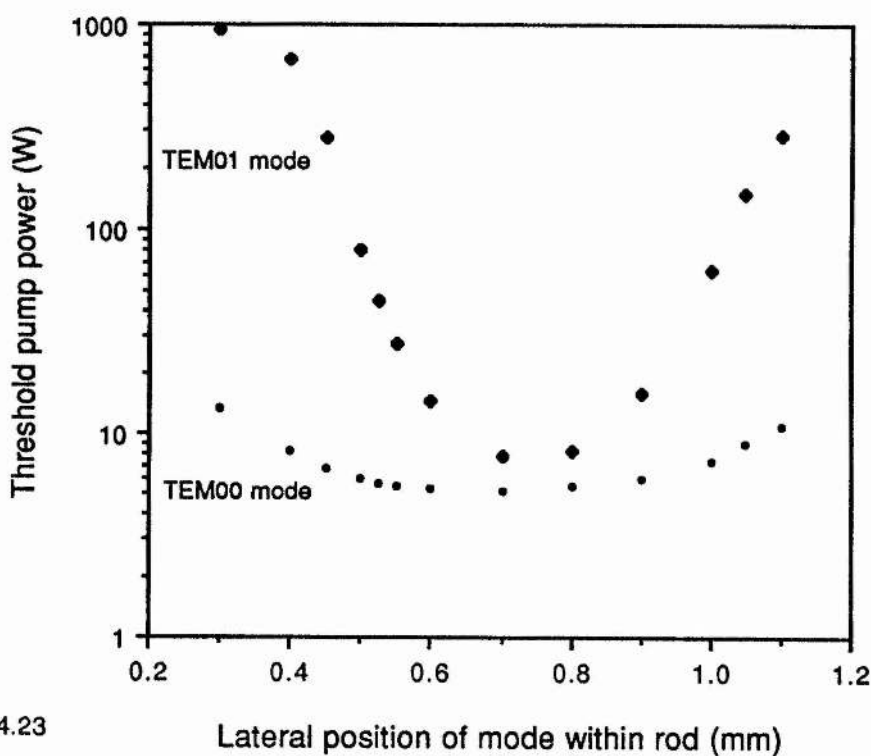


Figure 4.23

Thresholds for the TEM<sub>00</sub> and TEM<sub>01</sub> modes modelled by the program OVERLAPD as a function of lateral position of the mode within the rod with respect to the edge of the rod adjacent to the laser bar. The parameters used for this figure are those given in tables 4.1 and 4.3, but for a mode radius of 420  $\mu\text{m}$  and an output coupling mirror of 90% reflectivity. The experimental findings for this laser were in qualitative agreement in that the laser would only operate in the fundamental mode when the mode was centred either close to the laser bar, or towards the back surface in which case the output power was diminished. This indicates that the Nd:YAG laser is being used to aperture the higher order transverse modes.

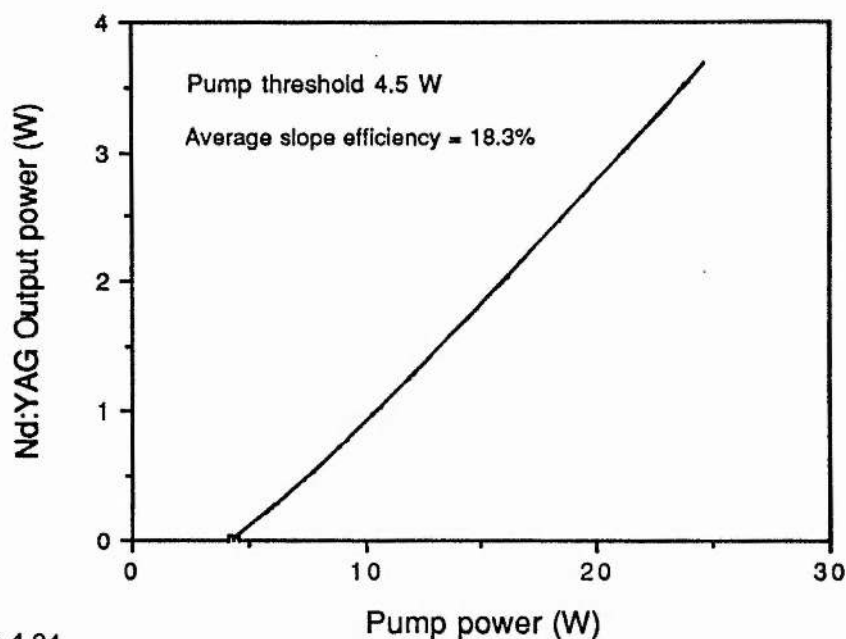


Figure 4.24

TEM<sub>00</sub> output power obtained from the OVERLAPB program. This indicates that one might expect the slope efficiency from the transversely pumped laser to be slightly non-linear at pump power levels well above threshold. This non-linearity is due to the asymmetric pump volume which reduces the saturation of the gain at low pump powers. The experimental measurements of the output power against input power were not sufficiently precise to confirm this finding.

## Chapter 5

### Q-switching of holosteric Nd:YAG lasers

---

#### 5.1 Introduction

Q-switching is a process whereby the energy storage capacity of laser materials with long upper-state lifetimes of typically greater than 100  $\mu\text{s}$  is utilised to create relatively short optical pulses of around 20 ns duration and of high peak power [5.1]. The potential for Q-switching of flashlamp pumped solid-state lasers was realised at an early stage, and it was a natural progression for this technique to be applied to diode-pumped lasers [5.2,5.3]. As laser-diodes have short upper-state lifetimes of around a nanosecond, Q-switching of laser-diodes themselves is neither useful nor practical.

A listing is given in this chapter of the considerations necessary for good pumping and extraction efficiency of a diode-laser pumped Q-switched Nd:YAG laser along with a description of the acousto-optic and electro-optic Q-switching mechanisms that were exploited in this work. Two acousto-optic and one electro-optic Q-switch were used during this project, and their characteristics are given in the appendix to this chapter.

Repetitive Q-switching was applied in the first instance to the longitudinally cw diode-pumped Nd:YAG laser that is described in chapter 3. A key component of this chapter is the Q-switching of the transversely pulse-pumped Nd:YAG laser described in chapter 4, and a full characterisation of the dependence of the output power on pump power shows the well-behaved nature of this laser. An analysis of the frequency characteristics of this laser preceded the use of the stabilised single-frequency cw holosteric laser for injection seeding which resulted in high quality Q-switched pulses in a single-longitudinal and single transverse mode. To satisfy the sometimes

conflicting demands of single transverse mode and good extraction efficiency from the transversely pumped laser using an acousto-optic Q-switch proved difficult, and the alternative scheme involving an electro-optic device was adopted. This was more appropriate to the high powers from this laser.

### 5.1.1 Pumping interval

It is necessary during the pumping interval that there is sufficient intracavity loss introduced into the cavity to prevent the onset of lasing. This state of low intracavity flux due to low Q allows the build up of a large population inversion in the Nd:YAG gain medium. Once the cavity loss is removed such that a high cavity Q is restored, the large gain available results in the population inversion being extracted in pulses of high peak power and durations that are typically 20 ns. An illustration of the temporal evolution of a Q-switched pulse with regard to loss, population-inversion and optical flux is given in figure 5.1.

The first part of the Q-switching process is the pumping interval, in which the Q-switch prevents the oscillation of flux within the cavity. During the pumping interval a population inversion builds up from zero to approach a maximum asymptotically. The instantaneous population inversion is given by,

$$N(t) = R_p \tau_2 \left( 1 - \exp\left(-\frac{t}{\tau_2}\right) \right), \quad (5.1)$$

where  $R_p$  is the pumping rate into the upper laser level and  $\tau_2$  is the upper-state lifetime. This instantaneous population inversion when plotted for Nd:YAG as a function of the pumping interval is illustrated in figure 5.2. Once the population inversion approaches its maximum,  $N_{\max} = R_p \tau_2$ , further pumping has a minimal effect upon the inversion as the rate of increase in population inversion is close to the rate of decrease in population due to spontaneous emission.

The reduction in the population inversion due to spontaneous emission can be characterised by the fluorescence efficiency,  $\eta_f$ . This is the ratio of the total number of ions that remain excited at the end of the pumping interval,  $N_i$ , to the number of ions that have been excited during the pumping interval,  $N_p$ ,

$$\eta_i = \frac{N_i}{N_p} = \left( \frac{1 - \exp(-T_p/\tau_2)}{T_p/\tau_2} \right). \quad (5.2)$$

The fluorescence efficiency which is plotted for Nd:YAG in figure 5.2 as a function of pumping interval, shows that 67% of the excited ions remain so at the end of a 200  $\mu$ s pumping interval. A comparison between the curve for fluorescence efficiency and that for population inversion shows that the goal of maximum Q-switched pulse energy is necessarily achieved at the expense of pumping efficiency.

## 5.2 Acousto-optic Q-switching

Acousto-optic (AO) devices are well suited as Q-switches in low gain lasers as the amount of passive loss they present to the cavity is small. They are particularly suitable for the Q-switching of continuously pumped lasers, as they may be operated at repetition rates of several kilohertz. An additional feature of acousto-optic devices is that the drive circuitry operates at low voltages, which is in contrast to electro-optic Q-switches which operate at potentials above a kilovolt.

In a laser using an acousto-optic Q-switch, the high-loss/low-Q state is achieved by the creation of a phase-grating within the cell which diffracts optical flux from the cavity. This phase-grating is created by the application of a radio frequency acoustic wave to a piezo-electric transducer which induces an acoustic strain field in the normally transparent material. Acousto-optic Q-switches are normally single-pass devices which have an absorber such as lead at the opposite side of the Q-switch from the transducer that prevents the reflection of the acoustic wave. The acoustic strain field is coupled into a modulation of the refractive index of the material via the photoelastic effect. The



effect of the sinusoidal refractive index grating is to diffract light incident on the grating when the Bragg condition is met. That is, when

$$m\lambda = 2\Delta \sin\theta , \quad (5.3)$$

where  $m$  is the order of diffraction,  $\lambda$  is the optical wavelength in the material,  $\Delta$  is the period of the acoustic wave in the material, and  $\theta$  is the angle for the diffracted light.

Two acousto-optic Q-switches were employed at different times in this work: these were a Newport N30027-FS10 and an Isle-optic QS080, and are described in the appendix. Both of these were operating in the Raman-Nath regime causing the transmitted light to be diffracted into several orders. The angular dispersion of the diffracted light is not important with regard to Q-switching, and it is only the fraction of the incident light diffracted from the zero order,  $\eta_{\text{diffraction}}$ , that is of concern. It was found experimentally, as described in section 5.4.1, that the gain from the transversely pumped laser was such that the 15% diffraction efficiency of the Newport Q-switch was insufficient to achieve hold-off when the reflectivity of the output coupler was greater than 80%. This necessitated its replacement with the Isle-optics device which had a diffraction efficiency of greater than 45%.

After a large population inversion has developed in the laser material, the rf drive-signal is switched off, and the Q-switch returns to a state of high optical transmission. This provides the conditions necessary for lasing to occur. As the laser is then well above threshold with a large amount of stored energy a short pulse with high peak power can develop [5.6]. It is essential that the Q-switch opens in a time shorter than that for the flux to build up in the cavity to a significant level, to prevent the residual loss from attenuating the emerging pulse. For the second cavity configuration of the transversely pumped holosteric laser it is shown in section 5.4.2.b that the minimum pulse build-up time was 130 ns. Consequently the two cavity configurations for the acousto-optic Q-switched lasers were designed to have relatively small beam radii of 110  $\mu\text{m}$  and 145

$\mu\text{m}$  in the AO Q-switches, which correspond to Q-switch opening times of  $\sim 70$  ns and 90 ns respectively.

---

### 5.3 Repetitive acousto-optic Q-switching of cw-pumped laser

Acousto-optic Q-switches have low insertion loss and high switching rates so they are well suited to use in cw diode-pumped lasers which exhibit low gain. Nd:YLF lasers are commercially available with peak output powers of 2 kW at pulse repetition rates of 1 kHz [5.4], and have applications in micromachining, surgery and second-harmonic generation. These lasers are likely to be eclipsed shortly in the laser market by a Q-switched Nd:YLF laser which will produce pulses with 30 kW peak power at 1 kHz [5.5].

As a preliminary experiment to Q-switching of the laser-bar pumped Nd:YAG laser, the longitudinally pumped laser described in chapter 3 was Q-switched by the Newport AO device (described in the Appendix). The cw diode-pumped laser cavity was lengthened to  $\sim 8$  cm to allow the insertion of the Q-switch component. The cavity was completed by an output coupler which had a radius of curvature of 10 cm and reflectivity 98-99%, as shown in figure 5.3. When pumped with 100 mW from the fibre-coupled SDL-2430-H2 laser-diode, the low output coupling was such that the 15% loss induced by the Q-switch was insufficient to prevent lasing when the Q-switch was in its high loss state. On the reduction of the pump power to 50 mW, pulses with energy of  $1.8 \mu\text{J}$  and 86 ns FWHM duration were produced at a repetition rate of 1 kHz. The pulse peak power of 21 W which this represents, is considerably less than the lower repetition pump pulsed Q-switched lasers described later in this Chapter.

It is worth noting that for repetitively Q-switched lasers, the maximum energy per pulse and also the maximum peak power occurs at a low pulse repetition rates, whilst the maximum average power occurs at high repetition rates and that an approximate value for the cross-over repetition rate between these regimes is 1 kHz for Nd:YAG.

## 5.4 Synchronised AO Q-switching of pulse-pumped laser

The attainment of high peak power pulses from a holosteric laser required the application of the Q-switching technique to the transversely pumped Nd:YAG lasers described in Chapter 4. The SDL-922-J laser-diode-bar pump source emitted pulses of 200  $\mu\text{s}$  in duration which resulted in a fluorescence efficiency of 67%, as described in section 5.1.1. With a peak pump power of 25 W, the laser-bar offered the potential for pumping well above threshold with commensurately high extraction efficiencies as discussed in section 5.4.2.b.

### 5.4.1 Initial cavity configuration

The pulse-pumped Q-switched laser configuration that was initially constructed was adapted from the transversely pumped free-running laser shown in figure 4.3. This involved lengthening the cavity to 19 cm, such that focussing in the cavity supported a wide difference in mode-sizes along the cavity. In this cavity, which is shown in figure 5.4, the Newport Q-switch was inserted at a point where the beam waist was just 110  $\mu\text{m}$ . For this beam waist, the Q-switch opening time was  $\sim 70$  ns, which was comfortably less than the measured pulse-build up time of 130 ns.

In the Nd:YAG rod the cavity mode waists were 230  $\mu\text{m}$  in the vertical plane and 420  $\mu\text{m}$  in the horizontal plane. It was anticipated that operating the laser in a Q-switched mode rather than in a long-pulse mode might make the laser more inclined to operate on a higher order transverse mode. This did not prove to be the case, and the good overlap between the pump volume and the fundamental mode volume, together with the aperture provided by the Nd:YAG rod itself, acted to ensure that the laser operated in a  $\text{TEM}_{00}$  mode.

It was not possible to achieve stable Q-switched operation when the reflectivity of the output-coupler was increased above 80%, as the 15% loss provided by the Newport Q-

switch would not prevent lasing during the pumping interval. With the 80% reflectivity output-coupler the average power from the laser when operating at 100 pps was 26 mW, which is equivalent to 0.26 mJ per pulse. These pulses were detected by a BPW28 photodiode and monitored by an Hewlett-Packard HP54111D oscilloscope, and the recorded data indicates that the pulses were of  $37 \pm 2$  ns duration (FWHM), corresponding to peak powers of about 7 kW. No optical damage was observed on the Q-switch element even with the optical flux density at  $\sim 100 \text{ MWcm}^{-2}$  which was twice the specified damage limit of the device.

#### 5.4.2 Second cavity configuration

In the second Q-switched laser cavity configuration the Nd:YAG rod with facets cut at Brewster's angle was replaced with one which had anti-reflection coated faces parallel to the cavity axis. A result of this was that the cavity mode volume within the rod was transformed from elliptical to circular. In order to maintain single transverse mode operation it was necessary to change the mirror geometry such that the cavity mode waist in the plane that was parallel to the pump direction matched the pump depth in this plane. It was also necessary to maintain a small beam waist within the cavity at a position accessible for the acousto-optic Q-switch.

The solution was an almost hemispherical cavity with a mirror of 10 cm ROC, as shown schematically in figure 5.5. This had a circular mode within the rod with a beam radius of  $420 \mu\text{m}$ , and a waist size at the plane mirror of  $150 \mu\text{m}$ . This resulted in a Q-switch opening time of 90 ns, which is necessarily less than the pulse-build up time of around 130 ns. As the waist size at the plane mirror becomes increasingly small as the cavity is lengthened towards the stability condition, care was required in choosing the length of the cavity so as to prevent optical damage to the plane mirror.

#### 5.4.2.a Transverse mode structure

As with the free-running transversely pumped laser, operation in the fundamental transverse mode, and the suppression of higher order modes, was a prime consideration. For all of the transversely pumped laser configurations that were studied, this was achieved by implementing resonator designs that gave the optimum beam waist within the rod, combined with self-aperturing by the laser-rod to ensure that the TEM<sub>00</sub> has lower clipping loss than next higher-order transverse mode.

It was anticipated that operation of the Q-switched laser in a single transverse mode would be more difficult than for the long-pulsed laser as there would be less time for the dominant mode to saturate the gain. In addition, the undepleted gain in the wings can encourage higher order modes to oscillate some time after the start of lasing of the fundamental mode, resulting in dynamic changes in the output beam profile. These fears proved to be unfounded, and the combination of matching the cavity mode to the pumped region close to the diode and using the clipping loss of the TEM<sub>01</sub> mode by the Nd:YAG rod to suppress higher order modes proved effective. Fundamental mode operation in the vertical plane occurred routinely without consideration of the mode volume or its position within the cavity.

#### 5.4.2.b Output power characterisation

Despite the high intensities and short pulses obtained from Q-switched lasers, useful results can be obtained from a simple rate-equation model. The basic rate equations for instantaneous population inversion  $N(t)$  and the flux intensity  $I(t)$  are given by,

$$\frac{dN(t)}{dt} = R_p - \frac{N(t)}{\tau_2} - c\sigma_s N(t) I(t) , \quad (5.4)$$

$$\frac{dI(t)}{dt} = c\sigma_s N(t) I(t) - \frac{I(t)}{\tau_{cav}} , \quad (5.5)$$

where  $R_p$  is the pumping rate per unit volume,  $\tau_{cav}$  is the cavity decay time, and  $\sigma_s$  is the stimulated emission cross-section. A solution for the pulse envelope of a Q-

switched laser cannot be derived analytically and must therefore be obtained by numerical techniques. However, expressions for the key characteristics of a Q-switched pulse may be derived from the above equations by combining them to eliminate the temporal dependence. This is done in Siegman's treatment, and the derivation for all the following expressions may be found there [5.6].

### Pulse build-up interval

When the cavity Q is switched, there are almost no photons within the cavity, so that there is a short but finite time interval before the pulse occurs. This is the pulse build-up time,  $T_b$ , which is arbitrarily defined to be the time between the opening of the Q-switch, at which time a few photons contribute towards the flux intensity  $I_i$ , and the time when the flux has reached a level that is equivalent to the steady state flux intensity,  $I_{ss}$ . The relationship between the pulse build-up time and the rate of pumping above threshold is given by,

$$T_b = \frac{\tau_{cav}}{(r-1)} \ln\left(\frac{I_{ss}}{I_i}\right) \quad (5.6)$$

where  $r$  which is the ratio of the inversion at the end of the pump interval to the threshold pump inversion which is also equivalent to the ratio of the pump energy to the threshold pump energy under the same conditions.

$$r = \frac{N_i}{N_T} = \frac{E_i}{E_T} \quad (5.7)$$

The ratio between the flux intensity  $I_i$  when the Q-switched is opened to the steady flux intensity  $I_{ss}$ , is typically around  $10^{-10}$ , so the pulse build-up time may be approximated to,

$$T_b \approx 25 \frac{\tau_{cav}}{(r-1)} \quad (5.8)$$

For the Q-switched laser in the second cavity configuration, the pulse build-up time is plotted in figure 5.6 as a function of the pumping energy. This was measured from the instant the trigger pulse was delivered to the drive unit, and as such it is substantially



longer than the true pulse build-up time. When the pulse build-up time is plotted against  $1/r-1$ , it can be seen from the extrapolation of the graph that the true pulse-build up time is 130 ns when the laser is pumped 2.2 times above threshold. In addition the slope of the straight line fitted through the points in figure 5.7 shows that the cavity decay time is  $\sim 5$  ns, which corresponds to a parasitic round trip loss of 9%.

### Pulse energy

The total energy delivered to the Q-switched pulse is the difference between the energy stored in the population inversion before the Q-switch is opened, and the energy remaining in the inversion after the pulse. This can be expressed as,

$$E = N_T h\nu V \eta_e r, \quad (5.9)$$

where  $V$  is the pumped volume, and  $h\nu$  is the energy of a lasing photon and  $\eta_e$  is the extraction efficiency, which is itself a function of the rate of pumping above threshold.

$$r = \frac{-\ln(1-\eta_e)}{\eta_e} \quad (5.10)$$

The solution to this equation is given graphically in figure 5.8 and shows that the laser must be pumped at around 5 times above threshold for an extraction efficiency close to 100%.

The energy per pulse from the laser was obtained from a measurement of the output power from the laser with a Scientech power meter. Division of this measured power by the pulse repetition rate of 100 pps gives the pulse energy as plotted in figure 5.9 as a function of the pump energy. The slope of the graph of pulse energy against  $r\eta_e$ , which is given in figure 5.10, shows that  $Vh\nu N_T = 0.24$  mJ, which gives a threshold population inversion of  $8.3 \times 10^{13} \text{ cm}^{-3}$ .

### Pulse duration

The pulse durations of the Q-switched pulses were measured with a BPW28 photodiode and a Hewlett-Packard HP54111D oscilloscope, and are shown as a function of pump energy in figure 5.11. Pulse duration is related to the pumping rate above threshold by the following expression,

$$\tau_p = \frac{r\eta}{r-1-\ln(r)} \tau_{cav} . \quad (5.11)$$

The plot of the pulse duration as a function of  $\frac{r\eta}{r-1-\ln(r)}$  which is given in figure 5.12 confirms the cavity decay time as 5.1 ns.

### Peak power

Values for the peak power of the Q-switched pulses were determined by division of the pulse energy by the pulse duration, and are shown in figure 5.13 as a function of pump pulse energy. The relationship between the peak power and the pumping rate above threshold is given by,

$$P_p = \frac{Vh\nu N_T}{\tau_{cav}} (r - 1 - \ln(r)) . \quad (5.12)$$

The good linearity of the peak power when plotted as a function of  $(r - 1 - \ln(r))$  in figure 5.14 highlights the well-behaved nature of this laser.

Because the laser was operating at a maximum of only 2.2 times above threshold, greater extraction efficiency and consequently higher output power could be achieved if this laser was pumped further above threshold. To this end, the 80% reflectivity output coupler was replaced with one of 90% reflectivity. This had the unfortunate consequence that the damage threshold for the coatings on the Isle-Optics acousto-optic Q-switch were exceeded. This occurred at a power density of around 100 MWcm<sup>-2</sup>, which was 20 times the manufacturers' stated maximum. It was not possible to move the Q-switch to a position in the cavity with a larger beam waist as the opening time of

the Q-switch had to be less than the pulse build up time. This constraint imposed by the optical damage limit was a prime motivation behind the later adoption of electro-optic Q-switching as the mode size in an electro-optic Q-switch does not affect its switching time. As it is envisaged that a number of laser bars will be used in a subsequent transversely pumped laser to increase the output power, the use of an electro-optic Q-switch becomes imperative.

#### 5.4.2.c Longitudinal mode structure

To measure the longitudinal mode structure of this laser, the static plane parallel interferometer described in chapter 4.3.3 was used. The results from this interferometer take the form of an interference pattern that was recorded by a frame-store based imaging system that was controlled by an Archimedes computer. A typical single shot interference pattern is shown in figure 5.15. This shows that in the absence of any longitudinal mode control the laser operated on around 10 cavity modes. Each laser mode was not necessarily oscillating on each shot, but came in and out almost at random. The bandwidth covered by these modes was calculated from the free-spectral range of the interferometer to be  $\sim 25$  GHz.

#### Injection-seeding

A common technique to obtain single longitudinal mode operation is to include one or more etalons within the laser cavity to provide additional loss for all but the centremost mode. This is less successful for Q-switched lasers than for cw lasers, as the intracavity flux makes fewer round-trips so there is less time for the dominant mode to saturate the gain. For this reason, the approach taken to achieve single longitudinal mode was injection seeding, in which one longitudinal mode received additional flux during the pulse build-up interval [5.7]. This involved injecting the narrow linewidth flux from a single longitudinal mode laser into the Q-switched laser cavity at a frequency close to that of a longitudinal mode of the Q-switched cavity. As this mode

saturates the available gain, the pulse builds up in this mode preferentially over the other modes which must build up from optical noise.

It is worth highlighting the difference between injection seeding and injection locking. In the former, the injected signal provides one of the modes of the slave laser with additional flux at the start of the pulse and the pulsed laser oscillates at its own frequency. There is no phase relationship between the modes in the two lasers. In the latter, the injected signal dominates the slave cavity entirely such that the output from the slave is phase-locked with respect to the master. Injection locking, for the most part has been achieved with cw lasers, though it has also been shown to be applicable to Q-switched CO<sub>2</sub> lasers [5.8].

The experimental arrangement for injection seeding is shown schematically in figure 5.16. The injection seeding laser which is described in detail in chapter 3 consisted of a miniature Nd:YAG rod that was longitudinally pumped by a fibre-coupled laser-diode array. The cavity was formed by a dichroic coating on the Nd:YAG rod and by a 10 cm ROC 1.5% T output coupling mirror. A quartz etalon and a plate at Brewster's angle were introduced into the cavity to constrain the laser to operate on a single-longitudinal-mode. The short-term linewidth was 40 kHz, and the long-term frequency drift was minimal as the laser was locked to the transmission peak of a confocal Fabry-Perot interferometer.

A number of different arrangements for coupling the cw seeding laser into the pulsed laser cavity were evaluated, but the most convenient configuration was the injection seeding of the 0.2 mW of cw radiation through the nominally high reflectivity mirror of the pulsed laser cavity via suitable mode-matching optics and a Faraday isolator. The length of the cavity of the Q-switched laser was controlled via the piezo-ceramic mounting for one of its mirrors. The cavity length of this laser was adjusted to match the frequency of one mode of the pulse-laser to that of the injecting beam. The pulsed laser was then induced to operate on a single longitudinal mode as seen by the

transmission characteristic of the Fabry-Perot interference given in figure 5.17. Seeding the laser in this way proved to be both straightforward and reliable.

### Self injection seeding

An alternative technique that was examined for achieving a single longitudinal mode Q-switched laser was self injection seeding. This technique involves adjusting the intracavity loss introduced by the Q-switch such that at the end of the pumping interval the laser is oscillating just above threshold. This introduces flux of a single-longitudinal mode into the cavity, that will saturate the gain more effectively on the opening of the Q-switch than the other modes which must build up from noise.

Self-injection seeding was achieved in the cavity shown in figure 5.5 using the Isle-Optics Q-switch which had its hold-off adjustable via the rf power supply. Typical values for the normal and the self-injection seeding bandwidths were 20 GHz and 2 GHz respectively, with the laser occasionally operating on a single longitudinal mode. To reduce the effect of spatial hole burning on the generation of additional modes, a twisted cavity mode laser was adopted. The AR coated Nd:YAG rod was placed between a pair of quarter wave plates so that flux passing through the rod was circularly polarised. This prevented a standing wave from forming in the gain medium with nodes at which undepleted gain might encourage alternative longitudinal modes. The change to the twisted mode cavity resulted in more reliable self-injection seeding, though it was still not wholly satisfactory as the Q-switch was not guaranteed to open at the instant at which the seeding flux was circulating within the cavity.

More effective self-injection seeding is achievable through the use of an electro-optic Q-switch allied to a photo-diode to monitor the instant at which the Q-switch should be opened. The result of pumping the laser just above threshold is that the laser operates on a small gain switched spike or relaxation oscillation. To achieve effective self-

seeding the Q-switch must be opened at the instant at which the self-seeding flux is at its maximum which necessitates the use of a fast Q-switch.

#### Effect of seeding on pulse profile

Further examination of the longitudinal mode structure and the effect of injection seeding involved looking in detail at the temporal evolution of the Q-switched pulses. The three aspects of the pulse envelope that were studied were high-frequency amplitude modulation, average pulse amplitude and the build-up time for the pulse with respect to the opening of the Q-switch.

Mode-beating between longitudinal modes manifests itself in an amplitude modulation on the pulse profile at the difference frequency between the modes. If there are only two longitudinal modes this modulation is sinusoidal whereas a more complex profile results from the presence of more than two modes, though the underlying modulation remains at the difference frequency.

The pulse envelope for an unseeded laser which is running on several longitudinal modes is shown in figure 5.18. The intermode frequency was 684 MHz which corresponds to an effective cavity length for the cavity of 21.9 cm. Measurement of this effect required the full  $2 \text{ Gbits}^{-1}$  sampling rate of the Hewlett Packard 54111D digital oscilloscope. When seeded the modulation disappeared, and the smooth temporal profile of a single-longitudinal-mode Q-switched pulse was obtained as shown in figure 5.19. The measurement of the amplitude stability of these pulses was limited by the noise of the detector to be better than  $\pm 6\%$  over 100 pulses as shown by figure 5.20.

The effect of injection seeding upon the temporal response of the Q-switched pulses is also evident in the reduction in the pulse build-up time. A number of consecutive pulses were stored using the digital oscilloscope as the laser was injected seeded, and are shown in figure 5.21. This shows that for a remarkably low injected power of 165



nW there was a reduction in the pulse-build up time of 45 ns between the unseeded pulses and the seeded pulses.

Also evident from figure 5.21 is the reduction in total energy within the Q-switched pulse with the unseeded pulses and seeded pulses having energies of 0.36 mJ and 0.25 mJ, which corresponds to a seeding efficiency of 70%. The reduction in output energy was due to spatial hole burning within the Nd:YAG medium which left a fraction of the total gain which could not be accessed by a single standing-wave cavity mode. To overcome this, a pair of quarter-wave plates were placed at either side of the Nd:YAG rod to convert the laser into a twisted-mode configuration. This encouraged the total extraction of the energy within the Nd:YAG rod after seeding, but the power in the seeded pulse remained the same as that for the standing-wave cavity because the inclusion of the two quarter-wave plates had introduced intracavity losses.

The dependence of the pulse build-up time upon the power in the cw seeding laser was examined experimentally, and the results are shown in figure 5.22. Injection seeded pulses appear at a shorter time after opening the Q-switch because the pulses built up from the injected signal rather than noise. The relationship between the level of initial intracavity flux and the pulse build-up time has been shown to be [5.6],

$$T_b = \frac{\tau_{cav}}{(r-1)} \ln\left(\frac{I_{ss}}{I_i}\right) . \quad (5.13)$$

$I_{ss}/I_i$  is the ratio between the flux intensity  $I_i$  when the Q-switched is opened to the steady flux intensity  $I_{ss}$ .

A servo-loop arrangement based upon the pulse build-up time [5.9] may be used to lock the pulsed-cavity resonance to the cw oscillator. In practice, the stability of the holosteric system was sufficient that only occasional adjustment of the pulsed cavity length was necessary to maintain effective seeding. With 0.2 mW from the seeding laser incident on the 0.02% transmitting mirror of the pulsed laser, the detuning tolerance was approximately  $\pm 150$  MHz.

### 5.5 Electro-optic Q-switching of pump-pulsed laser

In the work of the previous sections on Q-switched diode-pumped lasers acousto-optic devices were used. These offered the advantages of low switching voltage, low insertion loss and high repetition rate. However, optical damage proved to be a serious problem which could only be alleviated through the use of an electro-optic Q-switch in which the mode waist may be larger, and for which the optical power density is correspondingly lower. The Lasermetrics electro-optic Q-switch that was chosen is detailed in the Appendix. This  $\text{LiNbO}_3$  device had a maximum repetition rate of 1.5 kHz, which was more than adequate as the pump laser-bars had a maximum repetition rate of 100 pps. Though the device was specified to have low loss of  $<1\%$  per pass, care was necessary to minimise the losses from the Pockels cell/polariser combination and to obtain extraction efficiencies comparable with acousto-optic Q-switching.

A schematic of the electro-optically Q-switched laser which was set-up in the quarter-wave design is shown in figure 5.23. The polariser acts to ensure that only linearly polarised light that is oriented at  $45^\circ$  to the axes of the Pockels cell may circulate within the cavity, and to direct orthogonally polarised light from the cavity. During the pumping interval, an electric field is applied to the Pockels cell to introduce a quarter wave retardation between the orthogonal components of the incident beam. The application of the quarter-wave-voltage converts the linearly polarized light into circularly polarized upon a single pass through the Q-switch. Upon reflection by the cavity mirror, this circularly polarized light returns through the Q-switch to exit with a linear polarization that is perpendicular to the original direction. This light is then ejected from the cavity by the polariser, and the cavity is in its high loss, or low Q state.

At the end of the pumping interval, the voltage is switched to zero in  $<10$  ns. In the absence of a transverse field, the uniaxial Pockels cell has the same refractive index for both orthogonal polarizations of the incident beam. Hence, when there is no voltage

applied to the Q-switch, the incident beam is unaltered, and the cavity is in a state of low loss and high Q. This switch in the Q of the cavity causes a rapid build up of cavity flux from the large stored population inversion, which exits through the output coupler as a short intense pulse.

### 5.5.1 Cavity configuration

As with the other transversely pumped lasers, to obtain operation of the electro-optically Q-switched laser in a single transverse mode it was necessary that there should be a good overlap between the cavity mode volume and the pump volume. Since electro-optic Q-switches do not require the tight focus that is necessary in acousto-optic Q-switches, this constraint on the cavity configuration was removed. This allowed the cavity configuration shown in figure 4.7 that was used to obtain a  $TEM_{00}$  mode in free-running mode to be adapted for use in the electro-optic Q-switched laser. Fundamental transverse mode operation was achieved by having a plane output coupler and a high reflector of 1 m ROC that were separated by ~20 cm, as shown in figure 5.23. This made the beam radius 450  $\mu\text{m}$  within the Nd:YAG rod. It was found that on lengthening the cavity further, single transverse mode operation was maintained but at reduced output power.

As there was no limitation imposed on the reflectivity of the output coupler by hold-off problems or optical damage, an output coupler with 90% reflectivity was chosen. Operating free running with and without the polariser the output energy was 0.48 and 0.40 mJ respectively when pumped by 5 mJ. Upon Q-switching the maximum pulse energy in the  $TEM_{00}$  mode was 0.32 mJ, which in a pulse of 48 ns duration corresponds to a peak power of 6.7 kW. The increased output power that was envisaged by pumping further above threshold was not observed as this was negated by the reduced output coupling efficiency.

As for the acousto-optically Q-switched laser, the output energy and the pulsewidth were measured as a function of pump energy, with the analysis showing a round-trip parasitic cavity loss of 10%. As was shown in chapter 4, the intracavity loss for the side-pumped system is around 3.5%, due in part to aperturing by the laser rod. To reduce the remaining loss, an etalon mounted in the cavity at Brewster's angle was used instead of the polariser. This increased slightly the Q-switched pulse energy to 0.34 mJ, but the pulses suffered from prelasing as the Brewster plate provided insufficient hold-off. Subsequent examination of the polarizer by a probe beam at 1.064  $\mu\text{m}$  showed the polarizer presented a round trip loss of 6%, and as such is largely responsible for the high overall parasitic loss in the electro-optically Q-switched laser.

### 5.5.2 Cavity dump Q-switching

A technique that is currently being tackled is the use of cavity-dump Q-switching to generate shorter optical pulses with commensurately higher peak power [5.10]. Alternatively called transmission-mode Q-switching, this technique involves using the electro-optic Q-switch to dump the flux out of the side of the cavity when the pulse has built up to a maximum. The first advantage of cavity-dump Q-switching over conventional Q-switching is that through the use of a high-reflector "output-coupling" mirror, the laser will be operating higher above threshold and, as such, the rising edge of the Q-switched pulse is shortened. Cavity-dump Q-switching also shortens the tail of the optical pulse as the cavity decay process no longer acts as a limit on the time required to extract intracavity flux.

Of the alternative cavity configurations for cavity-dump Q-switching, the one that has been selected is shown in figure 5.24. During the pumping interval both terminals are high at the  $\lambda/4$  voltage, such that the retardation introduced by the  $\lambda/4$  plate acts along with the polariser to put the laser in a state of low-Q and inhibit oscillation. Upon switching one of the terminals to ground via a chain of avalanche transistors, the  $\text{LiNbO}_3$  cell will act as a quarter-wave plate and allow the build-up of oscillation within

the cavity. At the peak of the optical pulse, the other terminal is switched to ground in less than 4 ns, so causing the flux to be ejected from the cavity. It is envisaged that when the conventionally Q-switched laser described in this chapter is adapted to cavity dump Q-switching, the pulse duration and the peak power will be around 5 ns and 50 kW respectively. Conversely, the extraction of the flux from the cavity can be controlled through a feedback loop to the electro-optic Q-switch to obtain pulses of up to around 1  $\mu$ s which have lower peak power [5.11].

---

## 5.6 Conclusions

The use of acousto-optic Q-switches in holosteric lasers was extended in this work from longitudinally cw pumped lasers to quasi-cw transversely pumped lasers, from which optical pulses with peak powers of up to 15 kW were obtained. Acousto-optic devices were in the first instance chosen in preference to electro-optic Q-switches because it was considered that their lower insertion loss was a significant advantage. This advantage was found to be marginal, and that the peak power achieved from the transversely pumped laser was restricted by the capabilities of acousto-optic devices.

It had been a concern that whilst Q-switching the transversely pumped laser the achievement of single transverse mode would prove to be more difficult than was the case when the laser was free-running. This fear proved unfounded, and single transverse mode Gaussian-profile pulses were achieved. An examination of the longitudinal mode structure showed that the number of longitudinal modes oscillating was adversely effected by Q-switching. To induce the laser to operate on a single longitudinal mode this laser was injection seeded, which proved straightforward and effective.

The use of an electro-optic Q-switch eliminated the problem of optical damage to the Q-switch as it allowed the cavity mode size to be enlarged in the Q-switch. In addition, as electro-optic Q-switches have more hold-off than acousto-optic devices, they are the

necessary option for holosteric lasers that are pumped by a larger number of laser-bars. Furthermore, the fast switching time of the electro-optic device of around 4 ns should permit cavity-dump Q-switching, as well as pulse-lengthening and effective self-injection seeding.

In summary, a table of the relative efficiencies of the acousto-optic and electro-optically Q-switched lasers is given below in Table 5.1. Based on these figures, the modelled results show that an increase in the pump power to 240 mJ would result in significant increases in the efficiencies of absorption, extraction and output coupling, with a predicted overall optical conversion efficiency of 17%. The results recently obtained by Fibertek for an injection seeded electro-optically Q-switched oscillator pumped by 400 mJ which are also shown in the Table demonstrate the feasibility of this level of performance



Efficiency	Single 5 mJ pump		240 mJ pump	400 mJ pump (Fibertek) <sup>1</sup>
Pump Fresnel-coupling	0.90 <sup>2</sup>		0.85 <sup>3</sup>	0.95
absorption in Nd:YAG	0.61 <sup>4</sup>		0.87 <sup>5</sup>	0.90
pump/mode overlap	0.65 <sup>6</sup>		0.75 <sup>7</sup>	0.80
Nd:YAG Stokes shift <sup>8</sup>	0.76			
quantum defect <sup>9</sup>	0.95			
fluorescence decay <sup>10</sup>	0.67			
Output Q-switch extraction <sup>11</sup>	AO 0.76 <sup>12</sup>	EO 0.80 <sup>13</sup>	0.98 <sup>14</sup>	0.50 <sup>18</sup>
output coupling	0.68 <sup>15</sup>	0.50 <sup>16</sup>	0.94 <sup>17</sup>	
injection seeding	0.69 <sup>19</sup>	not-seeded	0.69 <sup>20</sup>	
Calculated optical efficiency	6.1 %	6.9 %	17.1 %	16.5 %
Calculated output energy	0.30 mJ	0.35 mJ	40.8 mJ	66 mJ
Experimental efficiency	4.8 %	7.0 %		18.7 %
Experimental output energy	0.25 mJ	0.36 mJ		75 mJ

Table 5.1 Summary of diode-pumped Q-switched efficiency

- <sup>1</sup> Modelled efficiencies given for Fibertek system are those presented by Fibertek at an MOD colloquium for a total pump energy of 800 mJ. Experimental efficiencies, were presented for a pump energy of 400 mJ in paper CMF3 at CLEO 90.
- <sup>2</sup> This value was obtained from the SIDEPUmp program (chapter 4) for Fresnel coupling loss for uncoated Nd:YAG and a diverging source.
- <sup>3</sup> An increased value of Fresnel-coupling loss is given to take into account loss from concentric flow cooling tubes.
- <sup>4</sup> Value obtained from the SIDEPUmp program (chapter 4) for a 1.5 mm diameter rod, with an experimentally determined absorptivity of 0.52 mm<sup>-1</sup> and 30% reflection from the back face of the rod.
- <sup>5</sup> This approximate value for the absorption efficiency, is the single-pass percentage absorption for 4 mm of laser medium and pump light absorptivity of 0.52 mm<sup>-1</sup>. Less control of the laser-diode temperature will reduce the absorptivity, such that consideration may be given to a rod with a larger diameter though this would adversely affect the extraction efficiency and output coupling efficiency.

- 
- 6 Obtained from program OVERLAPB (chapter 4) for the pump/mode overlap integral in the presence of flux that saturates the gain. A more accurate evaluation of this factor is important with regard a full design study.
- 7 This approximate value for the pump/mode overlap is based on improved parity between the pump volume and the fundamental-mode volume, and also the increased pump symmetry that is commensurate with operation at higher power.
- 8 Stokes shift is obtained from the ratio between pump wavelength and lasing wavelength.
- 9 This figure is the fraction of absorbed pump photons that yield ions within the upper lasing level of Nd:YAG. Values from the literature are not definitive and vary between 0.9 and 1.
- 10 Alternatively called the storage efficiency, this is the fraction of pumped ions that are in the upperstate of the 1.064  $\mu\text{m}$  transition, (fluorescence lifetime 230  $\mu\text{s}$ ), given uniform pumping for 200  $\mu\text{s}$ . This accounts for both radiative and non-radiative decay from the upper level level.
- 11 The Q-switch extraction efficiency, is the fraction of inversion available at the end of the pumping interval which is extracted in the Q-switched pulse. The extraction efficiency is a nonlinear function of the pump inversion above the threshold pump inversion,  $r$ .
- 12 This extraction efficiency corresponds to a pumping rate above threshold of  $r = 1.88$
- 13 This extraction efficiency corresponds to a pumping rate above threshold of  $r = 2.00$
- 14 The extraction efficiency asymptotically approaches its maximum value of unity at a value of  $r$  around 5, which should be achieved with 240 mJ of pump power.
- 15 Total parasitic loss for the AO-Q-switched laser was 9%, as determined by the cavity decay time. This includes around 2.5% loss from clipping loss for the mode by the edge of the laser rod, as shown by model OVERLAPD. The output coupling mirror was nominally 20% transmitting.
- 16 Total parasitic loss for the EO-Q-switched laser was 10 %, as determined by the cavity decay time. The output coupling mirror was nominally 10% transmitting.
- 17 The anticipated increase in output coupling efficiency is due to the increased gain, which should allow efficient energy extraction with a 50% transmitting output coupling mirror.
- 18 FIBERTEK do not individually list the factors involved in the extraction efficiency.
- 19 This was the fractional power in single longitudinal mode obtained upon injection seeding of the Q-switched standing wave cavity laser.
- 20 This value should be closer to unity upon implementation of a ring cavity or a twisted-mode cavity which would reduce spatial hole burning. However, there would be the penalty of increased loss from the additional intracavity elements, which will manifest itself in lower Q-switch extraction efficiency and/or lower output coupling efficiency.

---

## 5.7 Chapter 5 Appendix - Q-switch devices

### 5.7.1 Newport AO Q-switch & driver

The Q-switch head was from the Newport N30027 system and consisted of a block of optical quality SF10 Flint glass with a piezoelectric transducer bonded to it. For an input beam aperture of 1.0 mm the minimum rise time was 285 ns, loss modulation was >15%, and the maximum optical power density was rated at 50 Wcm<sup>-2</sup>.

The driver for the Newport Q-switch was a Spectra-Physics model 7250 Q-switch driver, which is commercially available as part of a package for a Q-switched diode-pumped laser system. Consequently, it was necessary to provide the 7250 driver with a +5 V and  $\pm 12$  V external power supply. Otherwise, the driver was well-packaged with integral control of the Q-switch pulse repetition rate between 10 Hz and 9.99 kHz. The RF power module supplied an internally set 4 W at 27.12 MHz.

### 5.7.2 Isle Optics AO Q-switch & driver

The Isle-Optics Q-switch head was a LM080 (LM = Laser Modulator) which had modified connections to allow it to act as a Q-switch. This modified device was later released as a product in its own right as the QS080 (QS = Q-Switch). The lead molybdate, PbMoO<sub>4</sub>, interaction material device was birefringent, so it was necessary to align the axis of the Q-switch with that of the preferred polarisation of the cavity. The polarisation independent diffraction efficiency was >45% at 1.064  $\mu$ m for 1 W of RF, with a rated maximum RF input power of 2 W. With a beam diameter of 1.0 mm, the rise-time was 275 ns, and the maximum optical power density was specified at 5 MWcm<sup>-2</sup>.

The rf driver for the QS080 Q-switch was an Isle-Optics MD080 package consisting of an electronic switching circuit with an 80 MHz crystal with power amplifier. Specified

with a rise time of less than 5 ns, the RF power was user controllable to greater than 1 W. A summary of the relevant parameters for both Q-switches is given in table 5.1.

Q-switch type	Newport N30027	Isle-Optics QS080
Interaction material	SF10 glass	lead molybdate
Interaction length L (cm)	1.4	1.7
Acoustic-frequency (MHz)	27.12	80
Refractive index	1.73	2.62
Acoustic-velocity (kms <sup>-1</sup> )	3.50	3.63
Rise-time for 1.0 mm aperture (ns)	285	275
Diffraction efficiency (%)	> 15	> 45 (1 W RF)
Max. optical power density (Wcm <sup>-2</sup> )	50	5

Table 5.2 - Acousto-optic Q-switch parameters

### 5.7.3 Lasermetric EO Q-switch & driver

A LiNbO<sub>3</sub> Pockels cell was chosen primarily because it offered low insertion loss. A further advantage lies with the LiNbO<sub>3</sub> in that a transverse modulation geometry can be employed without introducing intrinsic birefringence. This ensures a lower switching voltage than KD\*P which is normally modulated longitudinally. The general disadvantage of LiNbO<sub>3</sub>, namely a lower damage threshold, is not significant at the current power levels of diode-pumped lasers. An additional consideration was that the relevant electro-optic coefficient,  $r_{22}$ , is less sensitive to temperature, which could be an important consideration for practical laser designs.

The Pockels cell that was chosen to act as a Q-switch was a Lasermetric LiNbO<sub>3</sub> model 3904-106. This had an 8 mm clear aperture, and was specified to have a quarter-wave voltage of 1.26 kV at 1.064  $\mu\text{m}$ . Its surfaces were protected by removable fused silica protective windows which had "V" type AR-coatings giving a specified overall

transmissivity for this device of >99%. The maximum optical power density of the Q-switch was specified at 350 MW/cm<sup>2</sup>. The polariser was a high quality Glan-Taylor calcite polariser with anti-reflection coatings and a recommended maximum optical power density of 150 MW/cm<sup>2</sup>. It was specified by the manufacturer that the optical axes of the Pockels cell was to be coaxial with the cavity axis to within 2 arc-minutes, so a gimbal mount was required to mount the Pockels cell.

The Pockels cell was driven by a Lasermetrics model 8042 supply, which has switching voltage ratings of 3 kV at up to 1.5 kHz. The driver consisted of two modules; an avalanche transistor high voltage switching circuit (model 8037) and a high voltage power supply and triggering unit. It was found that the quarter wave voltage of 1.2 kV was insufficient to cause breakdown in the avalanche circuit upon triggering, so it was necessary to short out four of the transistors in module 8037.

## Chapter 5    References

- 5.1     G. Wagner & B.A.Lengyel "Evolution of the giant pulse in a laser" J. Appl. Phys. **34** (1963) 2040
- 5.2     F.J. McClung & R.W. Hellwarth "Giant optical pulsations from ruby" J. Appl. Phys. **33** (1962) 828
- 5.3     G.T. Maker & A.I. Ferguson "Single-frequency Q-switched operation of a diode-laser-pumped Nd:YAG," Opt. Lett. **14** (1989) 435
- 5.4     Spectra Physics 7900 series Diode-pumped Q-switched Nd:YLF laser.
- 5.5     T.M. Baer, D.F. Head & P. Gooding "High peak power Q-switched Nd:YLF laser using a tightly folded resonator" paper CMF2, Conference on Lasers and Electro-Optics, Anaheim CA, May 1990.
- 5.6     A.E. Siegman "Lasers" University Science Books, Mill Valley, Ca 1986
- 5.7     Y.K. Park, G.Giuliani & R.L. Byer "Single axial mode operation of a Q-switched Nd:YAG oscillator by injection seeding" IEEE J. Quan. Electron. **20** (1984) 117
- 5.8     C.J. Buczek, J. Freidberg & M.L. Skolnick "Laser injection locking" Proc. IEEE **61** (1973) 1411
- 5.9     L.A. Rahn "Feedback stabilisation of an injection-seeded Nd:YAG laser", Appl. Opt. **24** (1985) 940
- 5.10    K. Chan "Generation of high-power nanosecond pulses from laser diode-pumped Nd:YAG lasers" Appl. Opt. **27** (1988) 1227
- 5.11    W.E. Schmid "Pulse-stretching in a Q-switched Nd:YAG oscillator" IEEE J. Quan. Electron. **16** (1980) 790



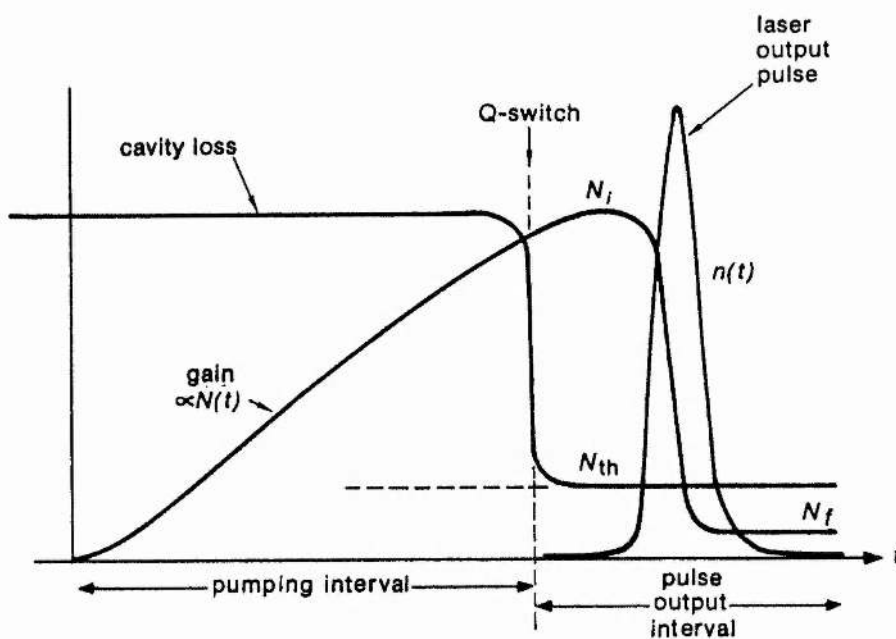


Figure 5.1 Illustration of the evolution of a Q-switched pulse in a pulse-pumped oscillator. In a real laser the duration of the Q-switched pulse at around 20 ns is much less than the pump pulse interval. Schematic by Siegman [5.6]

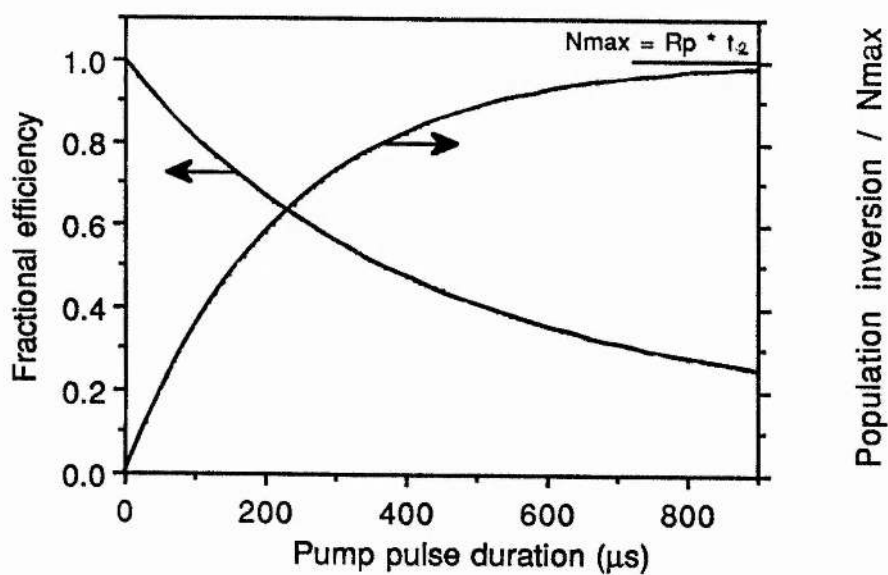


Figure 5.2 Population inversion and fluorescence efficiency in a Nd:YAG crystal as a function of pumping rate.

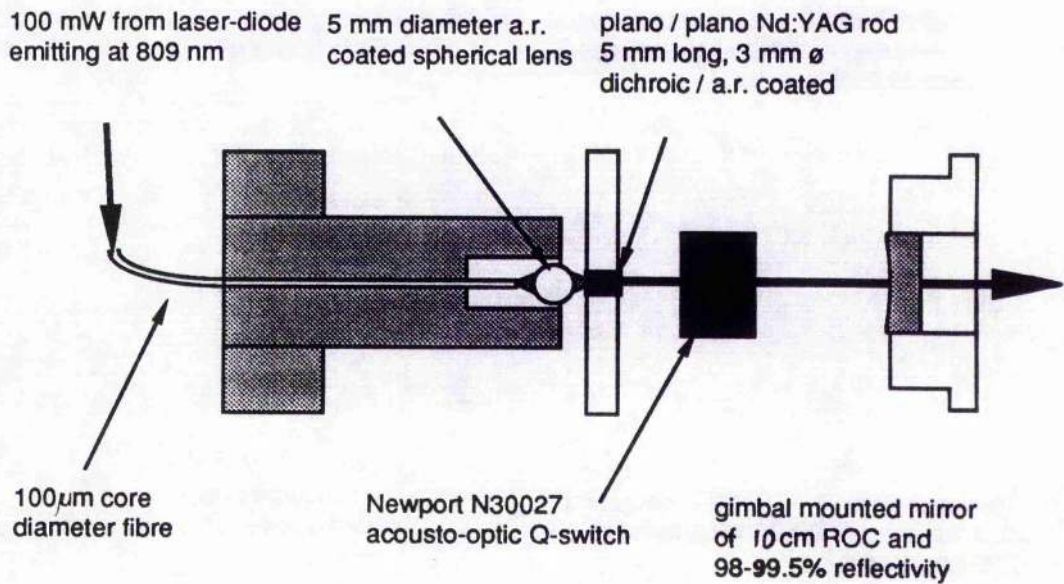


Figure 5.3 Acousto-optically Q-switched Nd:YAG laser longitudinally pumped by a fibre-coupled cw laser-diode.

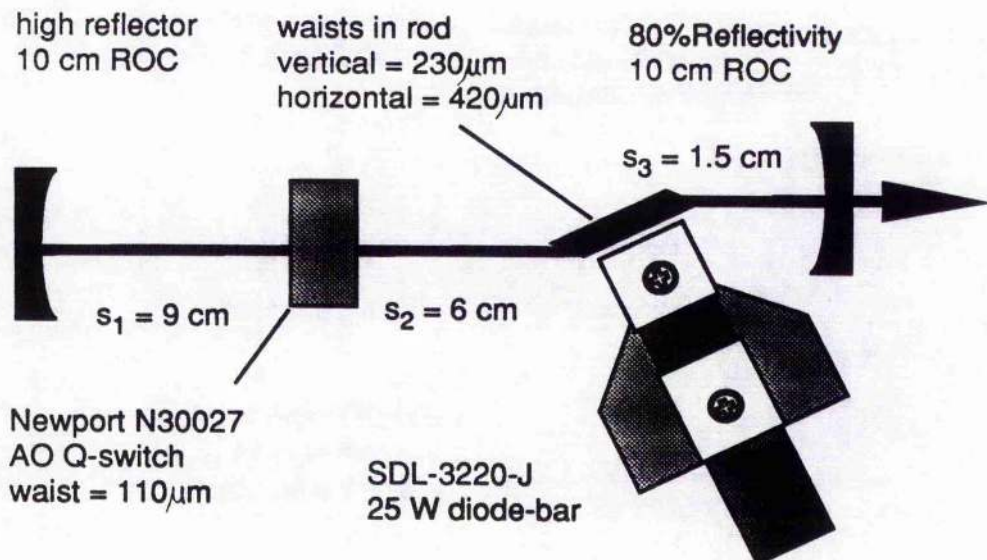


Figure 5.4 Acousto-optically Q-switched laser, with a Brewster angled Nd:YAG rod transversely pumped by a quasi-cw laser bar. The output from this laser was in a single transverse mode at pump powers up to 15 W.

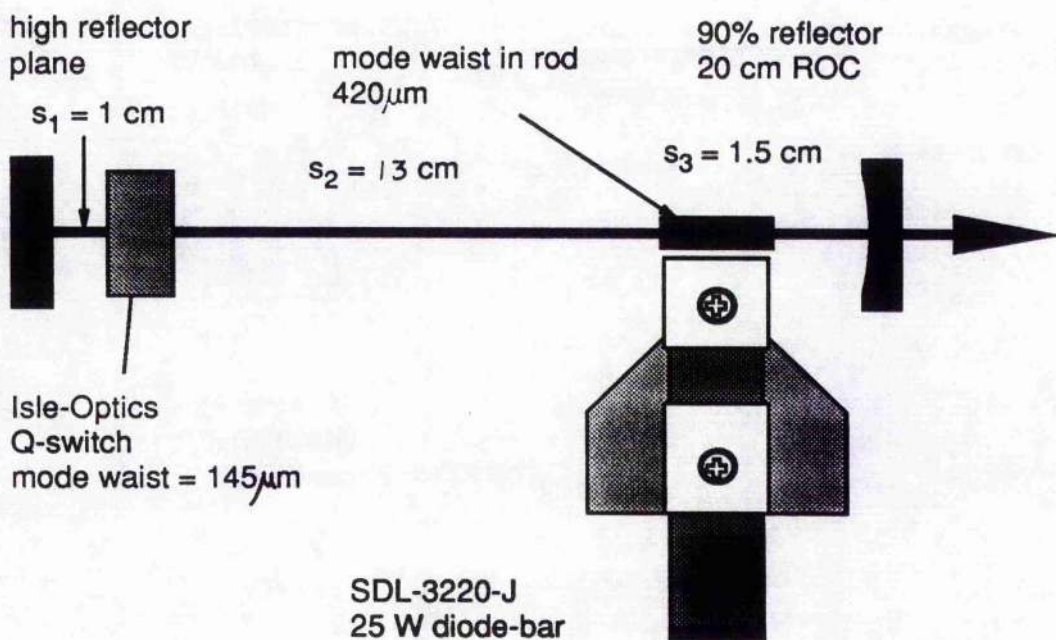


Figure 5.5

Acousto-optically Q-switched laser, with an AR coated Nd:YAG rod transversely pumped by a quasi-cw laser bar. The output from this laser was in a single transverse mode at pump powers up to 25 W.

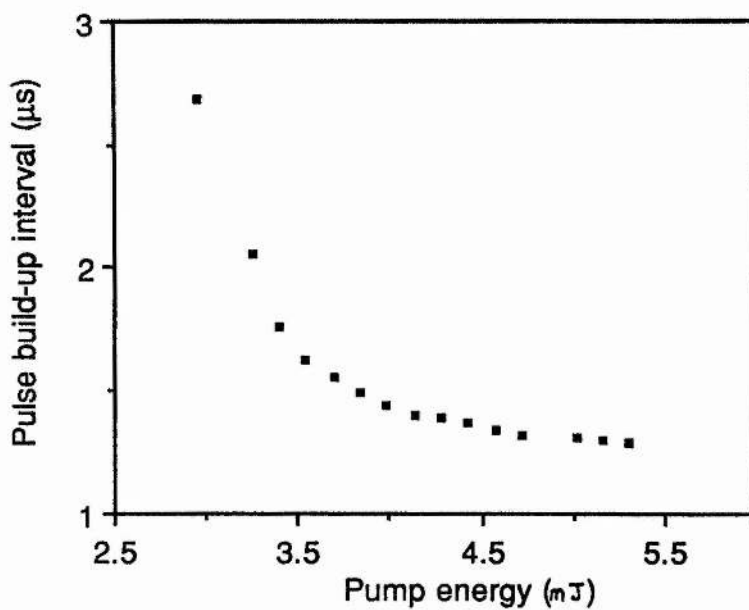


Figure 5.6 Pulse build-up interval as a function of pump energy for the transversely pumped acousto-optically Q-switched Nd:YAG laser shown in figure 5.5.

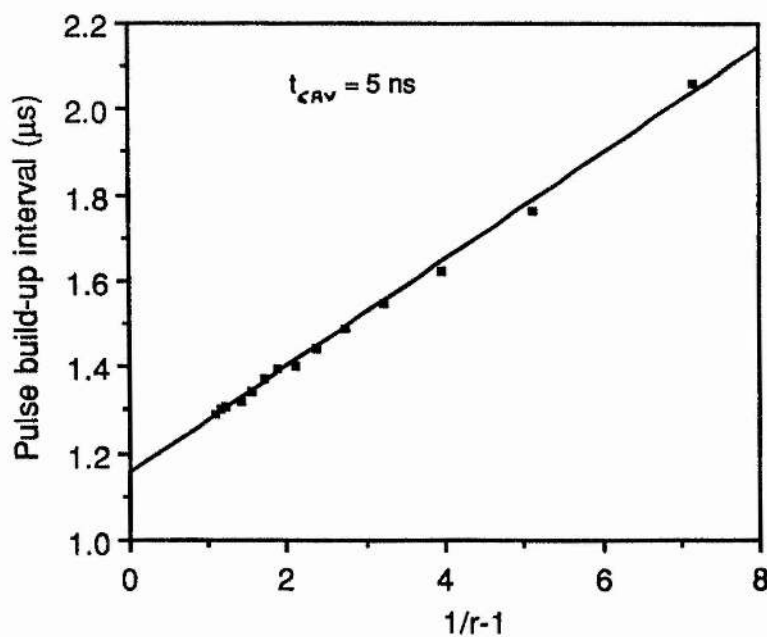


Figure 5.7 Q-switched pulse build-up interval as a function of  $1/r-1$ , where  $r$  is the pumping rate above threshold, with linear regression giving a cavity decay time of 5 ns.

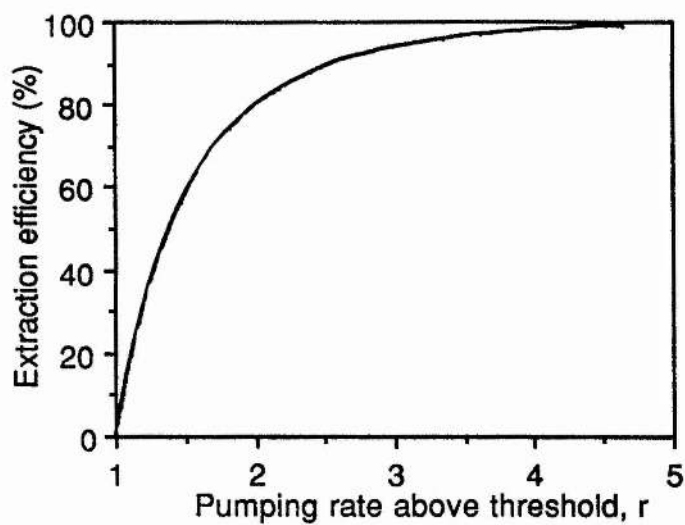


Figure 5.8 Efficiency of extraction of population inversion from a Q-switched laser as a function of the pumping rate above threshold.

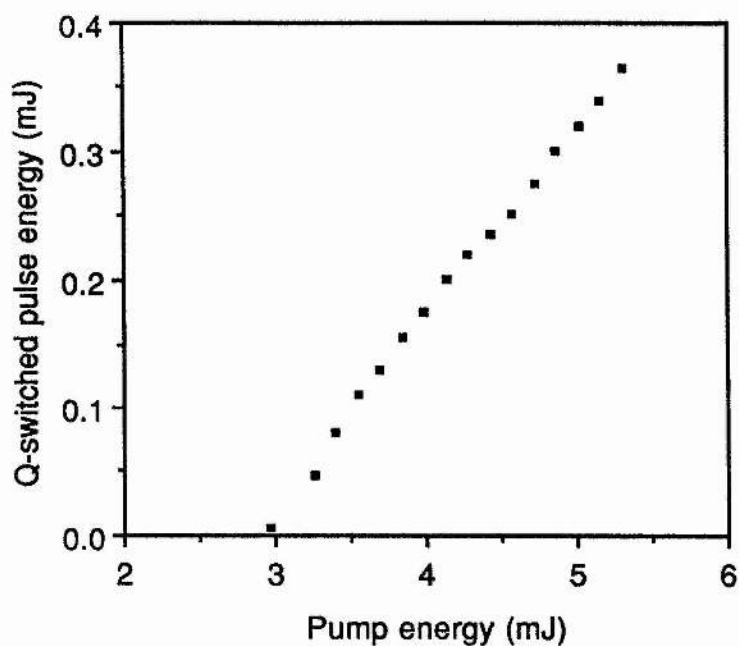


Figure 5.9 Pulse energy as a function of pump energy for the transversely pumped acousto-optically Q-switched Nd:YAG laser shown in figure 5.5.

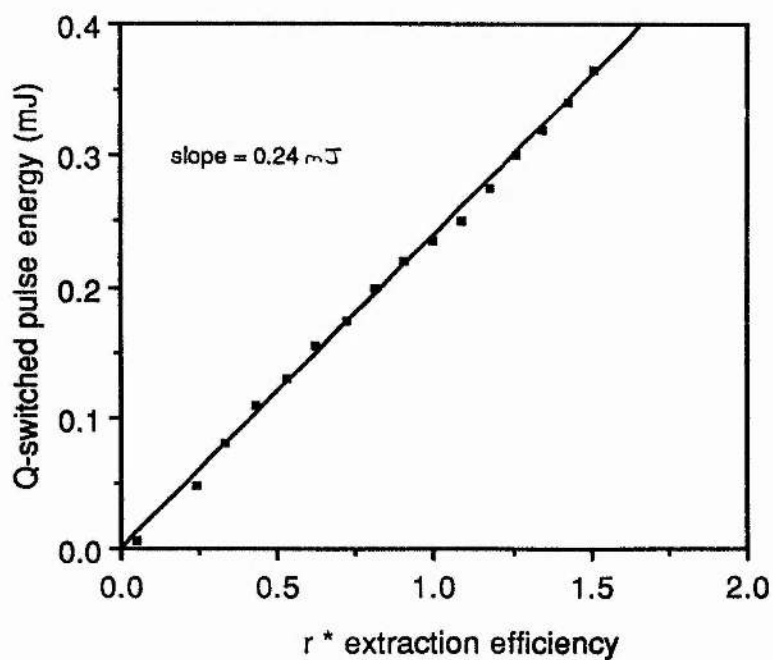


Figure 5.10 Q-switched pulse energy as a function of  $r\eta_e$ , where  $\eta_e$  is the extraction efficiency.



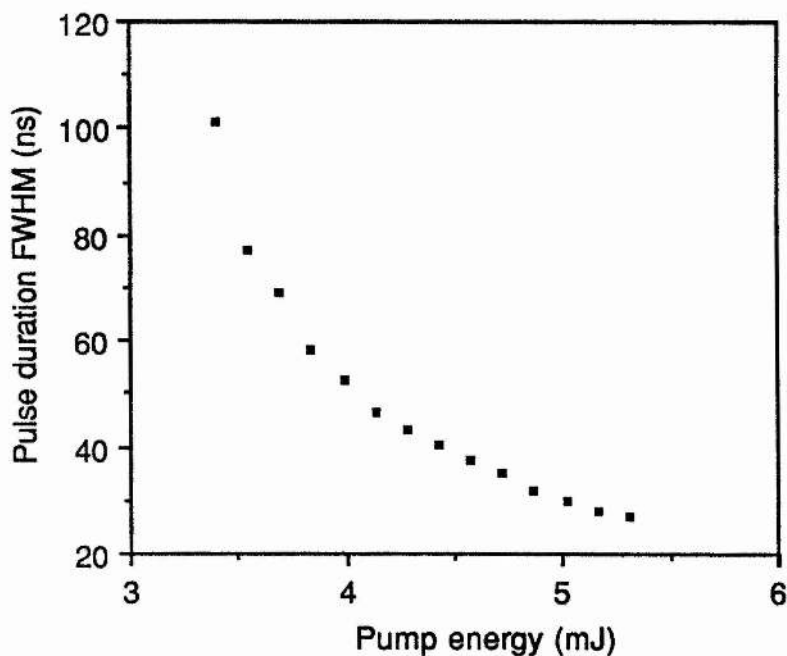


Figure 5.11 Pulse-duration as a function of pump energy for the transversely pumped acousto-optically Q-switched Nd:YAG laser shown in figure 5.5.

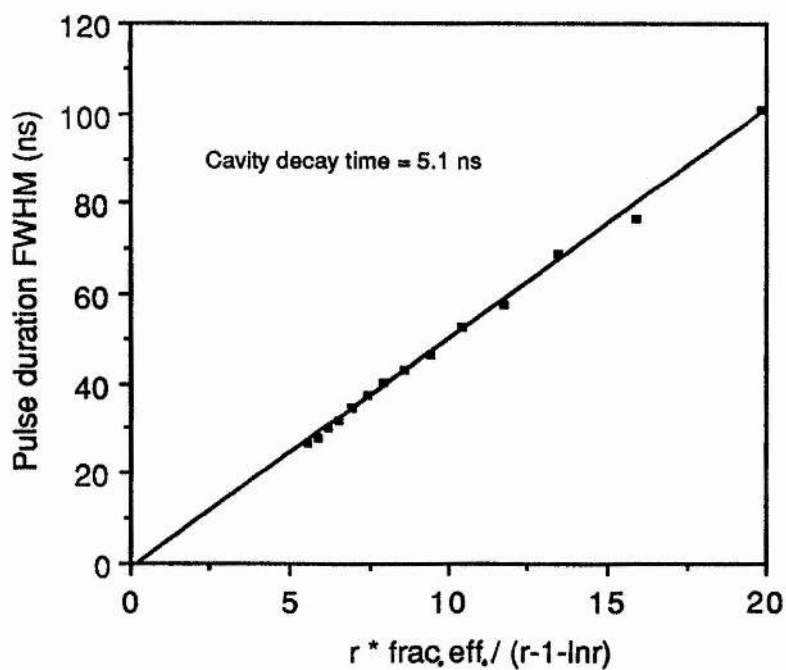


Figure 5.12 Q-switched pulse-duration as a function of  $\frac{\eta_e}{r-1-\ln r}$  with linear regression which indicates a cavity decay time of 5.1 ns.

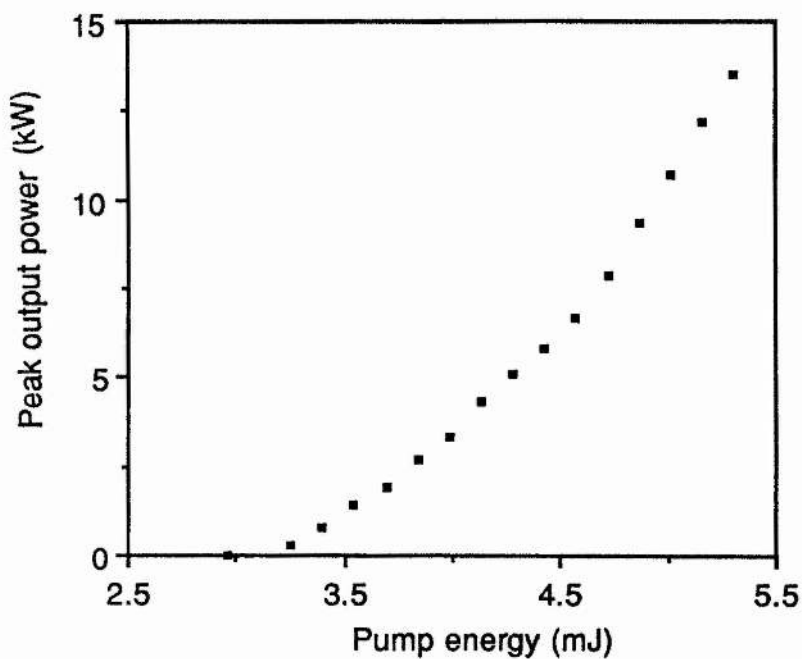


Figure 5.13 Peak power as a function of pump energy for the transversely pumped acousto-optically Q-switched Nd:YAG laser shown in figure 5.5.

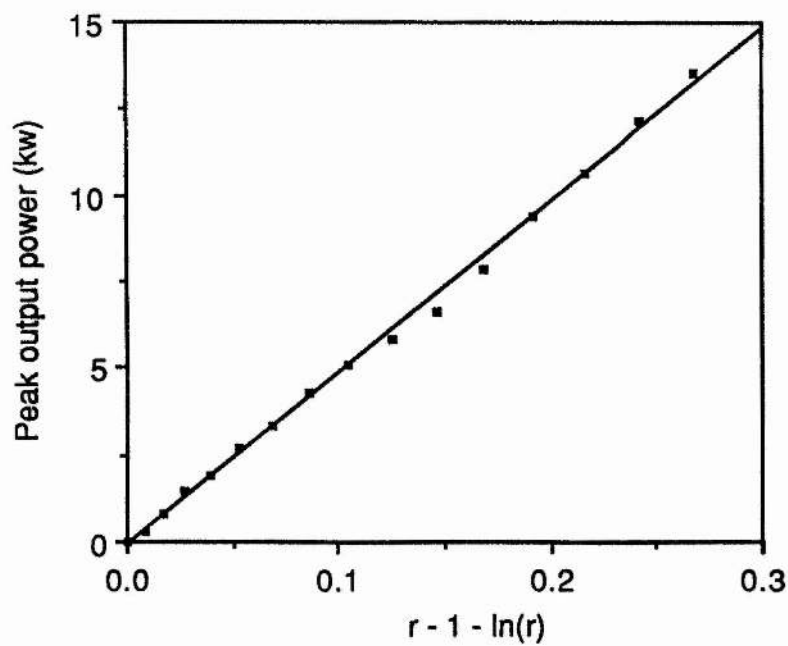


Figure 5.14 Q-switched peak power as a function of  $r-1-\ln(r)$  with linear regression.

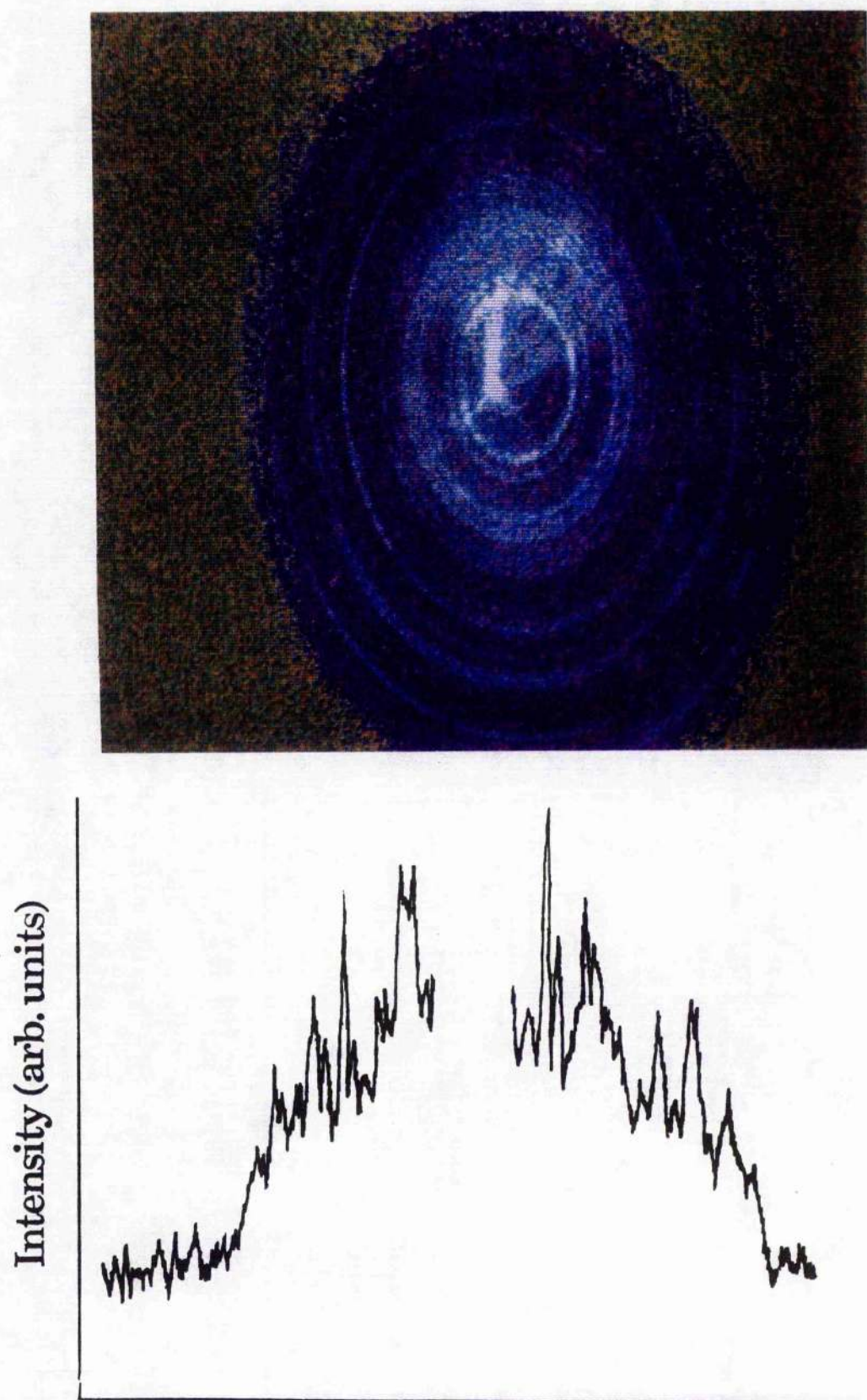
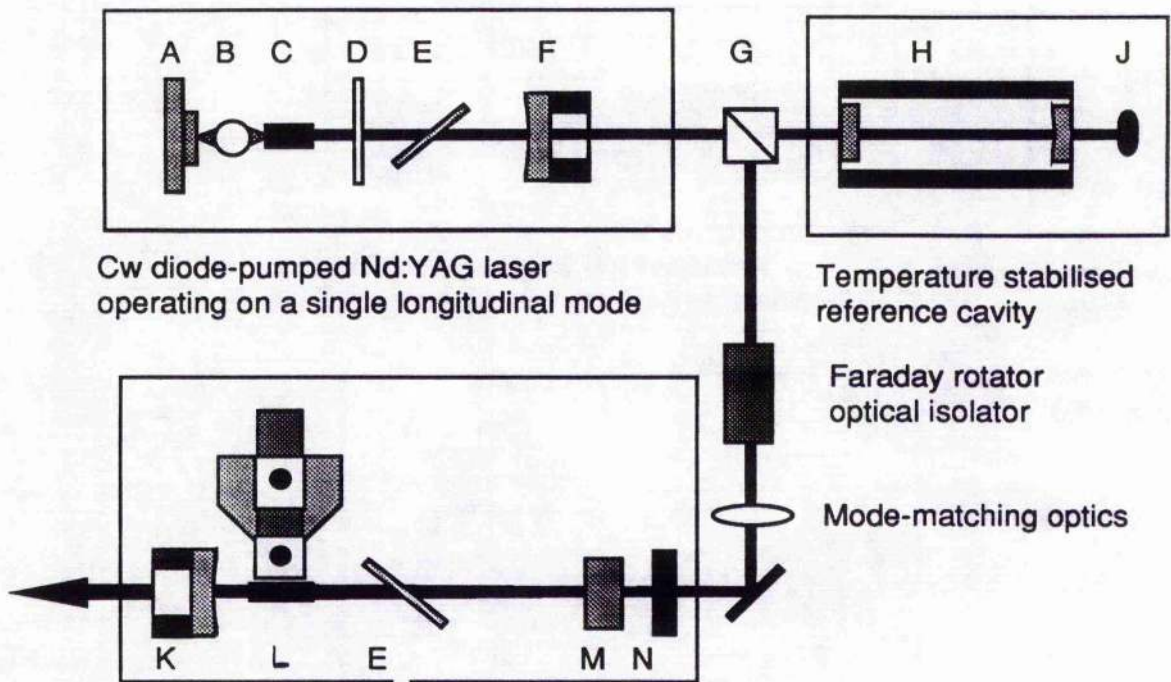


Figure 5.15 Photograph of interference fringes for the acousto-optically Q-switched laser, taken using a computer aided interferometry system, and a linear scan across the pattern. This shows the Q-switched laser in figure 5.5 operating on around 10 longitudinal modes.





Cw diode-pumped Nd:YAG laser  
operating on a single longitudinal mode

Temperature stabilised  
reference cavity

Faraday rotator  
optical isolator

Mode-matching optics

Acousto-optically Q-switched Nd:YAG laser  
transversely pumped by a quasi-cw laser bar

- A:SDL 2430 H2 fibre-coupled laser-diode array
- B:5 mm diameter spherical lens
- C:5 mm long Nd:YAG rod with dichroic and a.r. coatings
- D:1 mm thick etalon
- E:Etalon at Brewster's angle
- F:Output coupling mirror on piezo-adjustable mount
- G:Beam splitter
- H:10 cm long reference cavity with 97% reflectivity mirrors
- J : photodetector providing signal for PSD control of cw laser
- K:20 cm ROC output coupling mirror on piezo mount, 10% transmittance
- L:1.5 mm diameter Nd:YAG rod
- M:Isle Optics acousto-optic Q-switch
- N:Plane mirror with 0.02% transmittance at  $1.064\mu\text{m}$ .

Figure 5.16 Schematic of a frequency stabilised laser-diode pumped single-longitudinal mode Nd:YAG laser injection seeding a transversely pumped acousto-optically Q-switched Nd:YAG laser.

Intensity (arb. units)

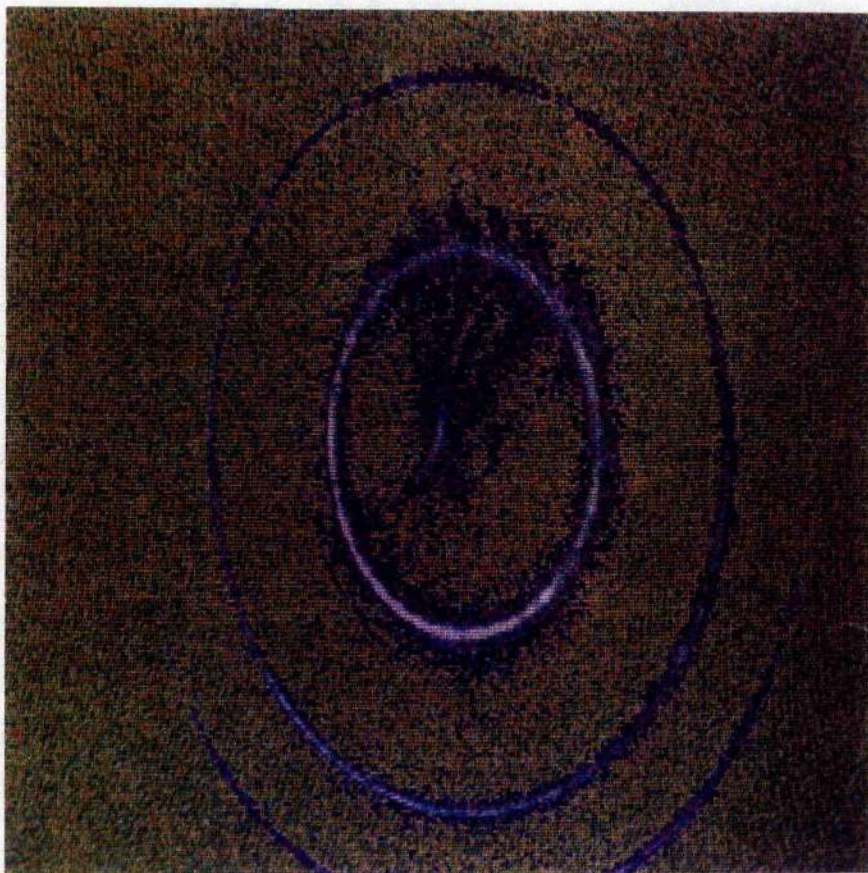
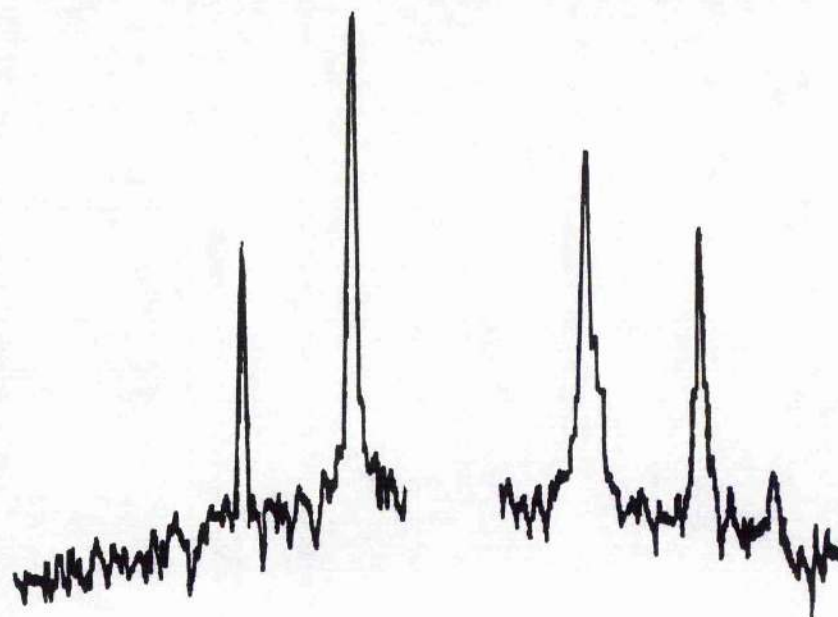


Figure 5.17

Photograph of interference fringes for the injection seeded transversely pumped Q-switched laser, taken using a computer aided interferometry system, and a linear scan across the pattern. This shows the laser operating in a single longitudinal mode.



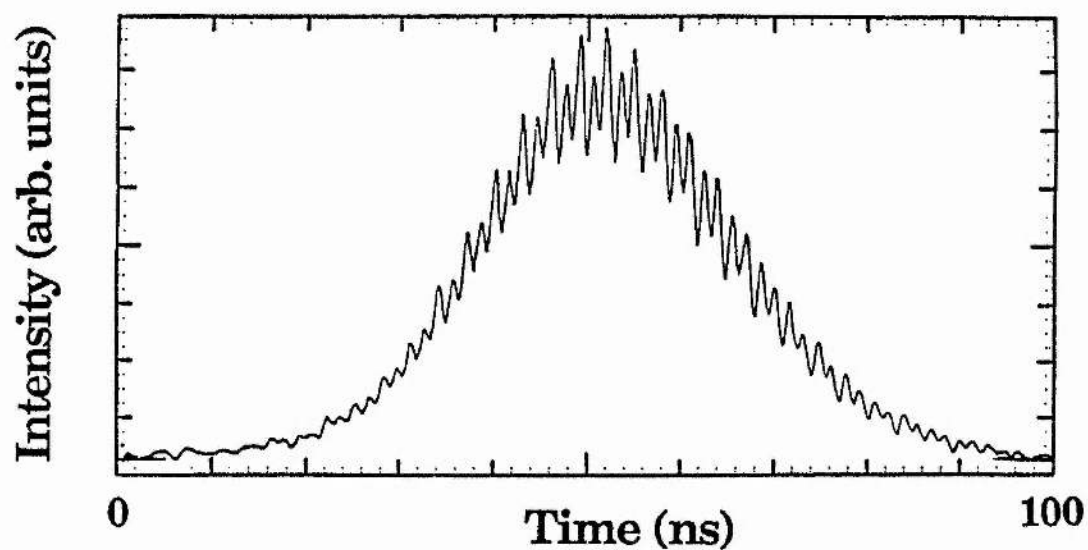


Figure 5.18 Mode beating on the pulse envelope from a unseeded Q-switched pulse indicating laser operation on more than one longitudinal mode.

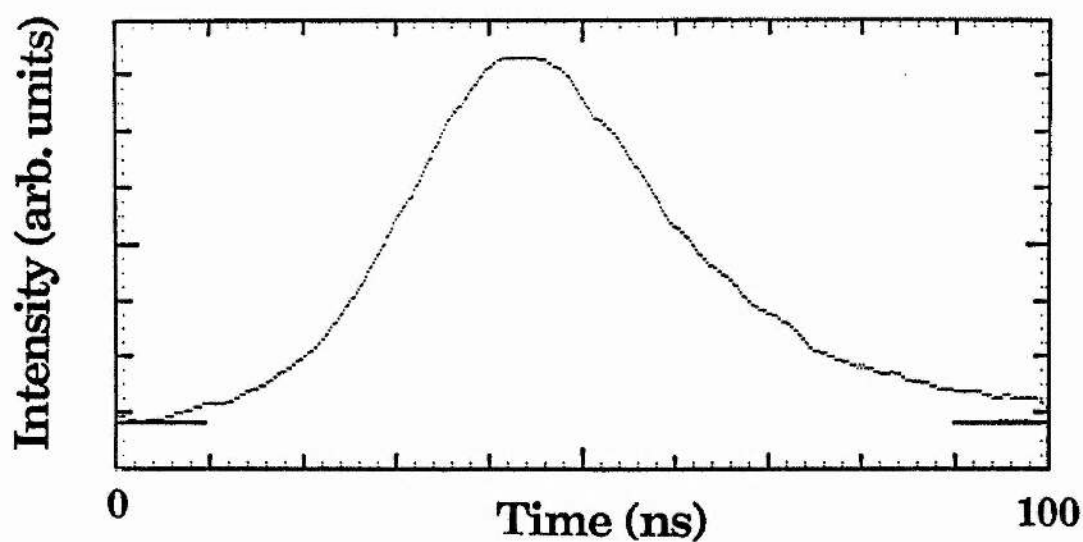


Figure 5.19 Clean pulse envelope from a pulse from the injection seeded Q-switched laser indicating laser operation on a single longitudinal mode.



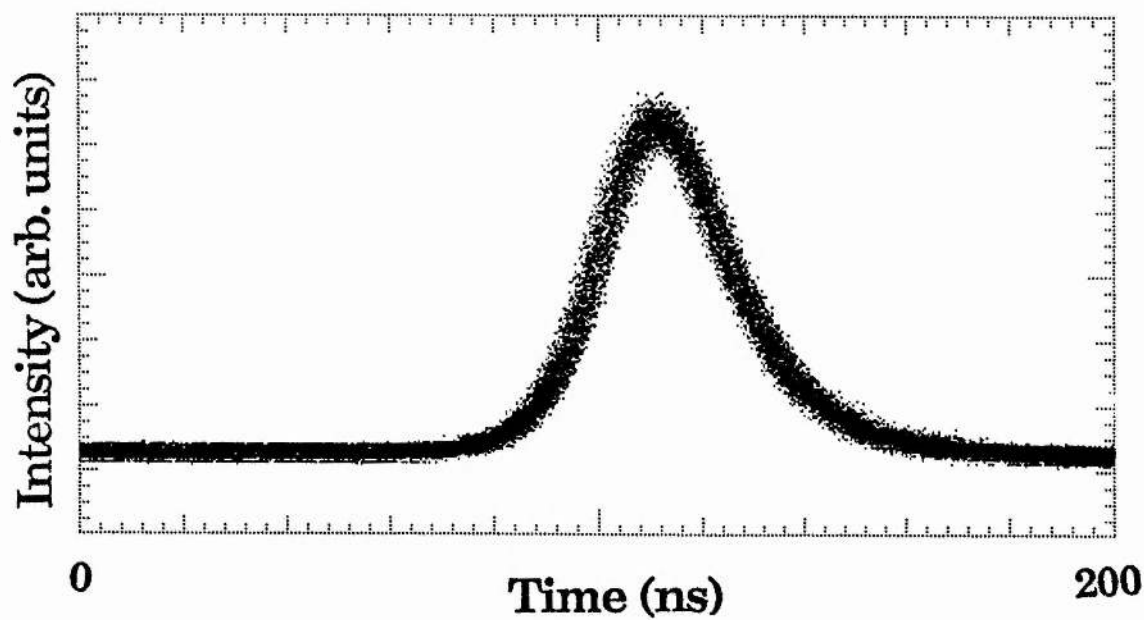


Figure 5.20      100 consecutive Q-switched pulses showing that the amplitude stability is better than 6%.

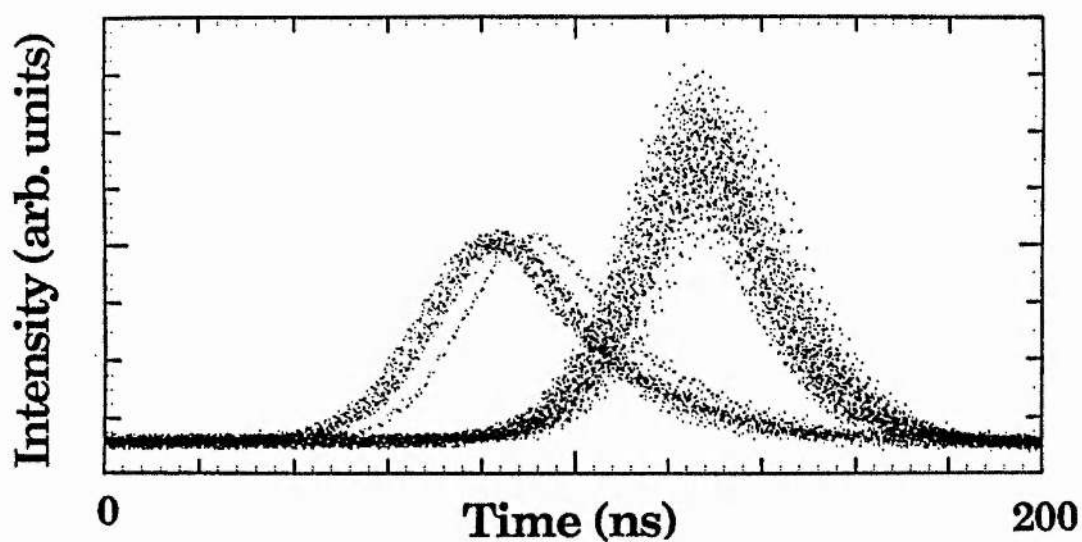


Figure 5.21 A number of consecutive Q-switched pulses showing a reduction in pulse build-up interval and pulse energy upon injection seeding.

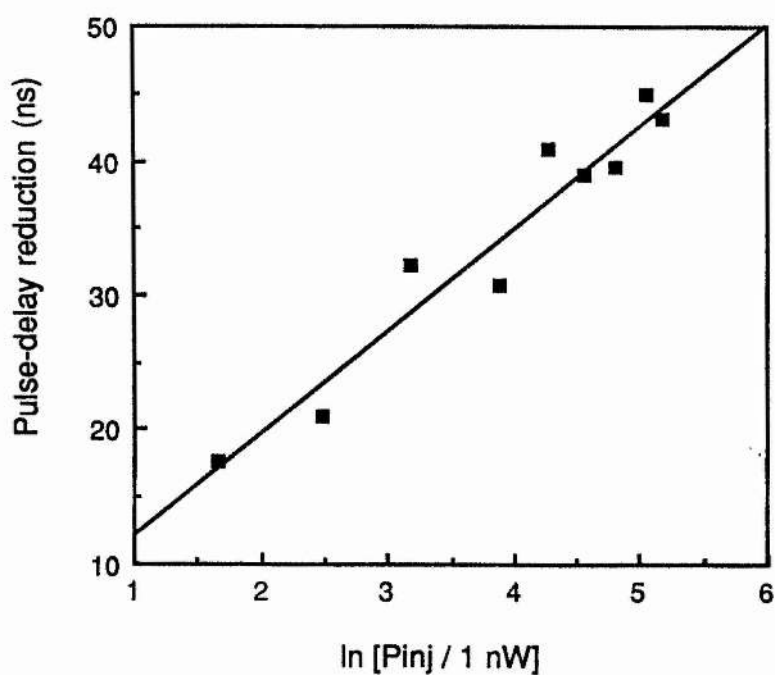


Figure 5.22 Reduction in pulse build-up interval as a function of optical power injected into the cavity.

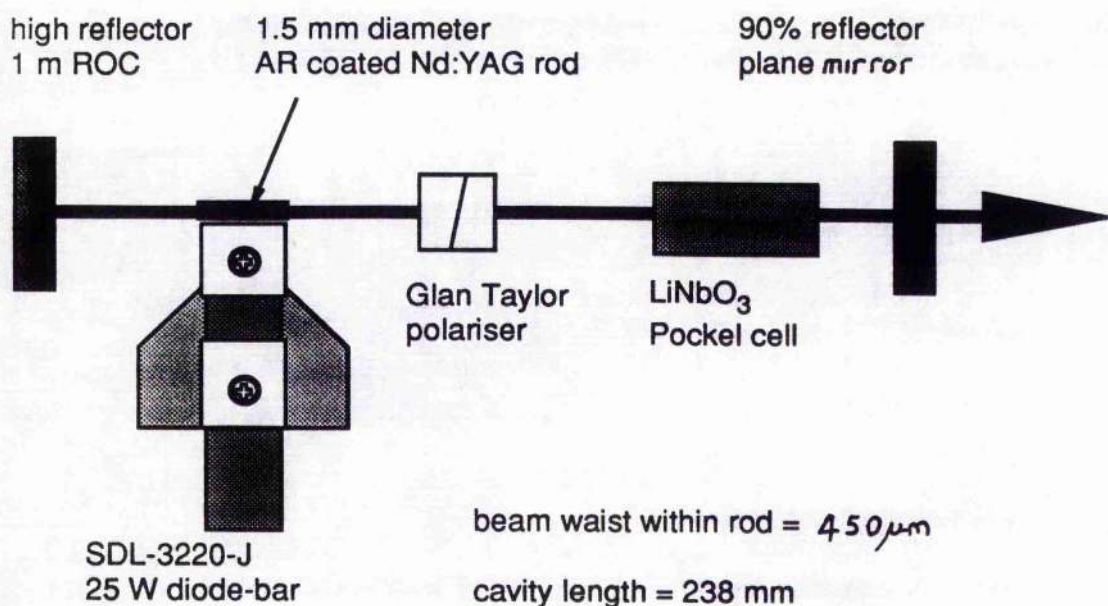


Figure 5.23 Schematic of the electro-optic Q-switched cavity configuration.

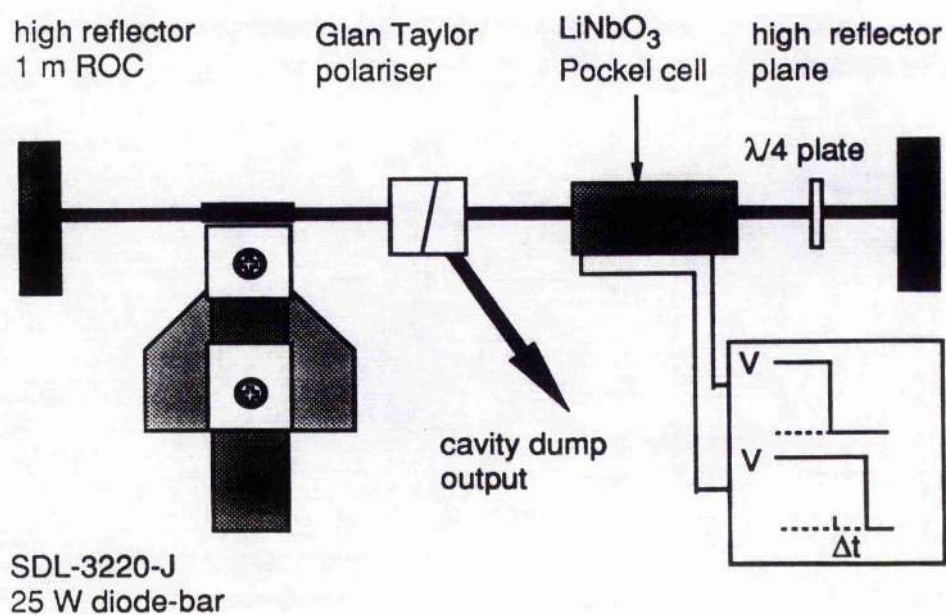


Figure 5.24 Cavity configuration for cavity-dump Q-switching.

## Chapter 6

### General conclusions and future work

The work on the cw SDL-2430-H2 laser-diodes in chapter 2 showed that this fibre-coupled laser was well behaved and that the drive-current threshold for the laser-diode that was purchased in April 1987 increased only slightly over the 3 years during which it received extensive use. Temperature tuning of these laser-diodes to match the absorption peak of the Nd:YAG medium was achieved using small internal Peltier components. This proved convenient in practice and, although the laser-diode threshold is also a function of temperature, the internal photodiode allows one to maintain a given output power. The choice of a fibre-optic coupling for the laser-diode proved satisfactory, with the symmetric beam pattern that emerges from the optical fibre allowing simple and effective pumping with a spherical lens. Results from a ray-tracing programme show that pump spot size is dominated by aberrations, but that the pumping intensity within the Nd:YAG rod proved sufficient for high gain on the 1.064  $\mu\text{m}$  line. For lasers that require a particularly high pump intensity, such as the 946 nm transition in a Nd:YAG crystal, fibre-coupled laser-diodes are not appropriate as the optical fibre acts to decrease the brightness of the emission.

It was shown in chapter 3 that the end-pumped Nd:YAG laser required either an intracavity etalon or a twisted cavity mode configuration to obtain single-longitudinal-mode operation. The short-term stability of the etalon-controlled laser was  $<10$  kHz in 10 ms which was more than adequate for the injection seeding of the transversely pumped Q-switched laser. This frequency stability compares poorly with the monolithic Nd:YAG ring laser though neither this technique nor the twisted cavity mode technique can be applied to birefringent gain materials such as Nd:YLF. In consequence a source for injection seeding of a Q-switched Nd:YLF laser would have to include an etalon or use the microchip approach.

For the lasers described in chapters 4 and 5 the use of the Peltier cooler to temperature stabilise the laser-diode-bar was essential to obtain adequate pump absorption. This was due to a combination of the narrowness of absorption peak of Nd:YAG at 809 nm, the dynamic frequency chirp in the output of the laser bar, and the level of pump intensity which necessitated a small pump volume to ensure sufficient gain. The poor efficiency of Peltier coolers becomes important for more powerful lasers pumped by multiple laser bars so making it desirable that Peltier coolers should be replaced by water-cooling. The necessity for high absorption in such a high power laser will however be relaxed by the larger pump volume, though gain materials with broader absorption features should also be considered.

The computer modelling of the transversely pumped laser described in chapter 4 has proved valuable and aided our understanding of the nature of the pump process. However, the discrepancy between the calculated threshold pump power and that measured experimentally prevents us from regarding this model as wholly satisfactory. Deficiencies may be attributed to an incorrectly modelled pump rate distribution which was in rather poor agreement with the pump rate distribution as determined by the small-signal gain measurements. It is perhaps also necessary to include time-varying absorption within the model because of the frequency chirp of the laser-diode, though this would not be required to allow modelling of a true cw laser pumped by the recently available 10 W cw laser bars. Extending the model to Q-switched laser operation, multiple pump sources and arbitrary laser-crystal geometries such as slabs would further increase the usefulness of this model.

It was shown in chapter 5 that the Q-switching of the transversely pulse pumped laser could be effectively achieved with an acousto-optic Q-switch but that flux limit imposed by optical damage necessitates that the electro-optic Pockels cell which was also investigated will be essential for a laser which is pumped by more than one laser-diode bar. The fast switching time of the electro-optic Q-switch should also allow more reliable self-injection seeding, shorter cavity pulses through cavity-dump Q-switching

and longer pulses through controlled extraction of the optical flux. Enhanced frequency stability can be anticipated from the use of a sealed mechanically stable laser cavity.

The recent reduction in the cost of laser-bars has enhanced the prospect for a more powerful Q-switched laser to be built with a pulse energy of between 30 and 100 mJ. In Table 5.1 it is shown that the overall optical/optical efficiency for an injection seeded Q-switched Nd:YAG laser should be approximately 17%. This could be increased further through more efficient extraction of the pump energy that is deposited around the circumference of the multiple pumped rod. This may be achieved by the use of super-Gaussian mirrors or variable reflectivity birefringent filters that would create a “flat-topped” mode which would also improve the extraction efficiency from a subsequent chain of optical amplifiers.

The work undertaken in the course of this thesis on diode-pumping has provided a basis for other research activity within the department which seeks to exploit the quality nature of holosteric lasers. The cw laser has been developed with progression towards a source of increasing frequency stability to be used as a master oscillator. Expertise gained with regard to effective diode-pumping has been exercised pumping the more difficult 946 nm transition in Nd:YAG, and which has resulted in blue frequency doubled Q-switched pulses. The excellent beam from the transversely pumped Q-switched Nd:YAG laser is now acting as a source for the ongoing research into the generation of tunable light through optical parametric oscillation.

Historically the development of holosteric lasers has depended largely upon the capabilities of laser-diodes, and it is envisaged that surface emitting arrays will provide a further impetus to this progress. Economics is also significant, with the historical trend towards reduced cost per watt for laser-diode pump power. This is stimulating increasing interest in more powerful diode-pumped lasers, which may perhaps result eventually in holosteric lasers used for fusion research.



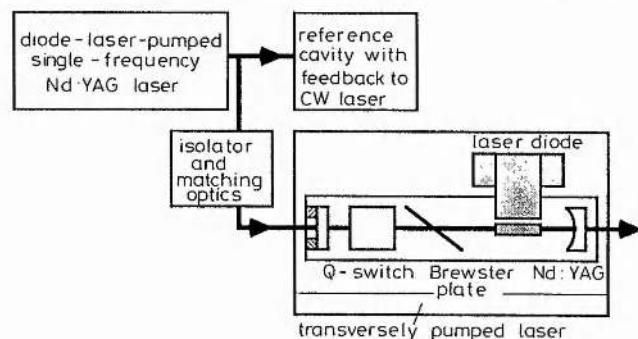
# SINGLE-FREQUENCY OPERATION OF DIODE-LASER-ARRAY TRANSVERSE-PUMPED Q-SWITCHED Nd:YAG LASER

**Indexing terms:** Lasers and laser applications, Optics, Q-switching

Single-longitudinal-mode and single-transverse-mode operation of a miniature Nd:YAG laser transversely pumped by a quasi-CW diode-laser array is described. By injection-seeding this oscillator with a diode-laser end-pumped Nd:YAG microlaser, single-frequency Q-switched pulses of 0.25 mJ energy and 35 ns duration were generated.

Diode laser pumped solid-state lasers are becoming increasingly attractive sources of high-quality coherent radiation.<sup>1</sup> In their end-pumped configurations the excellent spatial and spectral match of the pump and lasing modes ensures efficient TEM<sub>00</sub> operation, with single-longitudinal-mode power levels up to 490 mW reported.<sup>2</sup> End-pumping geometries are limited in the amount of diode-laser power that may be focused into the solid-state laser, whereas transverse pumping, which uses diode-laser arrays of larger dimensions, permits much higher power operation.<sup>1,3</sup> However, the poorer spatial overlap of pump and lasing modes encourages multitransverse mode operation so that few TEM<sub>00</sub> systems have been described, and none has been operated in a single-longitudinal mode. We report here single-transverse-mode and single-longitudinal-mode performance characteristics of a transversely pumped Nd:YAG microlaser. This has been achieved with an optical-optical (809–1064 nm) slope efficiency of 13%.

We designed and constructed the Nd:YAG laser shown in Fig. 1. The pump source was a 25 W, 200  $\mu$ s pulsewidth diode



[199/1]

**Fig. 1** Injection-seeded laser system

laser array (SDL 3220J), which had 1000 emitting stripes across its 1 cm-wide facet. The Nd:YAG laser rod was 12 mm long with antireflection coated end faces; the curved side of the 1.5 mm-diameter rod acted as a lens for the diode-laser radiation and a polished brass housing was used to reflect any transmitted pump light back into the rod. (The thermally induced frequency sweep of the diode-laser-array output reduces the average amount of absorption in the rod.)<sup>4</sup> A resonator geometry was chosen to ensure that the fundamental cavity mode filled a substantial part of the pumped volume. A highly reflecting plane mirror and an 80% reflecting 20 cm radius-of-curvature mirror were separated by 19 cm, leading to a beam diameter (full width 1/e<sup>2</sup> maximum) of 0.8 mm in the rod. Linear polarisation (better than 100:1) was obtained by incorporating an intracavity Brewster-angled plate, and Q-switching was accomplished using an acousto-optic Q-switch (Isle Optics model LM080).

When free-running this laser produced 0.36 mJ, 27 ns pulses at up to 100 Hz (the recommended limit on the repetition rate of the diode-laser-array). Although this operation was in a single transverse mode, many longitudinal modes were oscillating, as seen by the modulation at the intermode frequency on the pulseshape reproduced in Fig. 2a. Analysis of the

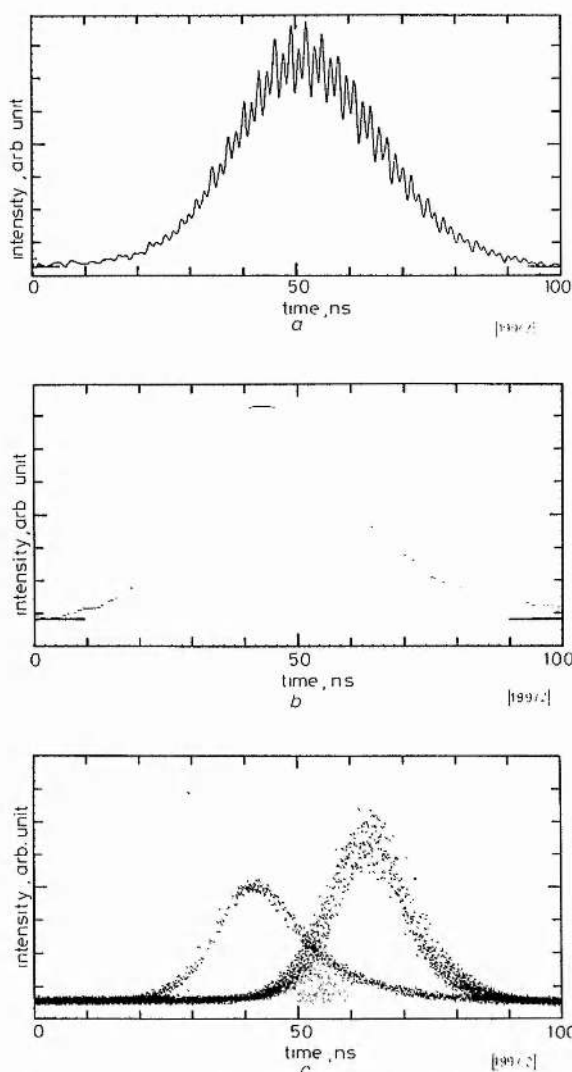


**Fig. 2** Temporal profiles of (a) unseeded laser pulse, (b) seeded laser pulse, and (c) several superimposed seeded and unseeded laser pulses

pulsed radiation with a plane-parallel Fabry–Perot interferometer confirmed this multifrequency operation.

Injection-seeding flashlamp pumped solid-state lasers to produce single-longitudinal-mode operation is now an established technique.<sup>5</sup> This was the approach that we adopted to create an entirely solid-state (holosteric) single-frequency Q-switched system. The seeding laser, which consisted of a 5 mm long Nd:YAG rod, a 1.5% reflectivity output coupler and a quartz etalon, was longitudinally pumped by a fibre-coupled diode-laser array (SDL-2422-H2). 10 mW of single-frequency 1064 nm radiation was generated with a short-term (jitter-induced) linewidth of 40 kHz, and long-term thermal drift was reduced by locking the laser to a transmission peak of a confocal Fabry–Perot interferometer. A number of different arrangements for coupling the CW seeding laser into the pulsed laser cavity were evaluated, but the most convenient configuration was the injection of the CW radiation through the high-reflectivity mirror of the pulsed laser cavity via suitable mode-matching optics and a Faraday isolator (Fig. 1).

Seeding the pulsed laser was found to be both straightforward and reliable. When the pulsed laser cavity length was adjusted to match the frequency of a mode of the pulsed-laser to that of the injecting beam, the transmission characteristic of the Fabry–Perot interferometer condensed into that of single-frequency laser. The smooth temporal profile of a single-longitudinal-mode pulse obtained from this system is included in Fig. 2b. These 0.25 mJ pulses had durations of 35 ns (FWHM) with 7 kW peak power. The reduction in pulse energy was due to spatial hole burning effects which left some residual gain in the rod. (This effect was eliminated when the

rod was surrounded by quarter-wave plates, but the extra intracavity loss introduced by these elements merely reduced the output power level to that of the original system.) A number of consecutive pulses were stored on a digital oscilloscope and are shown as Fig. 2c. The right-hand traces are of multimode unseeded pulses, as evidenced by the mode-beating. The left-hand traces are of the single-longitudinal-mode pulses, which appear at a shorter time after opening the  $Q$ -switch because they build up from the injected signal rather than the lower power noise. These pulses exhibited excellent stability and the absence of mode-beating is also evident. Despite the lack of special precautions the amplitude stability was measured to be  $\pm 6\%$  over 100 pulses.

A servoloop arrangement based upon the pulse build-up time<sup>6</sup> may be used to lock the pulsed-cavity resonance to the CW oscillator. In practice, the stability of the holosteric system was sufficient that only occasional adjustment of the pulsed cavity length was necessary to maintain effective seeding. With 0.2 mW from the seeding laser incident on the 0.02% transmitting mirror of the pulsed laser, the detuning tolerance was approximately  $\pm 150$  MHz.

We believe that this is the first report of an injection-seeded diode-laser-array side-pumped laser system. The excellent spatial and spectral beam quality make it useful for applications where reliability and efficient operation are required. One advantage of injection-seeding over pre-lase  $Q$ -switching is that the  $Q$ -switched pulse can be of a well defined frequency, determined (within a small tolerance) by that of the frequency-stabilised seeding laser. Moreover, the inherent scalability of the side-pumping geometry permits the same techniques to be scaled to much higher energy levels.

**Acknowledgments:** This work was performed under contract to the Procurement Executive of the UK Mod. We also gratefully acknowledge personal support from the same source (BDS), the SERC (NG), and SERC/British Aerospace (CJN).

C. J. NORRIE  
B. D. SINCLAIR  
N. GALLAHER  
M. H. DUNN  
W. SIBBETT

5th June 1989

*J. F. Allen Physics Research Laboratories  
Department of Physics & Astronomy  
University of St. Andrews  
North Haugh, St. Andrews, Fife KY16 9SS, United Kingdom*

## References

- 1 FAN, T. Y., and BYER, R. L.: 'Diode laser-pumped solid-state lasers', *IEEE J. Quantum Electron.*, 1988, **24**, pp. 895-912
- 2 WALLMERTH, K., and PEUSER, P.: 'Single frequency TEM<sub>00</sub> diode-pumped Nd:YAG laser emits 0.5 W', *Laser Focus World*, 1989, (4), pp. 38-40
- 3 BURNHAM, R., and HAYS, A. D.: 'High-power diode-array-pumped frequency-doubled cw Nd:YAG laser', *Opt. Lett.*, 1989, **14**, pp. 27-29
- 4 NORRIE, C. J., SINCLAIR, B. D., GALLAHER, N., SIBBETT, W., and DUNN, M. H.: 'Measurement of frequency sweep in a quasi-cw diode-laser array, and its implication for pumping solid-state lasers', *J. Mod. Opt.*, 1989, **36**, pp. 1-6
- 5 PARK, Y. K., GIULIANI, G., and BYER, R. L.: 'Stable single-axial-mode operation of an unstable-resonator Nd:YAG oscillator by injection locking', *Opt. Lett.*, 1980, **5**, pp. 96-98
- 6 RAHN, L. A.: 'Feedback stabilisation of an injection-seeded Nd:YAG laser', *Appl. Opt.* 1985, **24**, pp. 940-942

## Letter

### Measurement of frequency sweep in a quasi-c.w. diode-laser array, and its implication for pumping solid-state lasers

C. J. NORRIE, B. D. SINCLAIR, N. GALLAHER,  
W. SIBBETT and M. H. DUNN

J. F. Allen Physics Research Laboratories,  
Department of Physics and Astronomy, University of St Andrews,  
St Andrews, Fife KY16 9SS, Scotland

(Received 22 October 1988)

**Abstract.** Temporally and spatially resolved measurements of the spectral output of a commercially available 25 W quasi-c.w. diode-laser array have been made. The 5 nm temperature-induced wavelength sweep during the 200  $\mu$ s pulse reduces the effectiveness of the array as a pump for solid-state lasers. By using a reflector behind a side-pumped Nd:YAG rod to minimize the effects of the wavelength sweep, the 1.06  $\mu$ m laser produced 6.5 W, 180  $\mu$ s pulses, and 6.1 kW, 44 ns pulses when Q-switched.

#### 1. Introduction

High power quasi-c.w. monolithic diode-laser arrays [1-4] are currently attracting attention for the efficient side-pumping of miniature solid-state lasers [5, 6]. Such arrays are commercially available at specified power levels as high as 25 W [7], and linear arrays rated at 40 W have recently been advertised. One major advantage of diode arrays over flashlamps is their narrow spectral-output which may be temperature tuned to match an absorption peak in the solid-state material. We report on a time and space resolved study of the spectral output of a 25 W quasi-c.w. array manufactured by Spectra Diode Laboratories [7] and the implications that these results hold for the transverse pumping of a Nd:YAG microlaser.

The use of continuous-wave diode-laser arrays for end-pumping solid-state lasers is well established [8]. This form of pumping is highly efficient due to the good spectral match of the diode-laser output to the absorption peak in the solid-state material and the good spatial-overlap between the pump beam and the cavity mode. Optical-optical pumping efficiencies as high as 64% have been obtained, with overall wall-plug efficiencies of 15.8% reported [9]. Because this type of pumping is not readily scalable to high powers, side pumping of solid-state rods or slabs is attractive in configurations where many diode-laser arrays may be used to increase the total power. Although the overall efficiency of the system is lower due to the poorer spatial overlap of pump and laser modes, the constraints on the brightness of the pump beam are relaxed as compared to the end-pumping case. This allows diode-laser arrays with large emitting areas to be used, where the individual stripes need not be mutually phase-locked. The diode-laser array used in our work was comprised of 1000 stripes across a 1 cm long GaAlAs crystal facet [7]. Its operation may be described as 'quasi-c.w.' because the 200  $\mu$ s maximum pulse-length of injection current reflects the limitation arising from the problem of removing heat from the active region sufficiently quickly to permit true c.w. operation. This 200  $\mu$ s

pulse length is particularly well suited for pumping a Nd : YAG gain medium which has an upper laser-state lifetime of 230  $\mu\text{s}$  [10].

Although it is well known that c.w. diode-laser arrays have a narrow bandwidth which closely matches the absorption peak in Nd : YAG at 809 nm, it is not generally appreciated that the spectral matching is worse for the quasi-c.w. operation of high-power diode-laser arrays. The rise in temperature of the active region of the diode laser during the driving current pulse may be expected to cause a shift in wavelength of  $0.25 \text{ nm } ^\circ\text{C}^{-1}$ , and any variation in composition and temperature across the 1 cm wide laser-array facet may also cause a spatial non-uniformity of lasing wavelength.

## 2. Experiment

We operated the laser array at maximum average-power (25 W, 200  $\mu\text{s}$ , 100 Hz) and imaged portions of the output beam onto the input slit of a 1 m scanning monochromator (Monospek 1000). The spectral content of the laser emission was analysed at eight instants during the laser pulse and the results are presented in figure 1. It can be seen that the individual laser modes are spread over an instantaneous

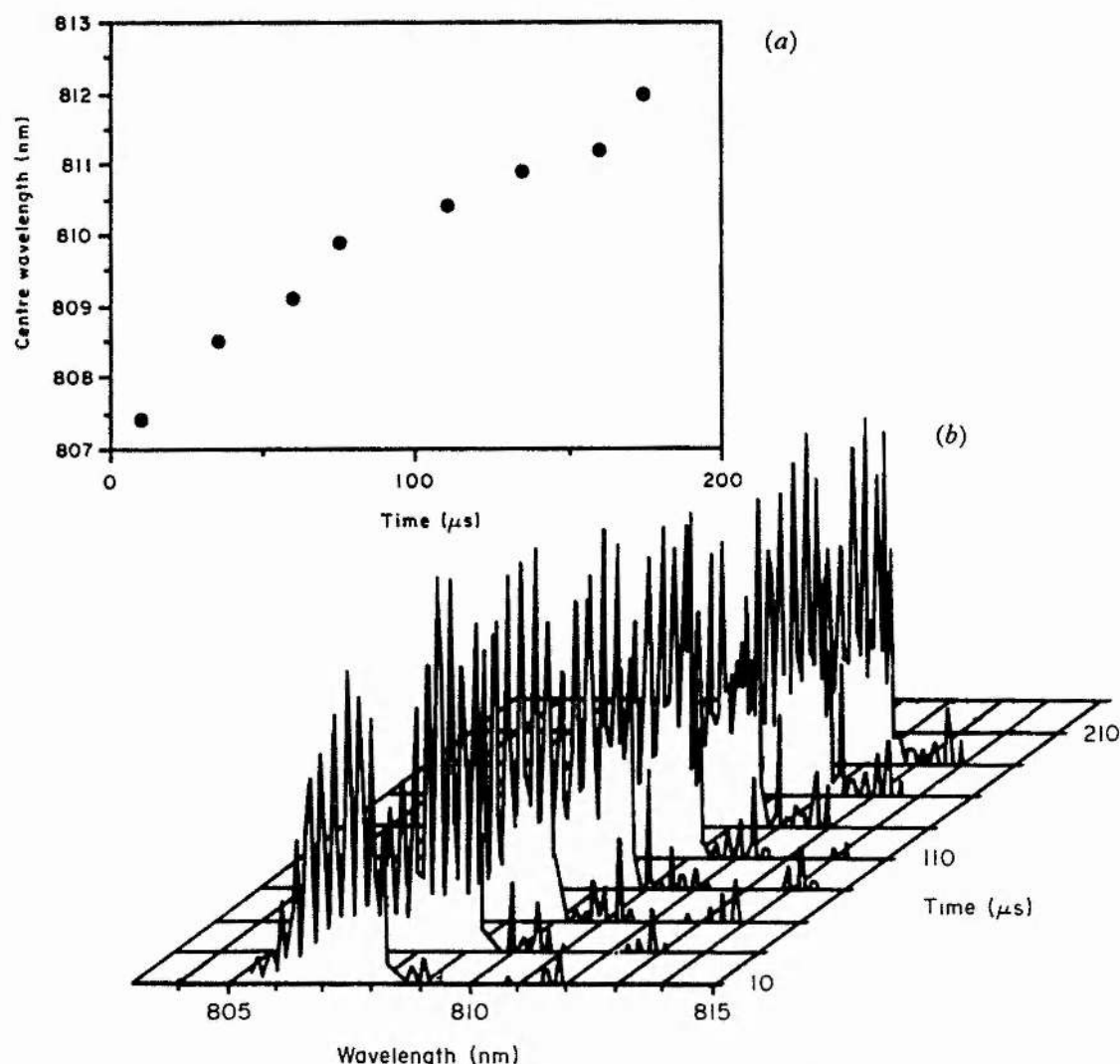


Figure 1. (a) Spectral output of the diode-laser array measured at several instants during the 200  $\mu\text{s}$  long pulse (100 Hz repetition rate, 25 W pulsed power). (b) Sweep of the central wavelength as a function of time into the current pulse.



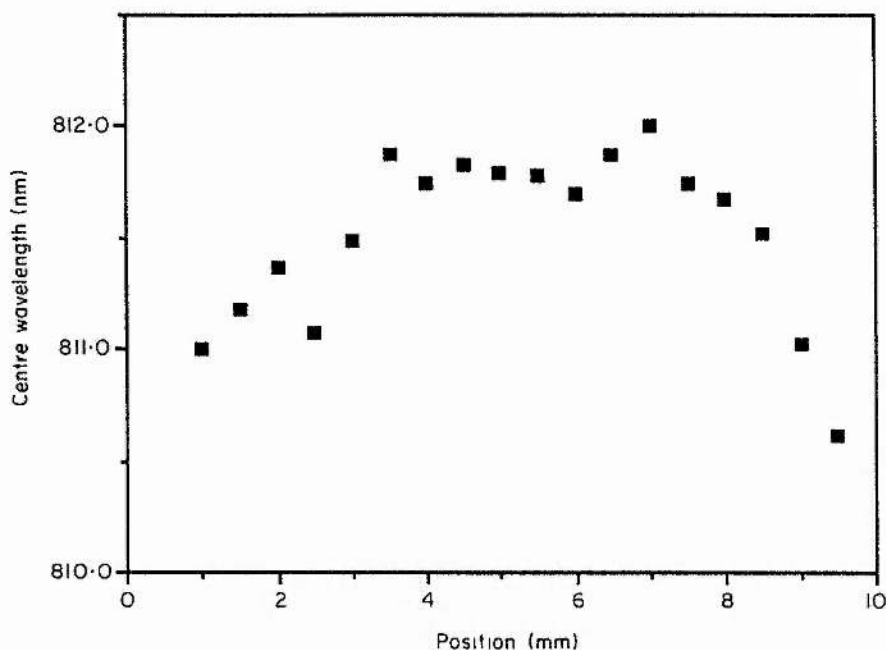


Figure 2. Variation in lasing wavelength of the laser array across its 1 cm emitting facet (conditions as for figure 1).

bandwidth of some 2 nm (comparable to that observed from similar c.w. laser arrays), but the centre of this spectral band shifts during the pulse, due most probably to the thermally-induced change in the bandgap of the GaAlAs. The sweep of the central wavelength was 4.8 nm in 200  $\mu$ s, which corresponded to a time-averaged bandwidth of some 5 nm. The centre wavelengths of the output from different portions of the array were also measured using the same method and the results are shown in figure 2. This spatially resolved study of the output shows a variation in wavelength of 1.5 nm across the laser bar. This may be attributed to slight non-uniformities in the growth of the structure, or temperature variations across the array. (Although we have performed these measurements on only one such laser, our data suitably complement those taken by the manufacturer for a range of diode-arrays [G. L. Harnagel 1988, private communication].) A combination of these two effects resulted in a linewidth of approximately 6 nm when the laser was operated at maximum average-power, and it is to be expected that this increased linewidth will adversely affect the pumping efficiency of the Nd:YAG laser.

The observed 4.8 nm wavelength sweep during the pulse is considerably greater than the 2 nm f.w.h.m. absorption peak in Nd:YAG at 809 nm (see figure 3 [11]). The absorptivity of Nd:YAG drops to 0.34 mm<sup>-1</sup> at the sides of a 6 nm bandwidth, which corresponds to only 50% absorption in the 2 mm diameter of the miniature Nd:YAG rod that was used. This rod was 11 mm long with Brewster-angled faces, and had a polished flat along its length for coupling in the pump radiation (the small diameter was necessary to increase the amount of usefully pumped material). In order to improve the pumping efficiency we used a reflective mount for the rod, to focus the transmitted pump-light back into the active medium, thus reducing the deleterious effects of the frequency sweep of the pump radiation on the operation of the Nd:YAG laser.

The influence of the frequency sweep on the small signal gain in the Nd:YAG rod was studied. A diode-laser-pumped single-frequency c.w. Nd:YAG laser was

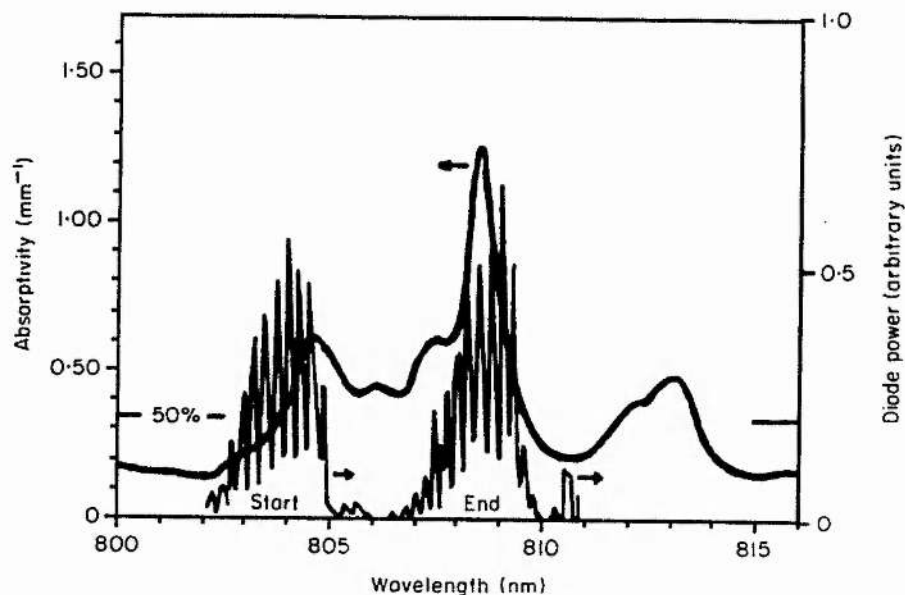


Figure 3. Absorption spectrum of Nd:YAG with the spectral output of the diode-laser array near the start and end of the pulse superimposed upon it. The 50% line indicates the absorptivity at which half the pump light is absorbed in a 2 mm path length.

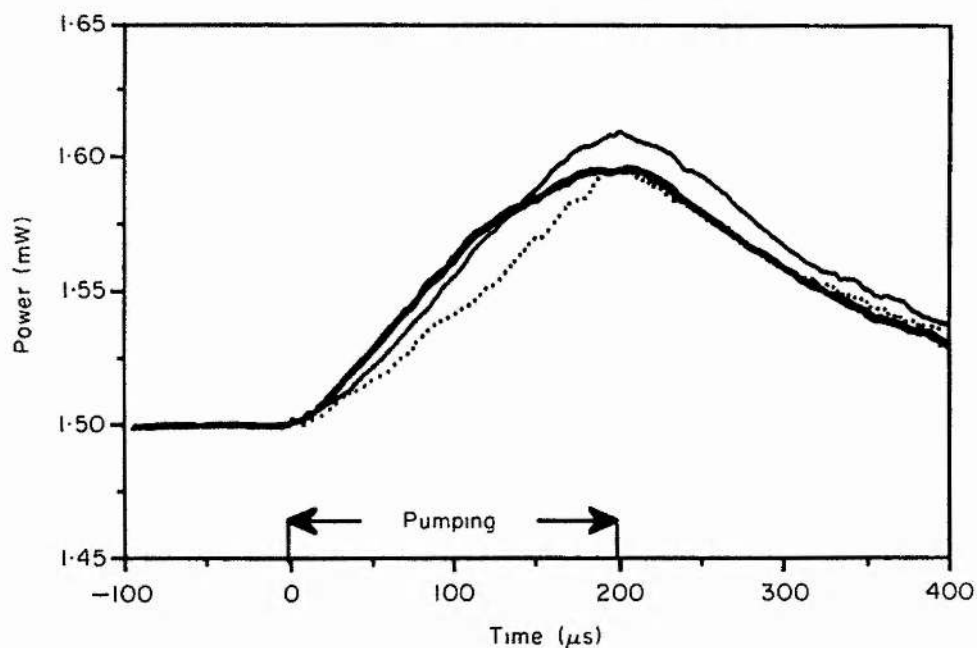


Figure 4. Small-signal gain in the side-pumped Nd:YAG rod measured during the 200  $\mu$ s long, 25 W pump-pulse, with different temperatures of the diode-laser heat-sink (and therefore different wavelengths of the diode-array output): 4°C (dotted curve), 8°C (thin curve) and 20°C (thick curve).

used to provide 1.5 mW of 1.06  $\mu$ m radiation which was focused axially through the side-pumped rod. Figure 4 shows the rate of rise of small-signal gain (seen as the gradient of the detected power) falling at the start or end of the pumping pulse for temperatures below or above the optimum, respectively. When the diode-laser was temperature-tuned to the optimum range of swept wavelengths the final gain (see as the maximum detected power) is greatest, and the rate of rise of small-signal gain



remains tolerably high throughout the pulse. Although the reflector eased the effects of the decreased absorption due to the frequency sweep, the diode-laser radiation still had to be closely spectrally-matched to the optimum absorption band. An alternative approach to reducing the effects of the wavelength sweep would have been to use a solid-state medium with broader absorption bands, such as Nd:YVO<sub>4</sub> [9].

Lasing was obtained when two 10 cm radius-of-curvature mirrors were suitably incorporated to form an optical cavity, for which an output coupling of 5% was found to be near optimum. When pump light was coupled into the Nd:YAG rod using either lenses or close coupling, pulsed output-powers at 1.06  $\mu\text{m}$  of 1.9 W and 6.5 W were obtained respectively. The 1.06  $\mu\text{m}$  laser output consisted of damped relaxation oscillations, delayed by 35  $\mu\text{s}$  from the start of the injection current pulse to the diode array. This amplitude modulation of the output had decreased to 5% about 100  $\mu\text{s}$  after the onset of lasing. A slope efficiency of 22% was measured with the 5% output coupler and close coupling of the pump light into the rod. This is to be compared with the 31% efficiency that we obtained for an end-pumped c.w. system, and shows that if suitable steps are taken to limit the adverse effects of frequency-sweeping in the diode-laser array then good efficiencies may still be retained at high powers. These data were taken for the laser operating in a multi-transverse mode. Single transverse mode operation was obtained when the resonator was arranged to give a larger beam-waist (0.26 mm full-width) and the rod diameter was reduced to 1 mm. In this case, with a 15 W quasi-c.w. pump, 1.3 W of TEM<sub>00</sub> 1.06  $\mu\text{m}$  radiation was produced, with no intra-cavity apertures required.

We have undertaken preliminary studies of *Q*-switched versions of this laser system. A Newport Electro-Optics 9NSI acousto-optic *Q*-switch was inserted into the cavity, and the output coupling was increased to 20%. When the *Q*-switch was opened at the end of the 200  $\mu\text{s}$  pump-pulse the laser produced 44 ns, 6.1 kW peak power pulses in multi-transverse mode operation, and 50 ns, 1.2 kW pulses in a single transverse mode, using the modified system.

### 3. Conclusions

Substantial frequency sweep in the output of a quasi-c.w. diode-laser array has been measured. We have shown, that relatively simple measures can reduce the effects of the wavelength variation, and we have constructed a Nd:YAG laser operating at 1.06  $\mu\text{m}$  which produced 6.5 W, 180  $\mu\text{s}$  pulses, and a *Q*-switched version of this laser which produced peak powers of 6 kW. Such devices have considerable potential for many applications including semiconductor processing, coherent light detection and ranging (LIDAR), and remote-sensing.

### Acknowledgment

This work was supported by the Procurement Executive of the UK Ministry of Defence. Personal support was provided by the same source (BDS), by SERC (NG), and by an SERC CASE award with British Aerospace (CJN).

### References

- [1] CROSS, P. S., HARNAGEL, G. L., STREIFER, W., SCIFRES, D. R., and WELCH, D. F., 1987, *Science*, **237**, 1305.
- [2] HARNAGEL, G. L., CROSS, P. S., SCIFRES, D. R., and WORLAND, D. P., 1986, *Electron. Lett.*, **22**, 231.

- [3] HARNAGEL, G. L., CROSS, P. S., SCIFRES, D. R., WELCH, D. P., LENNON, C. R., and WORLAND, D. P., 1986, *Appl. Phys. Lett.*, **49**, 1418.
- [4] HARNAGEL, G. L., CROSS, P. S., LENNON, C. R., DEVITO, M., and SCIFRES, D. R., 1987, *Electron. Lett.*, **23**, 743.
- [5] HANSON, F., and HADDOCK, D., 1988, *Appl. Optics*, **27**, 80.
- [6] REED, M. K., KOZLOVSKY, W. J., BYER, R. L., HARNAGEL, G. L., and CROSS, P. S., 1988, *Optics Lett.*, **13**, 204.
- [7] Spectra Diode Labs model SDL-3220-J.
- [8] BYER, R. L., 1988, *Science*, **239**, 742.
- [9] FIELDS, R. A., BIRNBAUM, M., and FINCHER, C. L., 1988, *Conference on Lasers and Electro-Optics*, Anaheim, postdeadline paper PD3.
- [10] KOECHNER, W., *Solid State Laser Engineering*, 1976 (Berlin: Springer Verlag).
- [11] HADLEY, G. R., OWYOUNG, A., ESHERICK, P., and HOHIMER, J. P., 1988, *Appl. Optics*, **27**, 819.